SCUOLA DI DOTTORATO

UNIVERSITÀ DEGLI STUDI DI MILANO-BICOCCA

Department of Materials Science

PhD program in Materials Science and Nanotechnology, XXXIII Cycle

Spectroscopic avenues and photophysical phenomena in Colloidal Nanocrystals

Abhinav Anand

Matr. n. 835017

Tutor: Prof. Sergio Brovelli

Supervisor: Prof. Francesco Meinardi

Coordinator: Prof. Marco Bernasconi

ACADEMIC YEAR 2019/2020

Acknowledgements

The last three years have been one of the most important years in my life where I learnt a lot, not just in terms of academics but I also immensely matured and grew as a person. These three years cannot be just summarized in this book; there has been a lot more to it than what can be read in my thesis. These three years have not only been about the results presented in the following pages, but also about the experiences, the emotions, the lessons taught by life and so on. Most of all, it was about the kind of people I was blessed enough to be surrounded by, who made these years delightful and smooth.

First and foremost, I would like to express my sincere gratitude to my tutor Prof. Sergio Brovelli and my supervisor Prof. Francesco Meinardi for their constant support during my Ph.D. study and related research, for their patience, motivation, immense knowledge and teachings. Their guidance helped me in all the times of research and writing of this thesis. Needless to say, I would not be where I am today without them. Moreover, I would extend my gratitude to Prof. Marco Bernasconi, coordinator of PhD program in Materials science and nanotechnology and the doctoral school, University of Milano-Bicocca for their technical and financial support.

I would like to convey my appreciation and regards to all the collaborators I got a chance to work with during this time. I would like to extend my courteous thanks to Prof. Iwan Moreels, University of Ghent, Belgium, who hosted me for six months of my research period abroad and for the warm hospitality extended to me by his research group. During this time, I gained an additional dimension to my research and learnt the art of synthesis in his lab, in a way giving me a sense of completeness as a material scientist. Lots of thanks to Prof. Liberato Manna and his group for the perovskite samples, Prof. Marco Fanciulli for ESR measurements, Dr. Scott Crooker for the collaborative efforts in MCD measurements, Prof. Margherita Zavelani-Rossi and Dr. Andrea Camellini for TT measurements, Dr. Rosaria Brescia for elemental analysis and Glass to Power Spa. for all their efforts and resources during these years.

I would like to extend my sincere thanks to all my lab mates who are like a family away from home. Special thanks to Prof Angelo Monguzzi for his technical support. My sincere gratitude to Valerio for his immeasurable patience and help with spectroscopy and for being there as a

friend whenever I needed him, Graziella and Chiara for all the samples, Frappa for the discussions about synthesis protocols as well as his passion for chess, Sandra, Matteo, Andrea, Dario, Jacopo, Marina, Francesco Bruni and all the thesis students for their kind and enjoyable company throughout these years.

I would also like to express my deepest regards to Alina for being the closest all this way, Ali and Chandu for being the best of friends/mentors, and all the people in PCN, Ghent for making my stay there, one of the best periods during the course.

Specially, I would like to thank my parents for their blessings, motivation and support, all along the way and making their love felt, no matter the distance between us.

Last but not least, thanks to Almighty for blessing me with good health and surrounding me with such good people all along.

Preface

Since almost four decades ago that the quantum size effects in nanocrystals (NCs) were showcased, tons of research have been carried on in the field of semiconductor nanostructures. The revelation of their size dependent electronic energy levels enabled precise control over the energy band gap of such entities resulting in development of such materials in various optoelectronic and photon management devices. But with the advent and rapid development of solution synthesis technology, a large number of nearly monodisperse, solution based NCs of different sizes, shapes, chemical composition and crystal structures have emerged over the last thirty years. This enabled the tuneability of the emitted photons between ultraviolet to infrared spectral wavelengths. Moreover, passivation of the surface dangling bonds by the application of organic ligands, was shown to enhance the photoluminescence quantum efficiency. Also, improvement in florescence efficiencies and Stokes shift engineering of emission suitable for various photon management technologies was brought about through the emergence of core-shell heterostructuring with different core and shell materials controlling the individual charge carrier wave functions. These persistent efforts by research groups all over the world lead to these NCs being realised in diverse practical applications. During the last three years of my learning, thanks to their exceptionally favourable optoelectronic properties, I have focused my research in understanding such NC systems with unparalleled potential in photon management technologies such as Luminescent Solar Concentrators, solar cells, LASERs, LEDs and other devices of paramount significance to the humankind.

Through the course of this thesis, I showcase and discuss my work on four different NC systems split in four chapters following the chapter on introduction to nanostructures (Chapter 1: State of the Art) describing the evolution of diverse classes of NCs over the years and their standard synthesis techniques and photophysical properties. Apart from this in chapter-1, I describe the electronic states of these nanosized entities compared to their bulk counterparts, significance of Bohr radius and the effects of confinement of charge carriers and Coulombic interactions. Finally, I conclude this chapter by talking about the importance of the special optoelectronic properties of different NCs and various techniques like heterostructuring, impurity doping and using heavy metal free alternatives to enhance the emission quantum yield and induce a finite Stokes shift in emission to exploit the full applicative potential of these materials in photon management technologies.

In chapter 2, I studied the most favorable intrinsic ternary $CuInS_2$ NCs which inherently offers heavy metal free, non-toxic alternatives with a large Stokes shift and long photoluminescence decay time. The origin of these optical properties in $CuInS_2$ NCs were however not fully understood with conflicting theories describing its characteristic aforementioned properties. A recent theoretical model by Efros and co-workers suggested that their characteristic Stokes-shifted and long-lived luminescence arises from the structure of the valence band and predicts distinctive optical behaviors in defect-free NCs: the quadratic dependence of the radiative decay rate and the Stokes shift on the NC radius. Here, subsequential to experimentally confirming the valence band fine structure origin of luminescence in these nanostructures, we utilized the optimized NCs and fabricated a large area Luminescent solar concentrator of 30×30 cm^2 area with record Optical Power Efficiency of 6.8% to the date.

Then, in chapter 3, I report and discuss the effects of electronic impurity doping in binary chalcogenide NCs synthesized by a novel seeded growth procedure resulting in quantized dopants in each NC thus overcoming the Poissionian bottleneck for their diluted magnetic semiconductor properties. Structural, spectroscopic, and magneto-optical investigations trace a comprehensive picture of the physical processes involved, resulting from the exact doping level of the NCs. Gold atoms, doped here for the first time through the reaction protocol into II−VI NCs, are found to incorporate as non-magnetic Au^+ species activating intense size-tuneable intragap photoluminescence and artificially offsetting the hole occupancy of valence band states. Fundamentally, the transient conversion of Au^+ to paramagnetic Au^{2+} ($5d^9$ configuration) under optical excitation results in strong photoinduced magnetism and diluted magnetic semiconductor behavior revealing the contribution of individual paramagnetic impurities to the macroscopic magnetism of the NCs unlocking their potential to be exploited for applications in quantum and spintronic devices.

I then move on to the new kids on the block with exciting and intriguing properties- "Perovskites." Here, in chapter 4, I communicate the thus studied effects of substitutional doping with paramagnetic atoms and a peculiar energy transfer mechanism subsequently resulting in dual PL emission and inducing Stokes shift desirable for photon management technologies. This sensitization mechanism was far from understood and no comprehensive picture of the energy-transfer process had been proposed. Similarly, the role of shallow states, particularly abundant in defect tolerant materials, was still unknown. Here, I addressed this problem via spectroscopic studies at controlled excitation density and temperature on Mn:$CsPbCl_3$ NCs. The thus reported results in chapter 4 demystify anomalous behaviors of the

exciton-to-dopant energy-transfer mechanism and highlight the role of shallow defects in the photophysics of doped perovskite nanostructures.

Finally, I conclude the thesis in chapter 5 by outlining my ongoing work on colloidal two-dimensional CdTe nanoplatelet systems. Resulting from strong quantum confinement in only one direction and the large lateral size, the CdTe nanoplatelets exhibit large exciton binding energy, giant oscillator strength, narrow emission, large absorption cross-section, suppressed Auger recombination, and large optical gain. In this chapter I discuss the significance of such two-dimensional floating entities and try to develop an understanding of the various standard synthesis protocols developed to date and reaction kinetics involved in it. Moreover, I also report some very interesting preliminary spectroscopic data that presents these NC systems at great heed with respect to their application in lasing technology and in Ultrafast radiation detection applications. However, the work involving CdTe nanoplatelets' application in lasing was a part of my research period abroad and is an active ongoing research project in Physics and Chemistry of Nanostructures (PCN) group University of Ghent, under the supervision of Prof. Iwan Moreels.

Through the course of this work, I worked on the colloidal synthesis of nanostructures, a part of which is described in chapter 5 and studied the aforementioned NC systems using structural characterization techniques like X-Ray diffractions and Transmission Electron Microscopy. Spectroscopic techniques including Ultrafast Transient Absorption, Steady state and Time resolved photoluminescence spectroscopy at cryogenic temperatures, Magnetic Circular Dichroism and Electron paramagnetic resonance were used to study and report these nanostructures, thus trying to elucidate their fundamental photophysics and exploit their applicative potential in modern, next generation technologies.

Contents

List of figures

Chapter 1

State of the art

Synopsis

Colloidal NCs owing to their size tunable electronic properties and solution processability, have long been proposed as versatile, chemically synthesized alternatives for many photonic and optoelectronic technologies as well as super-atomic building blocks for bottom-up assembled artificial metamaterials. Since their discovery over 30 years ago, tremendous achievements in colloidal synthesis and surface chemistry, the NC physics and device applications have brought this vision closer to reality. During the last three years of my learning, thanks to their exceptionally favorable optoelectronic properties, I have focused my research in understanding such NC systems with unparalleled potential in photon management technologies such as Luminescent Solar Concentrators, solar cells, LASERs, LEDs and other devices of paramount significance to the humankind. Through the course of this I studied the most favorable intrinsic ternary $CuInS_2$ NCs which inherently offers heavy metal free, non-toxic alternatives with a large Stokes shift and long photoluminescence decay time. Subsequential to experimentally confirming the valence band fine structure origin of luminescence in these NC systems, we utilized the optimized NCs and fabricated a large area Luminescent solar concentrator of 30^x30 cm^2 area with record Optical Power Efficiency of 6.8% to date. Then, I studied the effects of electronic impurity doping in binary chalcogenide NCs synthesized by a novel seeded growth procedure resulting in quantized dopants in each NC thus overcoming the Poissionian bottleneck for their Diluted Magnetic Semiconductor properties and potential applications in quantum and spintronic devices. I then moved on to the new kids on the block with exciting and intriguing properties-"Perovskites." We studied the effects of substitutional doping with paramagnetic atoms and a peculiar energy transfer mechanism subsequently resulting in dual PL emission and inducing

Stokes shift desirable for photon management technologies. Through the course of this work, I worked on the colloidal synthesis of NCs and studied the aforementioned NC systems using Ultrafast Transient Absorption, Steady state and Time resolved PL spectroscopy at cryogenic temperatures thus trying to elucidate their fundamental photophysics in an attempt to be used for technological advancement.

1.1 Prologue

One of the most important attributes of a semiconductor material which distinguishes it from metals and insulators is its forbidden energy gap (E_g) which separates valence band from the conduction band and mediates the thermal excitation of a finite amount of charge carriers from valence to the conduction band. In macroscopic or so-called bulk semiconductors, the width of this inhibited gap is a fixed quantity dictated by the crystal structure and atomic composition of the respective material. Interesting photophysical properties arise when electrons from the packed valence band are promoted to the conduction band where they are relatively more mobile **(Figure 1.1)**. This process of an electron excitation can be executed upon an electromagnetic radiation falling incident on the material with energy equal to or more than the width of this forbidden E_g of the semiconductor material[2]. This process results in an excited electron in the semiconductor conduction band coulombically bound to a hole (vacancy of an electron) in the valence band termed as 'exciton'[3] neutral quasiparticle. This quasiparticle is formed in a semiconductor when the binding energy exceeds the thermal energy of the system. Subsequently, the excited charge carrier may radiatively recombine (or may involve other non-radiative recombination routes) with its counterpart, emitting photons with distinct energy equal to E_g of the material. However, when the size of such semiconductor systems is reduced beyond the characteristic bulk exciton Bohr radius (a_0) which typically ranges from as 2.1 nm in II-VI (ZnS) to 60 nm in III-V (InSb)[4] group semiconductors, the energy of emitted photons becomes dependent on the particle size leading to atomic-like optical behavior in NCs as the bulk bands become quantized **(Figure 1.1)**. This is a result of the electronic excitations 'sensing' the particle boundaries as a consequence of arising contributions from tight spatial confinement of the charge carriers and their localization in addition to the existing Coulombic interactions. The size regime in which this phenomenon becomes relevant and pronounced is called 'Quantum confinement regime' and the particles falling in this size regime are called 'Quantum dots (QDs).' Respecting the scope of this thesis, I refer to these QDs as spherical NCs throughout, unless otherwise specified for different

shapes of the same like nanoplatelets (NPs), nanorods (NRs) etc. It was almost four decades ago that the size dependence of semiconductor NC optical properties were discovered and reported independently in two different materials: semiconductor-doped glasses[5-8] and colloidal solutions.[9-11] The emitted colour from NCs in both cases exhibited strong correlation to their crystal sizes. Interestingly, the underlying thermodynamic process of microscopic phase separation in a supersaturated solution was common in the synthesis of NCs in both cases. The size of the NCs rooting from the nuclei of the new phase is controlled by diffusion of the atoms or ions to the growing nucleus and the degree of supersaturation and the duration of the phase separation process dictates their size distribution. It was shown by Itoh and Krihara[12] that the same NC growth mechanism can be employed in semiconductor crystal lattices as well as in liquid and solid solutions. Intriguing initial insights into the optoelectronic properties and photophysical aspects in confined NCs like the structure of electronic states[13, 14], electron-phonon interactions[15-18], intra-band gap relaxations[19, 20], non-linear optical effects[21], Auger recombination mechanisms[22-24] and the fundamentals of lasing[25] were studied on the glass based samples. However, owing to their solution processibility, easy and effective size control and improved surface passivation, colloidal NCs have gained immense attention in the last 30 years or so showcasing tremendous applicative potential.

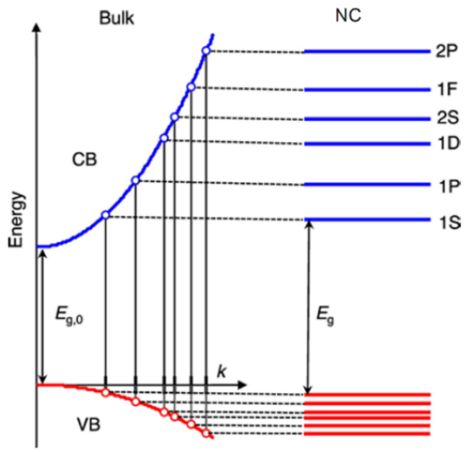

Figure 1.1: Idealized model of electronic states in a bulk semiconductor and a spherical NC made of the same material. Continuous bands of a bulk semiconductor with parabolic dispersion of carrier kinetic energies in the valence and conduction bands (denoted VB and CB, respectively) transform into discrete atomic-like levels in the case of the NCs. The vertical lines depict nominally allowed optical transitions according to the simple selection rules $\Delta n = 0$ and $\Delta L = 0$.[26] (Reprinted with permission from ref[27]. Copyright 2016 American Chemical Society.)

One of the most significant results in the domain of colloidal NC synthesis was contributed by Bawendi et al.[28] with synthesis and characterization of CdX (X=Se, Te, S) binary II-VI NCs through a novel and highly effective organometallic route employing strongly coordinated

ligands almost three decades ago. This route was subsequently applied for the development of colloidal compositions of III-V, IV-VI, III-VI and group IV nanostructures. Three years after this breakthrough report, Guyot-Sionnest, P et al.[29] introduced type I heterostructuring by using ZnS shelling on CdSe NCs to enhance the photoluminescence efficiency of the material thus marking another significant advancement in colloidal NC chemistry. This opened new avenues and directions in optimizing a material's electronic and optical properties including 'wavefunction engineering'[30-32] and methods for NC shape control.[33, 34] However, development of spectroscopic routes to understand the fundamental photo-physical processes resulting in emission in these nanostructures was of utmost importance. This underlying principle of light emission from binary NCs involving exciton fine structures[35, 36] was one such breakthrough. Moreover, significant progress has been made over the years in demystifying various processes like energy relaxation mechanisms[20, 37-39], charge carriers recombination physics[40], and multi carrier phenomena[41-43]. The evolution of single particle spectroscopy enhanced the understanding of these fundamental processes in individual NCs freeing them from the ensemble shortcomings[44-47]. Owing to the development and deeper understanding of the chemical synthesis, in-solution processing of these nanostructures and their underlying photophysics and expansion and implementation of this knowledge to other new materials has resulted in the emergence of first NC based technologies. Exploiting the technological potential from theses NCs in most applications warrant highly monodisperse, broadband absorption and highly efficient, colour tuneable and stable emission. For instance, quantum dot Light Emitting Diodes (LEDs) were fabricated and demonstrated as a proof of principle of the emission properties in CdSe NCs[48, 49] more than two decades ago have culminated in the research in this field almost reaching the roof in terms of device operating near fundamental power-conversion limit. More recently, narrow, highly emissive Cd based heterostructures were applied in quantum dot display technology as colour converters by Jang et al.[50] Apart from display applications, NCs exhibiting broad absorption and stoke shift engineered tuneable emission have been used in light harvesting applications such as active layers in photovoltaics.[51-53] This was for the first time, almost a decade ago, demonstrated by Luther et al.[54] obtaining a 3% power conversion efficiency using PbS/ZnO NCs heterojunction solar cells. Subsequently, with time and persistent efforts in chemical engineering methods in NC synthesis, the efficiencies of NC based photovoltaic devices have more than tripled now exceeding 10%.[55, 56] However, the recent research has been shown to be increasingly dedicated to the observation of current enhancement via multiexciton generation processes in photovoltaic devices.[57, 58] Moreover, a significant chunk of light harvesting research has been focussed on Luminescent

Solar concentrators (LSCs) for the development of almost transparent photovoltaic windows.[59-62] which will be discussed more elaborately in the subsequent sections and the next chapter. The development of highly emissive, biocompatible QDs allowed their use in biolabeling, bioimaging, and medical diagnostics[63-65] among many more applications.

1.2 Colloidal nanocrystal synthesis

Semiconductor NCs with critical dimensions less than 100 nm exhibit superior chemical, mechanical, electronic, and optical properties that are often significantly different from their corresponding bulk counterparts. These unique properties depend on the atomic structure, size confinement, composition, microstructure, defects, and interfaces, all of which can be tailored by synthesis and other designing processes. Well known methods of their fabrication of both physical (require high energy input) and chemical nature include molecular-beam-epitaxy, metalorganic chemical vapor-deposition, and vapor-liquid-solid, as well as particle growth in glasses, and colloidal chemical synthesis. However here, pyrolysis of metal-organic precursors in hot coordinating solvent stabilizers (120-360 °C) will be discussed at length.

Luminescent colloidal NCs provide an opportunity to cover a wide range of emission wavelengths across the visible spectrum. Their high-temperature synthesis procedures offer crystalline materials, soluble in both polar and nonpolar solvents, with precise dimensions, high monodispersity, and well-defined optoelectronic properties. To explain the underlying processes of colloidal formation of such QDs syntheses, the classical nucleation theory (developed by Becker and Döring in the 1930s) with its transformation to NCs by LaMer and co-workers in the 1950s is still seen as the basic model[66, 67]. According to the classical nucleation theory, the high temperature colloidal process is a two-step bottom-up process. The organometallic molecular precursors injected in the mixture first react to form an actual critical-sized monomer, could be dimer/trimer or so on, which is then consumed either by growth of existing particles or by the nucleation of new ones[68] as shown in the **Figure 1.2**. For new particles to form, first, 'nuclei' or small clusters have to be formed. As the concentration of the monomer increases, the concentration exceeds the solubility. At this point no nucleation will take place just yet. These nuclei have very high surface to volume ratio and are therefore high in energy. The energy required to first form these small clusters could be seen as the activation energy to form a particle. Therefore, the concentration must be even higher to surpass the nucleation threshold. Once this threshold is exceeded, a "nucleation burst" takes place. Since the nucleation rate is very sensitive to the supersaturation, a lot of new particles will be formed.

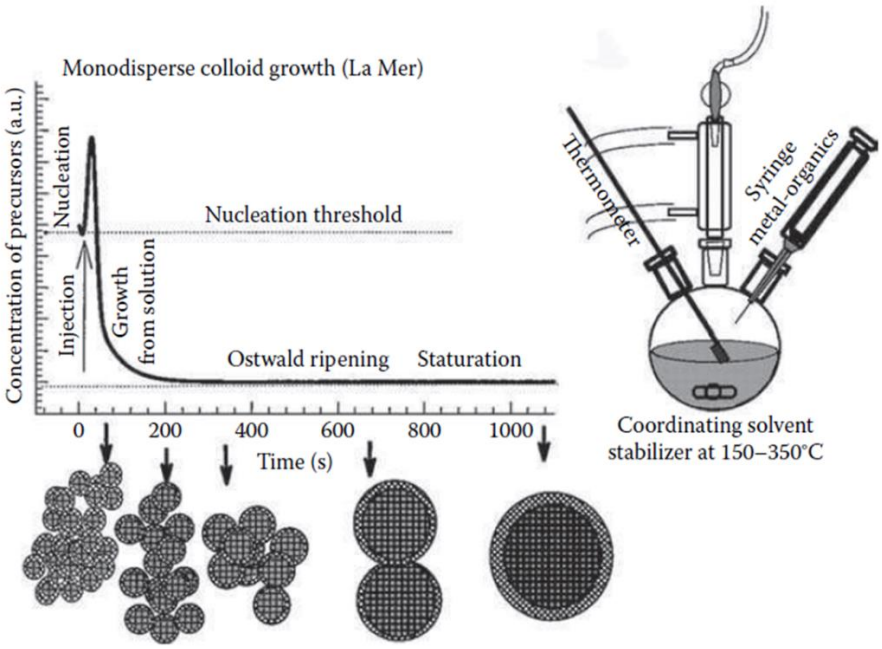

Figure 1.2: Schematic illustrating La Mer's model for the stages of nucleation and growth for monodisperse colloidal particles and representation of the synthetic apparatus employed in the preparation of monodisperse NCs. (Reprinted with permission from Murray, C. B., C. R. Kagan, and M. G. Bawendi, *Annu. Rev. Mater. Sci.*, 30, 545, 2000.)

The monomer will stop increasing once it is consumed by both nucleation of new particles and growth of existing ones. When enough are particles formed, the growth rate is faster than the monomer formation rate, the monomer concentration will fall below the nucleation threshold resulting in the formation of no new particles thereafter. Once the nucleation burst concludes, the remaining particles grow until the concentration drops to the solubility (solubility for particles at their size). Growth and nucleation rates are both supersaturation-dependent. By increasing monomer solubility, the growth is favored over the nucleation. Growth step stops the nucleation step earlier, which leads to the formation of larger NCs. An increase of the precursor concentrations results in an increase of the NC particle size, as the nuclei formed are larger in size. However, on the contrary, large precursor concentrations can also lead to a boost in nucleation, leading to a large amount of nuclei which subsequently grow into smaller NCs, because of the depletion of the amount of precursors during nucleation. Growth, as a surface-catalyzed process, is can be visualized as an interplay between three processes occurring at the interface: diffusion, adsorption and desorption. A narrower size distribution is seen during the growth period. In nanometer scale particles, nucleation suppresses the growth process. During the formation of the particle, diffusion rates to its surface may be significantly decreased by the steric bulk of either coordinating solvent stabilizers or the coordinating ligands, since both

may impose a steric hindrance to approaching monomers and therefore the growth rate would be decreased. To suppress the growth rate in order to get large number of small monodisperse NCs one could prevent the aggregation of nanoparticles by means of electrostatic (their functionalization with charged species) or steric stabilization (with polymers) so that adhesion does not occur. The disadvantage of the bottom-up approach over a top-down one lies in its difficulty to control the aggregation/nucleation effects while scaling up the amount of precursors. Smaller the NCs are, the higher the probability to stick together forming clusters resulting in less surface being exposed. LaMer model in a colloidal NCs synthesis does not concern polydisperse QDs ensembles.

The growth and its subsequent process, Ostwald ripening, have different impacts on the size distribution. During the former, the dispersity of the sizes of the particles remain narrow, while during the later, it widens up a lot. Ostwald ripening is the only dominant growth process at the end of monomer formation, which leads to a broadening of the size dispersion combined with a slow increase of the average diameter of the NCs. Ostwald ripening is the process where small particles dissolve while large ones grow. This is caused by the difference in solubility between small and large particles. In order to increase monodispersity of the colloidal NCs up to the desired value, which is usually a value of standard deviation being equal to 5% corresponding to one lattice constant, the nucleation window has to be narrow. In order to prevent a broadening of the NCs lateral size distribution, the synthesis should be stopped before the Ostwald ripening stage (by removing the heat source), in which large NCs grow in expense of small ones. Alternatively, this can also be achieved by adding additional precursor monomer after nucleation and before the Ostwald ripening starts, which ensures that the additional amount would be added to existing particles rather than new nuclei being formed. Moreover, its addition would rather give rise to smaller particles than to the larger ones, which guarantees the high monodispersity being achieved. Another known method to achieve the desired value of the size dispersion is the size selective precipitation, where upon the titration of a colloidal NCs solution with a “nonsolvent”, typically methanol, only the largest NCs precipitate which are unstable to salvation, and are removed from the solution by means of centrifugation.

The traditional La Mer model does not provide a sufficient general explanation to high temperature injection synthetic routes, since all the three stages, namely nucleation, growth and Ostwald ripening, of a particle growth can occur almost in the same time span. The first two may also be altered in case of strongly coordinating ligands, while Ostwald ripening was also described as a process, where the drop in the particle concentration is observed during its

growth. Manipulating the nucleation size of the newly-formed particles can be performed by changing the precursor concentrations or the injection temperature of the reaction. Controlling the average size of the particle is possible due to interplay of three factors: reaction time, nucleation temperature, and growth temperature. The larger particle size can be achieved through longer reaction times, lower nucleation temperature (lower monomer concentrations are pronounced), and maintaining a higher growth temperature (rate of monomer addition is enhanced).

The photoluminescence studies reveal the presence of two different characteristic emission bands: 'band-edge' and 'deep-trap emissions' on the low-energy side of the former one. Band-edge emission is associated with recombination of carriers in NC's intrinsic quantized states, while deep-trap PL band occurs due to the recombination of the charge carriers trapped on the surface of the particle. The best achieved method of optimizing photoluminescence efficiencies is inorganic epitaxial-shell surface-passivation as described later in this chapter. The other comparable techniques are the use of better coordinating ligands, which act as surface trap sites passivators (For example, because of the less steric hindrance the primary amine ligands pack more efficiently on the NC surface compared to TOP), and the limited reaction times, since PL efficiencies decline after they reach their maximum value with continued reactions.

1.3 Electronic states in NCs

The confinement effects as shown in the previous section, results in the discrete energy states in nanostructures. The underlying photophysics can be better realized by modelling the NC as a semiconductor inclusion in an insulating matrix as shown in **Figure 1.3.** In such a scenario, the photoexcited carriers could be pictured as being trapped in a three-dimensional potential well resulting in discrete, quantized energy levels of charge carriers. As a result of this effect, in contrast to continuous energy distribution in bulk above band gap of the semiconductor (E_{g0}), spectra from semiconductor NCs show series of quantized electronic transitions between the respective energy levels of charge carriers. Subsequently, as the energy levels of the excited charge carriers are extremely sensitive to the extent of confinement as will discussed later in this section, optical spectra of NCs strongly depend on the particle size.

Both linear and nonlinear optical properties of small semiconductor NCs emerge as a consequence of transitions between electron and hole energy sub levels. In a spherical NC surrounded by an infinite potential barrier, the energy of the electron and hole quantum-size

levels, characterized by angular momentum quantum number *L*, can be written in parabolic approximation[69, 70] as

$$E_{n,L} = \frac{\hbar^2 \phi_{n,L}^2}{2ma^2} \quad (1.1)$$

where $\hbar$ is Plank's constant, $\phi_{n,L}$ is the nth root of spherical Bessel function of Lth order, m is the particle mass which is replaced by effective mass of electron (m_e) or hole (m_h) in case of conduction or valence band, respectively, and a is the NC radius.

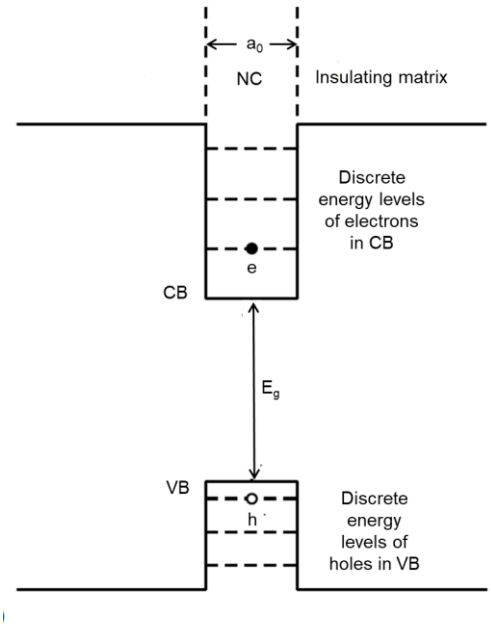

Figure 1.3: Visual interpretation of a NC being surrounded by an insulating matrix resulting in a particle in a box analogy resulting in the quantization of electronic states in CB and hole states in VB.

The energy of the lowest lying level of electron and hole becomes larger with decreasing NC size resulting in enhanced optical transition from E_g. For instance, in CdSe NCs, the E_g can be varied from 1.8eV, its bulk value through visible spectrum to 3eV.[28] However, the resultant optical spectrum is strongly influenced by the Coulombic interactions between the thus generated electron-hole pair as they are both confined in the same NC volume. Hence, size dependence of optical E_g in NCs can be visualized to be due to an interplay of the quantization energy arising from confinement effects and Coulomb interactions between the charge carriers. In terms of magnitude and effectiveness of the two energies, since quantization energy increases with decreasing size as $1/a^2$, and Coulomb interaction which grows as 1/a, becomes a small correction to the quantization energies of electrons and holes in small NCs and reduces transition energies by only a relatively small amount. Nevertheless, in large NCs Coulomb interactions play a larger role in optical transition than quantization energies of the excited

charge carriers. It has been exhibited that the optical properties of these NCs extensively depend on the ratio of NC size 'a_0' and the Bohr radius (a_B). Bohr radius of a particle is defined as:

$$a_B = \epsilon \frac{m}{m^*} a_0 \quad (1.2)$$

Where ε is the dielectric constant of the material, m is the rest mass of electron, m* is mass of the particle and a_0 is the Bohr radius of hydrogen atom.[71] In general, depending on the ratio of a and a_B, three confinement regimes can be determined; *Weak confinement regime ($a>>a_B$)*: In this confinement region, binding energy of an exciton is higher than the quantization energy of both charge carriers resulting in the optical properties of these NCs being determined by the exciton centre of mass. This phenomenon has been extensively studied in CuCl NCs where because of a_B=0.7 nm, the condition of $a>>a_B$ held good for all the investigated samples.[5, 72-74] *Intermediate confinement regime ($a_e>a>a_h$)*: Different values of effective masses of electron and hole in the region $a_e>a>a_h$ gives rise to a peculiar case where one charge carrier (electron) is strongly confined whereas the other (hole) is not. This effect has been observed in the absorption spectra of moderately sized CdS and CuBr NCs.[75-77] *Strong confinement regime ($a<<a_B$)*: In the smaller NCs where Coulomb interactions have minimal impact, optical transitions arise between discrete electron and hole energy sub levels according to the selection rules that allow only transitions between levels with the same quantum numbers. One of the first reports in this regime was shown in CdS NCs.[78] For the rest of the discussions this point forward, we consider only the case of strong confinement.

As stated in the earlier text, both linear and nonlinear optical properties of small semiconductor NCs emerge as a consequence of transitions between electron and hole energy sub levels. These energy states can be calculated, in the first approximation using the simple spherical 'quantum box' model in which the charge carriers are restricted uniformly in all three dimensions by an infinite potential barrier. The evaluation of these states can then be proceeded with by employing the effective mass approximation, in which NC wavefunction is introduced as a product of envelope wave function and a Bloch function.[79] The motion of charge carriers inside the NC is presented by the envelope wave function while Bloch function best describes the carrier motion in oscillating potential of the lattice. However, the interaction between different bands are often negligible and, therefore, the so-called '*single-band approximation'* to a

spherical particle of radius 'a' confined in an infinite potential barrier can be assumed. As a result, the envelope wave function of the spherical box is the product of the spherical Bessel (j_L) and harmonic ($Y_{L,M}$) functions:

$$\Phi_{n,L,M}(a,\theta,\phi) = \frac{\sqrt{2}}{R^3}\frac{j_L(\phi_{n.L}\, a/a_0)}{j_{L+1}(\phi_{n.L})}Y_{L,M}(\theta,\phi)$$

where n, L, M are quantum numbers of the corresponding mechanical problem, 'a' is the radial component and $'\theta' and '\phi'$ are angular components in the considered spherical polar coordinate system and $\phi_{n,L}$ is the nth root of spherical Bessel function of Lth order. The energy states are degenerate with respect to the quantum number 'M' as a result of which the designation of such quantum states involves only the principle quantum number 'n' and orbital angular momentum number 'L' (S, P, D… for L= 1, 2, 3… respectively) as shown in **Figure 1.1**. These quantized energy levels derived from bulk semiconductors, as stated in equation 1.1 are found to be:

$$E_{n,L} = \frac{\hbar^2\phi_{n,L}^2}{2ma^2} \tag{1.3}$$

where m is the particle mass which can be replaced by effective mass of electron (m_e) or hole (m_h) in case of conduction or valence band, respectively. The Bessel function $\phi_{n,L}$, determines the energy of these quantized levels. From the equation above, two observations can be made; the energies of quantized states increase with smaller particle size as the inverse square of 'a' and they are also inversely proportional to the particles' effective mass. This dependence on effective masses of the charge carriers has a substantial impact when it comes to II-VI and III-V semiconductors as here, effective masses of holes dominated by the p-type symmetry in ground state have much larger effective masses than that of s-type symmetry electrons. For example, in CdSe, m_h/m_e~6. This results in the valence band states being far more effected by quantum confinement as compared to the sparse conduction band states.

From equation 1.1, energy of the ground state (n=1) can be written as:

$$E_{1,0} = \frac{\hbar^2\pi^2}{2ma^2} \tag{1.4}$$

Subsequently, the E_g of the NC, calculated as the sum of bulk E_g and the ground state energies occupied by the charge carriers as:

$$E_g^{NC} = E_g^{bulk} + \frac{\hbar^2\pi^2}{2m_e a^2} + \frac{\hbar^2\pi^2}{2m_h a^2} \quad (1.5)$$

$$E_g^{NC} = E_g^{bulk} + \frac{\hbar^2\pi^2}{2m_{eh} a^2} \quad (1.6)$$

where m_{eh} is reduced mass of the electron-hole pair defined as:

$$m_{eh} = \frac{m_e m_h}{m_e + m_h} \quad (1.7)$$

The confinement energy which can be evaluated as the difference between the E_g of the semiconductor NC and its bulk counterpart can be then written as:

$$E_{confine}^{NC} = \frac{\hbar^2\pi^2}{2m_{eh} a^2} \quad (1.8)$$

From equation 1.8, it is evident that the confinement energy of a NC is inversely proportional to the square of particle size.

In the discussion till now, considering the strong confinement regimes, we have discussed exclusively about the confinement effects. Nevertheless, with the involvement of charge carriers, we also must discuss the effects of Coulomb interactions no matter how weak they may be in tightly confined NCs. The coulomb interaction between e-h pair can be formulated as:

$$V_{eh}(\boldsymbol{a}_e, \boldsymbol{a}_h) = -\frac{e^2}{\epsilon|\boldsymbol{a}_e - \boldsymbol{a}_h|} \quad (1.9)$$

where $'\boldsymbol{a}_e'$ and $'\boldsymbol{a}_h'$ are the vector coordinates of electron and hole respectively and $'\epsilon'$ is the dielectric constant. In such tightly bound NC systems dominated by the confinement effects, Coulomb interactions between charge carriers can be visualized to be a small correction to the electronic energies which can be calculated according to the first order perturbation theory. Once applied, this approach yields the first order Coulomb correction to the band gap as:[70, 80]

$$\Delta_{eh} = < \Phi_{1,0,0}(\boldsymbol{a}_e)\Phi_{1,0,0}(\boldsymbol{a}_h)|V_{eh}(\boldsymbol{a}_e, \boldsymbol{a}_h)|\Phi_{1,0,0}(\boldsymbol{a}_e)\Phi_{1,0,0}(\boldsymbol{a}_h) > \quad (1.10)$$

From equation 1.3, ground state envelope function can be calculated as:

$$\Phi_{1,0,0}(a, \theta, \phi) = \frac{1}{\sqrt{2\pi a_0}} \frac{\sin(\pi a/a_0)}{a} \quad (1.11)$$

Using equation 1.9 and 1.11 in equation 1.10, the first order Coulomb correction to the band gap will result in:

$$\Delta_{eh} = -\frac{1.765e^2}{\epsilon a} \tag{1.12}$$

Now because, in strongly confined NCs, confinement energy is enormous compared to the lattice vibration energies, we must limit equation 1.10 to high frequency dielectric constant ($\epsilon \sim \epsilon_\infty$). Thus the size dependent E_g in a NC, taking into account both, confinement effects and Coulombic interactions can be written as:

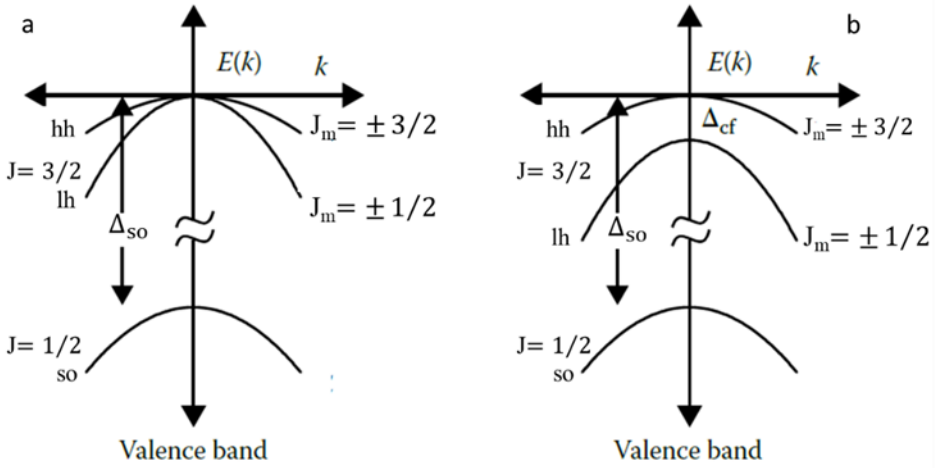

Figure 1.4: (a) Valence band structure at k = 0 for zinc blend semiconductors. Spin–orbit coupling (Δ_{so}) splits the VB into J = 3/2 and J = 1/2 levels at k = 0. Away from k = 0, the J = 3/2 band is further split into J_m = ±3/2 heavy hole and the J_m = ±1/2 light hole sublevels. **(b)** Valence band structure for wurtzite CdSe near k = 0. Owing to the crystal field of the hexagonal lattice, at k=0, $|J_m|$=3/2 and 1/2 bands are split by Δ_{cf} of 26 meV.

$$E_g^{NC} = E_g^{bulk} + \frac{\hbar^2\pi^2}{2m_{eh}a^2} - \frac{1.765e^2}{\epsilon_\infty a_0} \tag{1.13}$$

The single band model of electronic states, described well within the effective mass approximation yields a decent explanation to the conduction band states in NCs. Nonetheless, it majorly fails to justify and describe the valence band states in many materials because of the multi-sub band behavior of valence band arising due to the NC hole states being strongly influenced by mixing between different energy sub levels due to effects of confinement of charge carriers.[14, 81-83] For instance, in II-VI binary semiconductor NCs, CdSe in particular, which has been extensively researched using both theoretical[14, 84, 85] and experimental means[14, 29, 35, 36, 84, 86-102] presents a lucid case of shortcomings in using this single band approximation

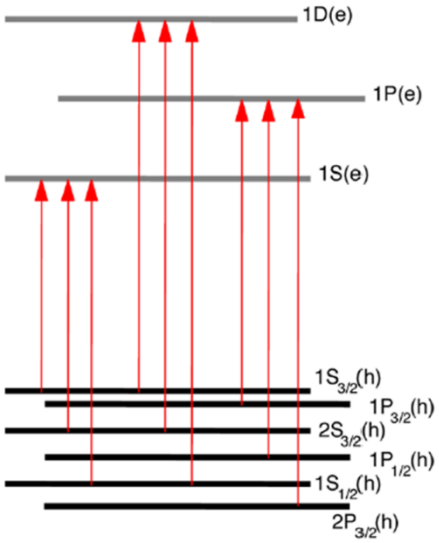

Figure 1.5: The multi-sub-band character of the valence band leads to a more complex structure of hole states in CdSe QDs compared to the single band model, which translates into a more complex structure of interband optical transitions (shown by arrows). (Adapted with permission from ref[26]. Copyright 2016 American Chemical Society.)

model of electronic states. The conduction band arising from S-type atomic orbitals (Cd 5s) is two-fold degenerate emerging due to possible spin orientations at k=0. The valence band on the other hand is derived from six-fold degenerate P-type atomic orbitals (Se 4p) at k=0 with their degeneracy arising from splitting by spin-orbit interactions into lower energy four-fold degenerate band with Bloch function angular momentum J=3/2 and a split-off high two-fold degenerate band with J=1/2 at higher energy. Moreover, the strong spin-orbit interaction in CdSe NCs means that the split-off energy is high (Δ_{SO}~ 0.42 eV[103]) resulting in a negligible contribution of this energy sub level in state mixing in valence band. Instead, most significant contributions to the state mixing inside the valence bands in these NCs are from the J=3/2 bands. Moving away from k=0, the J=3/2 band is further split into their angular momentum projections $J_m = \pm 3/2$ and $\pm 1/2$ sub levels. These two energy sub levels are generally called heavy hole (hh) and light hole (lh) bands respectively as shown in the **Figure 1.4.** Moreover, at k=0, depending on the crystal structure, the heavy hole-light hole splitting is zero for zinc blend NCs and exhibits a finite non-zero value (Δ_{cf}~ 26 meV[103] for CdSe) in the wurtzite form arising due to crystal field splitting in these hexagonal lattices as shown in the **Figures 1.4 a, b** respectively. This effect, which was first shown for bulk impurity centers,[104-106] also leads to hole state mixing[14, 81, 82, 107-109] in NCs. In case of NCs however, due to the spatial confinement, these hole energy sub-levels undergo intermixing and hence it is convenient to use total angular momentum **F** to characterize such hole levels. Total angular momentum **F** can be defined as

the vector sum of Bloch function angular momentum (**J**) and the orbital angular momentum (**L**) of the envelope wavefunction representing the hole energy levels. Moreover, the hole energy levels can be considered to be a result of superposition of the envelope wave functions from multiple orbital momentum values L and L+2 for, **F** would still be conserved, which in some cases can be called 'S-D mixing'. Thus, the lowest energy hole states can be written as $1S_{3/2}$, $1P_{3/2}$, $2S_{3/2}$, $1P_{1/2}$ and so on as shown in the **Figure 1.5** where the subscripts represent projections of total angular momentum and the preceding number represents the lower of the two orbital momenta involved in state mixing. This mixing effect of the valence band sub

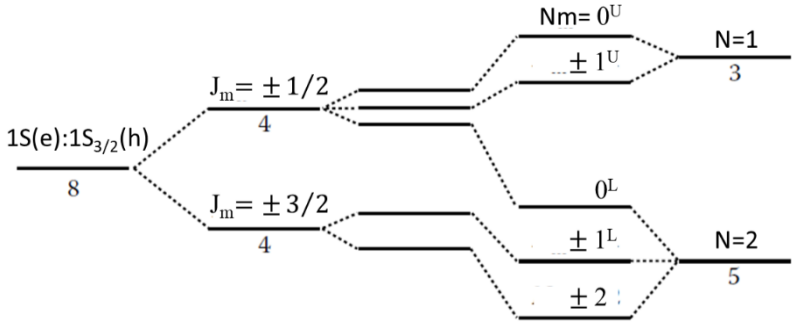

Figure 1.6: Energy-level diagram describing the exciton fine structure. In the spherical model, the band-edge exciton ($1S_{3/2}1S_e$) is eightfold degenerate. This degeneracy is split by the non-spherical shape of the NCs, their hexagonal (wurtzite) lattice, and the e-h exchange interactions.

levels, not only modify the energy representations and structures, but also alters the selection rules involved in optical transitions encompassing such mixed states. More precisely, only spin parity and total hole angular momentum (**F**) are good quantum numbers, while **J** and **L** quantum numbers are not strictly conserved in accordance with selection rules in dipole optical transitions.

As shown in **Figure 1.5** and mentioned previously, ground state exciton in spherical NCs is contributed by $1S_e$ electron in the conduction band and $1S_{3/2}$ hole in the valence band. The spin contributions of electron and hole (1/2 and 3/2 respectively) results in 2 and 4 spin projections respectively which introduces an eight-fold degeneracy of the exciton state. However, this eight-fold degeneracy of the exciton state in principle, is lifted as a result of various second order perturbations. First of these effects arise from the non-cubic crystal structure as described in the text earlier. A hexagonal symmetry in CdSe NCs (wurtzite lattice structure) leads to the splitting of valence band hole ground state of $1S_{3/2}$ into two different angular momentum projections (J_m) of $|J_m|$=3/2 and 1/2 corresponding to the heavy and light holes respectively as shown in **Figure 1.6**. The resultant energy splitting between heavy and

light hole sub levels Δ_{hl}, is independent of the NC size and is analogous to A-B splitting in bulk semiconductors. Nevertheless, Efros et al[110] reported that Δ_{hl} is subject to depend on the ratio (β) of effective masses of light hole (m_{lh}) and heavy hole (m_{hh}) in the valence band ground state.[110] It is also shown that this contribution to splitting of valence band energy levels is almost five times weaker than its counterpart A-B splitting in bulk semiconductors.

Second effect that manifests the lifting of degeneracy in NCs is the shape anisotropy. Electron microscopy experiments show that CdSe NCs are not spherical, but rather slightly prolate.[28] This shape discrepancy further contributes to splitting the electron–hole pair (exciton) states due to the effects on valence band hole state splitting.[111] The contribution to splitting Δ_{sh} is positive or negative in oblate or prolate NCs resulting in increase or decrease of the heavy hole-light hole splitting Δ_{hl} respectively.

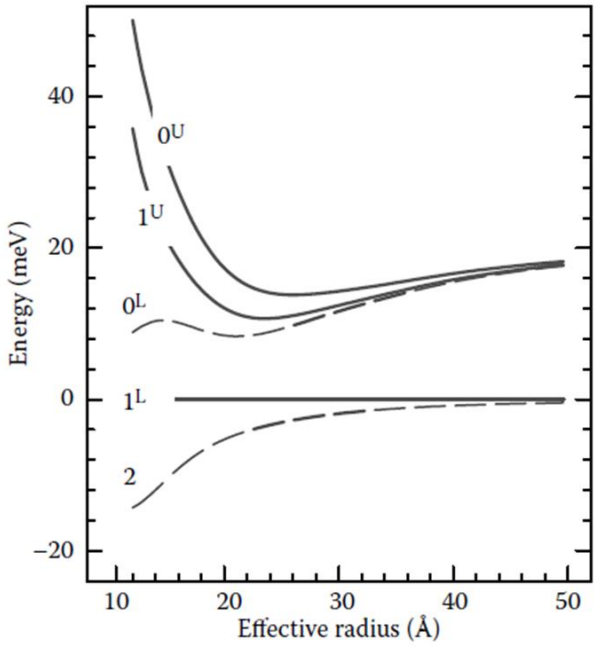

Figure 1.7: Calculated band-edge exciton structure versus effective NC radius. The sublevels are labelled by $|N_m|$ with superscripts to distinguish upper (U) and lower (L) sublevels with the same $|N_m|$. Positions are relative to 1^L. Optically active (passive) levels are shown as solid (dashed) lines. (Adapted from Norris, D. J., Al. L. Efros, M. Rosen, and M. G. Bawendi, *Phys. Rev. B*, 53, 16347, 1996.)

Finally, the electron–hole exchange interaction, which is negligible in bulk CdSe, can lead to level splitting in NCs due to enhanced overlap between the electron and hole.[112-115] This electron-hole interaction arises as a consequence of the wavefunction overlap of the charge carriers in the strong confinement regime in NCs. A combination of spin 1/2 electron in conduction band and spin 1/2 and 3/2 hole in valence band results in two excitonic states each with N_m=0 (0^L,0^U), 1 ($+1^U$, -1^U) and N_m=1 ($+1^L$, -1^L), 2 (+2, -2) respectively. This splitting can be viewed as the band edge exciton state being split into a five-fold degenerate N=2 state and

a three-fold degenerate N=1 state. As a result, crystal field, shape anisotropy and finally electron hole interactions result in five sublevels[35] labelled using the projection of total angular momentum N_m classified as one sublevel with $|N_m|=2$, two sublevels with $|N_m|=1$ and two with $N_m=0$ with the earlier two sub-levels being doubly degenerate as shown in **Figure 1.6**. The anisotropy and exchange interaction terms can be in principle added to the spherical model as perturbations[35] and the resultant exciton fine structure dependence with effective particle radius a_{eff} relative to the 1^L energy sublevel can be portrait as in **Figure 1.7.** The effective particle radius is defined as:

$$a_{eff} = \frac{1}{2}(b^2 c)^{1/3} \tag{1.14}$$

where b and c are the short and long axes of the NC respectively. It is perfectly evident that the fine structure effects arising from the contributions discussed earlier are the strongest for the smallest NCs while with increasing the NCs radii, these exciton energy states converge and approach the A-B splitting as evidenced in bulk semiconductors.

Moreover, in spherical CdSe NCs, $|N_m|=2$ forms the lowest exciton energy state and is deemed to be optically passive since a single photon cannot carry two units of angular momenta. As a result, this exciton state is generally referred to as 'dark exciton state.' The next exciton energy level 1^L as shown in **Figure 1.6** is optically active and hence is referred to as the 'bright exciton state.' The energy difference between these two lowest energy states is defined as dark-bright splitting energy $\Delta_{db,}$ which in larger spherical NCs is inversely proportional to the volume of NC ($\Delta_{db} \propto 1/a_0^3$) and saturates for the smaller NCs at $0.75\Delta_{hl}$.[110] These dark and bright exciton states have important implications in determining their photophysical and optoelectronic properties. While exciton recombination in bulk II-VI semiconductors occurs with radiative lifetime of around 1 ns,[116] CdSe NCs can exhibit a ~1 μs radiative lifetime at 10 K.[35, 88, 117-119] It was first proposed by Calcott et al.,[112] that the presence of exciton fine structures provide an alternative explanation for the anomalous emission behavior. Since emission from the lowest band-edge state, $|N_m| = 2$, is optically forbidden in the electric dipole approximation, relaxation of the exciton from the higher lying 1^L bright exciton state into this state, can explain the long radiative lifetimes observed in CdSe NCs. Because two units of angular momentum are required to return to the ground state from the $|Nm| = 2$ sublevel, this transition is one-photon forbidden. However, less efficient, phonon-assisted transitions can occur, explaining the stronger LO-phonon coupling of the emitting state. In addition, polarization effects observed in luminescence[88] can be rationalized by relaxation from the 1^L sublevel to the dark exciton.[114]

More experimental backing to the presence and influence of the dark exciton states is presented through magneto-optical measurements as was reported by Nirmal et al., also shown in **Figure 1.8.** It can be clearly seen how the external magnetic field influences the emission dynamics in small CdSe NCs. As discussed above, at cryomagnetic temperatures, since splitting between dark and bright exciton sublevels is larger than k_BT, the relaxation always occurs from the

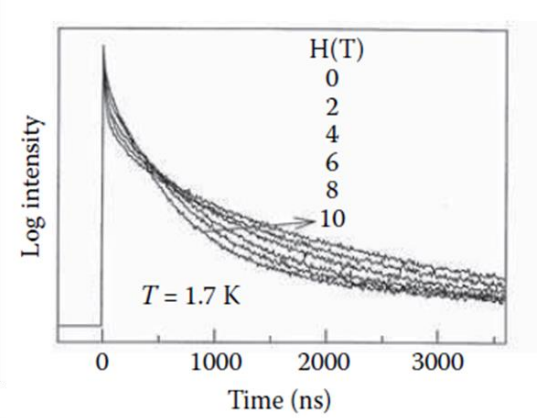

Figure 1.8: Magnetic field dependence of emission decays recorded at the peak of the luminescence. (Adapted from Nirmal, M., D. J. Norris, M. Kuno, M. G. Bawendi, Al. L. Efros, and M. Rosen, *Phys. Rev. Lett.*, 75, 3728, 1995.)

forbidden dark exciton state through highly efficient thermalization from bright exciton state resulting in long emission lifetimes. But, the presence of strong external magnetic field, couples the dark exciton states with optically active bright exciton sublevels resulting in acceleration of decay dynamics with increasing magnetic field as shown in **Figure 1.8.**

The understanding of these results and extensive knowledge of the origin of fundamental photophysics and the resulting optoelectronic properties in these semiconductor NCs are paramount in course of these materials being improved and idealized for exploiting their applicative potential in various photon management technologies.

1.4 NCs for Photon management technology

Photon management technologies like LSCs have historically been dominated by organic and organometallic materials which although offer stability but lack in providing the best combination of optical properties of broad and efficient absorption across the UV-visible spectrum, superior florescence and the desired Stokes shift to prevent reabsorption losses. In fact the best organic composites were seen to only partially fulfil the requirements to make an ideal photon management device in particular lacking due to limited solar coverage and/or enhanced reabsorption losses.[120, 121] In particular, in LSC technologies, as shown in the **Figure**

1.9 various organic and organometallic composite fluorophores include red emitting 4-dicyanomethyl-6-dimethylaminostiryl-4H-pyran (DCM) which offers sufficient Stokes shift negating the losses due to reabsorption but suffers from poor solar coverage,[122, 123] yellow emitting CrS040 dye with an even poorer performance suffering from insufficient

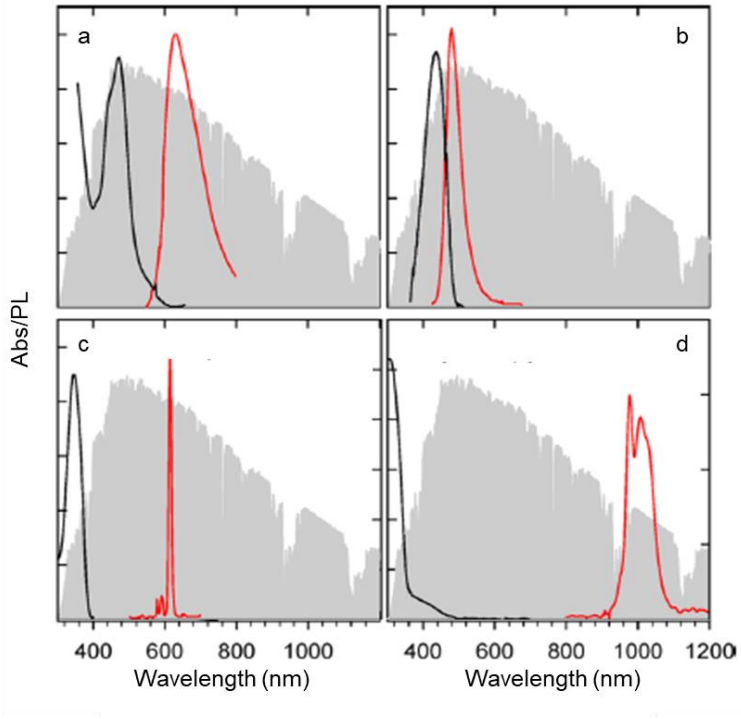

Figure 1.9: Optical absorption (black lines) and PL spectra (red lines) of some organic LSC dyes: **(a)** 4-dicyanomethyl-6-dimethylaminostyryl- 4H-pyran (DCM[120]); **(b)** yellow-emitting CrS040 Dye from Radiant Color;[122] **(c)** europium tris(2-thenoyl trifluoro acetonate)-di- (triphenylphosphine oxide) ($Eu(TTA)_3(TPPO)_2$);[123] **(d)** a near-IR emitting oxyiminopyrazole-based ytterbium chelate;[124] (Adapted with permission from ref[26]. Copyright 2016 American Chemical Society.)

Stoles shift[124] have failed to impress. Moreover, lanthanide based compounds like europium tris(2-thenoyl trifluoro acetonate)-di-(triphenylphosphine oxide) ($Eu(TTA)_3(TPPO)_2$)[125] exhibiting reabsorption free characteristics but effected by limited absorption capabilities and a near-IR emitting oxyiminopyrazole-based ytterbium chelate[126] which suffers from poor emitting efficiency resulting from PL quenching by coupling with C-H overtones render relatively useless when it comes to incorporating these materials in such photon management technologies. Also, materials made from perylene perinone derivatives[127, 128] considered to be one of the best organic fluorophores for such devices, suffer from undesirably high reabsorption losses despite showing decent absorption in the solar spectrum and high emission efficiency.

Colloidal NCs as viable alternatives

Colloidal NCs on the other hand present themselves as exceptionally viable replacements for organic and organometallic counterparts in such light management technologies.[61, 129-133] Colloidal NCs owing to relatively simple monodisperse synthesis procedures, versatile solution processibility, large absorption coefficients over a broad spectral range, high PL quantum yield and size tuneable emission properties are seen to be serious candidates with exploitable optoelectronic properties that can render near ideal materials for various photon management devices. Moreover, introduction of organic and inorganic passivation results in improved and controlled emission efficiencies and enhanced photostability over the organic chromophores.[59, 133-135] As a result, a wide array of nanomaterials of various anisotropy and composition have announced themselves as near ideal candidates for light management technologies. These materials include ternary I-III-VI_2 NCs with exceptional NIR emission efficiencies[136] (~85% at 800 nm) and Lead chalcogenide NCs with reported efficiencies of 50-90% at lower spectral energies[137, 138], Perovskites[139] and Cd based binary chalcogenide NCs among others. One of the challenges that hampers the usage of these nanomaterials, similar to their organic counterparts is the introduction of efficient Stokes shift to ensure minimum reabsorption losses. Stokes shift in these semiconductor NCs come from the fundamental optical effects arising due to intrinsic phenomena like crystal field splitting[26], shape anisotropy and exciton fine structure effects, size polydispersity[140] or surface defects. In this scenario, the resultant Stokes shift is of the same order of the width of emission spectra,[59, 61, 120, 141-144] inducing an overlap resulting in exceptional losses due to reabsorption. These shortcomings can however be overcome by employing charge engineering and lattice manipulation strategies like NC heterostructuring and doping respectively as well as turning to heavy metal free ternary semiconductor NCs.

Stokes shift engineering through NC heterostructuring:

One of the effectively proven methods to overcome the issue of reabsorption losses in photon management devices is to artificially engineer a finite controllable stokes shift by separating the absorption and emission functions between different structural confines through heterostructured NCs.[61, 120, 144] This process however, can also be useful in enhancing the PL QY of any system of NCs and to engineer the structural confines of different materials to bring out the best of their optoelectronic properties. Homostructured core-only NCs often suffer from poor PL efficiency rooting from competing non-radiative decay channels at the mid-bandgap states arising due to the unsaturated surface dangling bonds. This issue has been shown to be effectively solved by means of organic and inorganic passivation. The most general organic passivation involves covalently bonding organic molecules at the surface of NCs to fill in and

saturate the surface defect states and to provide isolation to the NCs from the external environment. This technique although owing to the versatility of the ligands and their efficient roles in targeted species manipulation can be potentially used in biomedical applications,[65, 145, 146] they also suffer from a drawback pertaining to the unsteady nature of ligands which easily may be damaged by exposure to light and heat results in unreliable QY resulting from photobleaching. Inorganic passivation on the other hand made possible through the shelling of core-only NCs with wider band gap materials not only result in efficiently muting the effect of external environment on the optical properties of the NCs, but also introduces an additional degree of freedom to customize the optoelectronic properties of a combination of different materials forming heterostructures of core/shell NCs with for the desired applications. Depending on the position of valence and conduction band minima of the respective materials forming the core and shell, the extent of spatial and structural localization of the photoexcited charge carriers give rise to distinct scenarios.

Type-I semiconductor heterostructures: Also known as 'nested structures', this class of heterostructured NCs typically consist of the band gap of core being surrounded by a wider bandgap material as shown in the **Figure 1.10a**. This results in strong localization of the charge

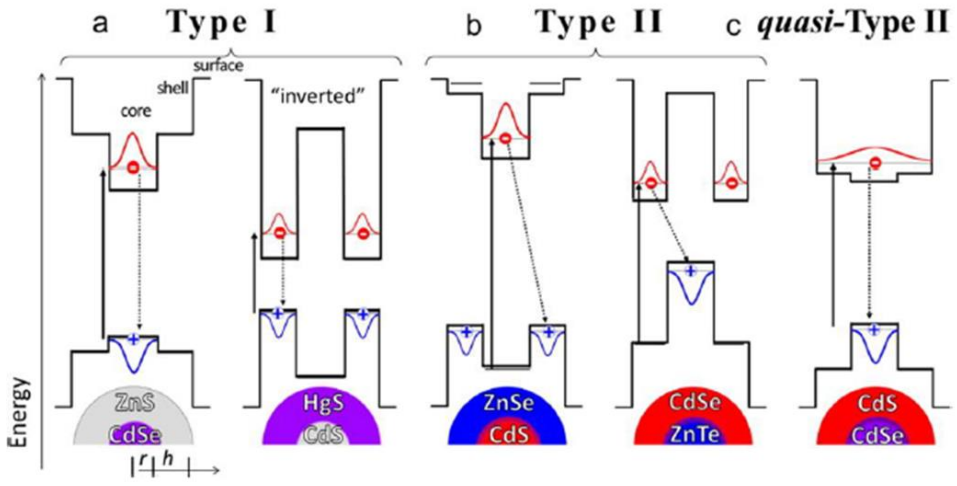

Figure 1.10: Band alignments between the materials in core/shell NCs result in three major carrier localization regimes, depicted using the qualitative alignments for known examples of each (at bottom) based on the bulk band alignments (heavy horizontal lines) modified by quantum confinement (thin horizontal lines) for arbitrary combinations of core/ shell size. The localizations of the wave function for band-edge electrons and holes are depicted in red and blue, respectively. The principal absorbing (solid arrows) and emitting (dotted arrows) transitions are also shown for each example. **(a)** Type-I NCs feature a nested alignment, causing both the electron and hole to reside principally in either the core (left) or the shell (right). **(b)** In Type-II NCs, a staggered alignment of conduction and valence bands pulls band-edge electrons and holes into separate parts of the core/shell NC. **(c)** In quasi-type-II NCs, one carrier remains localized in a single component of the heterostructure (here, the hole), while the other is largely delocalized throughout the entire NC. (Adapted with permission from ref[26]. Copyright 2016 American Chemical Society.)

carriers in the core of respective NC leading to exciton confinement within the core being efficiently passivated by wider band gap shell. As studied in detail in CdSe/ZnS core/shell NCs, due to the colocalization of both the charge carriers, inside the narrow band gap material, optical properties such as absorption spectrum, emission energy and radiative lifetimes[40] are determined by the narrow band gap material. This band alignment is usually referred to as "inorganic passivation" as the shell mostly serves as a barrier suppressing the interaction of the excited charge carriers with surface traps, effectively taking on the former role of the passivating organic ligands. An important variant of this class of heterostructures is the 'inverted band arrangement' where the narrow band gap material serves as shell to the wider band gap core NCs. In such a case, the charge carrier isolation does not materialize and this results in the charge carrier wavefunctions being localized in the narrow band gap shells resulting in poor passivation from the surface defects and external environment. Hence, these heterostructures are accompanied with poor PL efficiency and uninduced stokes shift are not favoured for light management devices. Nevertheless, they have been extensively studied[147-150] for the development and understanding of colloidal NCs synthesis since it offers the ease to study the optical properties which extensively shift to lower energies with increasing shell thickness.

Type-II semiconductor heterostructures: Also known as 'staggered structures' are typically observed in materials with similar and moderate E_g (>1.3eV). Unlike type-I heterostructures, here, both conduction and valence bands of either material (core or shell) are higher lying than those of the other as shown in **Figure 1.10b**. This results in the charge carriers being localized in different structural confines energetically separated into different spatial domains within the NC. This separation of charge carriers have important ramifications. As in the previously discussed class of NCs, the absorption onset is still dictated by the narrow band gap material, however, the emission is determined by a spatially indirect transition between separate charge carriers localized in respective spatial confines which is characteristically at considerably lower energy giving rise to large apparent stokes shift. Nonetheless, the larger spatial separation of charge carriers results in smaller overlap of the carrier wave functions giving rise to weaker oscillator strengths, slower radiative decay times and poorer PL efficiency.[30] Also, this type of charge separation gives rise to Coulomb interactions which subsequently affects the multiexciton dynamic processes.[151, 152]

Quasi Type-II semiconductor heterostructures: These forms of heterostructures can be considered as an intermediate to the type-I and type-II semiconductor heterostructures. The band alignment in these systems allows for one charge carrier to be strongly localized while

the other charge carrier to be delocalized across multiple materials as shown in **Figure 1.10c**. This type of heterostructuring is reported only in a handful of NCs[29, 92, 153-157] since it warrants that the valence or conduction bands of core and shell materials should be of similar energies. These heterostructures have been extensively researched and deemed to be optoelectronically suitable materials for photon management technologies owing to high PL QY and sufficiently large induced stokes shift. One such core/shell system is CdSe/CdS NCs with giant thick CdS shells.[144, 158] In such systems, the similar conduction band energy levels of core and shell materials allows the electron wave function to delocalize over the whole NC whereas the hole wave function is strongly confined in the lower lying CdSe core due to the large offset between the valence band levels of the two materials.[143] The giant CdS shells dominate photon absorption by virtue of its extraordinary volume and subsequently large absorption cross section while emission occurs through the recombination of charge carriers localized in NC core as a result of ultrafast localization of holes(<1ps)[159] in the CdSe core originating from the large valence band offset between CdSe and CdS. Consequently, this results in large apparent stokes shift around 500 meV as shown in the **Figure 1.11.** The combination of CdSe and CdS has been used to induce large stokes shift in a variety of structures, including spherical core/shell NCs,[144, 158-160] dot-in-bulk,[159, 161-163] dot-in-plate,[164] dot-in-rod[165] and rod-in-rod[166, 167] nanoparticles, tetrapods,[168] octapods[169] and nanoplatelets.[170-172] Moreover, the thick shell not only acts as a passivating cover for the NCs from surface defect states,[173] thus reducing the non-radiative decay losses and boosting the PL efficiency, it also accounts for near complete isolation of emitting core from environmentally harmful effects.

Stokes shift engineering through doping:

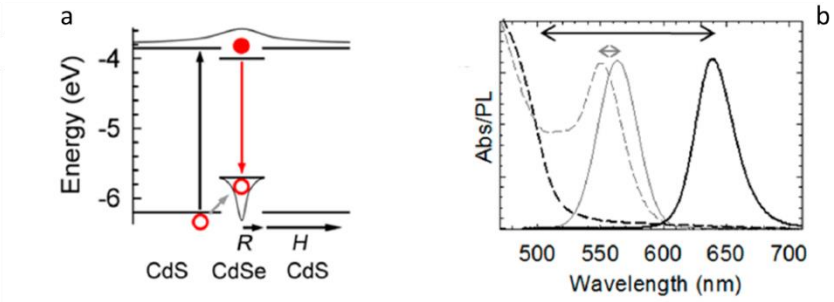

Figure 1.11. (a) Approximate band diagram of CdSe/CdS NCs. Following photon absorption in the shell (black arrow), photogenerated holes undergo rapid transfer to the core (gray arrow). The red arrow shows radiative recombination of a core-localized exciton. **(b)** Optical absorption (dashed lines) and PL (solid lines) spectra of reference core-only CdSe NCs with radius R = 1.5 nm (gray lines) and core/shell CdSe/CdS NCs with the same core radius and the shell thickness H = 4.2 nm (black lines). Figure adapted with permission from.[59] Copyright 2014 Nature Publishing Group

As discussed in the previous sections, unparalleled physical and optoelectronic properties rooting from the characteristic confinement of charge carrier wave functions have been achieved through control of NC size, composition, shape anisotropy and band gap alignment engineering between materials. Another very recognized method of engineering a finite stokes shift in order to minimize optical losses pertaining to reabsorption in photon management technologies can be achieved through doping strategies using finite number of luminescent metal impurities in the host semiconductor lattice.[174] In such NC systems, introduction of transition metal impurities like Copper (Cu), Silver (Ag) or Gold (Au) results in creation of optically active localized intragap energy states which participates in the recombination processes with a band edge electron or a photogenerated hole in the host NC. The doping procedures have been carried on through different approaches like introduction of impurity atoms during the process of crystal growth or through controlled post-synthesis cation exchange routes[175-189] resulting in a strongly red shifted and very long lived emission.[176, 180, 190] There has been extensive research on transition metal doping, especially Cu in II-VI NCs.[179, 182, 185, 187, 191-196] In such doped systems emission is majorly contributed through the recombination of a conduction band electron and a localized photogenerated hole in the energy level associated with the impurity atom. Magneto-optical studies have shown the evidence of paramagnetism in the presence of Cu^{2+},[191] Ag^{2+},[197] and Au^{2+} [198] cations resulting from acquiring a hole from the valence band upon photoexcitation in a d^{10} configuration giving rise to d^9 paramagnetic configuration of electronic levels. Such a hole, while not allowed to participate in absorption transition, plays a vital role in the radiative emission process. The photoexcited electron from the conduction band of host NC recombines with previously localized hole in the impurity levels resulting in an emission, stokes shifted by hundreds of meV arising from the difference in energy levels between this impurity energy level and host valence band energy level.[191, 197-199] Also, since the energy of dopant level is fixed, through suitable choice of the host semiconductor, it is in principle possible to realize transition metal (Cu, Ag, Au)-doped QDs that absorb across the visible spectrum and emit at IR wavelengths, and are thus immune to reabsorption losses while retaining suitably large stokes shift.[191-196, 199-202] Tremendous progress over time in this field has ensured the capability of production of high quality samples with utmost precise control over the level of doping determined by control over the concentration of dopant and host atoms.[193] However, such synthetic routes have been witnessed to fall prey to Poisonian bottleneck resulting from the stochastic interaction of dopant ions with the host NCs at the ensemble level. This leads to non-uniform and unpredictable distribution of dopant ions in the host ensemble. For instance, given an average ensemble doping level of

three dopants per NC, only 20% of the NCs have exactly three impurities whereas as high as 5% NCs are witnessed to be undoped. Such non-uniformities result in misleading, complicated and unexplained optical results which are paramount when it comes to improving their applicative potentials in light management devices. To this end in chapter 3, we focus on discussing our work involving a novel synthesis strategy for doping Gold (Au) impurities in binary CdSe NCs by using Au metal clusters as nucleation seeds for the colloidal synthesis of Au:CdSe NCs. Metal clusters resembling well defined organic molecules, are found to be stable only for cluster sizes known as 'magic clusters' and this stability is found to root from their intrinsic electronic and geometric structures in which a crucial role is played by their interactions with surrounding organic ligands. Au, a known p-type impurity capable of assuming +1, +2 and +3 oxidation states in bulk II-VI semiconductors,[203-208] not only induces a large stokes shift of around 500 meV deeming such systems favourable for light management technologies, but also upon photoexcitation is capable of exhibiting Diluted Magnetic Semiconductor (DMS) properties suitable for spintronic applications. During the course of chapter 3, we demonstrate, using monodisperse, magic-sized Au clusters composed of seven atoms and combining the results of elemental analyses and optical experiments, that indeed each NCs embeds seven Au ions, i.e. one single cluster.

Another very effective doping category can be looked at as substitutional doping strategy where a desired dopant atom isovalently replaces the cation in the host lattice. One of the most extensively researched and reported materials in this class of doping is Manganese (Mn) doped II-VI binary chalcogenide NCs. Owing to the strong magnetic properties of Mn^{2+} ($3d^5$), these NC systems have potential applications in magnetic memory and spintronics.[175-177, 180, 190, 209, 210] In II-VI chalcogenides, Mn^{2+} ions isovalently replace the cation involved in the host lattice with the introduction of $3d^5$ electronic configuration. Thus, the electronic states for such a Mn:II-VI chalcogenide system consist of valence band of P-type symmetry, conduction band of S-type symmetry and partially incorporated dopant states of $3d^5$ electronic configuration. This points to the presence of five unpaired electrons in the d shell of Mn^{2+} ions with a total spin of S=5/2 and total angular momentum L=0.[211] This constitutes the lowest energy ground state $^6A_1$ which is spherically symmetric and non-degenerate in the presence of crystal field perturbations arising due to the host lattice. The first excited state however, involves flipping of one out of the five electron spins leaving behind 3 unpaired electrons in the 3d orbital resulting in total spin S=3/2 and total angular momentum $L \neq 0$. This constitutes the first excited state $^4T_1$ which, due to the presence of the crystal field perturbation quantities, are lifted in degeneracy but retains its spherical symmetry.[211] Therefore, any optical transition from $^4T_1$ to

$^6A_1$ state has to be accompanied through flipping of an electron spin and hence this transition is sometimes also referred to as 'spin-flip transition' and its energy is relatively fixed at around 2.1 eV is independent of the host band gap. The photophysical processes in such Mn doped systems however, depend on the E_g of the host lattice. In the case where the E_g of the host <2.1eV,[175, 177, 190, 212] the quantum confined band edge host excitons interact with the dopant ions through sp-d exchange interactions. This exchange interaction results in photoinduced alignment of the unpaired dopant electrons leading to development of a non-zero localized magnetization in the NCs. This leads the exciton to feel a finite field thus further lowering its energy resulting in a bound state called 'Exciton magnetic polarons'.[213-215] Conversely, in the case where Eg> 2.1eV, the d-d transition is sensitized by energy transfer from host to dopant states. Since the absorption $^6A_1$ to $^4T_1$ transition is spin-forbidden with a negligible molar extinction coefficient ~$1M^{-1}cm^{-1}$,[216] compared to that of the host NC, the absorption occurs exclusively through the host NC while the dopant energy states are involved in emission processes. Hence, the combination of a fixed Mn based emission energy (2.1 eV through spin flip transition) and tuneable absorption of II-VI host NCs results in controllable stokes shift with values as high as 1 eV. Subsequently, rooting from broad and tuneable absorption properties of the host NCs and controllable stokes shift leading to minimizing the losses due to reabsorption while maintaining a tuneable decent absorption across the spectrum, these materials are suitable for being used in Photon management technologies like Luminescent solar concentrators. Along the same lines another similar class of NC systems that share similar properties are Mn doped perovskites with high PL efficiency and E_g>2.1 eV. Controlled insertion of small amount of impurities[217-221] provides an additional degree of freedom for controlling their optical properties[222-224] and introduces functionalities that cannot be obtained through size and composition control (i.e., halide substitution). To date, substitutional doping has been demonstrated using a variety of divalent cations including cadmium, zinc, tin,[225] and mostly, manganese,[218, 222, 226-228] which isovalently replace Pb^{2+} cations and have been shown to significantly stabilize PNCs.[219, 229] Importantly, similar to chalcogenide NCs, in PNCs with E_g > 2.1 eV (i.e., $CsPbCl_3$, $CsPbBr_3$, and mixed halide compositions),[222] the Mn^{2+} dopants can be excited from their $^6A_1$ ground state to the $^4T_1$ excited state by energy transfer (ET) from the NC host,[222, 230] giving rise to the characteristic dopant emission at 2.1 eV due to the $^4T_1 \rightarrow {}^6A_1$ spin-flip transition.[222, 225-227, 230] This results in a large "apparent" Stokes shift between the absorption spectrum of the NC host and the Mn^{2+}-PL that is particularly useful in photon management technologies.[225, 227] In chapter 4, we conduct spectroscopic studies at controlled excitation density and temperature on Mn:$CsPbCl_3$ NCs and demystify the two step energy

transfer mechanism involving exciton localization in a shallow metastable state that mediates the thermally assisted sensitization of the Mn^{2+} emission, thus giving a much clearer photophysical mechanism paramount to exploiting the applicative potentials of these NC systems in Light management technologies.

Heavy metal free NCs:

In the previous sections, most of the materials described contain heavy metals like Cadmium or Lead and hence are criticised and penalized due to the toxicity concerns. They require expensive disposal protocols and subject to restrictions due to health and environmental risks.[231] To mitigate this risk, shelling using a non-toxic material such as ZnS has been proposed to minimize the leakage of the hazardous materials into the environment. But such inorganic passivation proves to be futile and thus newer classes of nanomaterials have been proposed as alternatives. One such vital class of materials is ternary I-III-VI_2 NCs such as $CuInS_2$, $CuInSe_2$ and their alloys.[131, 132, 232] Moreover these highly efficient NCs like their chalcogenide counterparts, can be synthesized in large quantities via high-yield, non-injection techniques using easily available precursors.[131] Most importantly, they exhibit intrinsic large stokes shift of more than 100 meV without the above mentioned heterostructuring or doping strategies.[136, 233-235] Owing to their intrinsic broad tuneable absorption character through the NIR to visible spectrum, large, efficient absorption cross section and its superior intrinsic Stokes shifted, long-lived and highly efficient emission (reaching upwards of 80% with suitable inorganic passivation)[236, 237] make them ideal candidates to be used in photon management[238] and light harvesting devices.[239] Despite these brilliant features, the origin of optical properties of $CuInS_2$ NCs were still not fully understood as most studies on these systems attributed their spectroscopic signatures to arise from the recombination of a conduction band electron with a hole localized in copper-related defects.[240-242] Also, experimental proofs to this regard were provided by spectroscopic,[136, 241, 243-245] spectro-electrochemical,[246-248] electrical[249] and magnetico-optical[250] methods. A recent theoretical model by Efros and co-workers[251] suggests that their characteristic Stokes-shifted and long-lived luminescence arises from the structure of the valence band and predicts distinctive optical behaviors in defect-free NCs: the quadratic dependence of the radiative decay rate and the Stokes shift on the NC radius. In chapter 2, by studying the stoichiometric $CuInS_2$ NCs, we reported for the first time, the experimental validation for the spectroscopic signatures predicted for the free band exciton, thus supporting the VB-structure model. We evaluated the impact of the observed optical behaviors on LSCs

by Monte Carlo ray-tracing simulations. Based on the emerging device design guidelines, optical-grade large-area (30×30 cm^2) LSCs with optical power efficiency (OPE) as high as 6.8% were fabricated, corresponding to the highest value reported to date for large-area devices.

Chapter 2

Evidence for the Intrinsic Exciton and Fine Structure in the Energy Bands of $CuInS_2$ Nanocrystals

Synopsis

Ternary I-III-VI_2 NCs, such as $CuInS_2$, are receiving attention as heavy-metals-free materials for solar cells, luminescent solar concentrators (LSCs), LEDs, and bio-imaging. The origin of the optical properties of $CuInS_2$ NCs are however not fully understood. A recent theoretical model suggests that their characteristic Stokes-shifted and long-lived luminescence arises from the structure of the valence band (VB) and predicts distinctive optical behaviors in defect-free NCs: the quadratic dependence of the radiative decay rate and the Stokes shift on the NC radius. If confirmed, this would have crucial implications for LSCs as the solar spectral coverage ensured by low-bandgap NCs would be accompanied by increased re-absorption losses. In this work, I performed spectroscopic studies on stoichiometric $CuInS_2$ NCs, and in the process it was revealed for the first time, the spectroscopic signatures predicted for the free band-edge exciton, thus supporting the VB-structure model. At very low temperatures, I also observed dark-state emission from these NCs likely originating from enhanced electron-hole spin interaction. The impact of the observed optical behaviors on LSCs was evaluated by Monte Carlo ray-tracing simulations. Based on the emerging device design guidelines, optical-grade large-area (30×30 cm^2) LSCs with optical power efficiency (OPE) as high as 6.8% were fabricated, corresponding to the highest value reported to date for large-area devices.

2.1 Prologue

Ternary semiconductor NCs of I–III–VI_2 composition, such as $CuInS_2$, $AgInS_2$, or $CuGaSe_2$, are attracting considerable interest for numerous energy and optoelectronic technologies including photovoltaic (PV) cells,[252-257] luminescent solar concentrators (LSCs),[240, 258-260] light emitting diodes,[233, 261-264] as well as bioimaging[233, 234, 265] where their inherent lower toxicity offers a significant advantage over Cd- and Pb-based NCs. In addition

to their heavy-metal-free composition, I–III–VI_2 NCs feature important electronic and photophysical properties, such as degenerate p-type transport[249, 266] and broadband absorption, tuneable from visible to near infrared[237, 267-271] that is spectrally very well separated from an efficient, long-lived photoluminescence (i.e., a very large Stokes shift).[136, 272] This characteristic optical behavior makes I–III–VI_2 NCs the most promising chromophores for efficient LSCs, combining effective harvesting of the solar spectrum and reabsorption-free waveguiding of the propagating luminescence. As a result, efficient solar concentration has been demonstrated in large area devices[132, 232, 240, 258, 260, 273] that further feature neutral colouring particularly adapt for architectural integration of LSCs as, i.e., PV windows.[240, 274] Despite tremendous advancements in this field, the fundamental photophysics of I–III–VI_2 NCs is still not fully understood, in particular concerning the long luminescence decay time and the characteristic wide global Stokes shift, Δ_{SS}^{G} , between the absorption and emission spectra,[275] resulting in the lack of clear design guide lines for their optimization. As discussed in the following, the term "global" is used here to indicate that, in contrast to the norm, the electronic transitions determining the spectral energies for absorption and emission in I–III–VI_2 are not the same.[251, 275] Mostly based on the similarity between the luminescence spectral shape, lifetime, and Stokes shift of $CuInS_2$ NCs and those of copper doped II–VI NCs[275-277]—and by analogy those of $AgInS_2$ to silver-doped chalcogenides[197, 276]—most studies to date have considered the photoluminescence (PL) to arise from the radiative recombination of a conduction band (CB) electron with a hole localized in copper-related defects.[240-242] Experimental support to this argument was provided by spectroscopic,[136, 241, 243-245] spectro-electrochemical[246-248] and electrical[249] methods. Magneto-optical[250] experiments further revealed marked temperature dependent Zeeman splitting due to sp–d exchange interaction between band-edge carriers and paramagnetic Cu^{2+} cations (with $3d^9$ electronic configuration) in both Cu-doped II–VI NCs and nonstoichiometric $CuInS_2$ NCs (Cu/In ratios between 1.25 and 1.45).[250, 278] Strongly nonlinear magnetic field dependence of the circular polarization-resolved emission observed in both Cu:ZnSe NCs and $CuInS_2$ NCs[250, 277] with respect to the linear trend typically found in undoped CdSe NCs, further corroborated the picture that emission from nonstoichiometric $CuInS_2$ NCs involves localized dopant or defect states that feature a complex splitting of their level structure in applied magnetic fields. According to this picture, single particle experiments on copper deficient $CuInS_2$ NCs (1:2 Cu/In precursor ratio) by Zang et al.[245] revealed markedly narrower single NC PL spectra with respect to the ensemble (60 meV vs 400 meV) that, together with the weak temperature dependence of the PL

linewidth,[279, 280] suggest that the broad ensemble PL spectrum is mostly determined by the energy distribution of defect acceptor sites among different particles. Recent transport measurements[249] support this argument.[281] The same study further highlighted the presence of In-related substitutional and/or interstitial defects acting as donors in indium treated NCs, in agreement with the excitonic pathway mediated by donor defects proposed by Kraaz et al.[282] and Leach et al.[283] An alternative interpretation ascribes the photophysics of $CuInS_2$ NCs to the recombination of self-trapped excitons featuring a strongly localized hole in the highest occupied molecular orbital due to the 3d states of Cu+ cations.[277, 284]

However, a recent theory by Efros and co-workers[251] proposes a very different possibility, namely that the characteristic broadband optical absorption spectrum, long PL lifetimes and wide Δ_{SS}^{G} can be explained by the structure of the valence band (VB). Specifically, effective mass calculations highlight a VB structure featuring low-energy odd parity hole sublevels of p-type symmetry (corresponding to the high energy VB sublevel depicted in red in the single electron diagram of **Figure 2.1a** separated by a splitting energy, Δ_{EO}, from higher-lying even parity hole levels (corresponding to the green VB sublevel in **Figure 2.1a**, whose wavefunctions have s-type contributions. As a result of the parity selection rules, the absorption spectrum is dominated by the optical transition between the even hole VB sublevel with total angular momentum $F = 1$ and the $1S_e$ electron level (blue arrow in **Figure 2.1a**, also featuring a s-type symmetry. On the other hand, the long-lived PL (black arrow in **Figure 2.1a** arises from the parity-forbidden radiative transition of the $1S_e$ electron into the odd VB state also featuring $F = 1$. A recent work[285] provided experimental support for such a VB structure picture by showing the presence of an intense two photon absorption transition below the one-photon absorption band edge. However, the PL of such NCs was suggested to still occur via a defect-mediated pathway, resulting in size and shape independent Δ_{SS}^{G}, similarly to what observed by Xia et al.[243] and Grandhi et al.[286] and commonly exhibited by Cu-doped CdSe NCs.[191]

Importantly, the model by Efros and co-workers (hereafter indicated as the VB structure model) makes testable predictions:[251] the quadratic decrease of Δ_{SS}^{G} with the particle radius, a, and the linear growth of the radiative decay rate with a^2. These distinctive size dependences of the spectral and dynamical properties of I–III–VI_2 NCs arise from the linear proportionality of the admixture between the odd and even parity states with a. Specifically, as schematically depicted in **Figure 2.1b** (bottom panel), small $CuInS_2$ NCs exhibit a large Δ_{EO} and negligible absorption from the odd parity VB sublevels (highlighted in red) featuring vanishingly small

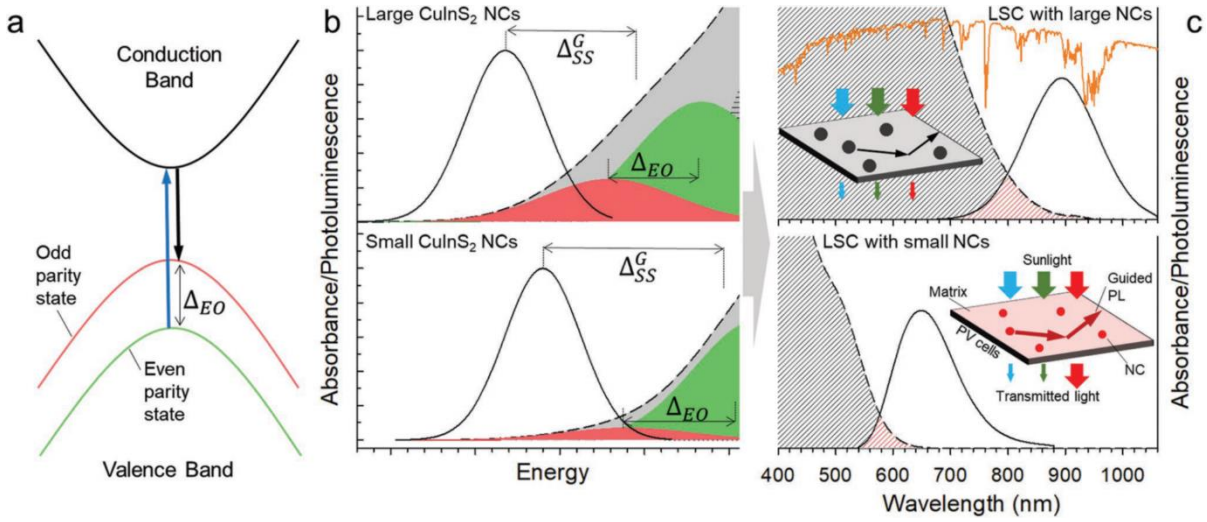

Figure 2.1. (a) Schematic depiction of the band structure of $CuInS_2$ NCs featuring odd and even parity VB sublevels separated by Δ_{EO}. Optical absorption (blue arrow) is dominated by the electronic transition coupling the even VB sublevel and the CB, whereas luminescence (black arrow) occurs by parity forbidden radiative decay of the electron into the odd VB sublevel. **(b)** Representative optical properties for large (top) and small (bottom) $CuInS_2$ NCs as predicted by the VB structure model.[12] In small particles, Δ_{EO} is large resulting in small intermixing between the VB substates and negligible oscillator strength coupling the odd parity VB substates and the CB (represented by the weak red absorption band). The absorption spectrum is dominated by the even parity substates (green band), the resulting Δ_{SS}^{G}, is large and the low-energy absorption tail is weak. Δ_{EO} drops in larger NCs leading to larger intermixing between the VB substates and consequent broader low-energy absorption tail and smaller Δ_{SS}^{G} . **(c)** Side-by-side comparison between the normalized PL (solid black lines, excitation at 400 nm) and optical absorption (dashed black lines) spectra of stoichiometric $CuInS_2$ NCs with radius a = 2.2 nm (top panel) and a = 1.0 nm (bottom panel). The absorption profiles are normalized to 1 optical density at the respective band-edge energy evaluated from the transient transmission spectra reported in **Figure 2.3**. The spectral overlap between the absorption and PL profiles are highlighted by red shading to emphasize the effect of broadened absorption tail with increasing a resulting in stronger reabsorption. Insets: schematic depiction of the LSCs under solar irradiation showing uniform spectral coverage for devices embedding large NCs resulting in no spectral distortion of the transmitted light. LSCs featuring small NCs instead transmit a larger fraction of the solar spectrum above 600 nm resulting in tinted devices and low colour rendering index of the transmitted light.

oscillator strength, thus resulting in a large Δ_{SS}^{G} . Upon increasing the NCs size, odd and even parity sublevels come closer in energy,[251] resulting in a linear trend of Δ_{EO} with a^{-2}. The resulting intermixing between such states intensifies the low energy absorption tail in large NCs (top panel in **Figure 2.1b** which ultimately leads to the linear dependence of Δ_{SS}^{G} on a^{-2}. On the same lines, increasing intermixing between VB substates should result in the linear growth of the radiative decay rate with a^2. To date, however, no study has experimentally investigated such spectroscopic signatures, leaving the model without direct experimental validation. Crucially, this photophysical scenario and in particular the progressive reduction of Δ_{SS}^{G} in larger NCs, would have important implications for the use of $CuInS_2$ NCs as reabsorption free emitters in LSCs. This is because the wide solar coverage (SC) enabled by

low bandgap (large size) NCs with broadband absorption extending the near-IR region would be accompanied by stronger reabsorption losses of the propagating luminescence with respect to smaller NCs, due to the larger overlap with the respective emission spectrum. This behavior is shown in **Figure 2.1c** for representative $CuInS_2$ NCs with different particle size (a = 2.2 nm vs a = 1.0 nm) discussed in detail in the subsequent sections. On the other hand, whilst small NCs would be less affected by reabsorption (**Figure 2.1c**, bottom panel) their SC would be limited to the visible spectral region. This would limit the maximum achievable device efficiency and result in coloured LSC panels which are not ideal for building integrated PV technologies. If the VB structure model is confirmed, the realization of efficient LSCs with simultaneously optimized solar harvesting and light concentration efficiency based on $CuInS_2$ NCs would require identifying the perfect trade-off between such antithetical size effects.

In this work, I studied the VB structure model with the aim to test the aforementioned theoretical predictions by performing optical and magneto-optical investigations on stoichiometric $CuInS_2$ NCs of varying sizes. Consistently with the model, optical absorption and transient transmission measurements reveal the gradual broadening of the absorption tail, resulting in the linear increase of Δ_{SS}^{G} with a^{-2}. Importantly, this behavior is accompanied by the linear growth of the PL radiative decay rate with a^2, also in agreement with the proposed excitonic mechanism.[251] In addition to this, PL measurements below $T \sim 50$ K show a 100-fold lengthening of the PL decay time, but no change in the PL quantum yield (Φ_{PL}), pointing to a further fine structure of the emitting band-edge exciton state, with splitting that scales as a^{-3}. Such photophysics had so far never been observed in I–III–VI_2 NCs and is similar to what is well known in conventional II–VI NCs,[35, 40] suggesting that also in this class of semiconductor NCs the fine structure of the first exciton manifold might emanate from enhanced exchange interaction.[110, 287] Crucially, side-by-side time-resolved PL measurements on non-stoichiometric $CuInS_2$ NCs and Cu-doped CdSe NCs of comparable size show exclusively the lengthening of the PL lifetime with decreasing temperature due to gradual suppression of thermally assisted nonradiative decay, strongly indicating that the observed fine structure effect derives from the very nature of the intrinsic band-edge exciton of defect free $CuInS_2$ NCs. In order to evaluate the implications of the observed size dependence of the optical properties of $CuInS_2$ NCs on their use as LSC emitters, Monte Carlo ray-tracing simulations based on the experimental spectra were performed. The calculations highlight the interplay between the positive effect of wider solar harvesting with increasing particle size and the detrimental stronger optical losses by reabsorption, thus suggesting guidelines for device optimization.

Based on such indications, a large area (30 cm × 30 cm) plastic LSC device embedding stoichiometric $CuInS_2$ NCs with optimal size was fabricated which was then optically coupled with c-Si solar cells, to achieve record optical power efficiency (OPE) of 6.8% that further confirmed the technological relevance of these fundamental findings.

2.2 Synthesis and Optical properties

$CuInS_2$ NCs were synthesized by my colleagues in the research group following the heat-up procedure that ensures production of stoichiometric particles by suitably tuning the reactant concentration.[136, 244, 267, 284] For the synthesis of such stoichiometric $CuInS_2$ NCs, a mixture of CuI (0.4 mmol), $In(OAc)_3$ (0.4 mmol), and 5 mL of DDT was loaded into a three-neck flask and was degassed under vacuum at 130 °C for 1 h. In order to grow particles of different sizes, the temperature was initially raised to 230 °C to let the particles nucleate and grow. Aliquots were taken at different reaction times (2.5, 5, 10, 20, 30, 40, and 60 minutes) in order to obtain different NC sizes. Finally, the reaction was quenched by cooling the solution to room temperature. The NCs were washed by repeated precipitation with acetone and redispersion in hexane. When a precursor ratio of 1:1 In:Cu was used, $CuInS_2$ NCs with In:Cu:S stoichiometric ratios close to 1:1:2 were obtained. This was confirmed by performing Inductively coupled plasma atomic emission spectroscopy (ICP-AES) using an iCAP 6500 Thermo spectrometer with samples dissolved in HCl/HNO_3 3:1(v/v); the analysis thus indicating a composition of $Cu_{1.04}InS_{2.01}$. The $CuInS_2$ NCs present tetragonal chalcopyrite-like structure. The respective NCs were imaged using High-resolution TEM (HR-TEM) and high-angle annular dark field-scanning TEM (HAADF-STEM) imaging performed on an image-CS-corrected JEOL JEM-2200FS microscope (Schottky emitter), operated at an accelerating voltage of 200 kV. TEM of two representative aliquots are reported in **Figure 2.2** showing size distribution consistent with previous reports[243, 288] which mostly show spheroidal particles, rather than well-faceted shapes, especially in the smaller NCs. This holds in particular for the smallest NCs (not shown here), which are harder to identify even by HR-TEM imaging, due to the low number of atoms, which hardly stabilize in an ordered (i.e., crystalline) structure, thus in an anisotropic shape.

We start our analysis by looking at the optical spectra of the $CuInS_2$ NCs reported in **Figure 2.3a** measured using Cary 50 UV-Vis Spectrophotometer. The spectra show the characteristic broadband absorption profile and the Stokes-shifted PL of I–III–VI_2 NCs progressively moving to lower energy with increasing particle radius. According to previous reports, the absorption spectra show no discernible first excitonic peak, but exclusively a low energy shoulder.[233, 243,

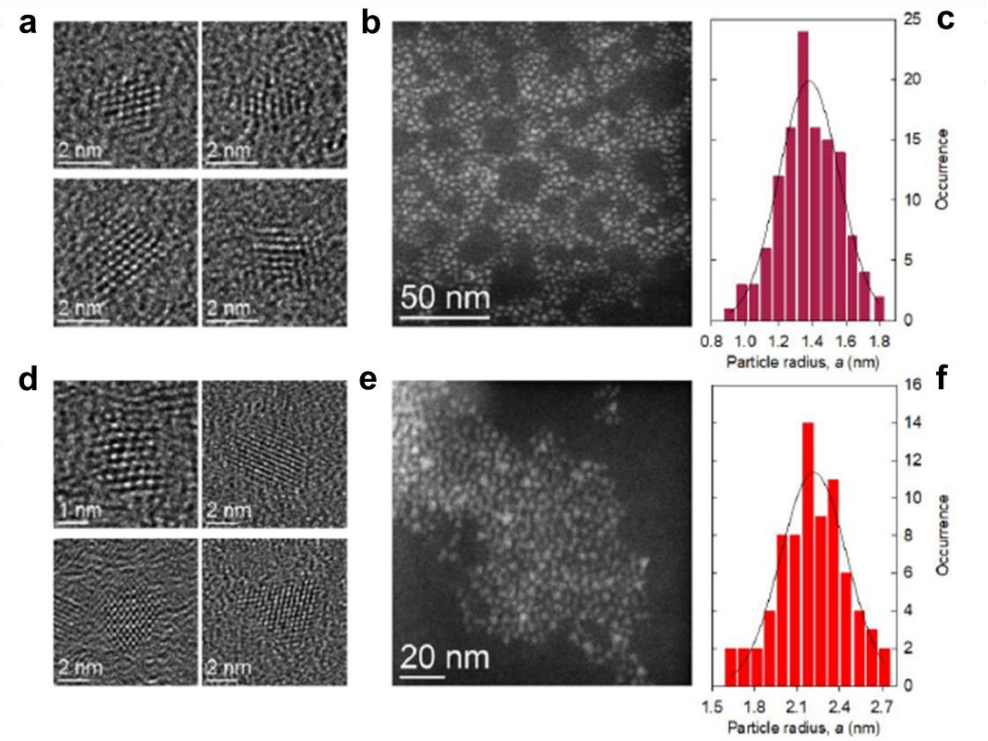

Figure 2.2. (a, d) HRTEM images of representative $CuInS_2$ NCs and **(b, e)** HAADF-STEM overview images $CuInS_2$ NC samples featuring mean radius **(c)** a=1.4±0.2 nm and **(f)** a=2.2±0.2 nm.

[289] To most accurately determine the spectral position of the dominant absorption feature, ultrafast transient transmission (TT) measurements were performed. For these measurements, we used a Ti:sapphire laser with chirped pulse amplification (Coherent LIBRA-HE), which provided 95 fs pulses at 800 nm at a repetition rate of 2 kHz. The excitation pulses at 3.1 eV with a pulse duration of 100fs were obtained by second harmonic generation through a 1 mm thick β barium borate crystal. The probe beam was a white light supercontinuum generated by focusing a small fraction of the fundamental beam onto a 2 mm thick sapphire plate. After chopping the pump beam at 1 kHz, pump and probe were focused on the sample by means of a lens and a spherical mirror. A computer-controlled optical multichannel analyzer working at the repetition rate of the laser source acquired the map of the differential transmission $\Delta T/T = (T_{on} - T_{off})/T_{off}$, as a function of the pump−probe time delay, where T_{on} and T_{off} are the probe spectra transmitted by the excited and unperturbed samples. The TT spectra were measured at low excitation fluence of 80 μJ/cm^2 i.e. when the number of photons absorbed per NC per pulse ($\langle N \rangle$) is much less than unity (dashed lines in **Figure 2.3a**—are dominated by a bleaching band due to the saturation of band-edge states where carriers accumulate following intraband relaxation.[136, 240] The bleaching peak energy was used to extract the mean particle radius for the various NC aliquots by using the sizing curve provided in ref.[243-245]

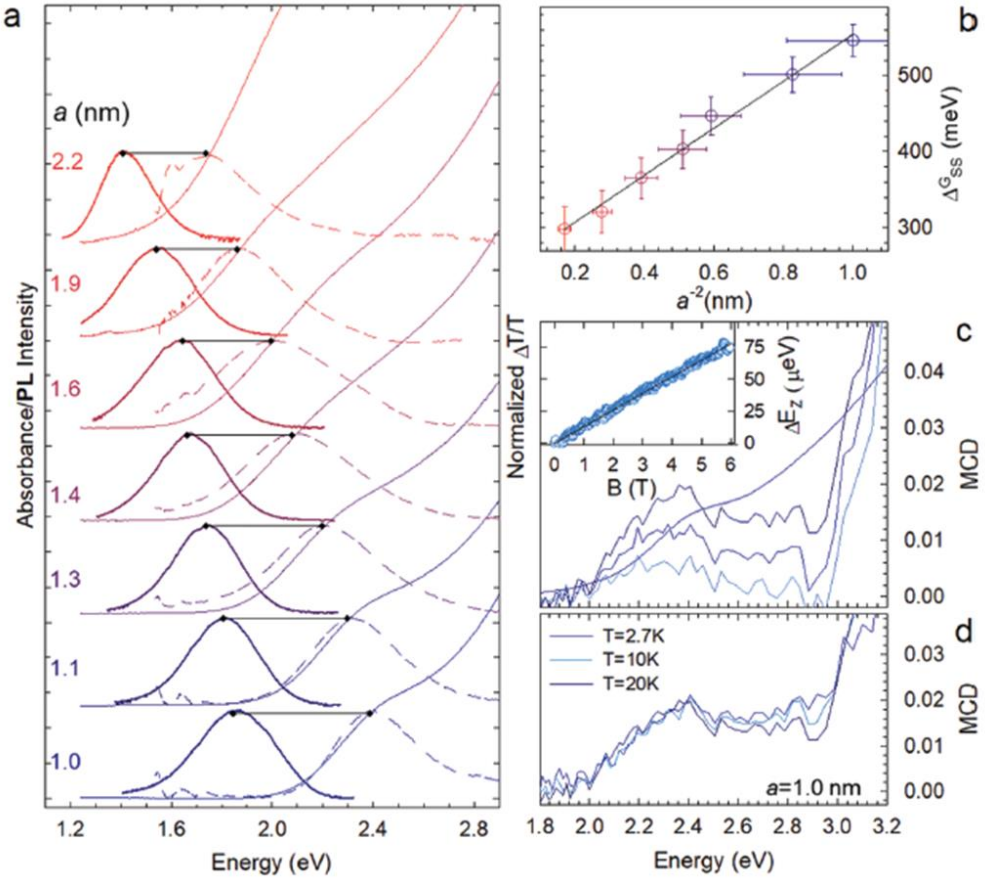

Figure 2.3. (a) Optical absorption (thin solid lines), PL spectra (bold solid lines) and normalized transient transmission (TT, dashed lines) spectra at 10 ps pump–probe delay of $CuInS_2$ NCs with increasing mean radius *a*. The global Stokes shift values, Δ_{SS}^{G}, between the absorption and PL spectra of each NC sample are indicated by black bars and reported as a function of *a* in panel **(b)** Δ_{SS}^{G} extracted as the energy difference between the peak energy of the TT and PL spectra in panel "a" as a function of the particle size *a*. **(c)** MCD of $CuInS_2$ NCs at 2.7 K and increasing magnetic field (B = 2, 4, 6 T). The linear absorption at 2.7 K is shown as a bold blue line. Inset: Zeeman splitting of the band-edge exciton versus magnetic field together with the fit to the linear Zeeman splitting function (black line, $R2$ = 0.994). **(d)** MCD of $CuInS_2$ NCs at 6 T showing no temperature dependence for T = 2.7–20 K.

The obtained NC radii for the largest NCs for which reliable TEM images were obtained, agree with the particle size estimated from the analysis of the respective micrographs reported in **Figure 2.2**. The peak energy of each TT spectrum that identifies the "center of mass" of the low energy absorption due to the interplay between Δ_{EO} and the respective oscillator strength of the even and odd parity VB sublevels shifts toward the low energy portion of the respective absorption spectrum with increasing *a*. This is consistent with the VB structure model predicting a larger contribution from the odd VB sublevels in larger particles (**Figure 2.1a**) progressively broadening the absorption tail. As a result, Δ_{SS}^{G}, extracted as the energy difference between the bleaching maximum and the respective PL peak (black bars in **Figure 2.3a** reported in **Figure 2.3b** increases linearly with a^{-2}, in agreement with the theoretical

prediction.[251] This represents a first experimental evidence of the VB structure origin of the Stokes-shifted PL in stoichiometric I–III–VI_2 NCs where the radiative exciton decay does not necessarily involve an intragap defect state.

As anticipated above, previous magneto-optical studies on non-stoichiometric $CuInS_2$ NCs revealed the presence of paramagnetic species in the NC, likely associated with copper-related defects,[250] similar to what observed in II–VI chalcogenide NCs doped with group-11 transition metals.[197, 198, 278] Therefore, magneto-optical experiments can be used to corroborate the absence (or reveal the presence) of such states in our stoichiometric NCs. With this in mind, magnetic circular dichroism (MCD) measurements as a function of temperature and magnetic field[190] were performed. MCD measures the normalized difference in transmission between left- and right-circularly polarized light through films of NCs in the Faraday geometry. NC films were mounted in the variable-temperature insert (1.5–300 K) of a 7 T superconducting magnet with direct optical access. Probe light of tuneable wavelength was derived from a xenon lamp directed through a spectrometer. The probe light was mechanically chopped at 137 Hz and was modulated between right and left circular polarizations at 50 kHz using a photoelastic modulator. The thus transmitted light was then detected with a silicon avalanche photodiode. In **Figure 2.3c**, I report the MCD spectra of $CuInS_2$ NCs (a = 1.0 nm) at increasing magnetic field up to B = 6 T at 2.7 K, together with the corresponding linear absorption spectrum. The MCD spectrum shows one main peak at ≈2.35 eV corresponding to the NC's absorption shoulder that intensifies with increasing magnetic field. In the inset of **Figure 2.3c**, the extracted Zeeman splitting energy (ΔE_Z) is observed to be growing linearly with the magnetic field thus suggesting the absence of paramagnetic species in these NCs. Accordingly, these data were perfectly fitted with the linear Zeeman splitting function:

$$\Delta E_Z = \mu_B F B g_{EX}$$

where μ_B is the Bohr magneton and g_{EX} is the Landé factor of the band-edge exciton responsible for optical absorption (mostly formed by a hole in the even VB substate and a CB electron). The obtained g-factor, g_{EX} = 0.22, was in agreement with previous results on $CuInS_2$ NCs.[250] Most importantly, the magnetic response of the absorption peak (**Figure 2.3d**) was found to be temperature independent, in contrast to the temperature-dependent MCD that was observed by Rice et al. in non-stoichiometric $CuInS_2$ due to paramagnetic defects.[250] Therefore, MCD data further corroborate the picture that the photophysical behavior of our stoichiometric $CuInS_2$ NCs is intrinsic in nature.

2.3 Temperature dependence of dynamics of Exciton recombination

Further support to the VB structure model emerges from the analysis of the exciton decay kinetics with increasing *a*. As anticipated in the previous sections, within this model, gradual intermixing between the VB substates results in an a^2-dependence of the radiative decay rate, k_{RAD}. To experimentally evaluate this effect, I performed steady state and time-resolved PL spectroscopy experiments. Since the Φ_{PL} and decay kinetics of $CuInS_2$ NCs are known to be strongly affected by temperature-dependent nonradiative processes,[246] I conducted the experiments at decreasing temperature from 300 to 5 K. This leads to suppression of phonon-assisted nonradiative decay phenomena and thereby the evolution of k_{RAD} versus *a*.

To start with this part of the analysis, in **Figure 2.4a,** the Φ_{PL}-values of five representative $CuInS_2$ NCs with increasing size (*a* = 1.0, 1.4, 1.6, 1.9, and 2.2 nm) from 300 to 5 K are reported. The inset shows the evolution with *T* of the PL spectra of the *a* = 1.0 nm NCs. Φ_{PL} of all systems increases with decreasing *T*, reaching saturation at ≈100 K, thus confirming the presence of temperature-activated nonradiative channels that are suppressed at lower *T*. For the sake of convenience in discussion, I labelled the 100 K ≤ *T* ≤ 300 K interval as range **I**. For lower temperatures (range **II**), Φ_{PL} is largely constant for all systems. Consistently with previous reports, the efficiency losses in range **II** are ascribed to ultrafast trapping of photocarriers by surface defects in the absence of a wide gap passivating shell that result in a subpopulation of non-emissive NCs in the ensemble.[246] Here, it is worthy to note that, for this study, core-only $CuInS_2$ NCs were preferred to be investigated, as the overgrowth of a protecting wide bandgap shell, such as ZnS,[289] typically leads to the formation of alloyed quaternary particles by diffusion of Zn, which modifies the electronic structure of the core.[267] Nevertheless, the invariance of Φ_{PL} of the NCs in range **II** confirms the temperature-independence of surface trapping and indicates that the photophysics for *T* ≤ 100 K discussed later in this chapter is purely due to radiative phenomena occurring in surface trapping-free NCs.

Looking first at the PL decay curves in range **I** (**Figure 2.4b**) for NCs with *a* = 1.0 nm, typical multiexponential kinetics of unshelled $CuInS_2$ NCs is observed that progressively slows down with decreasing T with no measurable variation of the zero-delay intensity, in agreement with the temperature independence of ultrafast charge trapping channels depleting the NC bands

faster than our temporal resolution.[246] Importantly, for *T* close to 100 K the PL decay curves accumulate indicating that the PL process is approaching its radiative regime.

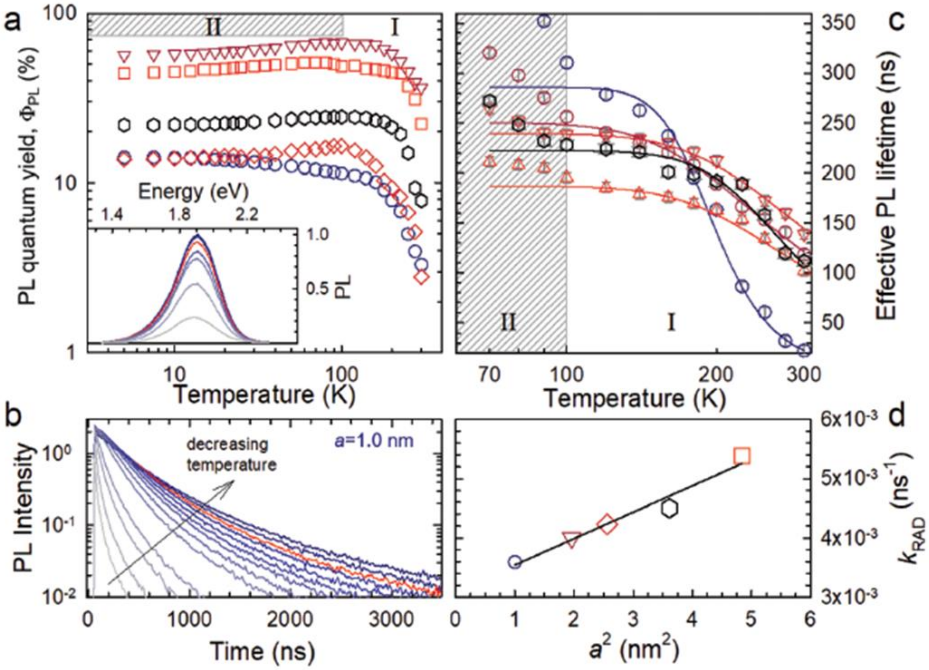

Figure 2.4. (a) Φ_{PL} as a function of temperature of $CuInS_2$ NCs of increasing size, a = 1.0 (circles), 1.4 nm (triangles), 1.5 nm (diamonds), 1.9 nm (hexagons), and 2.2 nm (squares). Inset: PL spectra of $CuInS_2$ NCs with a = 1.0 nm at decreasing temperature (from gray to dark blue). The red line corresponds to T = 100 K. **(b)** PL decay curves of NCs having a = 1.0 nm at decreasing temperature (indicated by the black arrow). The red line corresponds to T = 100 K. **(c)** Effective PL decay times as a function of temperature (from 300 to 70 K) of the same $CuInS_2$ NCs as in panel "a" together with the respective fitting curves to Equation (1). **(d)** k_{RAD} of the whole set of $CuInS_2$ NCs showing quadratic growth with a^2 in agreement with predictions from ref. [12]. The black line represents the linear fit of k_{RAD} versus a^2.

To better monitor the evolution of the PL kinetics in range **I** and to evaluate the radiative decay time as a function of *a*, in **Figure 2.4c,** I report the respective effective PL lifetimes (τ), extracted as the time after which the PL intensity drops by 1/*e*. At room temperature, the τ-values of the various NCs are uncorrelated to their respective Φ_{PL}, consistent with the major nonradiative channel being ultrafast carrier trapping that renders a subpopulation of NCs non-emissive without affecting the PL lifetime of the emissive particles. More importantly, in accordance with the Φ_{PL} trends, τ of all NCs increases and reaches a nearly constant value for $T \approx 100$ K, based on which we ascribe such a lifetime to the effective radiative exciton decay time, $\tau_{RAD}=1/k_{RAD}$, of the bright subpopulation of NCs in the ensemble. To evaluate τ_{RAD} for our NCs, we performed a global fit of the τ versus temperature trends in range **I** using the equation:

$$\tau^{-1}=\tau_{RAD}^{-1}+\tau_{NRAD}^{-1}(T) \quad (2.1)$$

that neglects ultrafast surface trapping and describes the nonradiative decay rate by the standard displaced harmonic oscillator model[290]

$$\tau_{NRAD}^{-1}(T)=A*e^{(-E_A/(k_BT))} \quad (2.2)$$

Through this fit, activation energies for the nonradiative decay of $E_A \approx 70 \pm 4$ meV was obtained. More importantly, the k_{RAD}-values obtained through the fitting procedure grow linearly with a^2 (**Figure 2.4d**), in agreement with theoretical expectations based on the VB structure model.

A closer look at the lowest temperature values in **Figure 2.4c**, highlighted by the grey patterned area and corresponding to constant values of Φ_{PL}, reveals further increase of τ_{RAD} for $T < 100$ K that is particularly evident for the smallest NCs in the set. This additional temperature trend becomes evident by looking at the time-resolved PL data in range **II** shown in **Figure 2.5** revealing the unexpected emergence of exciton fine structure effects in ternary I–III–VI_2 NCs. In **Figure 2.5a**, PL decay traces for $CuInS_2$ NCs (a = 1.0 nm) across the entire range of investigated temperatures are exhibited. The PL decay curve corresponding to 100 K is shown in red to highlight the accumulation of decay lines as the thermally assisted nonradiative losses are suppressed and to mark the passage from temperature range **I** to range **II**. Strikingly, by lowering the temperature further, the PL kinetics dramatically slows down and turns from multiexponential to markedly nearly double-exponential with an initial fast portion followed by a tens of microseconds long component, over two orders of magnitude slower than the radiative kinetics at ≈100 K. The effect is highlighted in **Figure 2.5b** where zoomed-in view of the first two decades of signal in the first 2.5 μs of decay is shown. This kind of kinetic behavior occurring at constant values of Φ_{PL} has been widely reported for binary chalcogenide NCs, including CdSe,[35, 40, 110, 287] CdTe,[291] ZnSe,[292] and their heterostructures (i.e., CdTe/CdSe or CdSe/CdS NCs)[143, 293] as well as in PbSe[294] NCs, where the fast initial decay at low temperature has been ascribed to coupling of the ground state to a confined acoustic phonon or to the thermalization of excitons from a higher-energy optically allowed state (commonly referred to as the bright exciton) to a lower-lying optically forbidden (dark) exciton state. The much slower decay, on the other hand, arises from the radiative recombination of dark excitons in thermal equilibrium with the environment.[40, 143] This decay becomes progressively faster with increasing temperature as a result of thermal excitation of dark excitons to the bright upper exciton state. **Figure 2.5c** reports the evolution of τ_{RAD} with temperature for five $CuInS_2$ NC samples of increasing size extracted following the procedure used in range **I** and by neglecting the initial decay portion due to rapid thermalization in range **II**. For the smallest NCs, τ_{RAD}

approaches 20 μs at temperatures below ≈20 K and undergoes two orders of magnitude decrease at higher temperatures (τ_{RAD} (100 K) ≈ 250 ns).

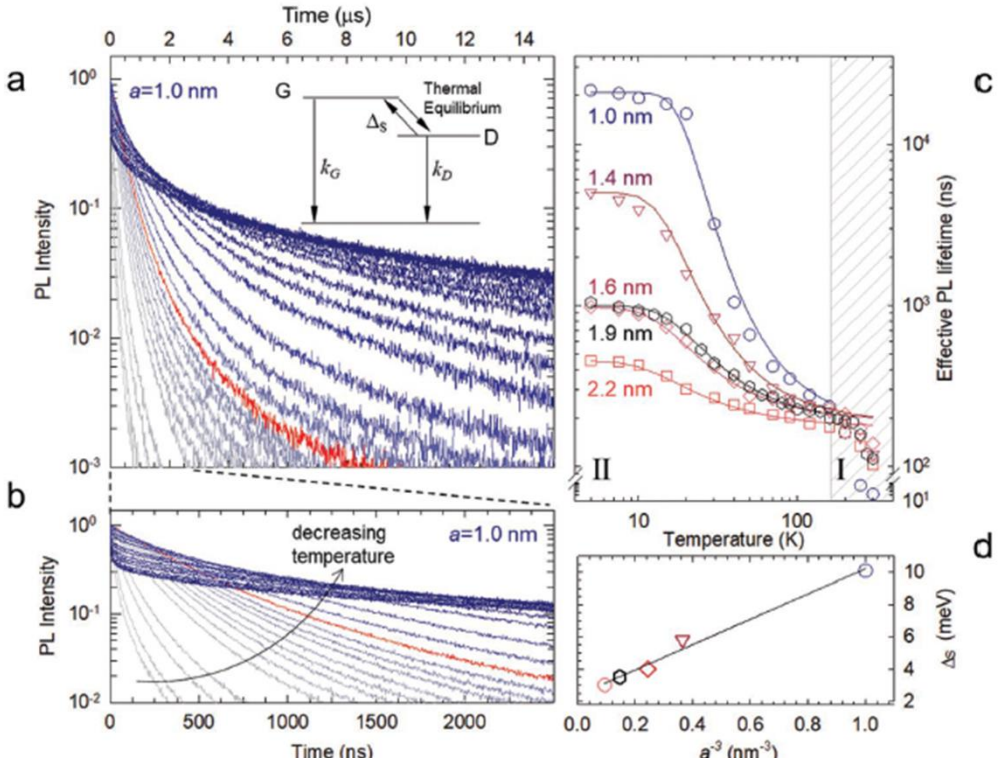

Figure 2.5. (a) PL decay curves for $CuInS_2$ NCs (a = 1.0 nm) at decreasing temperature from 300 to 5 K (from grey to blue). The red line corresponds to T = 100 K. Inset: Three-level model of grey (G) and dark (D) exciton states separated by energy Δ_S. **(b)** Enlargement of the initial portion of the PL decay versus T highlighting the appearance of the initial fast portion for T below 100 K. **(c)** Effective PL decay lifetimes of $CuInS_2$ NCs of increasing size as a function of temperature together with the respective fits to Equation (3). **(d)** Δ_S -values extracted through the fitting procedure as a function of a^{-3}, highlighting the inverse volume dependence of the dark-grey splitting energy.

In analogy to the behavior of CdSe NCs, this effect can be ascribed to the thermal activation between two substates of the exciton fine structure having markedly different emission lifetime. Note that, in contrast to CdSe NCs, in $CuInS_2$ NCs both such states belong to the weakly allowed exciton consisting of a CB electron and a hole in the odd parity VB sublevel. Therefore, in the discussion, I have adopted the language typically used to describe exciton states that are strongly and weakly forbidden by symmetry in transition metal dichalcogenide semiconductors[295] and label the long-lived exciton as dark and the higher lying emissive exciton as grey, so as to distinguish the current case from the norm, where the emissive state is optically allowed and therefore "bright." By assuming a Boltzmann distribution of excitons between these two dark (D) and grey (G) states, one can model the transition between the slow

and fast decay regimes in a simple three-level scheme (inset of **Figure 2.5a**), by expressing the radiative decay rate as:

$$k_{RAD} = \tau_{RAD}^{-1}(T) = (k_D + k_G e^{-\Delta s/kBT})(1+e^{-\Delta s/kBT})^{-1} \quad (2.3)$$

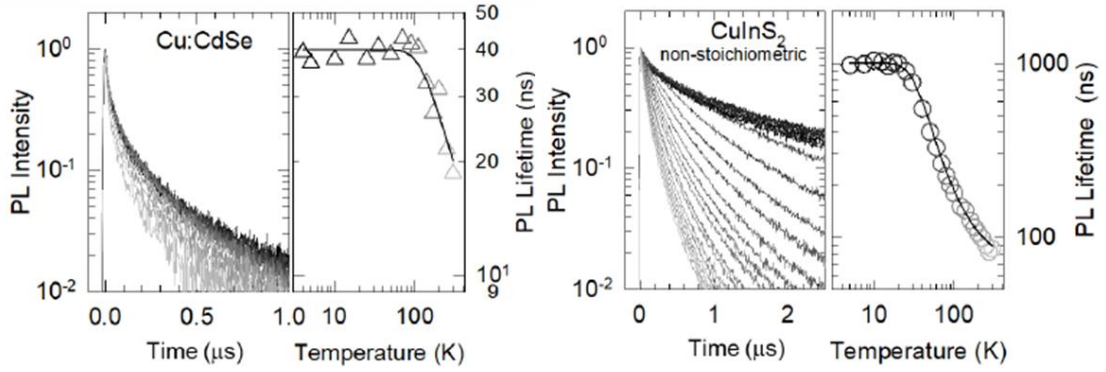

Figure 2.6. PL decay curves of Cu:doped CdSe NCs and off-stoichiometry $CuInS_2$ NCs (a=1.0 nm, Cu:In=1:4) at decreasing temperature (from 300T to 4K, grey to black curves). The respective effective PL decay times as a function of temperature are shown in the right panels together with the respective fitting curves to Eq.2. The extracted ΔE_A-values are 30 meV for the Cu:CdSe NCs and 15meV for the $CuInS_2$ NCs.

where k_D and k_G are the radiative decay rates of dark and grey excitonic states respectively and Δ_S being the respective splitting energy. The above model reproduces the experimental data well for all $CuInS_2$ NCs, yielding Δ_S-values comparable to those found in binary chalcogenide NCs of similar size (**Figure 2.5d**).[110] Interestingly, as observed in CdSe NCs, Δ_S is found to scale linearly with a^{-3}, suggesting that also in $CuInS_2$ NCs the fine structure splitting energy follows the linear dependence with the inverse of the particle's volume of the exchange energy of uncorrelated electron–hole pairs.[287] Importantly, time-resolved PL measurements on off-stoichiometry $Cu_{1-x}In_xS_2$ (x = 0.8) and Cu:doped CdSe NCs with a = 1.0 nm shown in **Figure 2.6** shows no evidence fine structure effects in either system. This supports the picture that the excitation responsible for the optical properties of stoichiometric $CuInS_2$ NCs is of different nature than the Cu-defect emission in both off-stoichiometry $CuInS_2$ NCs and in Cu:doped II-VI chalcogenides. It is also worth noting that time-resolved PL measurements at 5 K show nearly no acceleration of the PL kinetics upon the application of a magnetic field (B = 5 T, as is instead observed in CdSe NCs due to magnetic mixing of the dark and bright exciton state Hamiltonians.[35] Such an effect might be due to the optically forbidden nature of both the dark and grey excitons in $CuInS_2$ NCs resulting in substantial decrease of the coupling to external magnetic fields.

2.4 Implications on LSC performance and Optimization strategies

The agreement between the size dependencies of the spectral and dynamical parameters observed for our $CuInS_2$ NCs with the theoretical predictions by Efros and co-workers[251] provide strong indications that the optical properties of stoichiometric ternary I–III–VI_2 NCs are due to the detailed structure of the VB. This has important implications for the application of this class of NCs to light management technologies and in particular to LSCs. These devices typically consist of optical waveguides coated or doped with chromophores that absorb sunlight and emit longer wavelength luminescence that propagates by total internal reflection to the device edges, where it is converted to electricity by PV cells installed along the device perimeter. Such an all-optical functioning mechanism makes LSCs particularly suitable for building integrated PV applications spanning from sound barriers[296] to coverages[297] and electrodeless solar windows,[298] and could even help architects in enhancing the aesthetical value of a building. As anticipated above, the realization of efficient LSCs relies on the combination of broadband optical absorption to ensure effective solar harvesting and minimized spectral overlap between the absorption and PL spectra of the chromophores, so as to suppress losses to re-absorption (other critical aspects are the optical quality and transmittance of the waveguide matrix[274] and the type of PV cells[299]).

For building integration and in particular for solar glazing applications, a further key parameter that is directly connected to the spectral coverage is the colour of an LSC panel, which determines both the indoor-to-outdoor vision and the quality of the transmitted sunlight illuminating indoor settings. In the case of NCs featuring a continuous optical absorption spectrum, a large SC and a neutral colouring can be achieved by using particles featuring an absorption edge in the near infrared spectral region.[240] However, in the case of the stoichiometric $CuInS_2$ NCs discussed here, mitigation of quantum confinement in large particles is accompanied by the gradual reduction of Δ_{SS}^{G} , resulting in stronger reabsorption of the propagating PL that is detrimental for the device efficiency. In order to evaluate the impact of such a behavior on the device performance, the optical absorption and PL spectra of the $CuInS_2$ NCs with increasing *a* reported in **Figure 2.3a** were used to perform Monte Carlo ray-

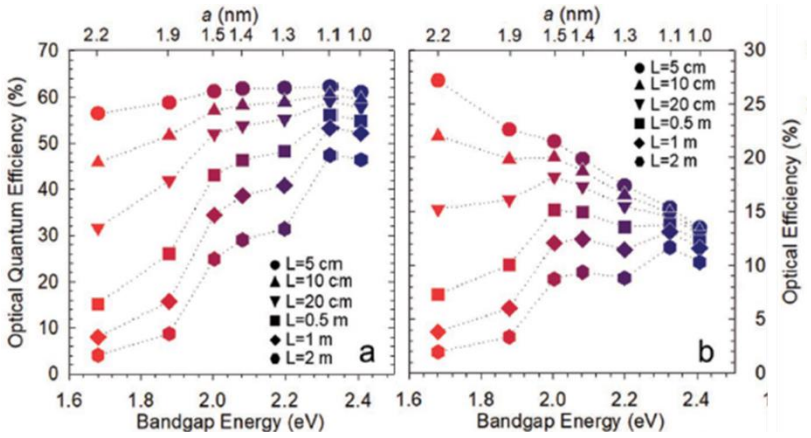

Figure 2.7. Monte Carlo ray-tracing calculation of the **(a)** OQE and **(b)** OE of squared LSCs (thickness 0.5 cm) with increasing lateral size (L), embedding the $CuInS_2$ NCs with different bandgap energy shown in **Figure 2.3a**. The simulated LSCs feature the same integrated optical absorption below the band edge of the respective NCs.

tracing simulations of light propagation in squared LSCs of increasing lateral dimension, L (thickness 0.5 cm). To avoid parasitic effects due to the different PL quantum efficiency of the NCs, in our calculations we imposed Φ_{PL} = 95% for all systems and neglected optical absorption by the matrix material, so as to focus exclusively on the NC properties. The simulations of the squared LSC with increasing lateral size (L = 5 cm, 10 cm, 20 cm, 50 cm, 1 m and 2 m) were performed via a Monte Carlo ray-tracing method, in which the photon propagation follows the geometrical laws of optics. Because the LSC thickness (0.5 cm) is much larger than the light coherence length, interference was neglected. The stochastic nature of the simulations is reflected in the fact that the ray is transmitted or reflected with the probabilities proportional to respective energy fluxes given by Fresnel Laws. The dependence of these probabilities on the state of polarization of the incident ray (e.g., s- or p-polarized) is also considered. A specific event (i.e., transmission or reflection) is chosen according to random Monte Carlo drawing. Monte Carlo ray-tracing simulations of the LSC were performed using the experimental absorption spectra of the NCs in solution and their relative photoluminescence spectra. AM 1.5G Solar spectrum is employed as LSC excitation source. Once a photon is absorbed by a NC, the subsequent fate of the excitation (i.e., re-emission or non-radiative relaxation) is again determined by the Monte Carlo sampling according to the emission quantum yield, set as equal for all the samples (Φ_{PL} = 95%). The direction of re-emission is distributed uniformly, and the re-emission wavelength is determined using the rejection sampling applied to the accurate NCs PL spectra obtained from experiment. The

ultimate fate of each photon is either loss due to non-radiative recombination or escape from the LSC via one of the interfaces. A single-ray Monte Carlo simulation is typically repeated 10^6–10^7 times to have a proper statistical averaging. The stochastic nature of simulations allows one to easily evaluate LSCs performance, such as the optical quantum efficiency (edge-emitted photons per absorbed solar photons) and the optical efficiency (edge-emitted photons per impinging solar photons). The LSC performance are evaluated by estimating the number of photons emitted from the waveguide edges, independently on the type of PV cells coupled to the device perimeter.

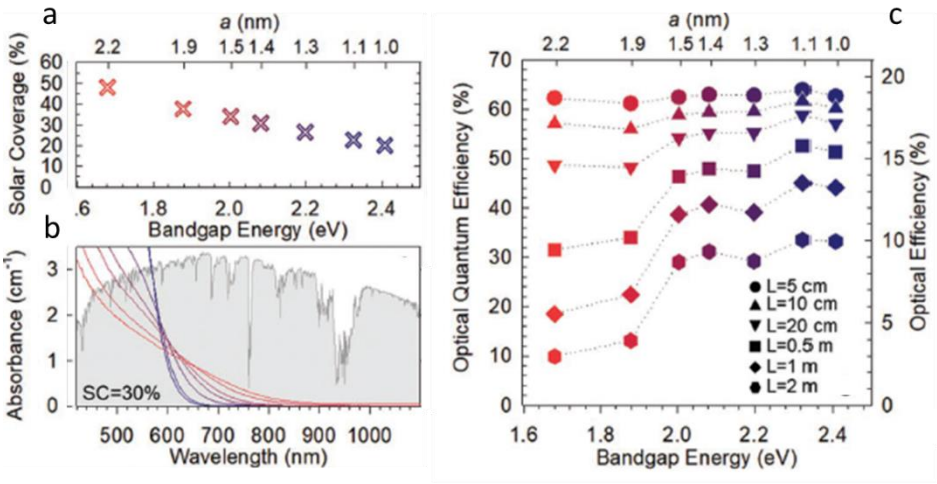

Figure 2.8. (a) SC of the same devices as in **Figure 2.7a,b** calculated in the 280–1100 nm wavelength range. **(b)** Absorption spectra of LSCs based on the same $CuInS_2$ NCs assuming identical spectral coverage of SC = 30%. The AM 1.5G solar spectrum (expressed in photons m^{-2} s^{-1}) used for the simulations is reported in grey. **(c)** Calculated OQE and OE as a function of the NC size (bandgap energy) for LSCs with identical SC (30%) and increasing *L*

To evaluate the effect of the progressively smaller Δ_{SS}^{G} and the broader low-energy absorption tail with increasing *a*, in **Figure 2.7a,b** we first compute the behavior of LSCs featuring the same absorptance below the effective bandgap energy of the respective NCs (corresponding to the peak energy of the 1S bleach in the TT spectra; **Figure 2.3a**). The SC of the various LSCs calculated in the 280–1100 nm wavelength range, corresponding to the maximum spectral portion exploitable by LSCs coupled to silicon PV cells, is shown in **Figure 2.8a**. Consistent with the evolution of the absorption spectra with *a*, the optical quantum efficiency—OQE, defined as the ratio between the number of photons emitted from the waveguide edges and the number of absorbed solar photons—of LSCs embedding large NCs drops with increasing device dimensions due to progressively stronger reabsorption losses (**Figure 2.7a**). However, as highlighted in **Figure 2.7b** by the optical efficiency (OE) of the same devices—evaluated

as the number of edge-emitted photons divided by the number of solar photons impinging on the device surface—this effect is partially mitigated by the progressively wider spectral coverage (SC) enabled by the use of larger NCs featuring a lower bandgap energy (**Figure 2.8a**). As a result, for small devices (L = 5 cm, 10 cm) where average light propagation distances are relatively short, reabsorption losses play a minor role with respect to solar

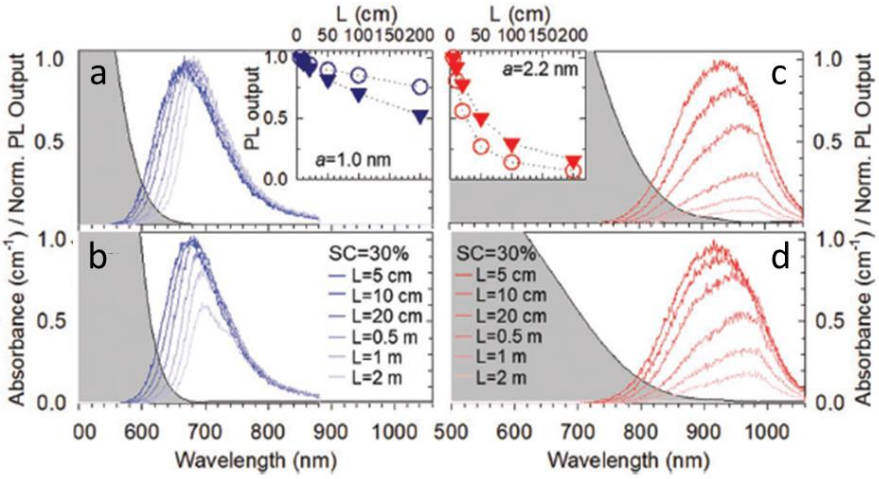

Figure 2.9. (a),(c) Edge-emitted PL spectra of NCs with a = 1.0 nm (blue lines) and a = 2.2 nm (red lines) embedded into LSCs with increasing L featuring the same below gap absorptance. The respective integrated PL intensities are shown respectively as blue and red circles in the insets of panels "a" and "c." **(b),(d)** Edge-emitted PL spectra of the same LSCs in the case of equal spectral coverage, SC = 30%. The respective integrated PL intensities are shown as blue and red triangles in the insets of panels "a" and "c."

harvesting, resulting in the monotonic growth of the OE with increasing NC size, reaching OE > 20% for L = 10 cm, despite a relatively low solar coverage (SC < 40%). For larger L-values, reabsorption becomes the dominant parameter, gradually lowering the OE for LSCs embedding large NCs. Importantly, an optimum is found for large LSCs (L = 0.5 m) embedding NCs with a = 1.5 nm showing OE as high as 15%. Notably, nearly constant OE > 10% versus a is calculated also for devices with 1 m^2 size, which would be particularly adapt for architectural integration. It is noteworthy that the use of NCs with $a \geq 1.4$ nm has the key advantage of enabling the fabrication of LSC devices of neutral colour, whose integration into glazing systems would introduce negligible distortion of the transmitted solar spectrum. For the devices discussed in this chapter, the transmitted sunlight would exhibit a Colour Rendering Index, R_a > 90, that fulfilled the highest requirements for indoor illumination (corresponding to CIE colour rendering group 1A).

Having evaluated the effect on LSCs of stoichiometric $CuInS_2$ NCs with different size by considering equal bandgap absorptance **(Figure 2.7a,b)**, we can compare the applicative

potential of such NCs in the more realistic case of LSCs featuring the same solar harvesting capability, corresponding to SC = 30%. The respective absorption spectra are shown in **Figure 2.8b** together with the AM 1.5G solar spectrum used for the simulations (expressed in photons m^{-2} s^{-1}). Consistent with the larger bandgap and steeper low-energy absorption tail of small NCs (a < 1.3 nm) due to negligible oscillator strength of the optical transition coupling the odd parity VB sublevel and the CB with respect to larger particles, the desired SC = 30% is achieved with LSCs featuring a high NC loading, resulting in a sharp absorption edge at ≈580 nm. Upon increasing a, progressively lower NC contents are required for the same SC and the resulting absorption spectrum is gradually more uniform across the visible/near-IR region. As a consequence, for LSCs featuring the same spectral coverage, reabsorption losses are enhanced (reduced) in LSCs with small (large) particles than in the example discussed in **Figure 2.7a,b** that compared devices with equal absorptance at the bandgap of the respective NC emitters. This is testified by the OE (and OQE) trend of LSCs with increasing L in **Figure 2.8c**—for equal SC conditions, the OQE and the OE follow an identical trend as a function of a as highlighted by the double y-axis—and by the side-by-side comparison of the edge emitted PL spectra of LSCs based on NCs with a = 1.0 nm and a = 2.2 nm shown respectively in **Figure 9**. Specifically, the spread of the OE values versus L is narrower (wider) for a = 2.2 nm (a = 1.0 nm) in **Figure 2.8c** with respect to **Figure 2.7a**, which is consistent with the corresponding trends of the integrated PL output with the LSC dimension reported in the insets of **Figure 2.9a,b**, showing opposite behavior for the two different NC sizes. Most importantly, **Figure 2.8c** indicates that, despite the significant transparency of 70%, OE as high as 12% could be achieved for large colourless LSCs (L = 1 m) embedding NCs with a = 1.5 nm and that increasing the device area to 4 m^2 would still yield efficiencies close to 10%.

2.5 Highly efficient Large area Luminescent Solar concentrators based on stoichiometric $CuInS_2$ NCs

Finally, to experimentally validate the design guidelines for efficient LSCs obtained from the Monte Carlo simulations, a prototype large-area semi-transparent LSC device (30 cm × 30 cm × 0.7 cm, 60% absorptance in the 400–750 nm spectral range) was fabricated that utilized stoichiometric $CuInS_2$ NCs. Based on the outcome of the theoretical modelling, we chose NCs with size a ≈ 1.5 nm, as they present the best trade-off between broadband SC and suppressed re-absorption capability. Prior to encapsulation, the NCs were shelled with a 1 nm thick ZnS layer to protect their surfaces from the radical initiators used for the production of the polymeric

waveguide. In agreement with previous reports, shelling substantially enhanced Φ_{PL} from 30 ± 5% to 85 ± 5% without modifying the spectral properties of the NCs.[237, 289, 300] The device was fabricated using the industrial cell-casting method for the production of optical grade poly(methyl methacrylate) (PMMA) waveguides free of scattering losses. The choice of PMMA as the waveguide material is dictated by its excellent optical properties,[274] high resistance to exposure to UV light, and various chemical treatments, as well as excellent performance in all-weather conditions. **Figure 2.10**a shows a photograph of the fabricated LSC containing 0.05 wt% of NCs under ambient illumination featuring the characteristic neutral

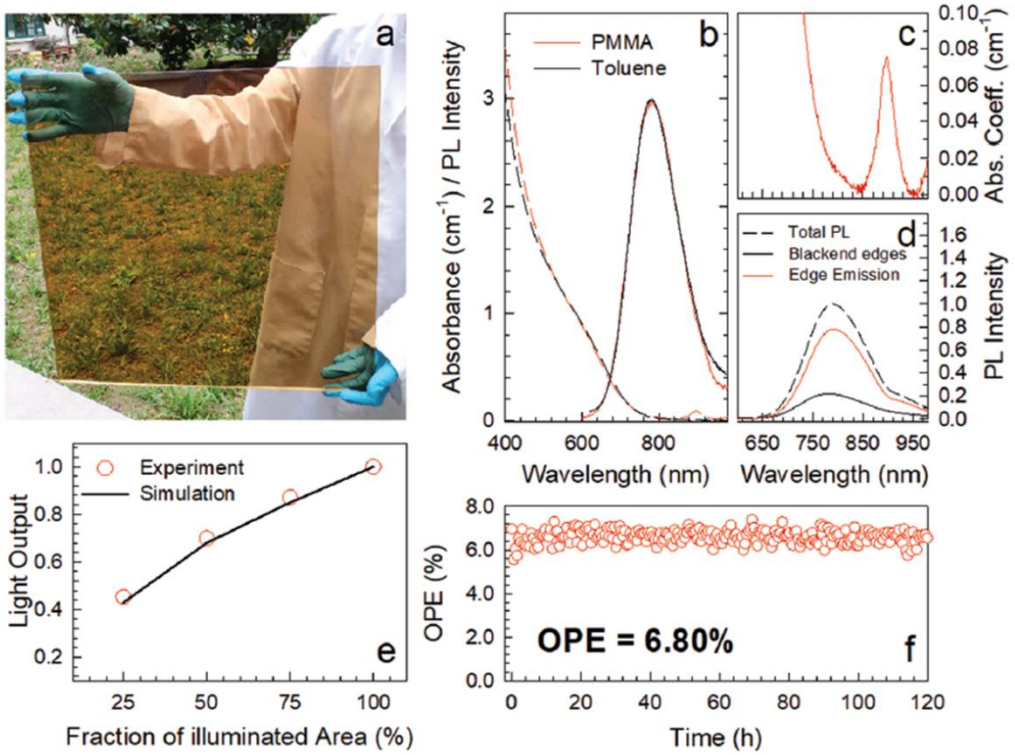

Figure 2.10. (a) Photograph under daylight of an NC:PMMA (NCs embedded in PMMA) nanocomposite waveguide (400–750 nm transparency ≈40%, dimensions: 30 cm × 30 cm × 0.7 cm). **(b)** Optical absorption (dashed lines) and PL (continuous lines) spectra of ZnS-capped $CuInS_2$ NCs (*a* = 1.5 nm) in toluene solution (black curves) and embedded into a PMMA nanocomposite (red curves, NC concentration of 0.05 wt%). **(c)** Enlargement of the absorption profile of the NC:PMMA LSC in the PL spectral region. No arbitrary baseline subtraction was applied to the data. **(d)** PL spectra of a portion (3 cm × 3 cm) of the same LSC with the edges clear (total PL, black dashed line) and blocked by black paint (solid black line, corresponding to light emitted from the slab surface). The red line is the difference between the total PL and the surface emission and corresponds to the PL emitted from the waveguide edges. **(e)** Relative optical output power measured from c-Si PVs coupled to one perimeter edge of the LSC as a function of the device area illuminated by a calibrated solar simulator (1.5 AM Global, circles). The theoretical trend obtained through Monte Carlo ray-tracing simulation of an ideal LSC with no scattering or re-absorption losses is reported as a black curve. **(f)** Stability test under stress conditions: artificial sunlight illumination (≈1 Sun); temperature of 55 °C. Point-to-point fluctuations in the OPE-values are due to oscillation in the intensity of excitation light.

brownish colouring well suited for architectural integration.[240, 260] The quality of the PMMA was assessed by gel permeation chromatography and nuclear magnetic resonance (NMR) spectroscopy indicating high average molar mass, $M_n \approx 225\,000$, and mass average molar mass, $M_w \approx 240\,000$, corresponding to a polydispersity value of 1.06, which indicates an extremely narrow chain length distribution. The amount of residual monomer in the final waveguides was <1% in compliance with international safety requirements. The optical absorption and PL spectra of the NCs in toluene solution and embedded into the PMMA waveguide are reported in **Figure 2.10b**, showing virtually identical spectral properties for the two samples (except for the absorption peak at 900 nm due to the vibrational overtone of the C–H stretching mode of the polymer). In agreement with previous reports,[240] side-by-side PL efficiency measurements show that Φ_{PL} of the pristine NCs is nearly completely preserved in the nanocomposite ($\Phi_{PL}^{PMMA} = 80 \pm 5\%$). To quantitatively demonstrate the absence of scattering losses, in **Figure 2.10c**, the enlargement of the optical absorption spectrum in the spectral range corresponding to the PL spectrum has been reported. The background absorption is $<1 \times 10^{-2}$ cm^{-1} (with no arbitrary baseline subtraction), highlighting the absence of light scattering contributions.

This is confirmed by PL measurements in an integrating sphere on the same nanocomposite sample (3 cm × 3 cm) with either clear or blackened edges, so as to distinguish between the light emitted from the LSC faces and the guided PL emitted from the slab edges. The PL data reported in **Figure 2.10d** show that the emission from the LSC edges corresponds to ≈76% of the total emission intensity, which closely matches the maximum theoretical value of light-trapping efficiency for a PMMA waveguide (≈74.1% considering a refractive index of the polymer matrix $n = 1.49$) defined by Snell's law. Having assessed the optical quality of our waveguide, we proceeded with quantifying the performances of our device by measuring the OE, the OQE and the Optical Power Efficiency (OPE), defined as the ratio between the optical power emitted by the LSC and the incident solar power. For these measurements, we index-matched the perimeter edges (A_{edge} = 120 cm × 0.7 cm = 84 cm^2) of the LSC shown in **Figure 2.10a** to calibrated c-Si solar cells and exposed the LSC to outdoors illumination perpendicular to its top surface (A_{LSC} = 30 cm × 30 cm = 900 cm^2) and used a calibrated photodiode to instantaneously monitor the solar irradiance impinging onto the LSC top surface. No reflector or back diffuser was placed at the bottom of the waveguide. Based on these measurements, an OPE = 6.8 ± 0.2% was attained, which was the highest optical power efficiency reported to date for a large area LSC. The corresponding OQE-value is 29.2%, corresponding to OE = 7.4%. The effective mitigation of reabsorption losses using $CuInS_2$ NCs with a = 1.5 nm,

together with the absence of scattering losses, resulted in a nearly ideal behavior of the LSC.[139, 301] This is highlighted in **Figure 2.10e**, where we show the light output emitted from one of the device edges (30×0.7 cm^2) measured using the same setup adopted for the OE measurements (with only one slab edge coupled to the photodiodes and no back reflector), but progressively exposing increasingly larger portions of the LSC area to the solar simulator. The same figure also reports the expected trend calculated using Monte Carlo ray-tracing simulation for an ideal scattering- and re-absorption-free device of identical dimensions embedded with emitters of the same Φ_{PL} as the used NCs, in which the light output is determined exclusively by the numeric aperture of the illuminated device area. The experimental data were found to be in very good agreement with the simulated trend, which supports the ascription that our LSC is close to an ideal device. Finally, to assess the stability of our stoichiometric $CuInS_2$ NCs and polymer waveguide in working conditions, an accelerated ageing test was performed by exposing the LSC to continuous illumination with solar light at 55 °C. Remarkably, as shown in **Figure 2.10f**, the OPE of the LSC remains constant for over 120 h of continuous operation, thus further supporting the technological potential of our approach.

2.6 Conclusions

In conclusion, I studied stoichiometric $CuInS_2$ NCs through the combination of optical and magneto-optical experiments as a function of size and temperature. Subsequently, it revealed, for the first time, the spectroscopic signatures predicted for the excitonic photophysics in I–III–VI_2 NCs. In agreement with effective mass calculations, measurements show quadratic dependence of the global Stokes shift and the radiative decay rate on the particle size, thus strongly supporting the theory by Efros and coworkers.[251] The absence of intragap defect states is consistent with magnetic circular dichroism experiments showing temperature independent MCD perfectly reproduced by the linear Zeeman splitting function. Time-resolved PL measurements performed below 50 K further reveal the dynamic signature of emission originating from a lower-lying dark-like exciton which are not found in Cu:doped CdSe NCs or off-stoichiometry $CuInS_2$ NCs. The splitting energy separating such a state from a grey exciton follows a linear trend with the inverse of particle volume as commonly observed in undoped II–VI chalcogenide NCs, suggesting that also in I–III–VI_2 NCs, such a behavior originates from enhanced electron–hole spin interaction. The impact of the observed size dependence of the Stokes shift in stoichiometric $CuInS_2$ NCs on their suitability to LSCs was evaluated, where I–III–VI_2 NCs are considered amongst the most promising candidates for

high performance devices. Monte Carlo ray-tracing simulations helped to decouple the beneficial effect of progressively wider solar harvesting efficiency with increasing particle size from the concomitant detrimental increase of reabsorption losses in large area devices and thereby to suggest compromise optimization strategies to realize efficient LSCs with size and aesthetics compatible with building integrated PV applications. Based on such theoretical guidelines, practical large-area LSC device was fabricated by embedding stoichiometric $CuInS_2$ NCs into mass polymerized PMMA waveguides. Thorough characterization of such a device revealed optical grade quality of the matrix and efficient NC emission, leading to an OPE as high as 6.8%, corresponding to the highest value reported to date for large-area LSC devices.

Chapter 3

Quantized Electronic Doping towards Atomically Controlled "Charge-Engineered" Semiconductor Nanocrystals

Synopsis

"Charge engineering" of semiconductor NCs through so-called electronic impurity doping is a long-standing challenge in colloidal chemistry and holds promise for ground-breaking advancements in many optoelectronic, photonic, and spin-based nanotechnologies. To date, our knowledge is limited to a few paradigmatic studies on a small number of model compounds and doping conditions, with important electronic dopants still unexplored in nanoscale systems. Equally importantly, fine-tuning of charge engineered NCs is hampered by the statistical limitations of traditional approaches. The resulting intrinsic doping inhomogeneity restricts fundamental studies to statistically averaged behaviors and complicates the realization of advanced device concepts based on their advantageous functionalities. Here we aim to address these issues by realizing the first example of II−VI NCs electronically doped with an exact number of heterovalent gold atoms, a known p-type acceptor impurity in bulk chalcogenides. Single-dopant accuracy across entire NC ensembles is obtained through a novel non-injection synthesis employing ligand-exchanged gold clusters as "quantized" dopant sources to seed the nucleation of CdSe NCs in organic media. In this work I attempt to carry out structural, spectroscopic, and magneto-optical investigations to trace a comprehensive picture of the physical processes resulting from the exact doping level of the NCs. Gold atoms, doped here for the first time into II−VI NCs, are found to incorporate as nonmagnetic Au^{+} species activating intense size-tuneable intragap photoluminescence and artificially offsetting the hole occupancy of valence band states. Fundamentally, the transient conversion of Au^{+} to paramagnetic Au^{2+} ($5d^{9}$ configuration) under optical excitation results in strong photoinduced magnetism and diluted magnetic semiconductor behavior revealing the contribution of individual paramagnetic impurities to the macroscopic magnetism of the NCs.

Altogether, the results demonstrate a new chemical approach towards NCs with physical functionalities tailored to the single impurity level and offer a versatile platform for future investigations and device exploitation of individual and collective impurity processes in quantum confined structures.

3.1 Prologue

Colloidal semiconductor NCs, owing to their size-tuneable electronic properties and solution processability, have long been proposed as versatile chemically synthesized alternatives for many photonic, optoelectronic, and quantum computational technologies as well as super-atomic functional building blocks for bottom-up assembled artificial metamaterials.[302-305] Since their original discovery over 30 years ago, tremendous advancements in colloidal and surface chemistry,[306-309] NC physics, and device application[27, 310, 311] have brought this vision closer to reality. At present, however, one challenge that remains outstanding in NCs science is so-called "charge engineering" by permanent and controlled introduction of optically or electrically functional charges into NCs.[312-316] Charge engineering of p-type and n-type bulk semiconductors through the insertion of heterovalent atoms with respect to the host lattice, commonly referred to as 'electronic impurity doping', is standard practice and arguably the most powerful material engineering paradigm underpinning contemporary microelectronics. Its extension to NCs synthesized directly in the liquid phase, aided by the enhanced interaction between the impurity charges and the spatially confined carriers, would unlock fundamental properties that cannot be achieved with other motifs such as unidirectional emission-only photophysics,[196, 312, 317] enhanced charge mobility,[313-316] and photocontrolled magnetic behaviors.[197, 278] These advantageous properties make charge-engineered NCs not only interesting systems to be investigated per se, but also potential cornerstones for ground-breaking advancements in applications ranging as widely as lasers,[191, 318, 319] transistors,[189, 315, 320] solar cells,[314, 321, 322] luminescent solar concentrators,[312, 317] and plasmonic[323] and spintronic devices[197, 278] fabricated via solution-based processes.[178, 324]

Despite this promise, our knowledge of electronically doped NCs is still limited to a relatively small number of model compounds and doping conditions. For example, direct colloidal synthesis or cation exchange routes are established only for II− VI or III−V NCs doped with copper, silver, iron, or indium,[178, 187, 193, 195, 315, 316, 325-328] whereas NCs doped with aluminium have been only once reported by Norris and co-workers.[329] On the other hand, doping with an important amphoteric electronic impurity such as gold, which is a known p-type dopant capable

of assuming +1, + 3, as well as +2 oxidation states in bulk II−VI semiconductors,[203-208] has never been reported in NCs. 'Au' doping has been successfully obtained in InP NCs where In^{3+} cations have been substituted with Au^{3+} cations.[193, 330]

Equally importantly, progress towards charge engineering of NCs has long been hampered by the intrinsic statistical limitations of traditional doping approaches, which operate at the ensemble level and lead to a Poissonian distribution of impurities across the NC population.[175, 176, 179, 331] This has historically restricted fundamental studies to statistically averaged behaviors and has complicated in-depth investigations of the physical impact of isolated charges (so-called solotronic effects) into nanoscale hosts due to parasitic effects by doping inhomogeneity in lightly doped NCs−for example, given an average doping level of three impurities per NC, only ∼20% of the NCs contain exactly three dopants and as much as 5% of the ensemble is entirely undoped. Recently, a first step toward overcoming the "Poissonian bottleneck" was achieved by the introduction of so-called quantized or exact doping strategies[280, 332-334] that propose the use of size-focused metal clusters or organometallic complexes as nucleation seeds for doped NCs. Since such seeds are composed of a "magic number" of atoms, these approaches enable one to achieve predetermined atomic resolution of the doping level in individual NCs and to produce homogeneously doped NC ensembles. However, quantized doping was only demonstrated using copper compounds, either in the form of chemically unstable benzenethiol complexes[335] or water-soluble clusters resulting in poor NC quality.[280] Crucially, no study has yet investigated the functional implications of quantized doping with electronic impurities. To the date this work was initiated, (i) the generalization of the strategy to electronic dopants, (ii) its extension to organic synthesis routes enabling enhanced control over the material quality, and (iii) the in-depth investigation of the emerging physical properties remained open challenges in NC science. The payback for such advancements will, in turn, be the long-sought capability to generate a library of chemically synthesized nanostructures finely engineered at the single charge level.

In this work, significant progress in these three directions was made by realizing, for the first time, CdSe NCs electronically doped with gold atoms through a new quantized-doping route using magic-sized gold clusters in organic media as nucleation seeds. The obtained Au:CdSe NCs are the first example of II−VI NCs incorporating gold dopants produced by any known route. Here, I report the studies on structural and analytical characterization, combined with spectroscopic measurements and chemical etching experiments, indicated that the clusters consist of seven gold atoms and that they seed the nucleation of CdSe NC containing an

equivalent number of gold impurities preferentially located in the particle core. Consistent with previous studies of bulk materials,[203-207] the dopants are found to incorporate as Au^+ acceptors. In NCs, owing to the quantum confinement effect, this results in long-lived, widely Stokes shifted luminescence, spectrally tuneable from the visible to the near-infrared by control of the particle size. Photoluminescence (PL) and transient transmission (TT) experiments on Au:CdSe NCs as a function of the excitation density highlight, for the first time, the effect of nonradiative Auger relaxation processes on the photophysics of electronically doped NCs. They also reveal the intimate link between the dopant and the intrinsic band-edge (BE) excitonic PL that is observed exclusively upon optical saturation of the Au^+ acceptor states with valence band (VB) photoholes. Also, importantly, magnetic circular dichroism (MCD) measurements reveal that the transient change of the oxidation state from Au^+ (with non-magnetic $5d^{10}$ electronic configuration) to Au^{2+} (with paramagnetic $5d^9$ electronic configuration) during the multistep exciton recombination process results in strong photoinduced paramagnetism. Fundamentally, such a phototriggered diluted magnetic semiconductor (DMS) behavior follows a step-like trend with the illumination intensity revealing the contribution of individual paramagnetic impurities to the macroscopic magnetism of the NCs. The process is formalized through a phenomenological dynamic model, indicating that the maximum paramagnetic response is obtained when all gold impurities in the NCs are photoconverted from their native nonmagnetic Au^+ state into the paramagnetic Au^{2+} configuration. Altogether, the results suggest a new chemical approach toward NCs with physical functionalities tailored to the single impurity level and demonstrates an unprecedented strategy for exquisite control of electronic impurity doping of NCs. This will provide a platform for future investigations and device exploitation of individual and collective processes in charge engineered quantum confined structures.

Figure 3.1. Schematics of the three-step synthesis strategy of quantized-doped Au:CdSe NCs. First, water-soluble Au_7-clusters were synthesized by chemical reduction of the metal precursor $HAuCl_4$ using glutathione (GSH), which also acts as capping ligand. Second, the clusters were phase-transferred from water to toluene by exchanging strongly polar GSH molecules with nonpolar 1-dodecanethiol (DDT) molecules. Finally, Au:CdSe NCs were seeded-grown using the Au_7 clusters.

3.2 Sample preparation of optimized Au doped CdSe NCs

The synthesis route for quantized-doped Au:CdSe NCs is schematically depicted in **Figure 3.1** and consists in a three-step procedure starting with the aqueous preparation of the Au clusters followed by phase transfer to a nonpolar medium via ligand exchange and the seeded growth of Au-doped CdSe NCs through a non-injection route. First, monodisperse clusters were obtained by direct reduction of $HAuCl_4$ (0.02 M) using L-glutathione (GSH, 0.1 M) that also acted as capping ligand.[336] After 24 h of vigorous stirring at 70 °C, the clusters were purified by adding isopropanol to the solution (1:2 volume ratio) and centrifuged at 6500 rpm for 20 min. This procedure was repeated thrice, and the purified clusters were then dispersed in ultrapure water. Before proceeding with the synthesis of the doped CdSe NCs, the clusters were characterized both for their core size and for the composition of their ligand shell by electrospray ionization mass spectrometry (ESI-MS), optical absorption, and X-ray photoelectron spectroscopy (XPS).

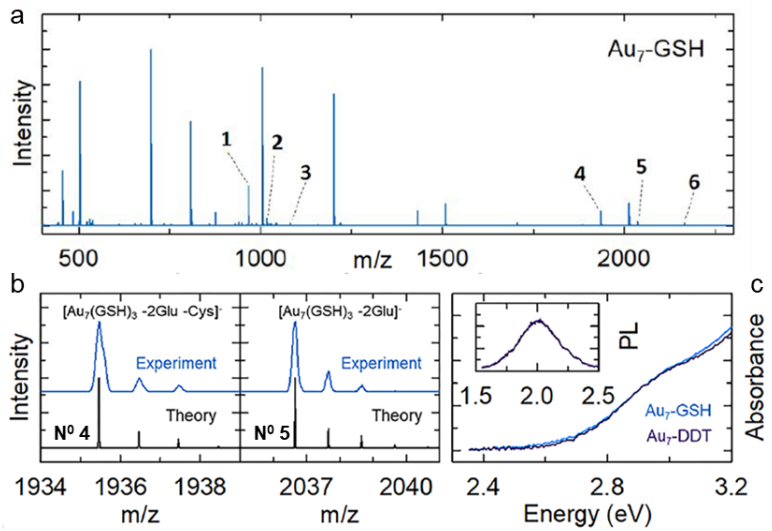

Figure 3.2. Positive mode ESI-MS spectra of gold clusters in aqueous solution. (a) The full spectrum with the assignment of all ESI-MS peaks is reported in the **table 3.1**. **(b)** Representative peaks $N^0$4&5 extracted from the ESI-MS spectrum of the Au_7-GSH clusters in water indicating $[Au_7(GSH)_3 -2Glu - Cys]^-$ (left) and $[Au_7(GSH)_3 -2Glu]^-$ (right) adducts. The respective simulated isotopic patterns are reported showing close agreement with the experiment. **(c)** Optical absorption spectra of GSH- and DDT-capped Au_7 clusters (blue and purple lines, respectively) showing invariance of the metallic core upon ligand exchange. Inset: PL spectrum of Au_7-DDT clusters in toluene under 3.1 eV excitation.

ESI-MS experiments, in positive-ion mode were performed on a hybrid quadrupole/time-of-flight instrument equipped with a nano-electrospray ion source (AB Sciex, Foster City, CA, USA). The samples were infused by borosilicate-coated capillaries of 1μm internal diameter (Thermo Fisher Scientific, Waltham, MA, USA). The main instrumental parameters were set

as: ion-spray voltage 1.1 kV; curtain gas 20 psi; de-clustering potential 80 V. The recorded spectra were averaged over a 1 minute of acquisition time is shown in the **Figure 3.2 a,b**. The simulation of the peak distributions of the ESI-MS spectra was performed by IsoPro 3.1 software, based on the Yergey algorithm. The ESI-MS data collected and the corresponding spectral peaks reported in **Table 3.1** indicate that the cluster population is nearly monodisperse and consists of systems composed of seven gold atoms capped by three GSH molecules. This is confirmed by the perfect agreement between the simulated isotopic distribution patterns and the respective experimental ESI-MS spectra and by the optical absorption spectrum in **Figure 3.2c** showing a first absorption feature at ∼2.9 eV corresponding to the E_g of Au_7 clusters predicted by the jellium model (∼2.89 eV)[337, 338] while recorded at room temperature on a Varian Cary 50 Scan UV−visible spectrophotometer under normal incidence in quartz cuvettes of 1 mm optical path length.

Peak	Chemical species	Theoretical average *m/z* (Da)	Experimental average *m/z* (Da)
1	$[Au7(GSH)3 -2Glu -Cys]^{2-}$	968.2	968.3
2	$[Au7(GSH)3 -2Glu]^{2-}$	1018.8	1019.4
3	$[Au7(GSH)3 -Glu]^{2-}$	1083.4	1083.9
5	$[Au7(GSH)3 -2Glu -Cys]^{-}$	1936.4	1936.0
5	$[Au7(GSH)3 -2Glu]^{-}$	2037.7	2038.9
6	$[Au7(GSH)3 -Glu]^{-}$	2166.6	2167.9

Table 3.1 - Peak assignment for the ESI-MS measurement of Au clusters in water reported in **Figure 3.2a** where Glu and Cys are, respectively, the glutamine and cysteine groups of the GSH molecules

To determine the composition of the state of existence of the Au clusters, XPS Measurements were performed on a Kratos Axis $Ultra^{DLD}$ spectrometer using a monochromatic Al Kα source operated at 15 kV and 20 mA. The specimen for XPS was prepared by drop casting 200 μL of a clean and concentrated sample solution onto a silicon wafer, thus obtaining a circular drop (approximately 1 cm wide in diameter) on it. All the analyses were carried out over an area of 300×700 μm^2. High-resolution analyses were carried out with a pass energy of 10 eV. The Kratos charge neutralizer system S4 was used during data acquisition. Spectra were charge corrected to the main line of the carbon 1s spectrum set to 284.8 eV (C−C bond) and were analyzed using Casa XPS software (version 2.3.16). The resultant XPS spectrum of the clusters in **Figure 3.3a** shows the typical $4f_{7/2}$ and $4f_{5/2}$ doublet of gold at 84.3 and 88 eV, both slightly

shifted with respect to the binding energy of metallic gold (84.0 eV, 87.7 eV).[339, 340] The fit of the XPS spectrum revealed that Au(0) accounts for 27% of total gold atoms, while 73% of the atoms are in Au(I) state, corresponding to 2 Au(0) and 5 Au(I) atoms per Au_7 cluster.

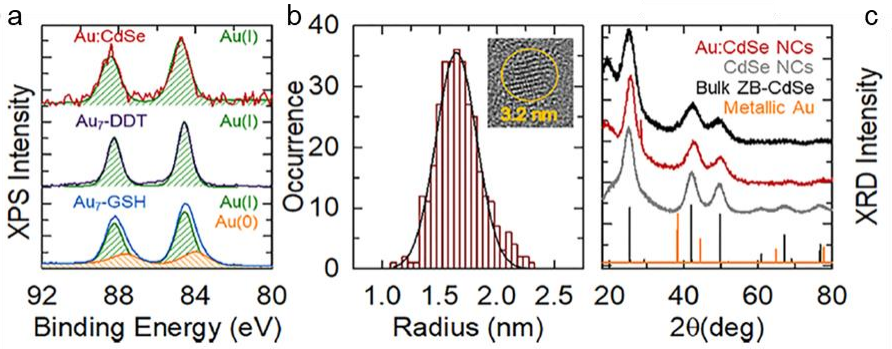

Figure 3.3.(a) XPS spectra for Au_7-GSH clusters (blue line), Au_7-DDT clusters (purple line) and Au:CdSe NCs (red line). Both samples show the characteristic doublet of gold 4f orbitals. For the Au_7-GSH clusters, the fit highlights both Au(0) (orange line) and Au(I) components (green line). The Au:CdSe NCs and Au_7-DDT clusters show exclusively Au(I) species (green line). **(b)** Size distribution and high-resolution TEM images of representative Au:CdSe NCs indicating an mean particle radius R = 1.65 ± 0.2 nm. The Gaussian fit to the experimental data is shown as a black line. **(c)** XRD pattern of undoped and Au-doped CdSe NCs (two sizes, R = 0.9 nm and 1.65 nm, black and red pattern respectively) indicating a zincblende crystal structure in all cases. The XRD pattern of bulk CdSe and metallic Au are shown as a black and orange lines respectively for references.

Once the Au_7-GSH clusters have been structurally characterized, ligand exchange reaction was performed with 1- dodecanethiol (DDT) that renders them compatible with the seeding reaction of CdSe NCs. To achieve this goal, the aqueous solution of Au_7-GSH clusters was first adjusted to pH ~9.0 by adding NaOH (1 M) dropwise. Then 5 mL of Au_7-GSH basic solution (76 μM) was destabilized with 5 mL of tetraoctylammonium bromide (TOA-Br) in ethanol (0.02 M). After 2 min of vigorous stirring, 5 mL of DDT (0.15 M) in toluene was finally added. The reaction mixture was then heated to 70 °C and kept under vigorous stirring to promote the phase transfer. After 1 h, the toluene phase was separated and washed thrice with ultrapure water to remove water-soluble impurities. Importantly, the ligand exchange procedure does not alter the size of the metallic core, as highlighted by the optical absorption spectrum of the DDT-capped Au clusters that resembles perfectly that of the Au_7-GSH analogues **(Figure 3.2c)**. It is however noted that, due to difficulties in sample ionization, ESI-MS measurements are inconclusive for the DDT capped clusters. XPS measurements on DDT-capped Au_7 clusters shown in **Figure 3.3a** highlight the presence of nearly exclusively Au(I) species, suggesting effective coordination of gold atoms by the DDT ligands. As a final step of the synthesis route, the Au_7-DDT clusters were introduced as nucleation seeds in the non-injection growth of CdSe NCs.[341] Undoped reference NCs were first produced to optimize the reaction parameters and

to estimate the concentration of the Au_7-DDT cluster required for seeding a monodisperse ensemble of Au:CdSe NCs. Here, selenium powder (0.05 mmol) and cadmium myristate (0.1 mmol) were added into a three-neck flask with 6.38 mL of 1-octadecene and 1 mL of oleic acid (OA). To synthesize doped NCs, 2.5 mL of Au_7-DDT (76 μM) was added to the reaction mixture. The mixture was degassed for 15 min in vacuum at room temperature and successively stirred and heated to 210 °C for 1 h under nitrogen flow. The samples were finally purified twice with hexane/ethanol co-solvents by centrifugation (4500 rpm, 10 min) to remove excess ligands and unreacted clusters. Importantly, in the cluster-seeded reaction, nucleation of doped CdSe NCs is observed at significantly lower temperature (~170 °C) with respect to the undoped counterparts (~210 °C), confirming that the gold clusters act as preferential nucleation seeds for CdSe NCs. As discussed below, in the presence of excess cluster seeds, such an effect further hinders the homonucleation of undoped CdSe particles leading to homogeneously doped Au:CdSe NCs ensembles. Representative transmission electron microscopy (TEM) image and size distribution statistics of the doped NCs are reported in **Figure 3.3b** showing spherical particles with average radius R = 1.65 ± 0.2 nm, as confirmed by the optical absorption data reported below.

In **Figure 3.3c**, we compare the XRD pattern of doped and undoped NCs of analogous size and of bulk CdSe in zincblende (ZB) crystal structure. These powder XRD patterns were acquired in Bragg−Brentano geometry with Cu Kα radiation (Panalytical X'Pert Pro powder diffractometer). The same cubic structure is observed for all systems indicating that the cluster seeding process does not affect the final crystal structure of the host NCs. No diffraction signal due to gold nanoparticles is observed for the doped NCs sample, indicating that Au nanoparticles do not nucleate during the growth of the Au:CdSe NCs.

To comprehensively determine the elemental composition of the resultant Au doped CdSe NCs, Inductively coupled plasma atomic emission spectroscopy (ICP-AES) was carried out using a iCAP 6500 Thermo spectrometer. All chemical analyses performed by ICP-AES were affected by a systematic error of about 5%. Samples were dissolved in HCl/HNO3 3:1 (v/v). The compositional analysis indicates that the atomic percentage of gold in these NCs is 0.8%, corresponding, as we demonstrate below, to seven Au atoms per NC.

First, we calculate the volume of the single NC in spherical particle approximation (using data from TEM analysis reported in **Figure 3.3b**):

$$V_{NC} = 4/3 \times \pi \times R^3 = 4/3 \times \pi \times (1.65 \pm 0.2)^3 = 18.80 \pm 6.84 \text{ nm}^3$$

Then, we calculate the volume of the unit cells of CdSe in cubic, ZB structure (as shown by XRD data reported in **Figure 3.3c)**,

Lattice constant of bulk ZB CdSe is a = 0.608±0.001 nm):

$$V_{cell} = a^3 = (0.608\pm0.001)^3 = 0.225\pm0.001 \text{ nm}^3$$

We can therefore obtain the total number of unit cell per NC

$$N_{cell} = V_{NC}/V_{cell} = (18.80\pm6.84)/ (0.225\pm0.001) = 84\pm31$$

and the total number of atoms

$$A_{QD} = N_{cell} \times A_{cell} = (84\pm31)\times8 \sim 692\pm247$$

Radius (nm)	Au %	Cd %	Se %
0.95	5.53	68.32	26.15
1.35	1.47	63.49	35.04
1.65	0.8	55.70	43.50

Table 3.2 – Atomic percentage of gold, cadmium and selenium as obtained from ICP-AES analysis of Au:CdSe NCs with radius R.

Considering the percentage of Au atoms obtained by ICP-AES data reported in **Table 3.2** (at% Au = 0.8%), we obtain that Atoms of Au per NC = 6±2.

The same procedure performed for R=0.9 nm and R=1.35 nm using the respective Au % also yields the similar value of gold atoms in each host nanoparticle.

3.3 Optical Properties of Au:CdSe NCs and Analytical Assessment of the Quantized-Doping Mechanism

Optical spectroscopy measurements provide an independent proof of the seeding effect by the Au_7-DDT clusters resulting in homogeneously quantized-doped ensembles of Au:CdSe NCs each containing the gold atomic equivalent of one Au_7 cluster seed. Importantly, they also demonstrate the incorporation of gold atoms as acceptor electronic dopants in the NCs and clarify their key role in the recombination process of BE excitons. In **Figure 3.4a**, I report the absorption and PL spectra of representative undoped and Au-doped CdSe NCs after 1 h of

reaction time. Optical absorption spectra thus reported were recorded at room temperature on a Varian Cary 50 Scan UV−visible spectrophotometer under normal incidence in cuvettes of optical path 0.1 cm. Photoluminescence (PL) measurements on the other hand were performed using a pulsed diode laser at 3.1 eV (Edinburgh Inst. EPL 405, 40 ps pulse width) as excitation source and collecting the emitted light with a TM-C10083CA Hamamatsu Mini-Spectrometer. Time-resolved PL experiments were conducted using the same excitation source and collecting with a Hamamatsu R943-02 time-correlated single-photon counting unit coupled to an Oriel Instruments Cornerstone 260 monochromator.

The absorption spectra of both doped and undoped NCs show a 1S peak at ∼2.23 eV, in agreement with R ≈ 1.6 nm[342] extracted from the TEM images. Similar to previously reported NCs doped with group 11 metals, the absorption spectrum of the Au:CdSe NCs is broader than the undoped analogues possibly due to some possible local structural disorder in the doped systems.[343] More importantly, I observed stark differences between the emission spectra and decay dynamics of the doped and undoped NCs due to the participation of the Au^+ impurities in the exciton recombination process. Specifically, the undoped NCs show the typical narrowband excitonic photoluminescence (BE-PL) at 2.17 eV, nearly resonant with the respective 1S absorption peak, with PL quantum yield Φ_{PL} = 35 ± 4%. The corresponding PL decay curve shown in **Figure 3.4b** is slightly multiexponential, as commonly observed for unshelled CdSe NCs, with effective exciton lifetime $<\tau_{BE}>$ ≈ 15 ns (as extracted when the emission intensity is reduced by a factor 1/e). In contrast, the Au:CdSe NCs exhibit exclusively a broad, (fwhm = 340 meV) near-infrared emission centered at 1.6 eV (hereafter indicated as Au-PL), Stokes-shifted from the respective absorption peak by Δ_S = 600 meV. The effective emission lifetime is $<\tau_{Au\text{-}PL}>$ ≈ 290 ns, around 20-fold longer than the intrinsic exciton lifetime **(Figure 3.4b)**. The PL efficiency is found to be Φ_{PL} = 13 ± 2%. The spectral and dynamical behaviors of the Au:CdSe NCs are in full agreement with the Au-mediated recombination process observed in gold-doped II−VI bulk chalcogenides, where the full d-shell of the Au impurity gives rise to a deep acceptor level in the host forbidden gap,[203-208, 344-346] which participates in the recombination process of BE excitons following the scheme depicted in the inset of **Figure 3.4a**. Specifically, following NC excitation (Step 1), the photo-hole in the NC valence band (VB) is rapidly captured by Au^+, which temporarily changes its oxidation state to Au^{2+} (Step 2), thereby becoming optically active for the subsequent radiative recombination of a conduction band (CB) electron (Step 3).[203, 205-208 345-348] Spectro-electrochemical measurements in **Figure 3.4c** support this picture, showing that the Au-PL intensity increases

under negative electrochemical potentials (V_{EC} < 0 V). In such conditions, which correspond to raising the NC Fermi energy (central scheme in **Figure 3.4c**), electron traps due to dangling bonds on the NC surfaces, are progressively passivated, which suppresses nonradiative trapping of photogenerated CB electrons. Concomitantly, excess electrons accumulating in surface defects become efficient traps for VB photo-holes. On the other hand, the application of positive V_{EC} depletes surface states of electrons, activating electron traps and passivating hole traps (rightmost scheme in **Figure 3.4c**).

It can be noticed that the spectro-electrochemical response is fully reproducible for many cycles as shown in **Figure 3.5**, indicating that NC surfaces are not damaged during the experiment. The ~70% brightening for V_{EC} < 0 V, with no modification of the PL dynamics, together with the essentially constant PL intensity for V_{EC} > 0V indicate that the PL intensity is mostly limited by electron trapping occurring on a faster time scale than radiative decay, whereas hole trapping is essentially negligible. This suggests that, similar to what is observed in ternary

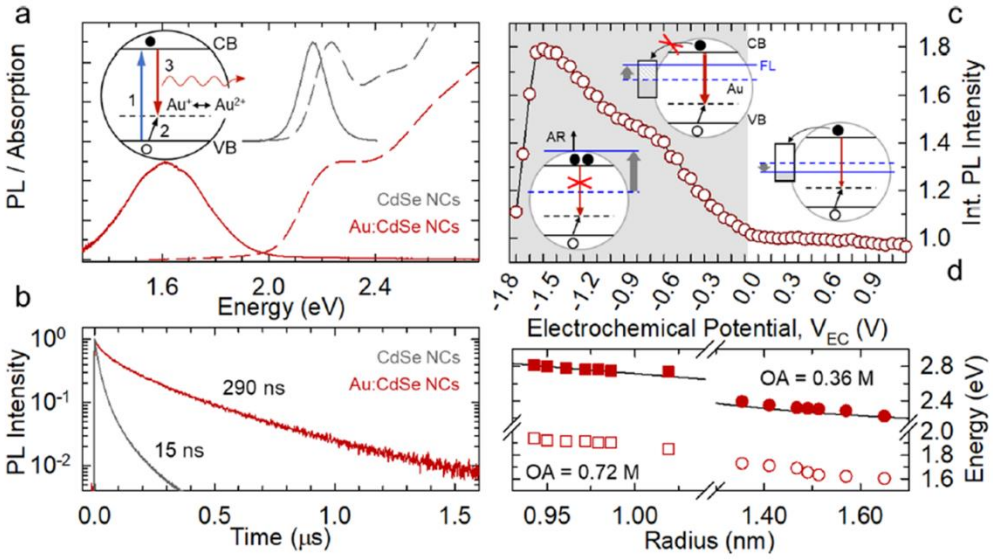

Figure 3.4. (a) Optical absorption (dashed lines) and PL (continuous lines) spectra of undoped (grey) and Au-doped CdSe NCs (red) in toluene (excitation energy E_{EX} = 3.1 eV). **(b)** PL decay traces of bare CdSe NCs (grey) and Au:CdSe NCs (red) in toluene under 3.1 eV excitation at room temperature with a pulse frequency of 200 kHz. **(c)** Integrated PL intensity of Au:CdSe NCs under applied electrochemical potential (V_{EC}). Negative V_{EC}-values (shaded in grey) lead to filling of electron traps likely localized on the NCs surfaces resulting in PL brightening (central scheme). Under positive V_{EC} that depletes electron-rich traps (rightmost scheme), the PL intensity is nearly constant, pointing to a situation in which trap states are positioned in energy just above the Fermi level (FL). For V_{EC} < −1.5 V, the Au-PL intensity drops due to nonradiative Auger decay of negative trions (leftmost scheme). **(d)** Spectral positions of the 1S absorption feature−together with the predicted trend with the NC size based on ref [340] (black line), and the Au-related PL band (open symbols) as a function of particle radius for two sets of Au:CdSe NCs synthesized in the exact same conditions except for the amount of OA.

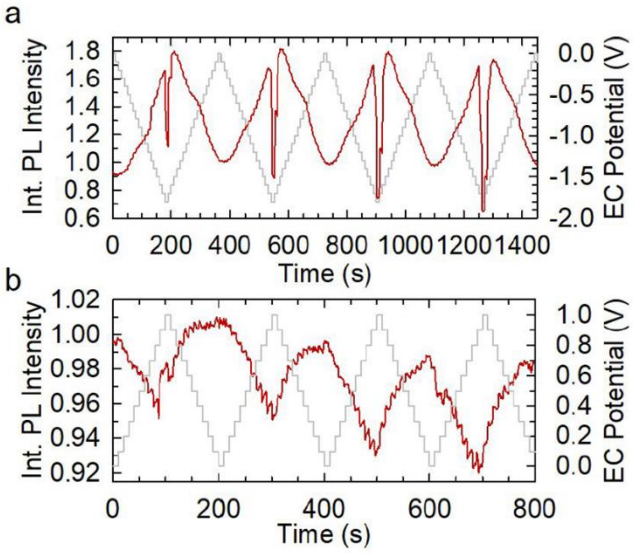

Figure 3.5 – Integrated PL intensity during four **(a)** negative and **(b)** positive EC cycles.

$CuInS_2$ and lead halide perovskite NCs,[280, 349] surface trap states are mostly positioned in energy above the Fermi level of the NC, that is, they are nearly devoid of electrons already at $V_{EC} = 0$ V and thus essentially unaffected by oxidative electrochemical potentials. In addition to probing the effects of surface states, spectro-electrochemistry experiments provide a first insight into the photophysics of charged Au:CdSe NCs. Looking at the traces for $V_{EC} < -1.5$ V, we observe that the Au-PL intensity undergoes a sudden ~50% drop with no changes in its time dynamics. The effect is fully reversible for many cycles **(Figure 3.5)** and is ascribed to efficient nonradiative Auger decay of negative trions formed by direct injection of electrons in the CB of the NCs **(**leftmost scheme in **Figure 3.4c).**[280, 350, 351] Transient transmission measurements as a function of the excitation fluence, That I have reported in the subsequent sections, corroborate this picture, showing an Auger dominated biexciton lifetime of ~10 ps, consistent with Auger relaxation of negative trions occurring on a time scale faster than the time resolution of our spectro-electrochemistry setup (~1.5 ns), even considering a strong asymmetry between the contributions by the negative and the positive trion pathways to the biexciton Auger decay.[352, 353] Importantly, since the Au^+ acceptor state is pinned to the host valence band,[195, 203, 326, 327, 329, 337-340] the dopant-mediated emission is tuneable by control of the particle size, whereas the Stokes shift is essentially independent of quantum confinement. The spectral tunability from the visible to the near IR regions achievable by doping CdSe NCs with gold is emphasized in **Figure 3.4d**, where I measured the energy positions of the 1S absorption peak and of the Au-PL for two sets of Au:CdSe NCs ranging different particle size regimes (~0.9−1.05 nm and~1.35−1.65 nm) controlled by the amount of OA ligands used in the

synthesis.[354] The XPS analysis of the Au:CdSe NCs, previously reported in **Figure 3.3a** corroborates this picture by showing the Au-4f $_{7/2}$ and Au-4f$_{5/2}$ signals, respectively, at 84.7 and 88.4 eV. Accordingly, the spectrum is well fitted by using exclusively the characteristic peaks of Au(I). Both peaks are shifted to higher energies with respect to the cluster seeds, in agreement with the acceptor role of the Au dopants in +1 oxidation state.

Crucially, the absence of residual BE-PL in the emission spectrum of any Au:CdSe NCs aliquot extracted at the various stages of the particle growth reported in **Figure 3.6a** indicates that the NC ensemble is composed solely of doped NCs. On the basis of this evidence, structural and spectroscopic experiments were combined with chemical microanalysis to demonstrate that, independent of the host size, each CdSe NC contains the atomic equivalent of one Au_7 cluster. **Figure 3.7a**, exhibits the Au atomic concentration (indicated as the "doping level") measured by ICP-AES analysis on Au:CdSe NC with increasing size synthesized using the same Au_7-DDT seeds (also reported in **Table 3.2**).

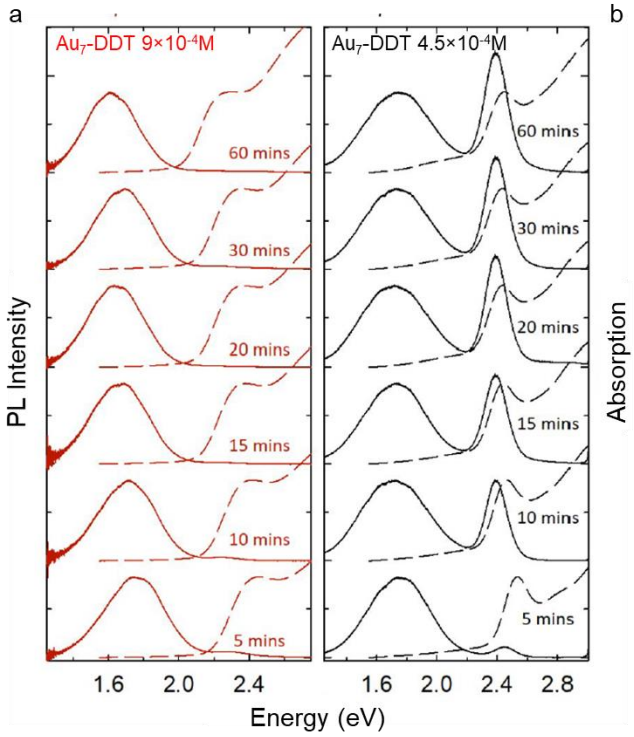

Figure 3.6: Optical absorption (dashed lines) and PL (continuous lines) spectra of various aliquots of Au:CdSe NCs produced with different concentration of gold cluster Au_7-DDT **(a)** 9×10^{-4} M and **(b)** 4.5×10^{-4} M. The condition with [Au_7-DDT]=9×10^{-4} M refers to the synthesis of the NCs mainly discussed throughout this chapter.

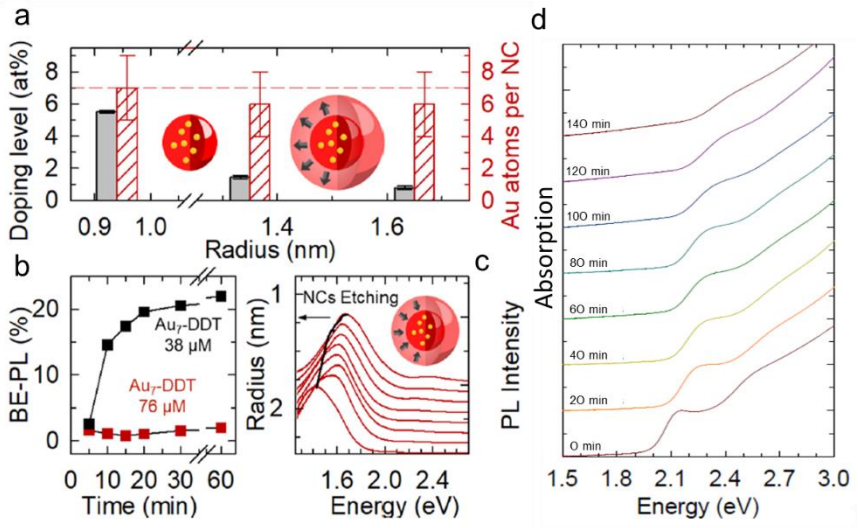

Figure 3.7 (a) Average NC doping level estimated by ICP-AES as a function of the particle radius. Au atomic content of doped NCs extracted by combining the spectroscopic, structural, and the elemental analysis data. **(b)** Integrated BE-PL intensity for CdSe NCs grown with different amounts of Au_7-DDT cluster seeds, highlighting that when an excess concentration of seeds is employed, only doped particles are obtained (the BE-PL intensity is indistinguishable from the background). Hetero-nucleation of undoped CdSe NCs is observed upon lowering the concentration of seeds, thus confirming the seeding role of the gold clusters. **(c)** PL spectra of Au:CdSe NCs during surface etching experiments with OA (initial NC radius R = 1.81 nm, E_{EX} = 3.1 eV, fluence 0.3 μJ/cm^2), showing progressive blue shift due to enhanced quantum confinement and no measurable emergence of BE-PL, indicating that most of the Au impurities are embedded in the NC interior. The spectra are offset for clarity. The black line represents the evolution of the NC size following the etching treatment extracted from ref [340]. **(d)** Normalized optical absorption spectra of Au:CdSe NCs during the etching process. As expected, the absorption edge progressively shifts towards higher energies due to larger quantum confinement.

For these measurements, the samples were purified by centrifugation and redispersion multiple times to remove any possible trace of residual unreacted clusters. According to the progressively larger volume of the NC host, the per-particle Au atomic percentage decreases with increasing the NC radius. Most importantly, considering the size and the cubic lattice of the NC hosts (refer to the discussion towards the end of previous section), the measured doping level of each sample corresponds, within the experimental error, to seven gold atoms per particle, thus indicating that each Au_7−DDT cluster seeds the nucleation of one quantized-doped Au:CdSe NC. Definitive confirmation of this effect is provided by optically monitoring the growth of two sets of Au:CdSe NCs produced in the exact same synthetic conditions and differing from each other only by the concentration of the Au_7−DDT seeds. As shown in **Figure 3.6** and quantified in **Figure 3.7b**, when a 76 μM solution of cluster seeds is used, the emission spectrum of the NCs shows exclusively the Au-PL at all stages of the particle growth, indicating no nucleation of undoped CdSe NCs. In contrast, when the cluster concentration is lowered to 38 μM **(Figure 3.6b)**, only the first aliquot (corresponding to 5 min' reaction time)

shows nearly negligible BE-PL, confirming the preferential nucleation of doped particles on the cluster seeds. However, as the concentration of unreacted cluster seeds drops over time, the BE-PL rapidly intensifies indicating the development of a subpopulation of undoped NCs in the ensemble. The seeding effect by the Au_7-DDT clusters acting as exact predetermined sources of impurities for individual Au:CdSe NC, leads to the relevant conclusion that through the quantized doping approach it is possible to tune the effective doping volume concentration of entire NC ensembles by simply controlling the particle size without affecting the doping homogeneity. It is also noteworthy that the quantized-doping approach enables us to introduce Au impurities markedly more effectively than through the direct addition of molecular gold precursors to the reaction medium. This is shown in **Figure 3.8**, where I report the optical spectra of CdSe NCs grown in the same synthetic conditions as our quantized-doped NCs, but using Au(I) chloride or Au acetate as dopant sources. In both cases, only the BE-PL is observed by using precursor concentrations as high as 5 wt % and partial doping of the ensemble is found by employing concentrations of 20 wt %, corresponding to 50 times the amount of gold provided by the Au_7- DDT clusters.

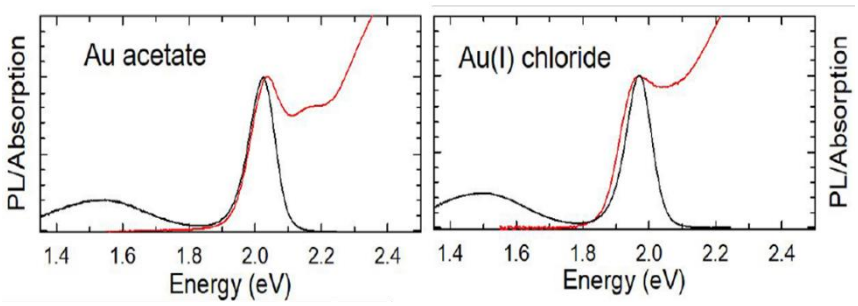

Figure 3.8: Normalized optical absorption (red) and PL spectra (black) of Au:CdSe NCs doped synthesized used with Au acetate (left panel) and Au(I) chloride (right panel) as gold precursors in the reaction synthesis.

It is also highlighted that, as a result of the seeded growth reaction, the dopants in Au:CdSe NCs are initially located in the inner core of the host particles, and the chemical microanalysis in **Figure 3.7a** indicates that their total number is retained also in the largest NCs. Nevertheless, it is instructive to investigate whether during particle growth the Au^+ ions remain in the interior or diffuse toward the NC surfaces, as this could affect their physical interaction with the host carriers and ultimately the NC functionality. To probe this aspect, we chemically etched our NCs using OA.[329, 355] In the case of surface segregation of dopants, chemical removal of the outer NC layers is expected to give rise to a subpopulation of undoped NCs that would be spectroscopically evident by the emergence of the BE-PL at the expense of the Au-PL intensity. Importantly, despite the NC size being reduced by nearly half (from 1.8 to 1.1 nm as extracted

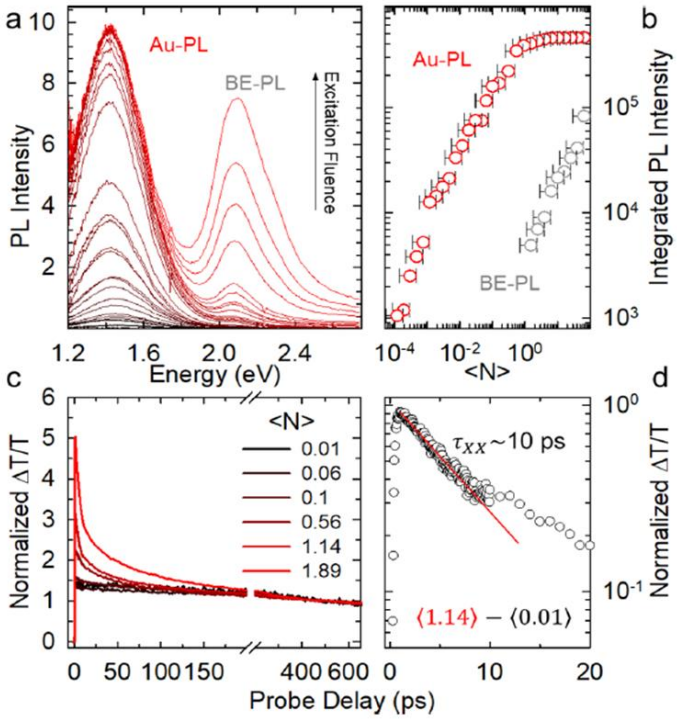

Figure 3.9. (a) PL spectra of Au:CdSe NCs (R = 1.81 nm) as a function of the excitation fluence (E_{EX} = 3.5 eV, from 4 μJ/cm^2 to 26 mJ/cm^2 as indicated by the arrow), showing saturation of the Au-PL band and the emergence of BE-PL at high fluence values. **(b)** Integrated PL intensity of the Au-PL (red circles) and BE-PL (gray circles) extracted from the spectra in panel 'a' as a function of the average NC exciton occupancy <N>. The error bars represent uncertainties on the dimensions of the excitation spot and the spread in the reported cross section values for CdSe[340] NCs. The measurements were conducted using ~5 ns long excitation pulses. Therefore, the average <N> values in high excitation conditions shown in **Figure 3.9b** might be overestimated due to ultrafast nonradiative relaxation during the excitation pulse. **(c)** Photobleaching dynamics of Au:CdSe NCs normalized when the pump−probe delay is 600 ps at the 1S energy for increasingly higher pump fluence corresponding to the displayed average instantaneous exciton occupancy <N>. **(d)** Dynamics of biexcitons (circles) extracted by subtracting the TT trace for <N> = 0.01 from the trace at <N> ≥ 1.14. The fit to a single exponential decay is shown as a solid red line. The obtained biexciton lifetime is $\tau_{XX} \approx 10$ ps. All measurements were carried out at room temperature.

from the 1S energy,[342] **(Figure 3.7c,d)** and the fact that the BE emission in undoped NCs has nearly thrice the Φ_{PL} than the dopant-related PL of Au:CdSe NCs, no significant BE-PL is detected at any stage of the etching treatment and the only observed effect is the blue-shift of the Au- PL due to enhanced quantum confinement in smaller (etched) particles. These results suggest that most dopants are located in the interior also for relatively large CdSe NCs. Nevertheless, since the PL measurements are conducted in the single exciton regime, we do not rule out the possibility that some dopants might be removed from the NC during surface etching. As a result, most, if not all, of the seven Au impurities are, in principle, expected to participate in the physics of the NC hosts.

A first glimpse of this effect is provided by the evolution of the emission spectrum of the Au:CdSe NCs (R = 1.65 nm) with increasing excitation power density. As shown by the PL spectra versus average exciton occupancy (<N> = σ × f, where f is the excitation fluence in photons/cm^2 and $\sigma_{3.49\ eV} = 1.55 \times 10^{-15}$ cm^2 is the absorption cross section at the excitation energy of 3.49 eV)[342] in **Figure 3.9a** and quantified in terms of the integrated PL intensity in **Figure 3.9b**, for <N> less than ~1, the NCs exhibit exclusively the broad Au-PL band at ~1.45 eV growing slightly sublinearly with the excitation fluence. For larger <N>-values, the Au-PL saturates at an essentially constant intensity. This, effect, I ascribed to the activation of nonradiative Auger recombination of multiexcitons, as confirmed by TT experiments highlighting the development of a sub-nanosecond component in the 1S bleaching dynamics at increasing excitation fluence for <N> ≥1 **(Figure 3.9c)**. The analysis of the 1S bleaching time trace for <N> ≥ 1 following the procedure in ref [41] yields a biexciton lifetime τ_{XX} = 10 ps, in nearly perfect agreement with previous reports on undoped CdSe NCs of comparable size (R = 1.1 nm, **Figure 3.9d**).[41] Invariant Auger recombination rates upon n-type doping of InAs NCs with electron donor Cu^+ ions have been reported by Yang et al. through transient transmission measurements.[356] In our case, however, such a behavior is somehow surprising since, in undoped CdSe NCs, the Auger recombination of biexcitons occurs predominantly by the so-called positive trion pathway,[353] where the energy of one exciton is non-radiatively transferred to a spectator excited hole. In Au-doped NCs, Au^+ dopants behave as hole acceptors depleting the VB from photoholes, therefore, based on the similarity between our Au-doped and undoped CdSe NCs, I speculate here that either the Auger process involves the holes localized in the Au^{2+} centers, which will then give no further contribution to the Au-PL, or that Auger decay takes place before hole capture by the dopants. A recent study on heavily doped CdSe NCs indicates that capture of the photohole by Ag^+ acceptors occurs in less than 2 ps,[197] seemingly supporting the first interpretation that has to be investigated in depth in a dedicated study. It is however noticeable that, in the nearly CW excitation conditions (excitation pulse length ~5 ns) used in PL versus fluence experiments **(Figure 3.9a,b)**, the observed efficient Auger recombination of multiexcitons might alter the estimate of the average exciton population per NC from the nominal <N>-values, due to ultrafast nonradiative relaxation during the excitation pulse. As anticipated above, the plateauing trend of the Au-PL is accompanied by the sudden emergence and intensification of the BE-PL peak at 2.12 eV, suggesting that radiative recombination of BE excitons is activated by the optical saturation of the Au^+ acceptor states with photoholes that offsets the VB hole occupancy. Thus, the BE-PL

appears for nominal <N>-values consistent, within the experimental error, with the quantized doping status of the NCs. In agreement with the above-mentioned effect of Auger decay on the estimate of <N>, the BE-PL shows no saturation with increasing excitation fluence and the biexciton spectral contribution to the high energy shoulder of the BE-PL peak appears for nominal <N>- values as high as ~10 excitons per NC**.** Details of the multiexcitonic processes and dynamics in Au:CdSe NCs are beyond the scope of this chapter and will have to be treated in a separate study in future.

3.4 Photo-triggered magnetism of Au doped CdSe nanocrystals

In addition to activating new light emission properties in CdSe NCs, quantized electronic doping by Au^+ introduces important magnetic functionalities not present in undoped systems,[89] conferring to Au:CdSe NCs, phototriggered paramagnetic behavior with amplitude and dynamics directly linked to the doping level and to the Au^+-mediated exciton recombination mechanism described in **Figure 3.4**. Specifically, the rapid localization of the photohole (h_{VB}) from the valence band into the Au^+ center optically converts it into a doubly charged Au^{2+} cation following the reaction $Au^+(d^{10}) + h_{VB} \rightarrow Au^{2+}(d^9)$. The resulting sp-d exchange interaction between the unpaired spin in the incomplete d-shell of Au^{2+} and the host material's

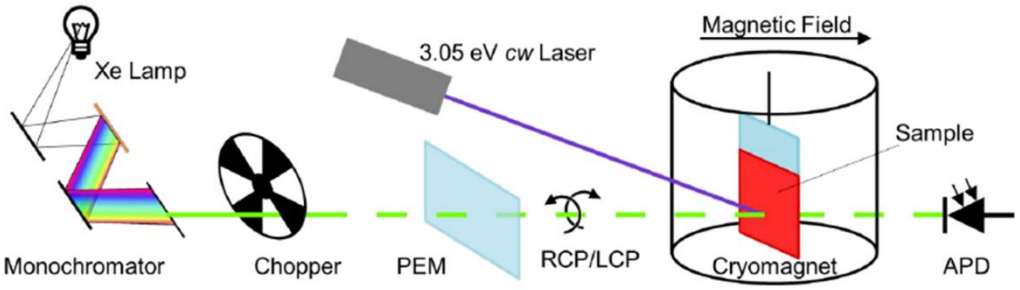

Figure 3.10: Schematics of the experimental setup used for MCD measurements under additional UV excitation. The probe beam is produced by a Xe lamp coupled to a scanning monochromator. The beam is chopped with a mechanical chopper and its circular polarization is modulated between right and left circularly polarized using a photo-elastic modulator (PEM). The light transmitted through the sample, which is positioned in the variable temperature insert of a 7T magnet with direct optical access, is collected by an avalanche photodiode (APD). The additional UV light is provided by a CW laser at 3.05 eV incident onto the same position of the sample as the weak probe beam.

conduction/valence bands effectively turns the NCs into optically activated DMS-nanomaterials.

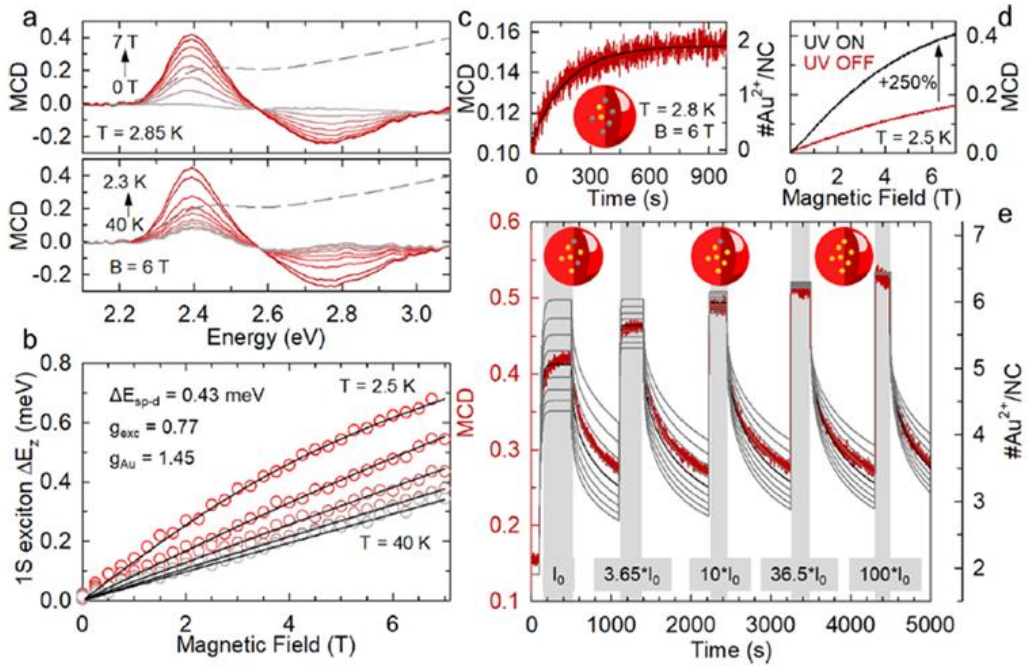

Figure 3.11. (a) MCD spectra of Au:CdSe NCs, from which the Zeeman splitting of the 1S exciton can be inferred. Top panel: MCD spectra are shown at 2.85 K in different magnetic fields from 0 to 7 T. Bottom panel: MCD spectra at 6T, at temperatures from 40 to 2.3 K. The linear absorption spectrum is reported as a dashed gray line in a and b. **(b)** Enhanced Zeeman splitting of the 1S band-edge exciton versus magnetic field, at various temperatures. The high field saturation and strong temperature dependence indicate the existence of sp−d exchange coupling between the conduction/valence bands of the semiconductor host and paramagnetic dopants in the NCs. This species is consistent with Au^{2+} dopants excited by fast localization (capture) of the VB hole. Lines are fit to a Brillouin function using a single set of parameters. **(c)** Evolution of the MCD signal of the 1S exciton of Au:CdSe NCs over time, measured at 2.8 K and 6 T using 25 nW/cm2 probe fluence. The black line represents the average number of photoexcited Au^{2+} species following the dynamic model described in the main text reaching saturation at ~2 Au^{2+} per NC. **(d)** Peak MCD signal (measured at 2.4 eV) as a continuous function of applied magnetic field with and without additional UV illumination (40 μWcm^{-2}). **(e)** Time evolution of the MCD signal as additional UV illumination is turned on (gray shading, I_0 = 0.3 μW) and off. Stronger UV intensity leads to larger MCD signal and faster dynamics of both on and off phases. In all cases, the MCD decay is markedly slower than the corresponding rise under UV excitation. The gray curves are the average number of paramagnetic centers calculated through the kinetic model explained in the main text using different k-values ranging from 0.0266 to 0.0506 s^{-1} with 0.003 s^{-1} steps. The black line is the solution of the kinetic model using the experimental k-value of 0.0386 s^{-1}. The MCD approaches saturation when the number of paramagnetic species per NC in kinetic equilibrium approaches seven, in agreement with the quantized doping level of the NC.

To investigate this photoinduced magnetic behavior, MCD spectroscopy was performed, which measures the Zeeman splitting of the 1S exciton absorption peak. Standard MCD method[89] was used to measure the field- and temperature-dependent Zeeman splitting (ΔE_Z) of the 1S exciton absorption resonance in our NCs, from which the presence of any additional *sp–d* exchange coupling of the exciton to paramagnetic dopants can be inferred. As in conventional diluted

magnetic semiconductors, paramagnetic moments in the NC are revealed via an enhanced and strongly temperature-dependent ΔE_Z. MCD measures, as a function of photon energy, the (normalized) difference in transmission between right and left circularly polarized light through the NC film in the Faraday geometry, $(T_R - T_L)/(T_R + T_L)$[190]. When the Zeeman splitting is small compared to the width of the 1S exciton absorption (as is the case here), the MCD spectrum is therefore derivative-like with a low-energy maximum proportional to ΔE_Z. NC films were mounted in the variable-temperature insert (1.5–300 K) of a 7 T superconducting magnet with direct optical access. Probe light of tunable wavelength was derived from a Xenon lamp directed through a spectrometer. The probe light as depicted in the schematic diagram in **Figure 3.10** was mechanically chopped at 137 Hz and was modulated between right and left circular polarizations at 50 kHz using a photo-elastic modulator (PEM). The transmitted light was detected with a silicon avalanche photodiode. Photomagnetization was induced with additional light from a continuous-wave 3.05 eV diode laser.

In particular, MCD can reveal the presence of paramagnetic dopants in the semiconductor host via the appearance of an enhanced and temperature-dependent Zeeman splitting that arises from sp-d spin exchange coupling between the paramagnetic dopants and the 1S exciton.[190] In our specific case, the probe light used in the MCD experiments, being resonant with the NC's absorption spectrum, also generates the paramagnetic species by photoexciting the NCs. **Figure 3.11a** presents the MCD spectra of the Au:CdSe NCs as a function of the applied magnetic field, B, and temperature T. The derivative-like spectrum is featured by two peaks at ~2.4 eV and ~2.75 eV corresponding to the Zeeman splitting of the 1S and 2S exciton spin states, respectively. The magnetic response intensifies strongly with increasing B from zero to 7 T (at 2.85 K) and also upon lowering the temperature from 40 to 2.85 K (at B = 6 T). The temperature-dependent MCD unambiguously indicates sp-d coupling between the 1S exciton and paramagnetic impurities in the NCs because the average magnetization of a paramagnet depends strongly on both field and temperature. The effect is quantified in **Figure 3.11b**, where we report the splitting of the 1S exciton (E_{probe} = 2.39 eV) as a function of B at several temperatures, clearly showing strong temperature dependence and saturation of the splitting energy. Both these behaviors are definitive signatures of sp-d exchange. Accordingly, the experimental data are well fitted with the standard Brillouin function for conventional DMS materials:[357]

$$\Delta E_Z = g_{ex}\mu_B B + \Delta E_{sp\text{-}d} \langle S_Z \rangle \quad (3.1)$$

where the first term represents the intrinsic, temperature independent linear Zeeman splitting of the CdSe exciton states determined solely by the exciton g-factor (g_{ex}), and the second term considers any additional splitting due to the sp-d exchange interaction with the Au^{2+} impurities, which are characterized by a temperature-dependent average spin projection along B, $<S_Z>$. Here, I describe the field- and temperature-dependent paramagnetism of spin-J ions S_Z with the Brillouin function

$$B_J(g_{Au}\mu_B JB/k_B T) \quad (3.2)$$

where g_{Au} is the Landé factor of the unpaired spin at the Au^{2+} ion, μ_B is the Bohr magneton, and k_B the Boltzmann constant. In II−VI semiconductors, the tetrahedral crystal field splits the d-states of the impurities in a six-fold degenerate t_{2g} state (at lower energies) and a four-fold degenerate e_g state (at higher energies). The Au-spin is therefore featured by J = 1/2, which has been used to fit the experimental data in **Figure 3.11b** with eq (3.1). g_{ex}, g_{Au}, and ΔE_{sp-d} have also been set as shared parameters and the best fit has been obtained using ΔE_{sp-d} = 0.43 meV, g_{Au} = 1.45, and g_{ex} = 0.77. The CdSe exciton g-factor is in agreement with previous results obtained via magneto-optical investigation of undoped CdSe NCs.[94] As per the Landé factor of Au^{2+}, the obtained value is consistent with previous results for Cu^{2+} and Ag^{2+} impurities with similar open d^9 configuration.[197, 278] Importantly, in agreement with the mechanistic picture of **Figure 3.4a**, the observed magnetic response is not an intrinsic ground state feature of Au:CdSe NCs, but is rather a direct consequence of their illumination by light: in this case, the weak probe light that is used to measure MCD. This is clearly demonstrated in **Figure 3.11c** showing progressive intensification of the 1S MCD signal as a function of the illumination time by the probe beam at 2.4 eV (25 nW/cm^2), reaching saturation after ∼10 min. The black line is the theoretical simulation of the number of Au^{2+} paramagnetic species per NC obtained through the kinetic model described below.

In these weak illumination conditions, equilibrium is achieved when each NC contains on average 1.9 Au^{2+} species. To further emphasize this effect, in **Figure 3.11d**, I have reported the evolution of the 1S MCD intensity as a function of B in the absence and in the presence of additional excitation with UV light (3.1 eV, 40 μW/cm^2) leading to over 250% enhancement of the MCD with respect to the case of probe light only. To investigate the dynamics of the photomagnetization mechanism and to correlate it to the quantized doping level of the NCs, the evolution of the MCD signal was monitored in successive ON/ OFF UV illumination scans. In this experiment (the experimental setup is sketched in **Figure 3.10**), the weak probe light

was kept constant for the whole duration of the measurement (25 nW/cm^2 as in **Figure 3.11c**), whereas the additional UV fluence is increased at each cycle from 0.4, 1.5, 4, 15 to 40 μW/cm^2. Before performing the first UV cycle, the sample was illuminated by the probe light to reach saturation of the photomagnetization following the trend in **Figure 3.11c**. As shown in Figure **3.11e**, increasing the fluence of the UV light results in higher MCD saturation values and faster magnetization/ demagnetization kinetics. For all fluences used, when the UV light is turned off, the MCD signal decreases slowly over several minutes, indicating that the persistence of the metastable paramagnetic state is not limited by the lifetime of the Au-PL but is likely determined by the release time of trapped electrons in surface defects, similar to what is observed for Cu^+ or Ag^+ doped NCs.[197, 278]

This assignment is in agreement with the spectro-electrochemistry measurements in **Figure 3.4c** showing over 50% brightening of the Au-PL upon raising the NC Fermi energy, which is indicative of the presence of localized states below the NC conduction band acting as efficient electron traps. A closer look at the MCD kinetics in **Figure 3.11e** reveals the presence of two main decay trends, possibly associated with de-trapping of electrons from intragap traps with different depth. Moreover, the MCD data in **Figure 3.11c and e** was used to model the evolution in time of the average number of paramagnetic centers associated with Au^{2+} cations when the sample is illuminated with the probe beam and by the additional UV light through the expression:

$$\frac{dP(t)}{dt} = < N > \phi_{HC} - k(< N >)P(t) \qquad (3.3)$$

where $N = N_{Probe} + N_{UV} = (\sigma_{1S} \times f_{Probe}) + (\sigma_{3.1eV} \times f_{UV})$ is the average number of excitons generated per unit time by continuous illumination (considering the exciton emission lifetime of 290 ns, in a NC with absorption cross section σ (respectively at the 1S energy, $\sigma_{1S} = 3.9 \times 10^{-16}$ cm^2 and at 3.1 eV, $\sigma_{3.1\ eV} = 1.0 \times 10^{-15}$ cm^2)[342] by a probe fluence (f_{Probe}) and by an additional UV fluence (f_{UV}). ϕ_{HC} is the capture efficiency of a VB hole in an Au^+ center, k is the relaxation rate of the Au^{2+} centers to the nonmagnetic Au^+ state (experimentally found to depend on the excitation conditions), and P(t) is the number of photogenerated Au^{2+} species. The first term on the right side of eq (3.3) represents the number of the Au^{2+} paramagnetic centers generated per unit time and the second term is the relaxation of the photoactivated Au^{2+} ions back to their Au^+ ground state. By using the experimental value of <N>, a decay rate $k = 3.86 \times 10^{-2}$ s^{-1} and assuming that $\phi_{HC} \approx 100\%$, the trend of the MCD response in **Figure 3.11e** is simply reproduced yielding a saturation P(t)-value of 1.9 Au^{2+}/NC due solely by the probe

beam. The same model also describes the behavior under UV illumination, with the term <N> now resulting from both the probe light and the additional UV excitation that accounts for most of the generated Au^{2+} over time. To best describe the decay trend of the MCD signal when the UV laser is switched off, the decay rate k that appears to be growing with the UV fluence has been extracted from the fast portion of the experimental MCD decay for each f_{UV} used. To further emphasize the role of k in the paramagnetic response of the Au:CdSe NCs, we calculated the rise and decay trends by varying the k-values by $\pm 0.012\ s^{-1}$ ($0.003\ s^{-1}$ steps), resulting in the gray curves in **Figure 3.11e**. It can be observed that, given the very slow demagnetization kinetics that prevented us from performing MCD measurements until full decay of the magnetic response, the initial number of Au^{2+} species per NC in successive ON/OFF cycles has been set as the calculated value after the decay of the previous cycle. Remarkably, with no other free parameter except the decay rate in the presence of the probe light only, this simple model describes the MCD response and shows that the system approaches equilibrium saturation when nearly all seven Au^{+} dopants are photoconverted to Au^{2+}. We finally notice that increasing the UV fluence further was not possible as that would lead to artifacts due to sample heating effects.

3.5 Conclusions

In conclusion, in this chapter, I reported the first example of colloidal NCs electronically doped with gold impurities using a fully redesigned quantized doping approach that enabled us to directly synthesize homogeneous NC ensembles where each particle contains an exact predetermined number of electronic impurities. The NCs were thoroughly characterized for their structural, optical and magnetic properties, showing distinct signatures of dopant related physical processes directly related to their quantized doping level. The approach that we have demonstrated with Au clusters is not size- or host-specific and could, in principle, be applied to different monometallic or alloyed clusters, allowing the realization of charge engineered NCs with predesigned optical, magnetic, and electronic properties for future fundamental studies and advanced optoelectronic, photonic, and spintronic devices.

Chapter 4

Trap-Mediated Two-Step Sensitization of Manganese Dopants in Perovskite Nanocrystals

Synopsis

Halide perovskite NCs hold promise for printable optoelectronic and photonic applications. Doping enhances their functionalities and is being investigated for substituting lead with environmentally friendlier elements. The most investigated dopant is Mn^{2+} that acts as a colour center sensitized by the host excitons. The sensitization mechanism is far from understood and no comprehensive picture of the energy-transfer process has been proposed. Similarly, the role of shallow states, particularly abundant in defect tolerant materials, is still unknown. Here, I address this problem via spectroscopic studies at controlled excitation density and temperature on Mn:$CsPbCl_3$ NCs. The results indicate a two-step process involving exciton localization in a shallow metastable state that mediates the thermally assisted sensitization of the Mn^{2+} emission, which is completely quenched for $T < 200$ K. At $T \leq 60$ K, however, such emission surprisingly reappears, suggesting direct energy transfer from band-edge states. Electron spin resonance supports this picture, revealing the signatures of conformational rearrangements below 70 K, possibly removing the potential barrier for sensitization. These results demystify anomalous behaviors of the exciton-to-Mn^{2+} energy-transfer mechanism and highlight the role of shallow defects in the photophysics of doped perovskite nanostructures.

4.1 Prologue

Inorganic Cesium lead halide perovskite ($CsPbX_3$, X = Cl, Br, I) NCs (referred to as PNCs), owing to their simple monodisperse synthesis,[158, 358-361] high defect tolerance,[362] and efficient photoluminescence (PL), have been rapidly gaining interest as tuneable optical materials in various optoelectronic and photonic applications including

lasers,[363] sensors,[364] light emitting diodes,[222, 365-367] photovoltaic cells,[368-370] photodetectors,[371, 372] and luminescent solar concentrators.[139] Controlled insertion of small quantities of impurities (doping)[217-221] provides an additional degree of freedom for controlling their optical properties[222-224] and introduces functionalities that cannot be obtained through size and composition control (i.e., halide substitution). To date, substitutional doping has been demonstrated using a variety of divalent cations including cadmium, zinc, tin,[225] and mostly, manganese,[218, 222, 226-228] which isovalently replace Pb^{2+} cations and have been shown to significantly stabilize PNCs.[219, 229] Importantly, similar to chalcogenide NCs, in PNCs with E_g>2.1 eV (i.e., $CsPbCl_3$, $CsPbBr_3$, and mixed halide compositions),[222] the Mn^{2+} dopants can be excited from their $^6A_1$ ground state to the $^4T_1$ excited state by energy transfer (ET) from the NC host,[222, 230] giving rise to the characteristic dopant emission at 2.1 eV due to the $^4T_1 \rightarrow {}^6A_1$ spin-flip transition.[222, 225-227, 230] Notably, since the corresponding $^6A_1 \rightarrow {}^4T_1$ transition is spin forbidden, the extinction coefficient of dopant absorption is vanishingly small ($\sim$1 M^{-1} cm^{-1}),[216] which results in a large "apparent" Stokes shift between the absorption spectrum of the NC host and the Mn^{2+}-PL that is particularly useful in photon management technologies.[225, 227] More recently, owing to the rapid and reversible quenching response of the Mn^{2+}-PL by exposure to O_2, Mn:$CsPbCl_3$ PNCs have been proposed for room-temperature detection of molecular oxygen.[373] Mn^{2+} dopants in NC hosts with E_g smaller than the $^6A_1 \rightarrow {}^4T_1$ transition energy have been shown to give rise to excitonic magnetic polarons by coupling with optically[213] or electrically[214] generated excitons in CdSe and CdSe/CdS NCs, and to act as storage centers for electrons in CdTeSe NCs.[215]

One important aspect of Mn:PNCs is that both the intrinsic band-edge (BE) emission and the Mn^{2+}-PL are observed in doped particles,[222, 226, 374] which indicates that the energy transfer from the host to the dopant ions is not fully outcompeting BE exciton recombination likely due to the high ionic character of the Pb−Cl/Mn−Cl bonds in perovskite materials that lowers the efficiency of Dexter-type ET.[222, 224, 227, 375] Accordingly, Liu et al. showed strong dependence of the exciton-to-dopant ET efficiency on the E_g of the host PNCs and pointed to the presence of efficient back-transfer (BT) from sensitized Mn^{2+} centers to the host BE that intensifies in PNCs with lower E_g, for example, by replacing Cl or Br with I.[219] Progressive dimming of the Mn^{2+}-PL intensity between 300 and 70 K recently pointed to a role of temperature in the dopant sensitization process, determining the branching ratio between the BE- and Mn^{2+}-PL.[375] To date, however, a comprehensive mechanistic picture of the host-to-dopant ET in Mn-doped PNCs is still lacking and so is the role of shallow defect states, which are particularly abundant

in this class of defect tolerant materials and we find playing a fundamental role in the dopant sensitization process. This is a marked difference between perovskite and chalcogenide NCs in which deep intragap defects typically quench the luminescence of both BE excitons and dopants. To address this problem, here I report a combination of spectroscopic measurements of the spectral and dynamical properties of undoped and Mn-doped $CsPbCl_3$ PNCs as a function of the excitation density and temperature from 300 to 3.5 K with Raman scattering and electron spin resonance (ESR) experiments. Through this approach, a two-step sensitization mechanism is revealed, consistent with a long-lived shallow trap state mediating the excitation of the Mn^{2+} center by the host BE excitons. Intense optical excitation leads to saturation of this state, lowering the dopant luminescence with no effect on its time dynamics. In combination with temperature-controlled PL data, these experiments also highlight a dominant nonradiative decay channel for BE excitons causing the relatively low BE-PL quantum yield $\Phi_{PL} \leq 5\%$ between 300 and 5 K. ET from trapped excitons to Mn^{2+} is found to be strongly temperature dependent, resulting in rapid disappearance of the dopant emission between 300 and 200 K at constant decay dynamics with no corresponding variation of the BE-PL intensity. Lowering the temperature further leads to the progressive intensification of the BE-PL due to suppressed vibrational quenching, as confirmed by Raman scattering measurements. Surprisingly, below 50 K, the Mn^{2+} luminescence suddenly reappears and rapidly intensifies with nearly constant decay kinetics. Such an unusual effect is accompanied by the acceleration and growth of the BE-PL intensity, indicating that also in Mn-doped PNCs the exciton fine structure is altered by the Rashba effect observed in undoped PNCs, resulting in a highly emissive triplet state leading to tens of picosecond fast BE decay at low temperature.[376] Side-by-side PL measurements vs temperature on undoped $CsPbCl_3$ PNCs show much stronger emission intensification than in doped PNCs (360% vs 70% between 50 and 5 K), suggesting that, at cryogenic temperatures, the dopant sensitization might occur directly from the host quantized states, hampering the PL brightening expected on the basis of exciton fine structure arguments. Finally, ESR and optical absorption measurements are conducted to provide preliminary insights on low-temperature conformational transitions possibly assisting the observed behavior. EPR spectra suggest the occurrence of structural modification of the local dopant environment as a function of temperature similar to that recently found in Mn:$CsPbCl_3$ nanoplatelets exposed to extended solvothermal treatments.[228]

4.2 Sample preparation and Optical characteristics

Monodisperse Mn-doped $CsPbCl_3$ PNCs were synthesized as described by Protesescu et al.,[377] with addition of $MnCl_2$. Briefly, 0.1 mmol of $PbCl_2$ and 0.1 mmol of $MnCl_2$, 5 mL of octadecene, 0.5 mL of oleic acid, and 0.5 mL of Oleylamine were loaded in a 25 mL three-neck flask and dried under vacuum for 1 h at 120 °C. After degassing, the temperature was raised to 180 °C and 0.4 mL of previously synthesized Cs-Oleate (0.4 g Cs_2CO_3 degassed in 15 mL octadecene and 1.75 mL oleic acid at 150 °C) was swiftly injected. Thirty seconds after the injection, the PNC solution was quickly cooled to room temperature with an ice bath. The PNCs were purified via centrifugation at 3000 rpm twice for 30 minutes each time, followed by redispersion in toluene.

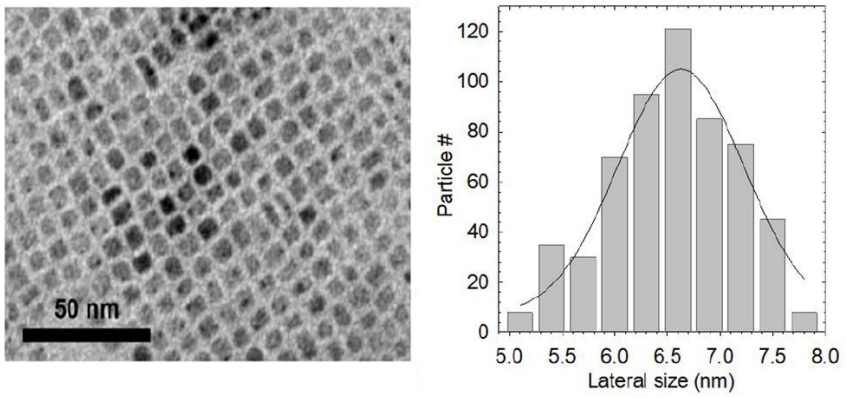

Figure 4.1. Transmission electron micrograph and related size analysis of Mn:$CsPbCl_3$ PNCs.

The resultant samples were subjected to structural and elemental characterization by means of (High Resolution) Transmission Electron Micrography (HR)TEM and Inductively coupled plasma optical emission spectroscopy (ICP-OES) respectively. Conventional TEM images were acquired on a JEOL JEM-1011 microscope equipped with a thermionic gun at 100 kV accelerating voltage. High resolution-TEM (HRTEM) imaging was performed on a JEOL JEM-2200FS microscope equipped with a Schottky gun operated at 200 kV accelerating voltage, a CEOS spherical aberration corrector in objective lens enabling a spatial resolution of 0.9 Å, and an in-column image filter (Ω-type). Samples were prepared by drop casting diluted PNC suspensions onto 200 mesh carbon-coated copper grids for conventional TEM imaging, and 400 mesh ultrathin/holey carbon-coated copper grids for HRTEM imaging, respectively. **Figure 4.1** shows TEM micrograph implicating monodisperse and crystalline 6.6

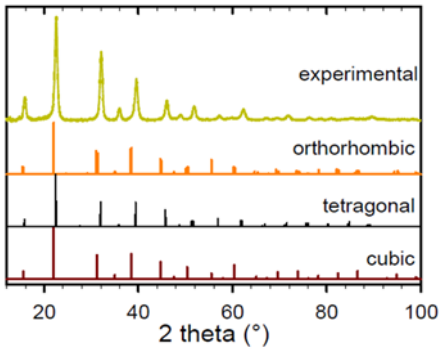

Figure 4.2. XRD pattern of Mn:$CsPbCl_3$ PNCs at room temperature (yellow line) compared to the XRD pattern of bulk orthorhombic (ICSD-243734) , tetragonal (ICSD-109294) and cubic (ICSD- 29067) $CsPbCl_3$ perovskite.

± 0.6 nm sized PNC nanostructures. Moreover, ICP-OES analysis on washed PNCs indicated a 3.9% Mn doping. It is noticeable that such Mn concentration could be partly overestimated due to the difficulty in removing the excess Mn ions from the reaction medium completely.[227] The structural characterizations of the samples were concluded with X-ray diffraction (XRD) analysis of the NCs as shown in **Figure 4.2**. XRD patterns were obtained using a PANalytical Empyrean X-ray diffractometer equipped with a 1.8 kW Cu Kα ceramic X-ray tube, PIXcel3D, 2x2 area detector and operating at 45 kV and 40 mA. The diffraction patterns were collected in air at room temperature using Parallel-Beam (PB) geometry and symmetric reflection mode. All XRD samples were prepared by drop casting a concentrated solution on a zero-diffraction silicon wafer.

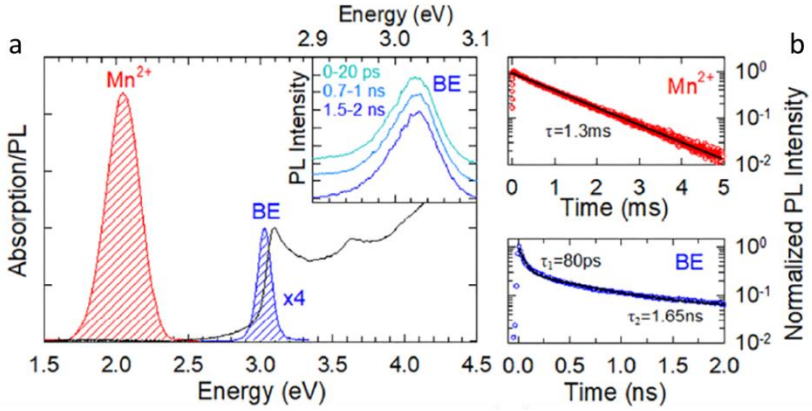

Figure 4.3. (a) Absorption (black line) and PL spectra of Mn-doped $CsPbCl_3$ PNCs in toluene. Two PL peaks are observed: A narrow BE-PL band peaked at 3.0 eV (enhanced by four times for clarity) and a broadband dopant emission at 2.1 eV (indicated as Mn^{2+}-PL). Inset: BE-PL spectra at increasing delay time after the excitation pulse, showing a constant emission profile during the decay process. **(b)** Time decay curve of the Mn^{2+}-PL (top panel) and BE-PL (lower panel) indicating single exponential dynamics with lifetime τ_{Mn} = 1.3 ms for the dopant emission and a double exponential decay of the BE-PL with a fast (τ_1 = 80 ps) and a slower (τ_2 = 1.65 ns) component.

The optical characterization was initiated with Absorption and PL measurements of the resultant PNCs dispersed in toluene at room temperature. Absorption spectra were measured using Cary 50 UV-Vis Spectrophotometer while for the PL measurements, the samples were excited using a frequency tripled Nd:YAG laser at 3.49 eV (355 nm) while the emitted signal was collected using a Si CCD camera coupled to a spectrometer. The results as depicted in **Figure 4.3a** shows the steep absorption band edge at ~3.1 eV and the characteristic two-colour emission of weakly quantum confined Mn:$CsPbCl_3$ PNCs, with a narrow BE peak at ~3 eV and a broad emission at 2.1 eV due to the $^4T_1 \rightarrow {}^6A_1$ transition of Mn^{2+} dopants.[216, 218, 222, 227] The time decay traces of the Mn^{2+}-PL and BE emission at room temperature are shown in **Figure 4.3b**. The Mn^{2+}-PL decay is single exponential with lifetime τ = 1.3 ms, in agreement with previous reports.[227, 378] The BE-PL decay follows instead a double-exponential dynamic with a fast portion (τ_1 = 80 ps, $k_1 = 1.25 \times 10^{10}$ s^{-1}) followed by a slower component (τ_2 = 1.65 ns, $k_2 = 6.05 \times 10^8$ s^{-1}) responsible for the majority of the emission (~85% of the total emitted photons).

Notably, the corresponding BE-PL spectrum **(inset of Figure 4.3a)** is constant across the whole decay, indicating that emission occurs from the BE at all times. This behavior is typical of the copresence of direct exciton recombination (faster component with lifetime τ_1) and slower decay of regenerated excitons by BT from non-emissive trap states (with lifetime τ_2) that thermally repopulate the BE and provides a first important indication of the involvement of localized shallow states in the photophysics of these PNCs, as schematized in **Figure 4.4** and

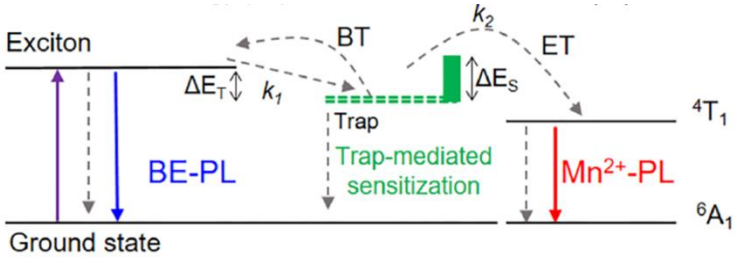

Figure 4.4. Jablonski diagram of the PNC and dopant states involved in the ET mechanism through intermediate shallow trap states (dashed green lines) which results in the $^4T_1$ to $^6A_1$ spin-flip transition of the Mn^{2+} atoms.

quantitatively discussed in the following sections.

It has to be considered that BT from excited Mn^{2+} to the BE is not possible in this system at room temperature because of the wide E_g of the $CsPbCl_3$ host PNC.[219] Accordingly, PL measurements excited at 2.0 eV show no BE-PL even under intense pumping, indicating the absence of dopant-assisted up-converted luminescence observed in undoped perovskites.[378-381]

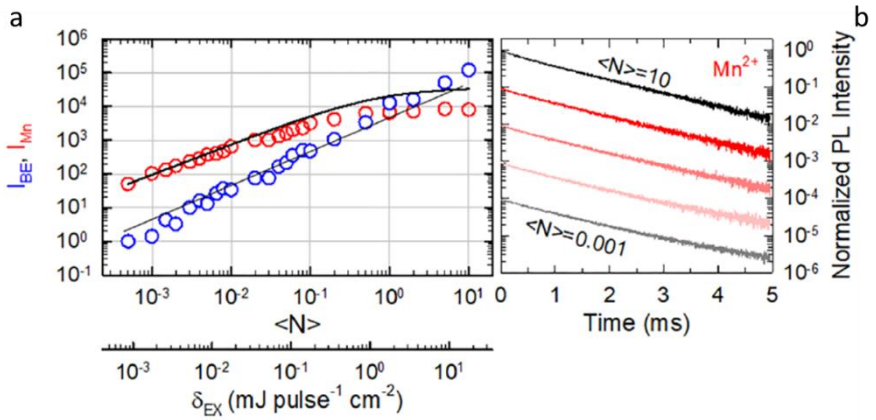

Figure 4.5. (a) Integrated intensity of the Mn^{2+} (red circles) and the BE (blue circles) PL as a function of the excitation density δ_{EX} (the corresponding average exciton occupancy ⟨N⟩ is also indicated). **(b)** Dopant intensity decay at increasing values of ⟨N⟩ (the curves are shifted vertically for clarity; each curve corresponds to a 10-fold variation of ⟨N⟩)

A first indication of a two-step sensitization process involving exciton trapping in a localized state mediating the ET from the BE is provided by the analysis of the excitonic and Mn^{2+} emission intensity at increasing excitation density, δ_{EX} (indicated in **Figure 4.5a** as the per pulse energy density). For the PL measurements as a function of the excitation density, a vigorously stirred solution in a quartz cuvette was excited using a frequency tripled pulsed Nd:YAG laser focused on a 60-micron diameter spot, at 3.49 eV (355 nm) with 200 Hz repetition rate so as to avoid pile up effect on the Mn^{2+}-PL and detected using a Si CCD camera coupled to a spectrometer. The BE- and the Mn^{2+}-PL show markedly different trends, with the intrinsic luminescence growing nearly linearly with δ_{EX} for the whole investigated excitation density range, whereas the dopant emission follows a linear trend only for ⟨N⟩ < 0.1 and then undergoes saturation with a plateauing behavior at average exciton occupancy ⟨N⟩ ~ 1. Here ⟨N⟩ is the average number of exciton per PNC obtained by convolving the excitation pulse (pulse width = 5 ns) with the BE exciton decay curves shown in **Figure 4.3b** and by using $\sigma_{ABS} = 1.142 \times 10^{-14}$ cm^2 as the absorption cross section of Mn:$CsPbCl_3$ PNCs.[374] Considering the high doping level of the PNCs (~3.9% corresponding to ~500 Mn atoms per PNC) and the low repetition rate of the pulsed excitation (200 Hz) compared to the lifetime of the Mn^{2+}-PL that avoids pile-up of Mn^{2+} excitation; this effect cannot be ascribed to optical saturation of the dopant centers by ET or by Auger-mediated pathways, as suggested in lightly Mn-doped chalcogenide NCs.[382] Notably, the decay dynamics of the dopant emission **(Figure 4.5b)** is constant across 5 orders of magnitude in δ_{EX}, which further excludes nonlinear quenching processes of the Mn^{2+}-PL and dopant−dopant annihilation processes as possible causes of the strongly sublinear power dependence at high excitonic occupancy as both such processes

would result in accelerated Mn^{2+}-PL decay. A possible scenario leading to such a behavior is reduced sensitization of the dopant by the BE via a metastable trap state undergoing saturation under intense optical excitation. Such a process is formalized by the simple proportionality:

$$I_{Mn} \propto T^*(\langle N \rangle) \text{ where,}$$

$$T^*(\langle N \rangle) \approx [(k_1/k_2)\,\langle N \rangle \Phi_T] / [(k_1/k_2)\,\langle N \rangle \Phi_T + 1)]$$

Here, $T^*(\langle N \rangle)$ is the number of trapped excitons available for dopant sensitization, k_1 is the population rate via trapping of their BE excitons, k_2 is the depopulation rate through ET to the Mn^{2+} ions, and Φ_T is the exciton trapping efficiency. Using $k_1 = 1.25 \times 10^{10}\ s^{-1}$ and $k_2 = 6.05 \times 10^{8}\ s^{-1}$ corresponding, respectively, to the fast and slow portions of the BE decay in **Figure 4.5b** and $\Phi_T = 0.28$. We notice that the experimental data reach saturation at slightly lower values of $\langle N \rangle$ with respect to the prediction, which is likely due to the fact that the reported occupancies refer to the average exciton density convoluted with the excitation pulse and not to the average occupancy level in the steady state. The states involved in this mechanism are depicted in the Jablonski diagram in **Figure 4.4** showing the PNC excited state (exciton) transferring energy to a shallow trap state (rate k_1) that successively pumps the dopant center (rate k_2). Here, I stress that the constant linear growth of I_{BE} with δ_{EX} indicates that saturation of traps is negligibly beneficial for BE excitons, which, at room temperature, are also strongly affected by thermally assisted nonradiative decay via lattice phonons and possibly by other trap states not involved in the sensitization process.

4.3 Temperature dependent steady state PL studies

In order to confirm and investigate in deeper detail the sensitization mechanism of the dopant site, I performed steady-state and time-resolved PL measurements as a function of temperature on both undoped and Mn-doped PNCs. Spectroscopic studies were carried out on toluene solutions and drop cast films of PNCs deposited onto quartz substrates. For the temperature-controlled PL measurements (both steady state and time resolved), a sample film was mounted in the variable temperature insert of a closed circle Helium-cryostat with direct optical access. The sample was mounted vertically at 45° with respect to the incident beam in anti-reflection geometry with respect to the output window, where the CCD was fibre-coupled to a spectrophotometer for detection and recording. In the case of Transient PL measurements, because of the very different lifetimes of the BE and Mn^{2+}-PL, two different excitation sources and detection chains were adopted. Specifically, <70 ps pulses at 3.5 eV from a frequency

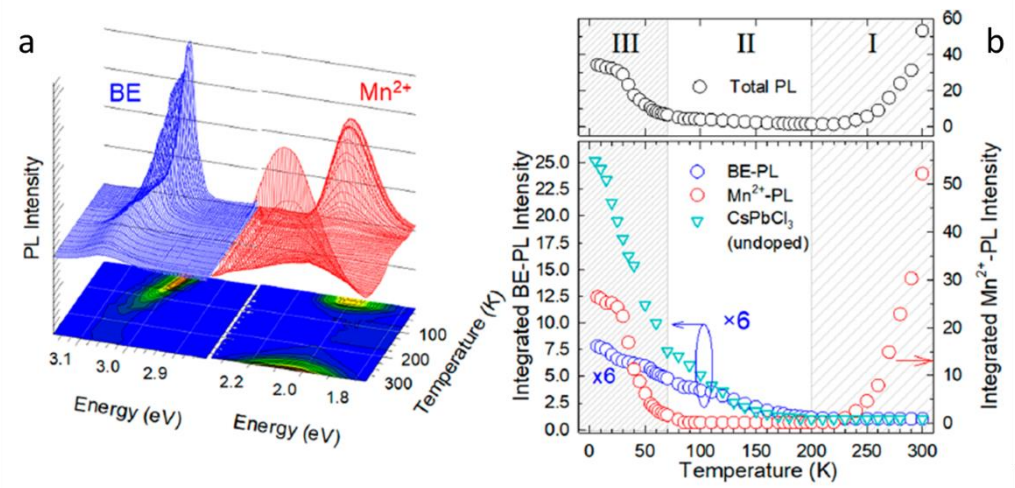

Figure 4.6. (a) 3D plot of PL spectra of the BE and dopant emission of Mn:$CsPbCl_3$ PNCs at decreasing temperature from 300 to 3.5 K. **(b)** Integrated intensity of the PL spectra in **(a)** as a function of temperature (BE-PL in blue circles and Mn^{2+}-PL in red circles). The values for the BE-PL have been scaled by 6-fold for clarity. The total integrated intensity is reported in black circles in the top panel. The temperature ramp is divided into three regions for clarity: 300−200 K (region I), 200−70 K (region II), and 70−3.5 K (region III).

doubled Ti:sapphire laser (repetition rate 78 MHz) and a Hamamatsu Streak camera with resolution better than 10 ps were used for the BE-PL. The Mn^{2+}-PL were excited using a frequency tripled pulsed NdYAG laser at 3.49 eV with 100 Hz repetition rate (pulse duration 5 ns) and the emitted light was collected with a photon counting unit (resolution better than the pulse duration).

Figure 4.6a reports the full set of PL spectra from 300 to 3.5 K of Mn:$CsPbCl_3$ PNCs showing a markedly different behavior of the BE and Mn^{2+}-PL with decreasing temperature. Specifically, the BE-PL monotonously intensifies, whereas the dopant PL initially drops rapidly to zero and successively reappears steeply, nearly completely recovering its initial intensity. To quantitatively describe the effect of temperature on the two emissions, in **Figure 4.6b** I have depicted the respective integrated PL intensity values during the temperature ramp, also compared to the total integrated emission (top panel) and to the BE-PL trend of undoped $CsPbCl_3$ PNCs. For clarity of discussion, the ramp is divided into three temperature ranges, each of which is characterized by a distinctive photophysical behavior. It can be observed that the dopant emission, when present, is dominant over the BE-PL, whose integrated intensity values have been scaled by a factor of 6. Accordingly, the total integrated PL intensity of the doped system follows the trend for the dopant emission except in range II (200−70 K) where the latter is absent.

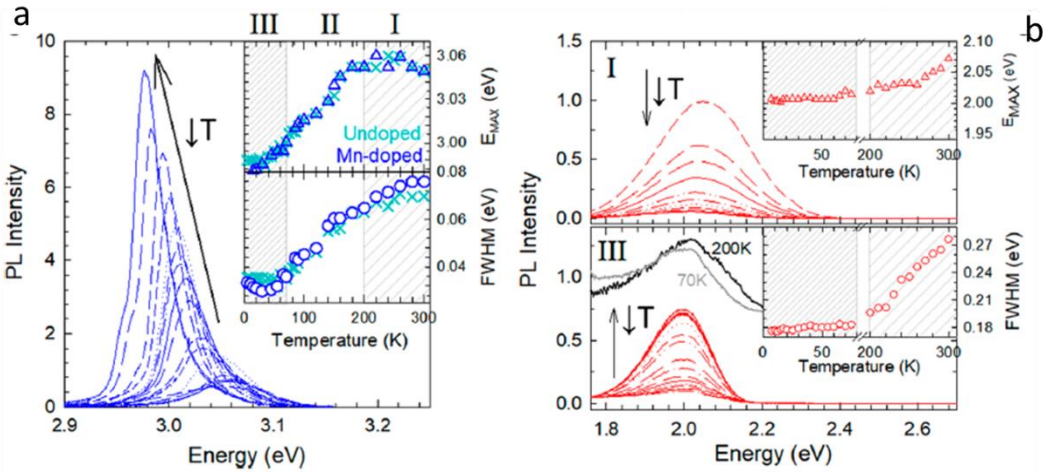

Figure 4.7.(a) BE-PL spectra at decreasing temperature from 300 to 5 K (as indicated by the arrow). Inset: temperature dependence of peak energy and fwhm of the BE emission spectra of doped (blue symbols) and undoped (light blue crosses) $CsPbCl_3$ PNCs. **(b)** Normalized Mn^{2+} emission intensity in region I (top) and region III (bottom). Arrows indicate the direction of temperature change from 300 to 200 K in region I and from 70 to 3.5 K in region III. Inset: peak energy and fwhm variation with temperature in region I and III.

Looking first at range I (300−200 K) in **Figure 4.6b**, we can observe that the BE-PL intensity of both doped and undoped systems is essentially constant, whereas the Mn^{2+}-PL drops steeply to zero. The respective PL spectra in **Figure 4.7a,b** show nearly constant peak energy for both emissions and ~60 meV narrowing of the dopant PL band compared to a $\Delta fwhm_{BE} < 5$ meV for the PL emission originating from the host. This suggests that, in this temperature range, the Mn^{2+} center is more affected by lattice dilation than the BE states.

Most crucially, the different behavior of the excitonic and dopant PL with temperature and the complete absence of anticorrelation between their intensity trends strongly support the picture emerging from the PL vs δ_{EX} data **(figure 4.5)** that the BE exciton is not directly connected to the dopant site. The sensitization process instead occurs via an intermediate step involving a shallow trap that first traps BE excitons and successively excites the Mn^{2+} centers by overcoming a potential barrier ΔE_S that is quantified by the time-resolved analysis in **Figure 4.9a,b**. Moving on now to temperature range II (200-70 K) **(Figure 4.6b)**, where the Mn^{2+}-PL is absent, we can observe similar intensifications of the BE-PL of both the doped and the undoped PNCs with decreasing temperature accompanied by a comparable red shift and line narrowing due to band gap renormalization. Most surprisingly, lowering the temperature further (temperature range III, T<70 K) leads to the unexpected steep reappearance of the Mn^{2+} emission that becomes dominant over the respective BE-PL for T < 50 K. We can notice a marked asymmetric narrowing of the dopant PL peak with strong suppression of its high-energy portion for T ≤ 200 K, indicating that the higher energy states of the Mn^{2+} manifold that

are thermally populated by the lower energy states at room temperature are no longer accessible at cryogenic temperatures. The narrowing effect of the dopant PL peak between 200 and 70 K is emphasized in the lower panel of **Figure 4.7b**. Also, interestingly, marked difference is found between the temperature behaviors of the BE-PL of the doped vs undoped PNCs: the first show progressive intensification with decreasing temperature essentially following the trend from range II, whereas the evolution of the PL intensity of the undoped analogues clearly steepens below 70 K, resulting in much stronger brightening at 5 K with respect to the doped systems (~350% vs ~70% between 70 and 5 K). These data point to direct energy transfer

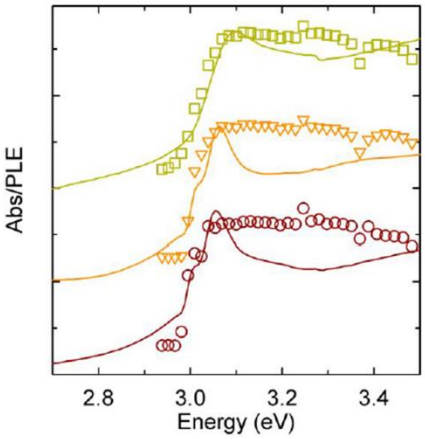

Figure 4.8. Absorption and PLE spectra of the dopant emission at 2 eV of Mn:$CsPbCl_3$ PNCs at 300K, 50K and 5K (from top to bottom).

from BE states to the dopant in temperature range III, leading to the re-emergence of the dopant luminescence, which might directly compete with radiative decay of BE excitons in doped systems, hampering the emission intensification expected in the absence of Mn^{2+} acceptors. Here, I report photoluminescence excitation (PLE) measurements of the Mn^{2+}-PL as a function of temperature in **Figure 4.8** showing close resemblance of the respective absorption spectrum, indicating that, at any temperature, the dopant luminescence is sensitized by the above band gap excitation of the NC host. The absence of measurable contributions of below gap radiation further suggests that the formation of BE excitons is a necessary step for the sensitization process.

4.4 PL dynamics investigation with temperature

Time-resolved PL measurements as a function of temperature enable us to gather deeper insights into the sensitization mechanism and to quantify the relevant potential barriers. Looking first at the Mn^{2+}-PL in temperature range I, we can see the progressive drop of the zero-delay PL intensity with decreasing temperature, whereas the decay dynamics is constant.

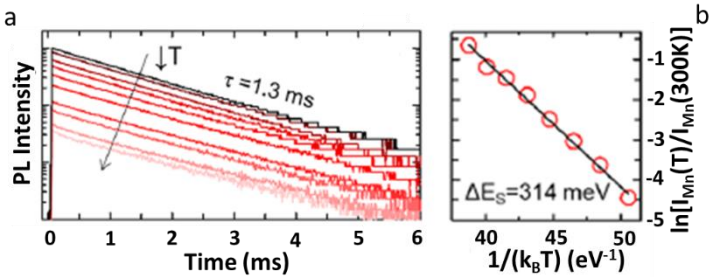

Figure 4.9. (a) Decay curves of the Mn^{2+}-PL of Mn:$CsPbCl_3$ PNCs in temperature range I showing essentially constant lifetime of 1.3 ms. **(b)** Boltzmann analysis of Mn^{2+}-PL intensity vs T yielding an activation energy ΔE_S = 314 ± 8 meV.

This behavior accounts in full for the PL dimming observed in CW excitation conditions **(Figure 4.9a,b)** and confirms that the excitation mechanism of the dopant site is thermally activated. The Boltzmann analysis of the time integrated Mn^{2+}-PL intensity vs T through the expression $I_{Mn} = I_0 \cdot e^{-\Delta E_S/k_BT}$ yields a sensitization activation energy ΔE_S = 314 ± 8 meV **(Figure 4.9b)**, indicating that, already at room temperature, the excitation of the Mn^{2+} center is partially inhibited, in agreement with the ubiquitous two-color luminescence of Mn:$CsPbCl_3$ PNCs. Notably, despite the nearly 100-fold drop of the dopant PL intensity, the decay dynamics of the BE-PL is only weakly modified in temperature range I, where the predominant observation is a minor, yet measurable, decrease of the relative weight of the slow decay component. As a result, the BE-PL dynamics progressively acquires a single-exponential character to the point that, at ~200 K, the long-lived tail accounts for less than 30% of the total emission **(Figure 4.10a)**. This indicates that thermal population of BE states by trapped excitons is progressively less efficient and further confirms the absence of direct channels between the BE and the dopant states. The energy difference between the trap state and the BE extracted through the Boltzmann analysis of the intensity of the slow decay component in the BE dynamics as a function of temperature (inset of **Figure 4.10a**) through the expression $I_{slow} = I_{slow,0} \cdot e^{-\Delta E_T/k_BT}$ is ΔE_T = 43 ± 2 meV. I would like to emphasize that, throughout temperature range I, the BE-PL intensity is essentially constant, indicating that trapping of free excitons has an activation barrier smaller than the available thermal energy. Furthermore, the absence of additional PL features at intragap energies highlights that trapped excitons are essentially non-emissive. Moving now to temperature range II, where no Mn^{2+}-PL is detected, we observe the progressive lengthening of the BE-PL dynamics reaching saturation at 70 K **(Figure 4.10b)**, in agreement with the gradual increase of the integrated PL intensity observed in **Figure 4.6b**. This effect can be ascribed to the suppression of phonon-assisted nonradiative recombination of free BE excitons. This is supported by the quantitative analysis of the PL decay rate vs temperature

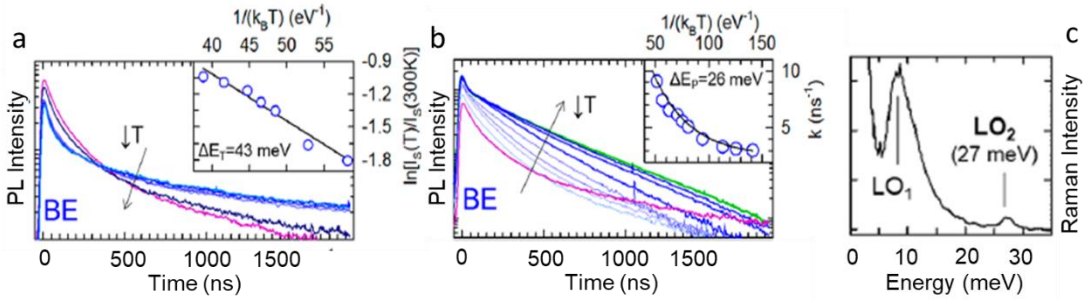

Figure 4.10. (a) BE-PL intensity decay in temperature range I. The purple line indicates BE decay rate at 200 K. Inset: Boltzmann analysis of the slow decay component in the BE dynamics as a function of temperature yielding a trap energy $\Delta E_T = 43 \pm 2$ meV. **(b)** BE dynamics in temperature range II. Purple and green lines represent BE decay rates at 200 and 70 K, respectively. Inset: dependence of BE-PL decay rate on temperature. **(c)** Raman spectrum of the Mn:$CsPbCl_3$ PNCs at room temperature.

shown in the inset of in **Figure 4.10b** and by the Raman spectrum in **Figure 4.10c**. Specifically, the evolution of the PL decay rate $k_{BE}(T)$ with $1/k_BT$ is reproduced by the expression $k_{BE}(T) = k_R + k_{NR}(T)$, where $k_{NR}(T) = \kappa \cdot e^{-\Delta E_P/k_BT}$ is the temperature dependent non-radiative decay rate and ΔE_P is the thermal activation energy associated with lattice phonons. The fitting procedure yields $k_R = 4 \times 10^8$ s^{-1}, $\kappa = 2.9 \times 10^{10}$ s^{-1}, and $\Delta E_P = 29 \pm 2$ meV that is consistent with the energy $E_{LO2} = 27$ meV of the longitudinal optical mode caused by the oscillation of Cs^+ ion in the lattice found in the Raman spectrum of the PNCs. By using the extracted decay rates, we estimate the trapping rate (k_T) and efficiency (Φ_T) of BE excitons at room temperature, using the expression $k_T = k_1 - k_R - k_{NR} = 3.0 \times 10^9$ s^{-1} and $\Phi_T = k_T/k_1 = 0.28$. This illustrates that only one-quarter of the total BE excitons are trapped in the shallow defect, whereas the majority decay through non-radiative channels.

As anticipated above, between 100 and 70 K, a faster component with $\tau \sim 30$ ps emerges in the BE-PL dynamics and becomes markedly dominant in range III **(Figure 4.11a)**, leading to the nearly complete disappearance of the slower radiative decay tail at 5 K. Similar dynamics are exhibited by undoped PNCs in agreement with previous reports **(inset of Figure 4.11a)**.[383] Here, the evolution of the BE dynamics with decreasing temperature is not due to trap-related processes but likely results from fast radiative decay of bright triplet states, in agreement with a recent experimental and theoretical study by Efros and co-workers.[376] Notably, the same effect is observed for the doped PNCs, indicating that the Rashba effect responsible for the inversion of the exciton fine structure[376, 384] of undoped systems is unaltered by the addition of Mn^{2+} substituents. We can notice that in undoped $CsPbBr_3$ perovskite NCs, trion emission has also been reported at low temperatures, leading to faster PL decay. In our case, however, considering a trion radiative rate $k_{TR} = 8 \times 10^8$ s^{-1} (corresponding to twice the exciton radiative decay rate $k_R = 4 \times 10^8$ s^{-1}) and the measured experimental decay rate $k_{EXP} = 3.3 \times 10^{10}$ s^{-1} at

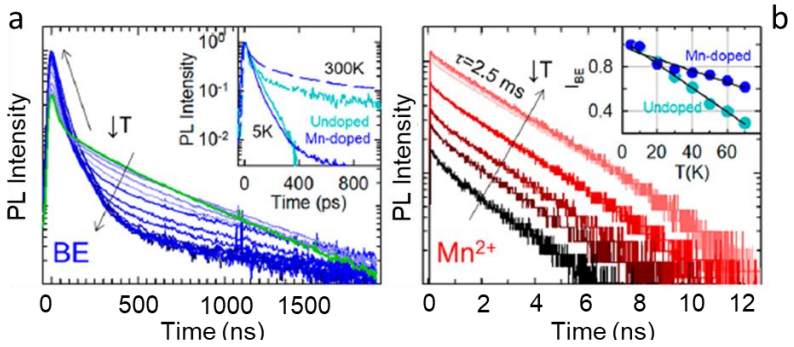

Figure 4.11. (a) BE-PL dynamics in temperature range III. Inset: BE-PL dynamics of doped (blue lines) and undoped (light blue lines) PNCs at 300 K (dashed lines) and 5K (solid lines). **(b)** Mn^{2+}-PL dynamics in temperature range III showing progressive intensification with nearly constant lifetime of ~2.5 ms. Inset: BE-PL of doped and undoped systems vs temperature.

5 K, a trion decay scenario would imply >90% drop of Φ_{PL} between 70 and 5 K due to nonradiative Auger recombination, which is in marked contrast to the observed nearly 2-fold brightening of the BE-PL in the same temperature range. Most importantly, in the temperature range III, the Mn^{2+}-PL of the doped PNCs rapidly intensifies with nearly constant lifetime **(Figure 4.11b)**, which is found to be longer than in temperature range I (τ_{Mn} ~ 2.5 ms vs 1.3 ms). The lengthening of the Mn^{2+}-PL dynamics, which is essentially saturated between 70 and 3.5 K, could be due to suppression of vibrational quenching upon lowering the temperature to 70 K analogously to what observed for the BE-PL decay **(Figure 4.10b)**. Here, however, the progressive effect on the Mn^{2+}-PL decay cannot be continuously monitored due to its negligible intensity in temperature range II. An alternative or complementary cause of the longer Mn^{2+}-PL lifetime could be temperature-induced changes of the ligand field, lowering the radiative decay rate of the $^4T_1 \rightarrow {}^6A_1$ transition of Mn^{2+}. More interestingly, the re-emergence of the dopant-related PL at low temperature indicates that the energy-transfer process becomes progressively barrierless, resulting in gradual sensitization of Mn^{2+} acceptors. A closer look at the intensity trends of the BE-PL of doped and undoped systems in **Figure 4.6b** suggests that, in temperature range III, energy transfer might occur also directly from BE excitons. Specifically, despite the BE-PL intensity of doped and undoped PNCs following very similar trends between 300 and 70 K, suggesting analogous temperature-activated nonradiative losses in the two systems, the PL of the undoped PNCs grows much more intensively than the doped analogues in temperature range III, resulting in over 5-fold stronger brightening between 70 and 5 K for the former. This suggests that, at cryogenic temperatures, energy transfer might directly deplete the BE states of Mn:$CsPbCl_3$ PNCs in favour of the Mn^{2+} acceptors. A closer insight into such an effect is obtained by plotting the normalized BE-PL intensity of the

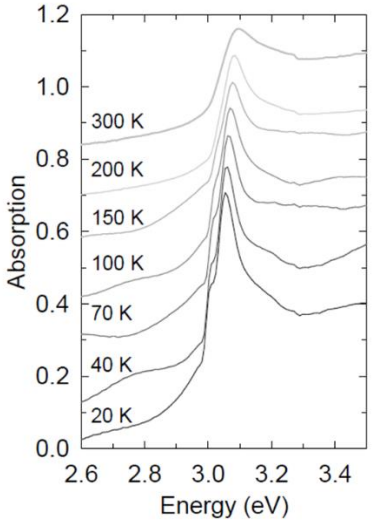

Figure 4.12. Absorption spectra of a film of Mn-doped $CsPbCl_3$ PNCs at progressively lower temperatures.

undoped and doped PNCs as a function of temperature in range III **(inset of Figure 4.11b)**, showing, in both cases, a clear linear correlation. However, the slopes of the two functions are markedly different: $\sim 5 \times 10^{-3}$ K^{-1} for the doped PNCs and $\sim 1 \times 10^{-2}$ K^{-1} for the undoped analogues, suggesting that part of the BE states of the doped PNCs are effectively transferred to Mn^{2+} centers. Unequivocal assignment of the origin of this phenomenon is nontrivial. One possible explanation could be the change of the nature of the BE excitonic transition below 70 K, modifying the donor−acceptor electronic coupling and thereby markedly increasing the ET rate. Such a dynamic effect is expected to lead to a faster BE-PL decay, which in our case is particularly difficult to probe experimentally due to the concomitant acceleration of the BE-PL by fine-structure effects. ET from higher energy excitonic states becoming favoured in temperature range III could also deplete the BE states in favour of the Mn^{2+} centers without affecting neither emission dynamics. An alternative explanation of the observed phenomenology could be the occurrence of a phase transition below 70 K, as recently shown in formamidinium lead bromide PNCs[385] and in Mn-doped $CsPbCl_3$ nanoplatelets,[228] drastically lowering the potential barrier for dopant excitation from trapped excitons. Optical absorption spectra at decreasing temperature **(Figure 4.12)** show typical narrowing and red-shift of the BE absorption peak and no dramatic change of the PL profile is observed in **Figure 4.6**. This suggests that structural rearrangements, if present, do not affect the band structure of the PNCs. Such a phase transition could, nevertheless, influence mostly, or nearly exclusively, the local environment of Mn^{2+} ions.

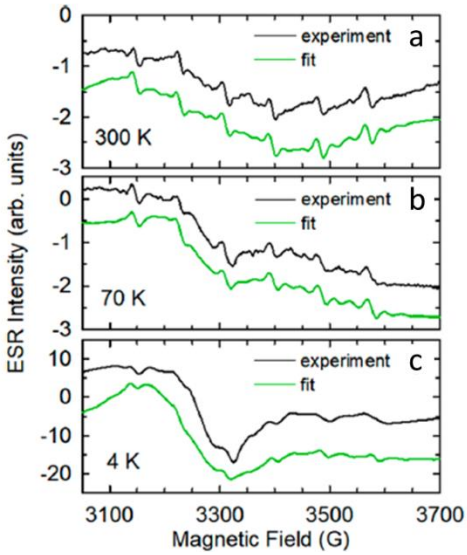

Figure 4.13. (a)−(c) ESR spectra of Mn-doped $CsPbCl_3$ PNCs recorded at 9.39 GHz frequency as a function of temperature (black curves) and respective fits with two components ascribed to isolated and interacting Mn^{2+} cations.

4.5 Probing changes in local environment of Mn^{2+} ions

In order to investigate this hypothesis, ESR measurements were conducted as a function of temperature which[219, 226, 227] are often employed to reveal modification of the local coordination of magnetic ions through changes in their characteristic spectrum. The ESR spectra were recorded with a Varian E15 spectrometer and a Bruker super high Q cavity operated at X-band, ~9.3–9.5 GHz, in the absorption mode. The static magnetic field was modulated at 100 kHz. The microwave frequency ν_0 and the magnetic field B_0 were monitored continuously with an electronic counter and a Hall probe. Sample temperatures in the range 4–300 K were obtained with an Oxford ESR 900 cryostat. BDPA was used as reference to determine the g-factors. EasySpin 5.2.17 was used to simulate and fit the spectra. The ESR spectrum of Mn^{2+} ions in a matrix is typically characterized by several lines due to the electron and nuclear spin states (S = 5/2, I = 5/2) leading to zero field splitting (ZFS) and hyperfine interactions determined by the Mn^{2+} point symmetry. For n non-equivalent sites we expect 2S(2I + 1)n allowed transitions. Other features may be observed depending on the Mn^{2+} concentration: dipolar and exchange interaction may lead to line broadening and narrowing effects. Additional lines due to forbidden transitions may also be observed, particularly in powder samples. The room temperature ESR spectrum of our PNCs shown in **Figure 4.13a** reveals the characteristic sextet expected for Mn^{2+} in a cubic symmetry, in agreement with previous reports.[219, 226, 227] However, additional lines due to ZFS clearly indicate that the local symmetry in our systems is lower,[386]

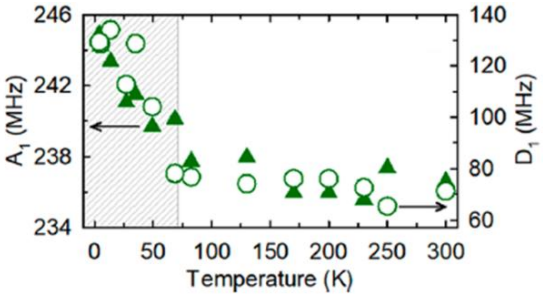

Figure 4.14. Temperature dependence of the hyperfine coupling (A_1) and zero field splitting (D_1) constants of isolated Mn^{2+} cations showing steep increase of both values below 70 K.

in agreement with the XRD data in **Figure 4.2** that are consistent also with an orthorhombic or tetragonal phase. At all temperatures, the hyperfine spectrum is superimposed to a broad background signal commonly arising from Mn−Mn interactions in heavily Mn-doped materials,[387-393] suggesting the copresence of Mn-rich and Mn-poor regions inside the PNCs, also possibly connected to the difficulty in removing excess Mn^{2+} cations after the reaction. Most importantly, a single line is clearly visible in the ESR data, becoming particularly intense below 70 K **(Figure 4.13b,c)**. A similar ESR feature has been recently observed in Mn doped $CsPbCl_3$ nanoplatelets exposed to extended solvothermal treatments, undergoing a gradual phase transition to pure $CsMnCl_3$.[228] Such a similarity between the ESR signature of $CsMnCl_3$ and the ESR spectra vs temperature of our PNCs suggests that also in our systems a local rearrangement of the perovskite lattice might occur. To gather deeper insights into the temperature evolution of the ESR of our PNCs, we fitted the spectra with two components respectively ascribed to isolated Mn^{2+} cations with isotropic g values, ZFS, and hyperfine coupling constants (respectively indicated as g_1, D_1, and A_1) and to interacting Mn^{2+} ions (single line with isotropic g_2). The line shape used in the fitting procedure was assumed Lorentzian. The spin Hamiltonian parameters at room temperature are $g_1 = 1.970 \pm 0.001$, $A_1 = 236 \pm 1$ MHz, $D_1 = 71 \pm 1$ MHz, and $g_2 = 2.02 \pm 0.01$. By lowering the temperature, we observe nearly constant A_1 and D_1 values down to ~100 K **(Figure 4.14)** followed by a marked increase of both constants for lower temperatures suggesting a structural phase transition at T ~ 70 K. Accordingly, such a trend is accompanied by the intensification of the single ESR line due to interacting Mn^{2+} species. The in-depth investigation of such structural modifications is beyond the scope of this work and will have to be treated in detail in a dedicated study also aided by low temperature X-ray diffraction techniques.

4.6 Conclusions

In summary, I conducted and reported spectroscopic studies at controlled excitation density and temperature on manganese-doped $CsPbCl_3$ PNCs revealing a two-step process involving the initial localization of band-edge excitons in a shallow trap that mediates the sensitization of the dopants and repopulates the band-edge by thermally activated back-transfer. This trap-mediated process dominates the photophysics of the PNCs for temperatures above 70 K and leads to the lack of correlation between the intrinsic and extrinsic luminescence intensities as a function of temperature and to markedly different power dependencies associated with optical saturation of the defect states. For $T < 70$ K, however, the sensitization becomes barrierless with contributions from direct energy transfer from BE states resulting in the re-emergence of the dopant luminescence. ESR and optical absorption measurements as a function of temperature suggest the occurrence of structural transitions possibly responsible for the suppression of the activation barrier for energy transfer. These results demystify some anomalous behaviors of the exciton-to-dopant energy transfer mechanisms in PNCs and highlight that the defect tolerant nature of perovskite materials not only results in effective trapping/de-trapping pathways of free excitons in shallow localized states but also affects the photophysics of impurity colour centers in strikingly different ways than in more traditional chalcogenide NCs.

Chapter 5

2D colloidal nanostructures: CdTe Nanoplatelets

Synopsis

In semiconductor NCs, shape anisotropy is a very important parameter since it heavily influences the electronic spectra of charge carriers as well as the optoelectronic and photophysical properties of the NCs. Compared with zero-dimensional NCs (quantum dots) and one-dimensional nanorods, two-dimensional nanoplatelets (NPs) exhibit many unique optical properties. Due to strong quantum confinement in only one direction and the large lateral size, the Cd based chalcogenide NPs show large exciton binding energy, giant oscillator strength, narrow emission, large absorption cross-section, suppressed Auger recombination, and large optical gain. In this chapter we discuss the significance of such two-dimensional floating entities and try to develop an understanding of the various standard synthesis protocols developed to date and reaction kinetics involved in it. We then move on to the optimization techniques involved to enhance the florescence efficiencies of these NPs. Then, we move on to the significance of the sparsely researched upon CdTe NPs. Moreover, I also report some preliminary results of the current ongoing work where we try to exploit the aforementioned intriguing characteristics of CdTe NPs to bring out their best applicative potentials in the field of lasing and ultrafast radiation detection technologies.

5.1 Prologue

Inorganic NC synthesis as emphasized in the previous chapters, is being extensively researched upon worldwide and is portrait as a rapidly developing field of research owing to not only new materials being synthesized but majorly as a result of advancements in synthesis procedures, reaction schemes empowering the fabrication of the desired, ultrahigh performing NCs with the utmost precise control of their dimensions,[28] anisotropy,[33, 394, 395]

chemical composition[396] and crystal structures.[397] For decades, NCs have been of growing interest as they exhibit unique intriguing properties due to their small size and resultant spatial quantum confinement of charge carriers as a result of which they are often described as 'artificial atoms'. Confinement of charge carriers in these nano-sized structures empower these NCs with characteristics which differentiate them from their bulk counterparts and can be used to enhance the material's optical, electric and magnetic properties.[398] The effect of size ($CuInS_2$ NCs in chapter 2), chemical composition (doping in chapter 3 and 4) and crystal structure (hexagonal, zinc-blend and perovskite in chapter 2,3 and 4) have been discussed in the earlier text and have been elaborately reported for various materials and NCs elsewhere in the literature.

Since almost four decades ago that the quantum size effects in NCs were showcased,[5] tons of research has been carried on in the field of semiconductor NCs. The revelation of the size dependent electronic energy levels of NCs in glass matrix[399, 400] enabled precise control over the energy band gap of such NCs resulting in development of such materials in various optoelectronic and photon management devices. But with the advent and rapid development of solution synthesis technology, a large number of nearly monodisperse, solution based spherical NCs have emerged over the last thirty years. This enabled the tuneability of the emitted photons between ultraviolet to infrared spectral wavelengths[401]. Moreover, passivation of the surface dangling bonds by the application of organic ligands, was shown to enhance the PL quantum efficiency. Also, improvement in PL quantum efficiencies and Stokes shift engineering[151, 402, 403] of PL suitable for various photon management technologies was brought about through the emergence of core-shell heterostructuring with different core and shell materials controlling the individual charge carrier wave functions.[144, 404] These persistent efforts by research groups all over the world lead to these NCs being realised in diverse practical applications. For instance, high quantum efficiency and colour tuneability exhibited by NCs propelled them to be a popular material in the field of displays and light emitting diodes(LEDs),[405-407] high quality samples for lasing[408-410] and biocompatible NCs for florescent labelling and biosensing.[65, 396]

However, in semiconductor NCs, shape anisotropy is another important parameter since it heavily influences the electronic spectra of charge carriers as well as the optoelectronic and photophysical properties of the NCs. The confinement of charge carriers in one or multiple dimensions results in the density of states changing from discrete levels for zero-dimensional structures, such as nanocrystal quantum dots, to a saw-like quasi-continuum in one-dimensional nanorods (NRs), and finally to the step-like quasi-continuum in two-dimensional

nanoplatelets (NPs) with confinement along the thickness dimension. In colloidal nanostructures, as a consequence of lower dielectric constant of the surrounding media, the strength of electron-hole Coulomb coupling is a function of the surface to volume ratio of the respective NCs which can be controlled with their shapes. This results in escalating exciton binding energy in one-dimensional NRs[411-414] and two-dimensional NPs[415-418] compared to zero-dimensional NCs. Moreover, the shape influences the strength of exciton-photon coupling resulting in shorter radiative decay times in these anisotropic NCs. This shortening of the exciton radiative decay time has been in many cases been attributed to giant oscillator strength transitions (GOST)[419, 420] resulting from enhancement in the absorption cross section, in one and two dimensional NCs connected with exciton centre of mass coherent motion.[421] This enhancement was however, reported to be proportional to the ratio of area of exciton coherent motion along the NC dimensions to the second power of exciton Bohr radius of the NC in two-dimensional epitaxial quantum wells at low temperatures.[422]

5.2 Synthesis Protocols and growth mechanism

To date, quite a few synthesis procedures to develop two-dimensional nanostructures with carrier confinement in one dimension have been reported for the growth of metals,[423, 424] oxides,[425, 426] and semiconductor NPs[427, 428] in colloidal suspension. With the development of various procedures and techniques for colloidal synthesis of NCs it was a couple of decades ago, shown that the shape anisotropy of these NCs could be modulated from spherical NCs to NRs to multi-pods and NPs by changing the choice of ligands used in the reaction protocols.[395, 429, 430] The change in shape anisotropy in these nanostructures yielded NCs with different crystal structures namely wurtzite and zinc blend which warranted separate growth mechanisms in these nanostructures. ***Wurtzite NPs:*** One of the first successful batches of

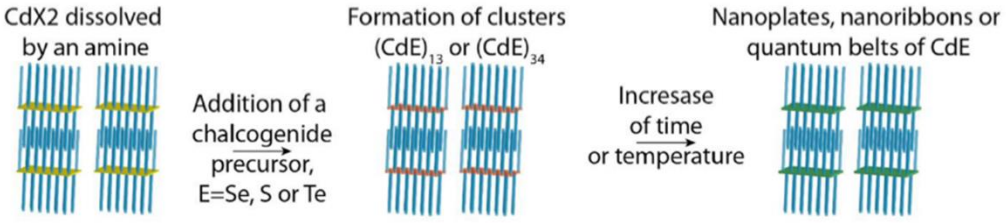

Figure 5.1: Scheme of the three-step synthesis in wurtzite 2D nanocrystals starting with dissolution of a salt in amines and then introduction of the chalcogenide precursor, finally leading to 2D nanocrystals. (Reprinted with permission from ref[1]. Copyright 2016 American Chemical Society.)

colloidal two-dimensional nanostructures were obtained and reported in the form of wurtzite structured nanoribbons in 2006 by Hyeon et al.**[428]** and in one of their following works[431]

outlined the growth mechanism attributing it to a templated growth synthesis where the dissolution of salts and precursors were reported to form laminar phases which in turn acted as templates for the respective NC growth in the form of nanoribbons of uniform thickness of 1.4 nm. Similar work on the laminar assembly of CdSe nanoclusters into quantum belts and the origin of their high PL efficiency was reported by Liu et al.[432, 433] describing, through spectroscopic means, the schematic mechanism of formation of such two-dimensional nanostructures as shown in the **figure 5.1**. It was observed that the formation of these nanostructures involved Cd precursors dissolved in amines leading to the formation anisotropically ordered layers which acts as primary growth template.

This step is followed by the introduction of Se precursor which then leads to the growth and nucleation of wurtzite two-dimensional nanostructures on the previously formed laminar templates. Through spectroscopic means, they spotted the early emergence of $(CdSe)_{34}$ and $(CdSe)_{13}$ magic-sized clusters which then subsided with reaction time to solely, the more thermodynamically stable $(CdSe)_{13}$ magic-sized clusters stabilized by amines present in the solution. These $(CdSe)_{13}$ clusters weakly bound to amines were reported to be stacked in the thickness and width directions which, with reaction temperature and reaction time convert to self-ordered quantum belts. These quantum belts post crystallization are reportedly unstacked in width direction while being piled up along their thickness. Finally, wurtzite two-dimensional nanostructures in the form of quantum belts of homogenous thickness down to a few monolayers were obtained following the separation of these stacked quantum belts through addition of primary or a mixture of primary and secondary amines[434] and sonication. Over the years, however, apart from CdSe NCs, many other two-dimensional nanomaterials have been reported with favourable optical properties like CdE (E=S,Te),[435] Copper based binary NCs,[436] Zinc based binary chalcogenides,[273, 437] PbS/Se NCs[273] and more recently perovskites[438] with efficient PL quantum efficiency. ***Zinc Blend structure:*** Although the optical properties showcased by the zinc blend CdSe NCs are similar to those with wurtzite structure, the reaction growth mechanisms are very different. On one hand, as described above, nanostructures with wurtzite crystal structure involve magic sized clusters as intermediaries of reaction, the same has not been proved for those having zinc blend structure.[439] Hence the growth mechanism of zinc blend NPs, as shown in **figure 5.2** can be classified as a two-step process involving

nucleation of NCs and subsequent formation of seeds followed by a preferential lateral growth of these seeds initiated by short chain carboxylate cation precursors.[439]

Colloidal CdSe NPs of zinc blend structure was, for the first time, synthesized in 2008 by Ithurria et al.[427] In this procedure, mixture of a long chain carboxylate Cadmium precursor (Cadmium myristate), Selenium precursor (Selenium powder mesh) and non-coordinating solvent (1-Octadecene) are degassed to get rid of the water molecules and then the reaction temperature is increased so as to dissolve the precursors and initiate the process of NP nucleation under inert conditions. At a specific temperature which dictates the thickness of the thus formed NPs, a short chain carboxylate Cadmium precursor (Cadmium acetate) is injected which propels the growth of NP's lateral dimensions whilst maintaining a uniformly precise thickness up to atomic level. The injection temperature, however is all-important because this determines how much the nucleation seeds grow in size which in-turn, upon injection of short chain carboxylate cation precursor, translates into the thickness of the thus formed NPs. Small seeds give rise to thinner NPs while bigger nucleation seeds result in thicker ones. The anisotropic preferential lateral growth upon injection of a short chain carboxylate has been extensively studied in reports by Ithurria et al.[439] and Chen et al.[440] Moreover, the lateral dimensions and aspect ratio of these colloidal NPs can be controlled by altering the reaction duration and the concentration of precursors used. Because of such precise control over thickness and shape anisotropy, these NPs have been reported to stack along and even exhibited self-assembling.[441-443] NPs of 3.5 to 5.5 monolayers thickness can be obtained through the above procedure. The half monolayer arises from the fact that each NP's top and bottom surfaces are terminated with the same cationic plane and passivated by organic ligands. So,

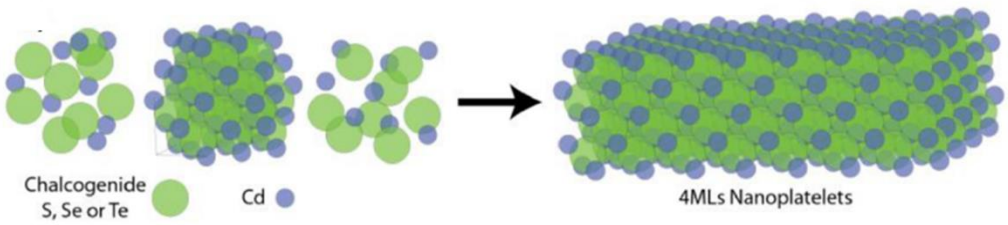

Figure 5.2: Scheme of the two-step growth of cadmium chalcogenide nanoplatelets involving nucleation of NCs and subsequent formation of seeds followed by a preferential lateral growth of these seeds initiated by short chain carboxylate cation precursors (Reprinted with permission from ref[1]. Copyright 2016 American Chemical Society.)

essentially 3.5 monolayer Cd chalcogenide NP represents three monolayers of successive combination of Cd plane and chalcogenide plane along the thickness direction. It has however, also been reported that thinner NPs tend to grow larger in lateral sizes to an extent that they

roll upon themselves.[444, 445] This larger lateral area of NPs in general results in lower PL quantum yield and is believed to be due to the introduction of larger probability of defect sites creeping on to the NP surface, hence introducing non-radiative decay pathways in the ensemble, making these materials undesirable for practical applications without further chemical processing. This has led to research groups focussing attention on developing thicker NPs. Chu et al.[446] and Christodoulou et al.[447] in 2018 in separate works reported different synthesis procedures to make thicker NPs starting from 4.5 monolayer NPs obtained from the above discussed procedures. The former incorporated Colloidal-Atomic layer deposition (c-ALD) technique to grow CdSe layers on the surface of 4.5 monolayers CdSe NPs ensemble attaining thicknesses up to 11.5 monolayers while the latter work involved a two-step synthesis procedure, where 8.5 monolayered CdSe NPs were formed by the addition of $CdCl_2$ starting with 4.5 monolayered NPs at high temperatures.

5.3 Optimization of the optoelectronic properties

Colloidal NPs coupled with their easy solution processibility, large absorption cross section and sharp and monodisperse optical features with fast PL decay (resulting from high exciton oscillator strength) are very promising materials for modern display devices and emitters. However, they suffer radiative luminescence losses like any other core only NC by virtue of surface defects and carrier wave function leakages. This makes the processes involved in enhancing their PL quantum efficiencies of paramount importance to incorporate them in the next generation technologies as efficient emitters. As discussed in chapter 1, it has been amply shown that heterostructuring in spherical NCs by epitaxial growth of another semiconductor material enhances and preserves its optical properties,[144] the most common being core-shell structures which have shown to achieve high PL quantum yield, self-inducing red shift and controlling the charge confinement resulting in tuning various optical behaviors of the material to exploit its applicative potential. Similar to those in their spherical counterparts, colloidal nanoplatelets also can be subjected to different procedures to bring out the best of their optoelectronic properties.

Core-shell heterostructuring: Most of the standard reaction protocols involved in core-shell heterostructuring in spherical NCs take place at high reaction temperatures post the growth of core NCs. This high temperature reaction procedure for shell growth however doesn't work in cadmium chalcogenide NPs since they are fragile at those temperatures. Moreover, low temperature procedures of introducing these core NPs in the presence of amines results in two

to three times emission line broadening due to ligand exchange but still manages to enhance PL quantum efficiency compared to the core only NPs. In 2012, two such low-temperature reaction procedures were reported. Ithurria and Talapin successfully synthesized and reported CdSe/CdS core/shell NPs by shelling CdSe NPs with CdS through a layer by layer deposition technique known as Colloidal Atomic layer deposition (c-ALD).[448] The shelling is achieved by alternatively depositing cation and anion monoatomic layers onto the core NPs. The shelling procedure involves sequential phase transfer of NPs between immiscible polar and non-polar phases resulting in immaculate control over the precise number of monolayers to be incorporated in the shell. However, this method like any other, has a downside too; It is not viable to use this procedure for depositing thick shells as the repetitive procedure is complicated, time consuming and more importantly, leads to dramatic decrease of PL quantum efficiency and poor photostability since the methods warrants washing and purification of NPs after each cycle of shell growth. The other low-temperature procedure was reported by Mahler et al.[170] where they proposed a one pot synthesis procedure for continuous H_2S shell growth. The reaction involves thioacetamide and octylamine which serve as the source of sulfur, and hydrogen sulfide is generated to react with the cadmium acetate added later to form a shell at room temperature. This method has also been used to grow shells of CdS and CdZnS with typical thicknesses of around 3.5 monolayers. With growth of shell, there is an apparent red shift in due to the decreased confinement in thickness direction and the highest PL quantum yield reported was about 80 %.[171] More lately, there have been reports of synthesizing CdS and ZnS shells on CdSe core NPs at high temperatures[449, 450] as well with better crystal quality and enhanced optical properties like improved PL efficiency and colloidal photostability.

Core-crown heterostructuring: The growth of the shell as described in the text above is isotropic and uniform in all the directions, i.e. occurs along all facets of the NPs, the two-dimensional shape of NP allows another growth mechanism of shell occurring only in the lateral directions of the NP and not along its thickness[164, 172, 451] and are known as core-crown heterostructured NPs. Since the crown material, unlike shell is always grown along the lateral directions, the formation of this heterostructure does not influence the overall thickness or the extent of quantum confinement along the vertical direction of the NPs. Such heterostructure was first reported in 2013 with the synthesis of CdSe/CdS core/crown structures.[172, 451] In a typical reaction, Cadmium precursor which is a mixture of Cadmium acetate (short chain carboxylate) and Oleate are added to the already prepared CdSe NP cores which is then followed by the addition of elemental sulphur dissolved in Octadecene as sulphur precursor.

The core NPs are used as nucleation sites and in the presence of a short chain carboxylate cadmium precursor, the surrounding CdS layer is formed along the lateral dimensions. The extent of growth of crown can however be controlled through the amount of introduced precursor. Core/crown CdSe/CdS have been shown to exhibit PL efficiency of about 60% while maintaining a narrow emission line width unlike their core/shell counterparts. The absorption in these NPs is reportedly dominated by crown CdS as shown in the figure while the emission is dominated by the core CdSe due to the efficient localization of hole carriers resulting in an induced Stokes shift which is very useful to exploit these materials in photon management technologies and display applications. Using a similar approach various combinations of Cd based core/crown heterostructures such as Inverted Type-I CdS/CdSe and Type-II CdSe/CdTe have been synthesized and investigated.[452, 453] Also recently, carrier wavefunction engineering has been attempted using core/barrier/crown multi-layered heterostructure.[454]

Alloying: One of the downsides of the spectral properties of NPs is the discrete steps of emission that they exhibit with respect to their thickness. In other terms, considering CdSe NPs, different ensembles of different thicknesses separated by a single monolayer such as 3.5, 4.5, 5.5 monolayers and so on emit at 460 nm, 510 nm and 550 nm respectively. This results in an inefficient continuous tuneability of the optical properties in NPs. To this end, alloying of CdSe NPs with other anionic species was reported and studied. CdSeTe and CdSeS were one of the first materials to be investigated.[452, 453, 455, 456] As shown in the **figure 5.6,** Te alloying in CdSe NPs induces a red shift in 3.5 monolayered NPs as studied and reported by Tenne et al.[456] also resulting in bowing effect which effectively induces a red shift in transition towards smaller energy compared to the energy of smaller bandgap material accompanied with measurably large broadening of emission line width. As far as synthesis procedure is concerned, it adheres to the standard synthesis protocols of Cd based chalcogenide NPs, but for the introduction of Se and Te in the form of TOP-Se and TOP-Te in specified ratio in concentration. Alloying with Sulphide on the other hand enhances tuneability between the blue and green wavelengths. As with the Te alloying, it is simply synthesized by mixing Sulphide powder with Selenium precursor.[457, 458]

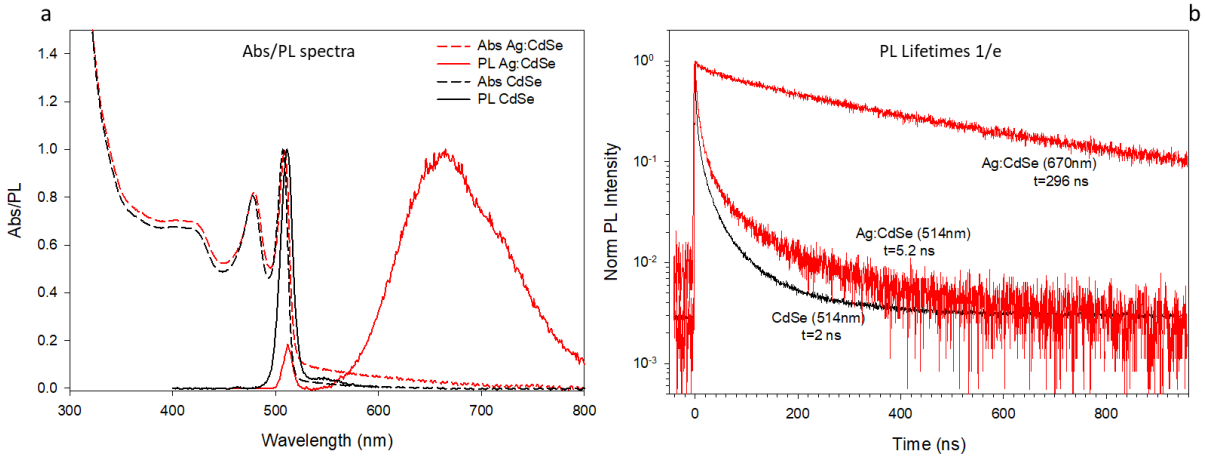

Figure 5.3: Ag doped CdSe 4.5 monolayer NPs (with a doping level of 20% as reported in ref.[460]) achieved through post synthesis cation exchange reaction. **(a)** Absorption spectra of doped and undoped NCs exhibit distinct sharp excitonic peaks attributed to e-HH and e-LH transitions. PL spectra of doped NPs show simultaneous emission from band edge as well as dopant states as also observed and reported in ref.[460] **(b)** Time dynamics of the undoped and Ag doped samples in solution recorded at room temperature.

Doping: As elaborately discussed in the previous couple of chapters, doping has been an established technique with various established synthesis protocols to tune the optoelectronic properties and photophysical aspects of spherical NCs. Doping binary chalcogenide NCs with metallic impurities like Cu, Au, Ag, Mn and so on introduces an additional degree of freedom to bring out the best of a material, thus exploiting its technological potential. It helps tune the optical, magnetic and electronic properties, induces efficient Stokes shift and is also shown to enhance the PL quantum efficiency. Similarly, they have also been successfully incorporated in NPs structure in the recent years. This was showcased in 2017 to synthesize Cu doped CdSe NPs using a hot injection based nucleation doping technique[317] where the dopant precursor was added post host seed formation along with a short chain carboxylate cation precursor to enhance the lateral growth. The thus produced NPs by Sharma et al. were further incorporated in LSCs. Using the same technique, last year, Mercury doped CdSe NPs were also synthesized[459] which exhibited dual emission behavior. Apart from the above mentioned hot injection technique, various research groups have recently channelled their work on an alternate post synthesis cation exchange route for doping metals like Cu and Ag into CdSe NPs[460, 461] thus achieving desirable tuneable optical emission between visible to near infrared regions of electromagnetic spectrum.

5.4 Why CdTe nanoplatelets?

CdTe is characterized by a low band gap of 1.44eV[462] compared to its Cadmium chalcogenide counterparts (CdSe~1.74 eV and CdS~2.24 eV). This makes CdTe very intriguing and manurable resource for their application in both photovoltaic[463] and photodetection[464] technology. These potential applications arising from its intrinsic semiconductor properties encouraged several research groups around the world to work on various synthesis procedures over the years[465] to synthesize colloidal free standing spherical NCs of different sizes through organometallic[466] and aqueous[467] synthesis protocols. These methods were also extended to make NCs of different shapes and morphologies resulting in the synthesis of colloidal CdTe nanorods,[468] nanowires,[469] and nanotubes.[470] However, colloidal synthesis of two-dimensional CdTe NPs and the studies conducted on them have somewhat lacked in terms of exploiting their applicative potential. CdTe NPs showcase high excitonic and bi-excitonic binding energy compared to its Cd chalcogenide counterparts, widely separated and distinct light hole (LH) and heavy hole (HH) features, narrow, tuneable emission line width and fast PL decay lifetimes among other interesting characteristics can have considerable impact in optoelectronics and photon management technologies. However, they are shown to suffer from low PL quantum yields resulting from possible lattice defects arising from high lattice atomic mismatch which pulls them down in priority of research compared to CdSe NPs. As a result, the pioneering work on CdSe colloidal two-dimensional NPs systems which have been over the years, extended in detail to CdS[435, 471] were only briefly replicated in CdTe.[431, 471] Two-dimensional CdTe nanostructures have been reported to date in the form of zinc blend structured NPs[471] where the electronic transitions were also studied, wurtzite structured nanoribbons have been synthesized[431] and CdTe nanosheets[472] of tetrahedral shape were also reported in the past. In 2013 however, Pedetti et al[473] optimized the synthesis protocol for the colloidal synthesis of CdTe NPs of zinc blend morphology yielding three NP populations of different thicknesses defined with atomic precision to study the photo-response of the respective NCs. They studied the dependence of NP formation on the reaction conditions and showed that the obtained NPs can be easily extended laterally to obtain nanosheets with dimensions in the micrometer regime. In this work, I attempt to replicate and improve the synthesis of colloidal CdTe NPs and nanosheets and study their optoelectronic and photophysical properties to exploit their applicative potential in the fields of lasing and inorganic scintillator technology.

5.5 Lasing and optical gain studies

Highly anisotropic Cadmium chalcogenide (Cd:S/Se/Te) two-dimensional nanostructures have gained immense attention in the recent past owing to their intriguing optoelectronic properties leading to their potential applications in a variety of emissive devices. These colloidal nanostructures quantum confined in one dimension typically 1-2 nm thick with lateral dimensions growing up to tens of nanometers exhibit exceptionally large excitonic and bi-excitonic binding energies resulting in sharp light hole (LH) and heavy hole (HH)-$1S_e$ excitonic features, supressed Auger recombination, narrow emission spectra and giant oscillator strength transitions (GOST) connected with exciton centre of mass coherent position. Such distinct traits have led to them being used to achieve stimulated emission in both pulsed and continuous wave excitation regimes.

Despite such remarkable properties and exceptional developments in their optical gain (OG) parameters such as gain coefficients and gain thresholds, research has been limited to CdSe and CdS and their respective heterostructures in Cadmium based chalcogenides. Cadmium Telluride (CdTe) nanoplatelets with higher excitonic binding energies and widely separated and distinct LH and HH features have been ignored for some reason widely used only in heterostructures with CdSe and CdS. In this work we attempt to investigate if core-only CdTe nanoplatelets can exhibit stimulated emission and as to how conducive they are for further research.

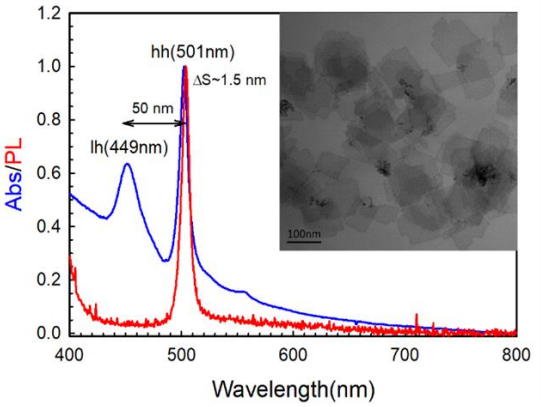

Figure 5.4: Absorption spectra (blue) exhibiting distinct HH-1Se and LH-1Se excitonic features overlapped on a broad scattering background and an almost resonant and sharp PL spectra (red) depicting uniform thickness of 3.5 ML nanoplatelets. Inset: TEM image for CdTe 3.5 ML nanoplatelets with an average lateral dimension of 63nm×47nm.

Colloidal synthesis procedure described by Peditte et al was followed for the synthesis of 3.5 monolayered CdTe NPs but for some reaction parameters such as Cadmium precursor, Injection rate of TOP-Te and the reaction temperature which were modified. Several

permutations of the above-mentioned parameters were tried out as shown in **table 1**. The following optimized procedure was employed for synthesis of these 3.5 ML nanoplatelets:

Chemicals: Cadmium acetate dihydrate $Cd(OAc)_2 \cdot 2(H_2O)$ (Sigma-Aldrich, 98%), oleic acid (OA, Sigma-Aldrich, 90%), 1- octadecene (ODE, Sigma-Aldrich, 90%), trioctylphosphine (TOP, Cytec, 90%), tellurium (Sigma-Aldrich, 99,997%), propionic acid (Sigma-Aldrich, 99%), CdO (Sigma-Aldrich, 99%), cadmium formate (Sigma-Aldrich, 99,9%), n-hexane (VWR, 95%), and ethanol (Carlo Erba, 99.8%) were used for the synthesis of the nanoplatelets without any further purification.

Synthesis of 3.5 monolayer CdTe NPs: A 50 mL three neck flask was charged with 133 mg $Cd(OAc)_2 \cdot 2(H_2O)$ (0.5 mmol) and 255 µL OA (0.8 mmol) in 25 mL of ODE and placed in near-vacuum at 95 ℃ for 1 hour while being stirred continuously. After complete degassing, mixture is then heated up to 210 ℃ in inert nitrogen environment. Then, 45 µL (0.1 mmol) of 2.24M TOP-Te diluted in 5mL ODE was injected using syringe pump at a constant rate of 10mL/hr. The reaction was allowed to continue at 210 ℃ for 15 minutes. 15 mL hexane and 20 mL isopropanol ware added to the product and centrifuged for 10 mins at 3500 rpm and the resulting precipitate was dispersed in n-hexane. Absorption and Photoluminescence spectra of the resultant samples are reported in **figure 5.4**.

CdTe 3.5 ML platelets thus formed had an average lateral size of 63 nm $\times$ 47 nm as computed from TEM images (inset **figure 5.4**). Thus, carrier confinement occurs only in one dimension with the other dimensions being comfortably larger than the exciton Bohr radius (7.3 nm in bulk). As shown in **figure 5.4**, absorption spectra exhibit distinct HH-1Se and LH-1Se excitonic transition features similar to their II-VI counterparts but overlapped on a broad scattering background while PL spectra shows an almost resonant and sharp band edge emission. This negligible Stokes shift possibly results from absence of strong phonon coupling and fine structure relaxations. However, broad emission from trap states was observed which was more evident in Transient Absorption (TA) measurements reported subsequent sections. The Intrinsic absorption coefficient (μ_i), a quantity independent of concentration of nanoplatelets, at 400nm was calculated to be 3.3326×10^5 cm^{-1} resulting in an Absorption cross section ($\sigma = \mu_i \times V$) of 1.283×10^{-12} cm^2, where V is the volume of nanoplatelets. For calculation of μ_i, optical constants of CdTe were used.

Cadmium precursor	Injection rate	Reaction temperature	Observations
$Cd(OAc)_2$	Slow	210 ̊C	• Well defined excitonic features imposed over a broad scattering background. • BE emission dominates over a broad emission from trap states. • Low Quantum yield. • For T > 210 ̊C, thicker nanoplatelets (4.5ML) start to form.
	Fast		• Absorption spectra is dominated by quantum dots. • Negligible emission observed.
$Cd(Prop)_2$	Slow	215 ̊C	• Sharp and well defined excitonic features imposed over a broad scattering background. • BE emission dominates but still emission from trap states evident. • High quantum yield compared to the above class of samples. • Resultant nanoplatelets degrade very fast and may not be suitable for TA studies.
	Fast		• Well defined excitonic features imposed over a broad scattering background. • Trap states emission dominates over the BE emission. • Poor quantum yield. • Quantum dots emission observed.
$Cd(Myr)_2$	Slow	220 ̊C	• No nanoplatelets were formed. • Broad absorption features indicate quantum dot formation.
	Fast		• Quantum dots are formed.
$Cd(OAc)_2$+ $Cd(Myr)_2$	Slow	215 ̊C	• Well defined excitonic features imposed over a broad scattering background. • Broad emission from trap states dominates over the BE emission. • Poor quantum yield.
	Fast		• Broad absorption features indicate quantum dot formation.

Table 5.1: Optimized reaction procedures and effect of modifying Cadmium precursors and reaction parameters. Fast and slow injection rate correspond to 16 mL/hr and 4 mL/hr respectively.

Ultrafast Transient Absorption spectroscopy: Transient absorption (TA) spectroscopy is a pump-probe spectroscopic technique used to measure the photogenerated excited state absorption energies and associated lifetimes of molecules and various materials. The pump-probe technique can be described by a sample being photo-excited by a light source (pump pulse), whereby a second light source (probe pulse) is measured for changes in absorption as a function of wavelength and time. This technique gives effective information about bleaching, dynamics of charge carriers and optical gain. In the measurements, 400 nm pump pulses (110 fs pulse width) with a repetition rate of 1KHz, produced from the 800nm fundamental using a BBO crystal (Spitfire Ace, Spectra Physics) was used to excite the sample. The broadband probe pulses measuring the change in absorbance $\Delta A(\lambda,t) = A(\lambda,t) - A_0(\lambda)$, where A is the absorbance after photoexcitation and A_0 the absorbance in absence of pump pulse, effectively detecting the region between 440 nm and 800 nm were generated using Sapphire crystal from the incident 800 nm fundamental beam. The probe pulses were delayed using a Newport TAS delay stage with a maximum delay of 3.3ns. Measurements were carried out on samples dispersed in n-hexane in Quartz cuvette of 2mm path length under constant stirring to prevent degradation of samples.

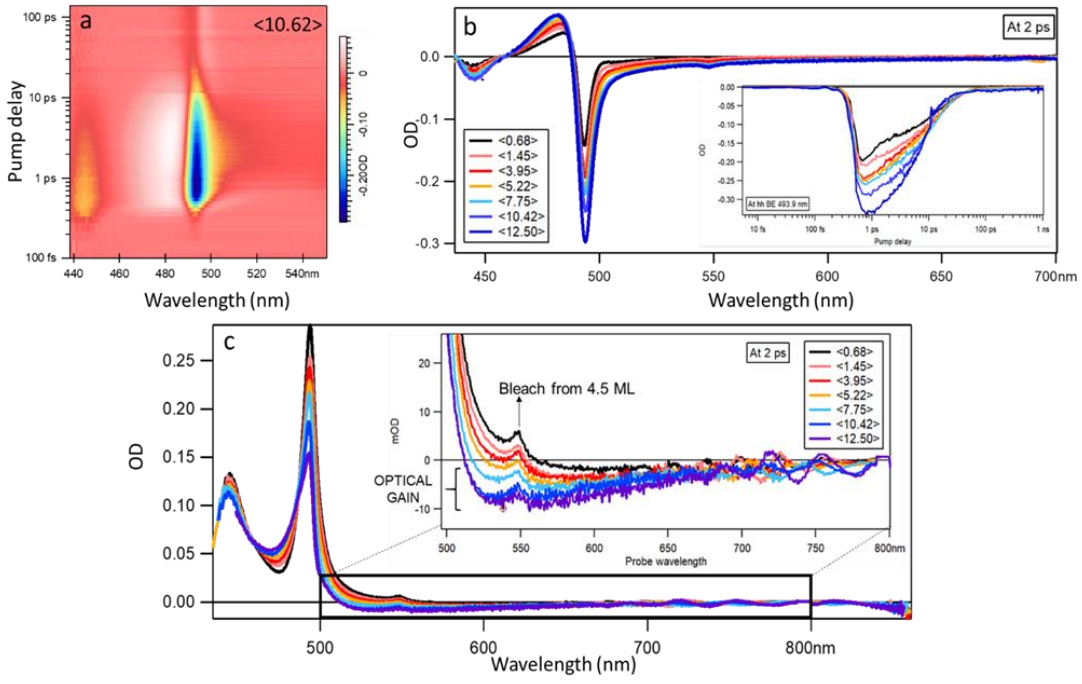

Figure 5.5: Ultrafast transient absorption (a) 2 D wavelength time map for <N>=10.62 excitons per nanoplatelet. **(b)** ΔA spectra evolution at 2 ps and (inset): HH bleach dynamics of CdTe 3.5 ML samples with incident fluence. **(c)** Optical Gain spectra at 2ps indicated in the region where A<0. OG is observed for <N> greater than 3.95 excitons per NP.

By virtue of pumping at various fluence (J_{in}) we were able to create 0.62 to 12.50 average number of excitons per nanoplatelet <N>. **Figure 5.5a** depicts evolution of the change in absorbance, ΔA with time for a pumping fluence (J_{in}) resulting in <N>=10.62. We observe pronounced and long-lived bleach features at heavy hole (HH) and light hole (LH) excitonic positions at 493nm and 443 nm respectively resulting from carrier relaxations and state filling as shown in **figure 5.5a**. At early times, photoinduced excited state absorption is evident which is eventually overpowered by bleach signal at around 350 fs and subsequently observe intensification of the same accompanied with decrease in photoinduced absorption as time progresses till around 2 ps. The biexciton formation on the low energy side of HH bleach subsequently turns negative giving an indication of involvement of Stimulated Emission or Optical Gain. **Figure 5.5b** shows the spectral evolution of ΔA at 2 ps for various values of <N> between 0.68 and 12.50 excitons per NCs. Predictably, with increasing <N>, photoinduced absorption and respective bleaches intensify accompanied with a stronger negative signal on the low energy side of bleach. The HH bleach lifetime more or less remains constant at around 50 ps as shown in the inset of **figure 5.5b**. This behavior asserts the minimum indulgence of Auger recombination channels. Pumping harder to create more than 12.50 excitons per nanoplatelet resulted in degradation of the sample.

For calculating the Optical Gain (OG), we compute $A=\Delta A+A_0$ where ΔA is differential absorption and A_0 is linear absorption of the selected sample and OG is observed in regions where A<0. In these CdTe 3.5 monolayered samples, OG is evident for <N>=3.82 excitons or more per nanoplatelets. Both HH and LH bleach persists, but for a slight saturation alongside a broadband OG ranging between 520-710 nm as shown in **figure 5.5c**. This broadband OG on the low energy side of the superimposed BE OG can be attributed to the trap states arising due to the defects in the NP surface itself. The OG thus seen is very short-lived with a lifetime of around 10 ps compared to their CdSe counterparts where OG lifetime ranges to about 100 ps. Though intrinsic OG coefficient could not be calculated due to the scatter subtracted linear absorption (A_0) used in calculations, maximum OG observed was around 10 mOD for <N>=12.50. The extent of stimulated emission could have increased by pumping harder but the sample starts to degrade after <N>=12.50 excitons per platelet. Such broad band and fast decay features indicate the presence and rather dominance of the inter-band trap states.

Synthesis of alloyed CdTeSe NPs: In order to tackle the two issues of large scattering background and presence and emission from trap states, we synthesize CdTe:Se alloyed nanoplatelets. The smaller Se ions should in principle reduce trap states and reduction of lateral

area of nanoplatelets could result in reduced scattering background. Procedure reported by Tenne et al.[456] resulting in the samples shown in **figure 5.6 a,b** with Te:Se ratio being 63:37 was followed for the synthesis of CdTe:Se alloyed nanoplatelets. A 25 mL three neck flask was charged with 120 mg $Cd(Myr)_2$ (0.21 mmol) in 12 mL of ODE and degassed at RT for 30 minutes while being stirred continuously. After complete degassing, mixture was then heated up to 240 ℃ in nitrogen environment. Then 60 mg $Cd(OAc)_2$ dihydrate (0.23 mmol) and 160 mg $Cd(prop)_2$ (0.63 mmol) were added. After a minute, a mixture of 150 µL of TOP-Te (1M) and TOP-Se (1M) in ratio of 2:1 and 200 µL oleic acid (0.63mmol) in 2mL ODE was added at a constant rate of 8mL/hr using syringe pump. The reaction was allowed to continue at 240 ℃ for 15 minutes. Then the heating mantle was removed and the mixture was cooled to room temperature after adding 1 mL oleic acid at 100 ℃. 15mL hexane and 20 mL isopropanol ware added to the product and centrifuged for 5 mins at 5000 rpm and the resulting precipitate was dispersed in n-hexane.

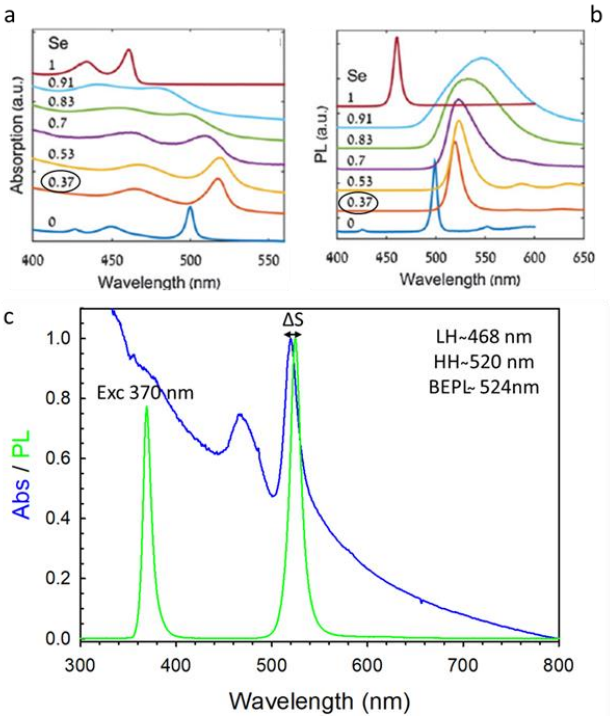

Figure 5.6: Alloyed CdTe:Se NPs (a,b) Absorption and PL spectra reported by Tenne et al. for various ratios of Te:Se concentrations. **(c)** Normalized Abs/PL spectra of thus prepared nanoplatelets with Te:Se ratio being 0.63:0.37 in close agreement with circled spectra in a,b.

Absorption and Photoluminescence spectra of the resultant samples are reported in **figure 5.6c**. Thus formed CdTe:Se NPs exhibit distinct LH and HH-$1S_e$ excitonic features at 468 nm and 520 nm respectively over an intense broad scattering background resulting from large lateral area. However, the platelets exhibit good BE PL quantum yield with almost no emission

signature from trap states which were dominant in CdTe nanoplatelets. A Stokes shift of 18.2 meV was observed. These results were in very close agreement with the one reported by Tenne et al. shown in **figure 5.6 a,b**. Now that we have overcome the issue of emission from trap states, we move on to address the second issue of large background scattering possibly a result of large lateral size of platelets. The large lateral area also leads to degradation and disintegration of platelets during spectroscopic studies involving high incident laser fluence. This issue is being addressed by changing ligands involved in the reaction to smaller chains (replacing $Cd(prop)_2$ with $Cd(OAc)_2$) and attempting to understand the use of growth limiting agents like Oleic acid. While, limiting the size of these nanoplatelets is still a work in progress the question in title of this report as to whether it is possible to witness stimulated emission from CdTe NPs has been answered partially in the positive favour for now. However, in order to be able to report this work, it is pivotal to gather deeper understanding about the reaction mechanics and growth dynamics of these intriguing NCs and optimise them for further spectroscopic studies.

5.6 CdTe NPs for ultrafast radiation detection

Efficient detection of ionizing radiation is the key parameter demanded by several applications in many fields, such as medical imaging, high energy physics, homeland security, oil drilling exploration and industrial control, among many others. Today, a substantial part of the market is occupied by inorganic scintillators, whose luminescence properties have been exploited for over a century. In the last three decades, a wide array of new scintillating materials have been discovered, progressively improving the performances of ionizing radiation detectors.

Several parameters describe the key properties of a scintillating material, primarily the light yield, the energy resolution, the decay time, the material density, its chemical stability and radiation hardness. To date, no scintillating material excels in all of these parameters and, therefore, each application relies on a different scintillator system satisfying the requirements of the respective most relevant physical parameters. The emergence of new scintillation applications, as well as technical advancements in consolidated ones, have led to more and more strict and tailor-made requirements for scintillator performances and no inorganic scintillator currently available satisfies such specifications.[474] For example, scintillation timing properties have become a key factor for the progress in applications relying on the time of flight (TOF) technique. These

include medical imaging in positron emission tomography (TOF-PET), where fast timing is critical for the image quality and their reconstruction process, and high energy physics experiments, where high event rates in high-luminosity colliders require a fast response to mitigate the high pile-up and localize the events vertices. Paramount to the study of rare events (e.g. double beta decay) in fundamental physics is the collection of statistically significant experimental data that requires new solutions for very large volume detectors, which nowadays are mainly based on tons of scintillating materials. A breakthrough in the design of detectors and in the improvement of the capability of fundamental physics experiments will, therefore, be the discovery of scalable and affordable production methods for new materials. Such materials will need to strongly interact with ionizing radiations and have an efficient scintillation that is largely Stokes shifted from their absorption spectrum, to suppress reabsorption losses.

NCs of direct bandgap semiconductors, such as metal chalcogenides or lead halide perovskites synthesized by scalable colloidal methods are very promising candidates for transformational breakthroughs in radiation detection. NCs are characterized by spectrally tuneable, highly efficient luminescence with fast timing properties. Also, their composition involves heavy elements, such as cadmium, tellurium or lead, whose high atomic number favours the interaction with high energy photons and charged particles. NCs can be fabricated in geometries and compositions that can be crucial for facing the above-mentioned challenges in scintillation: for example, sub-nanosecond emission lifetimes (suitable for TOF-PET) are obtained by exploiting the giant oscillator strength of two-dimensional NPs. Furthermore, through fabrication of precise core-shell geometries or by doping the NCs, it is possible to widen the emission Stokes shift required for applications where high material densities are required and thus self-absorption needs to be minimized. Up to now, however, research in NCs has been mainly focused on understanding their physical and chemical properties and on their implementation in artificial lighting or lasing devices, which use relatively low-energy optical pumping (UV or visible light). The specific engineering of NCs targeting scintillation applications lags much behind and so does the fundamental knowledge of the physical mechanisms under-pinning light emission from NCs under ionizing radiation excitation. These mechanisms are typically much more complex than those involved when using UV-Vis excitation and, thus, NCs exhibiting optimal photoluminescence properties are not necessarily also good scintillators. For example, the local energy deposition at the end of the ionization

track can be extremely high. This can lead to NCs populated by high order multiexcitons, resulting in dramatic efficiency losses by non-radiative Auger recombination.

Hence, CdTe NPs owing to their ultrafast lifetimes, efficiently high exciton binding energy, giant oscillator, suppressed Auger recombination and also very importantly large absorption cross sections (which minimizes the material volume required), tuneable and manurable absorption and narrow emission spectra which can be Stokes shifted through heterostructuring and or doping as described in Section 5.3, present themselves as potential candidates for ultrafast radiation detection in inorganic scintillator technology.

Hence, CdTe NPs, owing to their exceptionally large excitonic and bi-excitonic binding energies resulting in sharp LH and HH-1S_e exciton transition features, supressed Auger recombination, narrow emission spectra, giant oscillator strength transitions connected with exciton centre of mass coherent position leading to ultrafast PL decay lifetimes of the order of tens of picoseconds and most importantly enhanced absorption cross section which is a key feature in all detection applications, is significantly larger than their spherical counterparts by around two-three orders of magnitude present themselves as potential candidates for ultrafast radiation detection in inorganic scintillator technology. This ultrafast luminescence decay properties coupled with the possibility of inducing Stokes shift through methods described in section 5.3 make them ideal candidates for ionization radiation detection applications and scintillating technology.

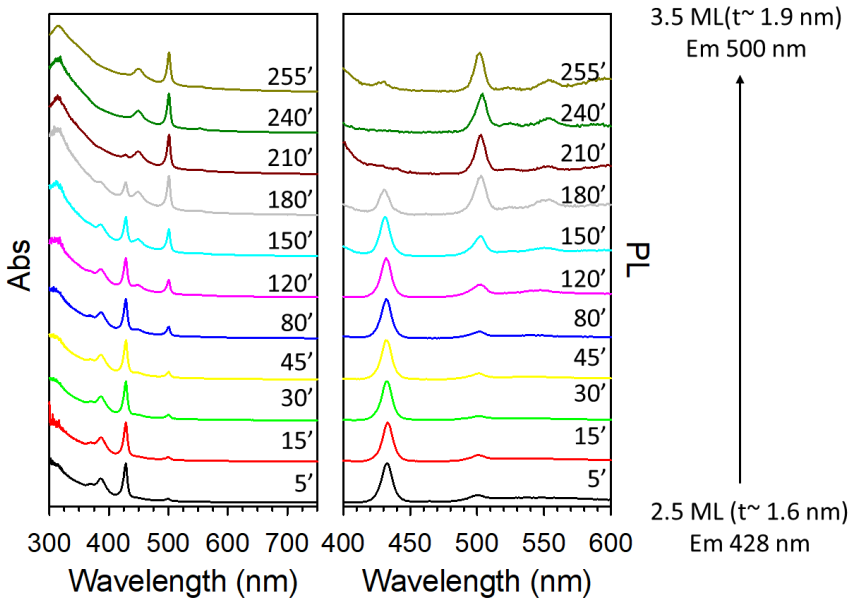

Figure 5.7: Absorption and photoluminescence spectra evolution during synthesis of 3.5 monolayered CdTe NPs.

To this end I synthesized CdTe NPs of 3.5 monolayer thickness and during the synthesis procedure also studied the reaction mechanism. *Synthesis of 3.5 monolayer CdTe NPs:* A 25 mL three neck flask was charged with 133 mg $Cd(OAc)_2 \cdot 2(H_2O)$ (0.5 mmol) and 95 μL OA (0.3 mmol) in 10 mL of ODE and placed in near-vacuum at 95 ̊C for 1 hour while being stirred continuously. After complete degassing, mixture is then heated up to 180 ̊C in inert nitrogen environment. Then, a mixture of 100 μL of 1M TOP-Te diluted in 0.5mL ODE was added swiftly. The reaction was allowed to continue at the same temperature for over four hours while monitoring and recording the absorption and photoluminescence spectra as reported in the **figure 5.7**. 15 mL hexane and 20 mL isopropanol ware added to the product and centrifuged for 10 mins at 3000 rpm to get rid of undesirable products like quantum dots and unreacted precursors. During the first step of the synthesis, 2.5 monolayered nanoplatelets were formed absorbing at 428 nm for their first excitonic peak. After 15 min the absorption at 350 nm, which reflects the total amount of crystalline CdTe is stable, so all precursors were consumed. Finally, after 120 min at 180 °C, we observe considerable population of the thicker 3.5 monolayered population. The thinnest nanoplatelets of 2.5 monolayers with time disappear in favour of the 3.5 monolayered NPs but with a constant optical density at 350 nm. It seems that the transformation comes from either an intra reorganization of the nanoplatelets or a dissolution of the 2.5 monolayered NPs and a fast recrystallization of 3.5 monolayered NPs. There is no addition of free precursors in solution on top of the already existing NPs since the total amount of crystalline CdTe remains constant. Moreover, we could have expected an increase of two monolayers instead of one (leading to nanoplatelets with their first excitonic peak at 556 nm), since the NPLs present two equal opposite surfaces which should react the same way. In general, higher temperature leads to thicker nanoplatelets. This transformation from 2.5 monolayers to 3.5 monolayers NPs may be explained by the really thin thickness of the initial NPs of only one lattice parameter. The relaxation of the top and bottom surfaces induced by the ligands may weaken the crystalline structure of the NPs which present 40% of their atoms on their surface. Besides, the annealing may cause a rearrangement of the atoms leading to more stable 3.5 monolayered crystalline NPs with only 28% (2/7) of their atoms on their surface. Another interesting feature is the total transformation from 2.5 monolayer-thick NPs to 3.5 monolayers-thick nanoplatelets. Indeed, once a 2D nucleus appears on the surface of a NP, subsequent monolayer growth happens rapidly in order to minimize the surface energy.[475]

However, these NPs suffer from low PL quantum yield as they are very fragile, thin and of large lateral area leading to larger possibility of surface defects. Moreover, since they are highly brittle and unstable, it is extremely difficult to further process them using heterostructuring or doping for enhancing their PL efficiency and inducing Stokes shift. For this reason, I synthesized CdTe NPs of 4.5 monolayer thickness using the procedure described by Pedetti et al. as reference. *Synthesis of 4.5 monolayer CdTe NPs:* A 50 mL three neck flask was charged with 133 mg $Cd(OAc)_2 \cdot 2(H_2O)$ (0.5 mmol) and 255 μL OA (0.8 mmol) in 25 mL of ODE and placed in near-vacuum at 95 ̊C for 1 hour while being stirred continuously. After complete degassing, mixture is then heated up to 235 ̊C in inert nitrogen environment. Then, 22.3 μL (0.05 mmol) of 2.24M TOP-Te diluted in 2.5mL ODE was injected using syringe pump at a constant rate of 15mL/hr. The reaction was allowed to continue at 235 ̊C for 15 more minutes. 15 mL hexane and 20 mL isopropanol ware added to the product and centrifuged for 10 mins at 3000 rpm to get rid of the thinner population of NPs and undesirable products like quantum dots and unreacted precursors. This process was repeated two times and the resulting precipitate was dispersed in n-hexane. The PL quantum yield of the resultant NPs was very low (<2%). The NPs thus formed as shown in the **figure 5.8a,** have large rectangular lateral dimensions of around 224 nm× 78 nm with Zinc blend crystal structure. Absorption spectra in **inset figure 5.8b** exhibit distinct HH-$1S_e$ and LH-$1S_e$ excitonic transition features at 556 nm characteristic of 4.5 monolayer NPs but overlapped on a large scattering background while PL spectra (**figure 5.8b**), not only shows an almost resonant and sharp band edge emission but also points to the presence of two distinct populations with minority NPs of 3.5 monolayers also creeping in. **Figure 5.8c** shows PL dynamics of the thus obtained NPs in hexane at room temperature. The samples were excited at the xx with <70 ps pulses from a frequency doubled Ti:sapphire laser (repetition rate 78 MHz) and a Hamamatsu Streak camera with resolution better than 10 ps were used for the BE-PL. As exhibited in the preliminary data, the PL lifetime of these NPs were found to be around 15 ps.

This luminescence lifetime however can be reduced further to less than 10 ps or so. This will be possible by the deposition of a thick shell of a larger-bandgap semiconductor such as CdS, ZnS or an alloy of the two **(figure 5.8 d)**. Also, core only CdTe nanoplatelets inherently contain defects (structural and optical) resulting in broadband emissions in near infrared and longer wavelength regions. This problem can also be tackled by the above-mentioned procedure of larger bandgap material shelling. Due to their flat structure, deposition of thick shells is easier

on NPLs compared to spherical NCs because the lattice mismatch of the different materials induces a lower stress on the structure.

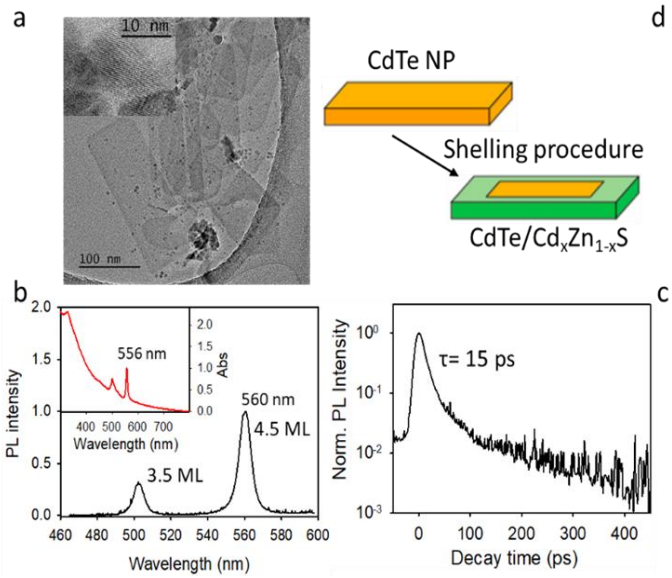

Figure 5.8: Preliminary results CdTe core only NPs: (a) TEM images of 4.5 monolayered CdTe core only NPs exhibiting large uniform surfaces with clear crystalline grains (inset). **(b)** Sharp, well defined heavy and light hole absorption peaks and almost resonant PL spectra at room temperature. **(c)** Ultrafast PL lifetime of around 15 ps acquired using a streak camera. **(d)** Schematic of shelling procedure to be employed to increase PL quantum yield.

5.7 Future prospects: the road ahead

Further tuning the surface chemistry will lead to a decay-dynamics at the picosecond time scale: to this aim, the influence of chalcogenide-rich ligands (e.g. thiols and thiol-containing polymers) or cation-rich ligands (e.g. cadmium or zinc halides or carboxylates) on the decay dynamics will be thoroughly studied. Thus, a novel core-shell system based on CdTe nanoplatelets would prove to be the ideal candidates for ionization radiation detection and scintillator technologies. This work however, is under progress, the challenge being faced at this point of time is related to the synthesis of defect free, optically high yielding CdTe NPs. The NPs synthesized thus far, suffer from extremely low emission efficiency and large scattering background, and high surface defect interference. Different approaches can be employed to rectify these issues. Heterostructuring, core-shell synthesis may prove to be a very useful ally to enhance the emission efficiency and also to induce Stokes shift. Shelling with a wide band gap material like CdS or ZnS through c-ALD technique is a viable option. However, given the large atomic radii and low reactivity of Te, it might be a challenge. Doping and

alloying on the other hand may prove to be a more viable option at this point. Doping these CdTe NPs with metal impurities like Ag or Cu can fill the already present surface defects introduce intraband defect levels thus increasing PL efficiency. Alloying with Se also yields improved emission efficiency. The other challenge of large scattering background can be rectified by synthesizing NPs of smaller lateral dimensions. This may be accomplished by further studying, in depth, the impact of different carboxylic chains involved in precursors, their concentrations and reaction parameters and kinetics.

Conclusions

During the last three years of my learning and research, thanks to the exceptionally favourable optoelectronic properties of colloidal nanostructures and more importantly, thanks to the state of the art chemistry and spectroscopy facilities in Advanced photophysics of molecular semiconductors lab headed by Prof. Sergio Brovelli, Prof. Francesco Meinardi and Prof. Angelo Monguzzi and through efficient collaborations fostered with other research groups over the years, I was presented with a remarkable opportunity to study the fundamental aspects of synthesis and photophysics in these nanostructures. During the discussed PhD studies, I focused my research in understanding such NC systems with unparalleled potential in photon management technologies such as Luminescent Solar Concentrators, solar cells, LASERs, LEDs and other devices of paramount significance to the humankind.

Through the course of this work, I had the privilege to learn and use colloidal synthesis and various advanced spectroscopic techniques reported in the previous chapters to study and report these nanostructures, thus trying to elucidate the fundamental photophysics involved, in an attempt to be used for technological advancement.

In chapter 2, I studied stoichiometric $CuInS_2$ NCs through the combination of optical and magneto-optical experiments as a function of size and temperature and it was revealed, for the first time, the spectroscopic signatures predicted for the excitonic photophysics in I–III–VI_2 NCs. In agreement with effective mass calculations, measurements showed quadratic dependence of the global Stokes shift and the radiative decay rate on the particle size, thus strongly supporting the theory by Efros and co-workers. Further proof of the underlying photophysics in these NCs was provided by time-resolved PL measurements performed below 50 K revealing for the first time, the dynamic signature of emission originating from a lower-lying dark-like exciton and magnetic circular dichroism experiments showing temperature independent MCD perfectly reproduced by the linear Zeeman splitting function. The particle size dependent stokes shift and reabsorption losses were studied and based on such theoretical guidelines provided by Monte-Carlo simulations, practical large-area LSC devices were fabricated by embedding the optimal stoichiometric $CuInS_2$ NCs into mass polymerized PMMA waveguides resulting in large area LSC device with a record OPE of 6.8%. This work

was published in the scientific journal "Advanced Functional Materials" (https://doi.org/10.1002/adfm.201906629)

Moving on from intrinsic systems, I studied the fundamental photophysics in impurity doped NC systems. Here I reported different studies on electronically doped II-VI NCs and substitutionally doped perovskite NCs. A novel quantized doping approach was employed to produce homogenous colloidal NCs electronically doped with gold impurities reported for the first time till date where it was showcased that each NC contained precisely seven electronic impurities. Structural, spectroscopic, and magneto-optical investigations trace a comprehensive picture of the physical processes involved, resulting from the exact doping level of the NCs. The results thus highlighted in chapter 3 shows strong photoinduced magnetism and diluted magnetic semiconductor behavior revealing the contribution of individual paramagnetic impurities to the macroscopic magnetism of the NCs coupled with the fact that this doping approach can be applied to different monometallic or alloyed clusters brings us closer to realising their potential to be exploited for applications in quantum and spintronic devices. This chapter was contributed as a journal article and was published in "ACS Nano Letters" (https://doi.org/10.1021/acs.nanolett.8b04904)

In chapter 4, I reported the results of spectroscopic studies conducted on manganese-doped $CsPbCl_3$ PNCs at controlled excitation density and temperature revealing a two-step process involving the initial localization of band-edge excitons in a shallow trap state that mediates the sensitization of the dopants and repopulates the band-edge by thermally activated back-transfer. This trap-mediated process was shown to dominate the photophysics for temperatures above 70 K. However, for $T < 70$ K, the sensitization seems to become barrierless possibly due to structural transitions as was supported by the results from ESR and optical absorption measurements as a function of temperature. These results demystify some anomalous behaviors of the exciton-to-dopant energy transfer mechanisms in PNCs and highlight that the photophysics of dopant colour centers is affected by the defect tolerant nature of perovskite materials in strikingly different ways than in more traditional chalcogenide NCs. This chapter was contributed as a journal article and was published in "ACS Energy Letters" (https://doi.org/10.1021/acsenergylett.8b02052)

Finally, in chapter 5, I outline my ongoing work on colloidal two-dimensional CdTe nanoplatelet systems. Resulting from strong quantum confinement in only one direction and the large lateral size, the CdTe nanoplatelets exhibit large exciton binding energy, giant oscillator strength, narrow emission, large absorption cross-section, suppressed Auger recombination, and large optical gain. Here, I also report some very interesting preliminary spectroscopic data that presents these NC systems at great heed with respect to their application in lasing technology and in Ultrafast radiation detection applications. However, this work on CdTe NPs is still in progress and props up different challenges from synthesis point of view. The challenge being faced at this point of time is related to the synthesis of defect free, optically high yielding and scatter free, lateral dimensions controllable CdTe NPs. The NPs synthesized thus far, suffer from extremely low emission efficiency, large scattering background, and high surface defect interference. As mentioned in the chapter though, various approaches may be employed to address these issues and warrants a specialized study by itself to overcome them, although preliminary results suggest a very promising and exciting avenues for this class of nanostructures.

References

1. Nasilowski, M.; Mahler, B.; Lhuillier, E.; Ithurria, S.; Dubertret, B. *Chemical reviews* **2016,** 116, (18), 10934-10982.
2. Pankove, J. I. In *Optical Processes in Semiconductors*, Dover, New York, 1971; Dover, New York, p 34.
3. Gross, E. *Il Nuovo Cimento (1955-1965)* **1956,** 3, (4), 672-701.
4. Yoffe, A. D. *Advances in Physics* **1993,** 42, (2), 173-262.
5. Ekimov, A. I.; Onushchenko, A. A. *Jetp Lett* **1981,** 34, (6), 345-349.
6. Ekimov, A.; Onuschenko, A.; Tsekhomskii, V. *Sov. Glass Phys. Chem* **1980,** 6, 511-512.
7. Golubkov, V.; Ekimov, A.; Onushchenko, A.; Tsekhomskii, V. *Fiz. Khim. Stekla* **1981,** 7, (4), 397-401.
8. Borrelli, N. F.; Hall, D.; Holland, H.; Smith, D. *Journal of Applied Physics* **1987,** 61, (12), 5399-5409.
9. Henglein, A. *Berichte der Bunsengesellschaft für physikalische Chemie* **1982,** 86, (4), 301-305.
10. Henglein, A. *Pure and Applied Chemistry* **1984,** 56, (9), 1215-1224.
11. Rossetti, R.; Ellison, J.; Gibson, J.; Brus, L. E. *The Journal of chemical physics* **1984,** 80, (9), 4464-4469.
12. Itoh T, K. T. J. L.; 120–22. *J. Lumin.* **1984,** 31/32, 120–22.
13. Vandyshev, Y. V.; Dneprovskii, V.; Klimov, V. *JETP letters* **1991,** 53, (6), 314-318.
14. Ekimov, A. I.; Hache, F.; Schanne-Klein, M.; al; Ricard, D.; Flytzanis, C.; Kudryavtsev, I.; Yazeva, T.; Rodina, A.; Efros, A. L. *JOSA B* **1993,** 10, (1), 100-107.
15. Klein, M.; Hache, F.; Ricard, D.; Flytzanis, C. *Physical Review B* **1990,** 42, (17), 11123.
16. Nomura, S.; Kobayashi, T. *Physical Review B* **1992,** 45, (3), 1305.
17. Machol, J. L.; Wise, F. W.; Patel, R. C.; Tanner, D. B. *Physical Review B* **1993,** 48, (4), 2819.
18. Trallero-Giner, C.; Debernardi, A.; Cardona, M.; Menendez-Proupin, E.; Ekimov, A. *Physical Review B* **1998,** 57, (8), 4664.
19. Woggon, U.; Giessen, H.; Gindele, F.; Wind, O.; Fluegel, B.; Peyghambarian, N. *Physical Review B* **1996,** 54, (24), 17681.
20. Klimov, V. I.; McBranch, D. W. *Physical Review Letters* **1998,** 80, (18), 4028.
21. Olbright, G. R.; Peyghambarian, N.; Koch, S. W.; Banyai, L. *Optics letters* **1987,** 12, (6), 413-415.
22. Roussignol, P.; Kull, M.; Ricard, D.; De Rougemont, F.; Frey, R.; Flytzanis, C. *Applied physics letters* **1987,** 51, (23), 1882-1884.
23. Dneprovskii, V.; Efros, A. L.; Ekimov, A.; Klimov, V. I.; Kudriavtsev, I.; Novikov, M. *Solid State Communications* **1990,** 74, (7), 555-557.
24. Klimov, V. I.; McBranch, D. W. *Physical Review B* **1997,** 55, (19), 13173.
25. Vandyshev, Y. V.; Dneprovskii, V.; Klimov, V.; Okorokov, D. *Jetp Lett* **1991,** 54, (8), 442.

26. Klimov, V. I., Ed., *Nanocrystal Quantum Dots*. Taylor & Francis

2009

Vol. 2nd ed.

27. Pietryga, J. M.; Park, Y.-S.; Lim, J.; Fidler, A. F.; Bae, W. K.; Brovelli, S.; Klimov, V. I. *Chemical reviews* **2016,** 116, (18), 10513-10622.

28. Murray, C.; Norris, D. J.; Bawendi, M. G. *Journal of the American Chemical Society* **1993,** 115, (19), 8706-8715.

29. Hines, M. A.; Guyot-Sionnest, P. *The Journal of Physical Chemistry* **1996,** 100, (2), 468-471.

30. Kim, S.; Fisher, B.; Eisler, H.-J.; Bawendi, M. *Journal of the American Chemical Society* **2003,** 125, (38), 11466-11467.

31. Balet, L.; Ivanov, S.; Piryatinski, A.; Achermann, M.; Klimov, V. *Nano Letters* **2004,** 4, (8), 1485-1488.

32. Ivanov, S. A.; Nanda, J.; Piryatinski, A.; Achermann, M.; Balet, L. P.; Bezel, I. V.; Anikeeva, P. O.; Tretiak, S.; Klimov, V. I. *The Journal of Physical Chemistry B* **2004,** 108, (30), 10625-10630.

33. Peng, X.; Manna, L.; Yang, W.; Wickham, J.; Scher, E.; Kadavanich, A.; Alivisatos, A. P. *Nature* **2000,** 404, (6773), 59-61.

34. Manna, L.; Scher, E. C.; Alivisatos, A. P. *Journal of the American Chemical Society* **2000,** 122, (51), 12700-12706.

35. Nirmal, M.; Norris, D. J.; Kuno, M.; Bawendi, M. G.; Efros, A. L.; Rosen, M. *Physical review letters* **1995,** 75, (20), 3728.

36. Norris, D. J.; Efros, A. L.; Rosen, M.; Bawendi, M. G. *Physical Review B* **1996,** 53, (24), 16347.

37. Efros, A. L.; Kharchenko, V.; Rosen, M. *Solid State Communications* **1995,** 93, (4), 281-284.

38. Peterson, M. D.; Cass, L. C.; Harris, R. D.; Edme, K.; Sung, K.; Weiss, E. A. *Annual review of physical chemistry* **2014,** 65, 317-339.

39. Cooney, R. R.; Sewall, S. L.; Dias, E. A.; Sagar, D.; Anderson, K. E.; Kambhampati, P. *Physical Review B* **2007,** 75, (24), 245311.

40. Crooker, S.; Barrick, T.; Hollingsworth, J.; Klimov, V. *Applied Physics Letters* **2003,** 82, (17), 2793-2795.

41. Klimov, V. I.; Mikhailovsky, A. A.; McBranch, D.; Leatherdale, C. A.; Bawendi, M. G. *Science* **2000,** 287, (5455), 1011-1013.

42. Fisher, B.; Caruge, J.-M.; Chan, Y.-T.; Halpert, J.; Bawendi, M. G. *Chemical physics* **2005,** 318, (1-2), 71-81.

43. Pandey, A.; Guyot-Sionnest, P., Multicarrier recombination in colloidal quantum dots. American Institute of Physics: 2007.

44. Nirmal, M.; Dabbousi, B. O.; Bawendi, M. G.; Macklin, J.; Trautman, J.; Harris, T.; Brus, L. E. *Nature* **1996,** 383, (6603), 802-804.

45. Empedocles, S. A.; Norris, D. J.; Bawendi, M. *Physical review letters* **1996,** 77, (18), 3873.

46. Blanton, S. A.; Hines, M. A.; Guyot-Sionnest, P. *Applied Physics Letters* **1996,** 69, (25), 3905-3907.

47. Kuno, M.; Fromm, D. P.; Hamann, H. F.; Gallagher, A.; Nesbitt, D. J. *The journal of chemical physics* **2000,** 112, (7), 3117-3120.

48. Colvin, V. L.; Schlamp, M. C.; Alivisatos, A. P. *Nature* **1994,** 370, (6488), 354-357.

49. Mattoussi, H.; Radzilowski, L. H.; Dabbousi, B. O.; Thomas, E. L.; Bawendi, M. G.; Rubner, M. F. *Journal of Applied Physics* **1998,** 83, (12), 7965-7974.

50. Jang, E.; Jun, S.; Jang, H.; Lim, J.; Kim, B.; Kim, Y. *Advanced materials* **2010,** 22, (28), 3076-3080.

51. Greenham, N. C.; Peng, X.; Alivisatos, A. P. *Physical review B* **1996,** 54, (24), 17628.

52. Nozik, A. J. *Physica E: Low-dimensional Systems and Nanostructures* **2002,** 14, (1-2), 115-120.

53. Sargent, E. H. *Nature photonics* **2012,** 6, (3), 133-135.

54. Luther, J. M.; Gao, J.; Lloyd, M. T.; Semonin, O. E.; Beard, M. C.; Nozik, A. J. *Advanced materials* **2010,** 22, (33), 3704-3707.

55. Kim, G.-H.; García de Arquer, F. P.; Yoon, Y. J.; Lan, X.; Liu, M.; Voznyy, O.; Yang, Z.; Fan, F.; Ip, A. H.; Kanjanaboos, P. *Nano letters* **2015,** 15, (11), 7691-7696.

56. Lan, X.; Voznyy, O.; García de Arquer, F. P.; Liu, M.; Xu, J.; Proppe, A. H.; Walters, G.; Fan, F.; Tan, H.; Liu, M. *Nano letters* **2016,** 16, (7), 4630-4634.

57. Semonin, O. E.; Luther, J. M.; Choi, S.; Chen, H.-Y.; Gao, J.; Nozik, A. J.; Beard, M. C. *Science* **2011,** 334, (6062), 1530-1533.

58. Böhm, M. L.; Jellicoe, T. C.; Tabachnyk, M.; Davis, N. J.; Wisnivesky-Rocca-Rivarola, F.; Ducati, C.; Ehrler, B.; Bakulin, A. A.; Greenham, N. C. *Nano letters* **2015,** 15, (12), 7987-7993.

59. Bomm, J.; Büchtemann, A.; Chatten, A. J.; Bose, R.; Farrell, D. J.; Chan, N. L.; Xiao, Y.; Slooff, L. H.; Meyer, T.; Meyer, A. *Solar Energy Materials and Solar Cells* **2011,** 95, (8), 2087-2094.

60. Erickson, C. S.; Bradshaw, L. R.; McDowall, S.; Gilbertson, J. D.; Gamelin, D. R.; Patrick, D. L. *ACS nano* **2014,** 8, (4), 3461-3467.

61. Meinardi, F.; Colombo, A.; Velizhanin, K. A.; Simonutti, R.; Lorenzon, M.; Beverina, L.; Viswanatha, R.; Klimov, V. I.; Brovelli, S. *Nature Photonics* **2014,** 8, (5), 392-399.

62. Bronstein, N. D.; Li, L.; Xu, L.; Yao, Y.; Ferry, V. E.; Alivisatos, A. P.; Nuzzo, R. G. *Acs Nano* **2014,** 8, (1), 44-53.

63. Bruchez, M.; Moronne, M.; Gin, P.; Weiss, S.; Alivisatos, A. P. *science* **1998,** 281, (5385), 2013-2016.

64. Chan, W. C.; Nie, S. *Science* **1998,** 281, (5385), 2016-2018.

65. Medintz, I. L.; Uyeda, H. T.; Goldman, E. R.; Mattoussi, H. *Nature materials* **2005,** 4, (6), 435-446.

66. Murray, C. B.; Kagan, a. C.; Bawendi, M. *Annual review of materials science* **2000,** 30, (1), 545-610.

67. LaMer, V. K.; Dinegar, R. H. *Journal of the American Chemical Society* **1950,** 72, (11), 4847-4854.

68. Murray, C. B.; Sun, S.; Gaschler, W.; Doyle, H.; Betley, T. A.; Kagan, C. R. *IBM Journal of Research and Development* **2001,** 45, (1), 47-56.

69. Efros AlL, E. A. *Sov. Phys. Semicond* **1982,** 16, 772–78.

70. Brus, L. E. *The Journal of chemical physics* **1983,** 79, (11), 5566-5571.

71. Ashcroft, N.; Mermin, N. *There is no corresponding record for this reference.[Google Scholar]*.

72. Ekimov AI, O. A. *Sov. Phys. Semicond* **1982**, (16), 775–78.

73. Ekimov AI, O. A., Plukhin AG, Efros AlL. . *Sov. Phys. JETP* **1985**, (61), 891–97.

74. Itoh, T.; Iwabuchi, Y.; Kirihara, T. *physica status solidi (b)* **1988,** 146, (2), 531-543.

75. Ekimov AI, O. A., Efros AlL. *JETP Lett* **1986**, (43), 376–79.

76. Ekimov AI, O. A., Shumilov SK, Efros AlL. *Sov. Tech. Phys. Lett.* **1987**, (13), 115–16.

77. Ekimov, A.; Efros, A. L.; Ivanov, M.; Onushchenko, A.; Shumilov, S. *Solid State Communications* **1989,** 69, (5), 565-568.

78. Ekimov, A.; Onushchenko, A. *JETP lett* **1984,** 40, (8), 1136-1139.

79. Efros, A. L.; Efros, A. L. *Soviet Physics Semiconductors-Ussr* **1982,** 16, (7), 772-775.

80. Grigoryan, G.; Rodina, A.; Efros, A. L. *Soviet physics. Solid state* **1990,** 32, (12), 2037-2042.

81. Koch, S. W.; Hu, Y.; Fluegel, B.; Peyghambarian, N. *Journal of crystal growth* **1992,** 117, (1-4), 592-597.

82. Xia, J.-B. *Physical Review B* **1989,** 40, (12), 8500.

83. Norris, D. J.; Bawendi, M. *Physical Review B* **1996,** 53, (24), 16338.

84. Lippens, P.; Lannoo, M. *Physical Review B* **1990,** 41, (9), 6079.

85. Rodina, A. V.; Efros, A. L. *Physical Review B* **2016,** 93, (15), 155427.

86. Lee, J. R.; Meulenberg, R. W.; Hanif, K. M.; Mattoussi, H.; Klepeis, J. E.; Terminello, L. J.; van Buuren, T. *Physical review letters* **2007,** 98, (14), 146803.

87. Meulenberg, R. W.; Lee, J. R.; Wolcott, A.; Zhang, J. Z.; Terminello, L. J.; Van Buuren, T. *ACS nano* **2009,** 3, (2), 325-330.

88. Bawendi, M. G.; Carroll, P.; Wilson, W. L.; Brus, L. *The Journal of Chemical Physics* **1992,** 96, (2), 946-954.

89. Kuno, M.; Nirmal, M.; Bawendi, M.; Efros, A.; Rosen, M. *The Journal of chemical physics* **1998,** 108, (10), 4242-4247.

90. Kulakovskii, V.; Bacher, G.; Weigand, R.; Kümmell, T.; Forchel, A.; Borovitskaya, E.; Leonardi, K.; Hommel, D. *Physical Review Letters* **1999,** 82, (8), 1780.

91. Gupta, J.; Awschalom, D.; Efros, A. L.; Rodina, A. *Physical Review B* **2002,** 66, (12), 125307.

92. Dabbousi, B. O.; Rodriguez-Viejo, J.; Mikulec, F. V.; Heine, J. R.; Mattoussi, H.; Ober, R.; Jensen, K. F.; Bawendi, M. G. *The Journal of Physical Chemistry B* **1997,** 101, (46), 9463-9475.

93. Jacobsohn, M.; Banin, U. *The Journal of Physical Chemistry B* **2000,** 104, (1), 1-5.

94. Johnston-Halperin, E.; Awschalom, D.; Crooker, S.; Efros, A. L.; Rosen, M.; Peng, X.; Alivisatos, A. *Physical Review B* **2001,** 63, (20), 205309.

95. Kucur, E.; Riegler, J.; Urban, G. A.; Nann, T. *The Journal of chemical physics* **2003,** 119, (4), 2333-2337.

96. Brokmann, X.; Messin, G.; Desbiolles, P.; Giacobino, E.; Dahan, M.; Hermier, J. *New Journal of Physics* **2004,** 6, (1), 99.

97. Cretí, A.; Anni, M.; Rossi, M. Z.; Lanzani, G.; Leo, G.; Della Sala, F.; Manna, L.; Lomascolo, M. *Physical Review B* **2005,** 72, (12), 125346.

98. Furis, M.; Hollingsworth, J. A.; Klimov, V. I.; Crooker, S. A. *The Journal of Physical Chemistry B* **2005,** 109, (32), 15332-15338.

99. Furis, M.; Htoon, H.; Petruska, M.; Klimov, V.; Barrick, T.; Crooker, S. *Physical Review B* **2006,** 73, (24), 241313.

100. Inamdar, S. N.; Ingole, P. P.; Haram, S. K. *ChemPhysChem* **2008,** 9, (17), 2574-2579.

101. Htoon, H.; Crooker, S.; Furis, M.; Jeong, S.; Efros, A. L.; Klimov, V. I. *Physical Review Letters* **2009,** 102, (1), 017402.

102. Liu, L.; Zhuang, Z.; Xie, T.; Wang, Y.-G.; Li, J.; Peng, Q.; Li, Y. *Journal of the American Chemical Society* **2009,** 131, (45), 16423-16429.

103. Hellwege, K. H., *Landolt-Bornstein Numerical Data and Functional Relationships*

in Science and Technology, New Series. Springer-Verlag: Berlin, 1982; Vol. Vol. 17b.

104. Baldereschi, A.; Lipari, N. O. *Physical Review B* **1973,** 8, (6), 2697.

105. Gelmont, B.; Dyakonov, M. *Sov. Phys. Semicond* **1905,** 5, 1972.

106. Lipari, N. O. a. B., A. *Phys. Rev. Lett.* **1973,** 42, 1660.

107. Vahala, K. J.; Sercel, P. C. *Physical review letters* **1990,** 65, (2), 239.

108. Sercel, P. C.; Vahala, K. J. *Physical Review B* **1990,** 42, (6), 3690.

109. Grigoryan, G.; Kazaryan, E. *Sov. Phys.–Solid State* 32, 1031.

110. Efros, A. L.; Rosen, M.; Kuno, M.; Nirmal, M.; Norris, D. J.; Bawendi, M. *Physical Review B* **1996,** 54, (7), 4843.

111. Efros, A. L.; Rodina, A. V. *Physical Review B* **1993,** 47, (15), 10005.

112. Calcott, P.; Nash, K.; Canham, L.; Kane, M.; Brumhead, D. *Journal of luminescence* **1993,** 57, (1-6), 257-269.

113. Takagahara, T. *Physical Review B* **1993,** 47, (8), 4569.

114. Chamarro, M.; Gourdon, C.; Lavallard, P.; Ekimov, A. I. *Japanese Journal of Applied Physics* **1995,** 34, (S1), 12.

115. Nomura, S.; Segawa, Y.; Kobayashi, T. *Physical Review B* **1994,** 49, (19), 13571.

116. Henry, C.; Nassau, K. *Physical Review B* **1970,** 1, (4), 1628.

117. O'neil, M.; Marohn, J.; McLendon, G. *Journal of Physical Chemistry* **1990,** 94, (10), 4356-4363.

118. Eychmüller, A.; Hässelbarth, A.; Katsikas, L.; Weller, H. *Berichte der Bunsengesellschaft für physikalische Chemie* **1991,** 95, (1), 79-84.

119. Nirmal, M.; Murray, C.; Bawendi, M. *Physical Review B* **1994,** 50, (4), 2293.

120. Krumer, Z.; Pera, S. J.; van Dijk-Moes, R. J.; Zhao, Y.; de Brouwer, A. F.; Groeneveld, E.; van Sark, W. G.; Schropp, R. E.; de Mello Donegá, C. *Solar energy materials and solar cells* **2013,** 111, 57-65.

121. Giebink, N. C.; Wiederrecht, G. P.; Wasielewski, M. R. *Nature Photonics* **2011,** 5, (11), 694-701.

122. Batchelder, J.; Zewai, A.; Cole, T. *Applied Optics* **1979,** 18, (18), 3090-3110.

123. Mulder, C. L.; Reusswig, P. D.; Beyler, A.; Kim, H.; Rotschild, C.; Baldo, M. *Optics express* **2010,** 18, (101), A91-A99.

124. van Sark, W. G. *Renewable Energy* **2013,** 49, 207-210.

125. Wang, T.; Zhang, J.; Ma, W.; Luo, Y.; Wang, L.; Hu, Z.; Wu, W.; Wang, X.; Zou, G.; Zhang, Q. *Solar Energy* **2011,** 85, (11), 2571-2579.

126. Sanguineti, A.; Monguzzi, A.; Vaccaro, G.; Meinardi, F.; Ronchi, E.; Moret, M.; Cosentino, U.; Moro, G.; Simonutti, R.; Mauri, M. *Physical Chemistry Chemical Physics* **2012,** 14, (18), 6452-6455.

127. Debije, M. G.; Verbunt, P. P.; Nadkarni, P. J.; Velate, S.; Bhaumik, K.; Nedumbamana, S.; Rowan, B. C.; Richards, B. S.; Hoeks, T. L. *Applied Optics* **2011,** 50, (2), 163-169.

128. Desmet, L.; Ras, A.; De Boer, D.; Debije, M. *Optics Letters* **2012,** 37, (15), 3087-3089.

129. Debije, M. G.; Verbunt, P. P. *Advanced Energy Materials* **2012,** 2, (1), 12-35.

130. Chatten, A.; Barnham, K.; Buxton, B.; Ekins-Daukes, N.; Malik, M. *Semiconductors* **2004,** 38, (8), 909-917.

131. Meinardi, F.; McDaniel, H.; Carulli, F.; Colombo, A.; Velizhanin, K. A.; Makarov, N. S.; Simonutti, R.; Klimov, V. I.; Brovelli, S. *Nature nanotechnology* **2015,** 10, (10), 878-885.

132. Knowles, K. E.; Kilburn, T. B.; Alzate, D. G.; McDowall, S.; Gamelin, D. R. *Chemical Communications* **2015,** 51, (44), 9129-9132.

133. Purcell-Milton, F.; Gun'ko, Y. K. *Journal of Materials Chemistry* **2012,** 22, (33), 16687-16697.

134. Shcherbatyuk, G.; Inman, R.; Wang, C.; Winston, R.; Ghosh, S. *Applied Physics Letters* **2010,** 96, (19), 191901.

135. Hyldahl, M. G.; Bailey, S. T.; Wittmershaus, B. P. *Solar Energy* **2009,** 83, (4), 566-573.

136. Li, L.; Pandey, A.; Werder, D. J.; Khanal, B. P.; Pietryga, J. M.; Klimov, V. I. *Journal of the American Chemical Society* **2011,** 133, (5), 1176-1179.

137. Buck, M. R.; Bondi, J. F.; Schaak, R. E. *Nature chemistry* **2012,** 4, (1), 37-44.

138. Semonin, O. E.; Johnson, J. C.; Luther, J. M.; Midgett, A. G.; Nozik, A. J.; Beard, M. C. *The journal of physical chemistry letters* **2010,** 1, (16), 2445-2450.

139. Meinardi, F.; Akkerman, Q. A.; Bruni, F.; Park, S.; Mauri, M.; Dang, Z.; Manna, L.; Brovelli, S. *ACS energy letters* **2017,** 2, (10), 2368-2377.

140. Otto, T.; Müller, M.; Mundra, P.; Lesnyak, V.; Demir, H. V.; Gaponik, N.; Eychmüller, A. *Nano letters* **2012,** 12, (10), 5348-5354.

141. Gallagher, S.; Norton, B.; Eames, P. *Solar Energy* **2007,** 81, (6), 813-821.

142. Bomm, J.; Büchtemann, A.; Fiore, A.; Manna, L.; Nelson, J. H.; Hill, D.; van Sark, W. G. *Beilstein journal of nanotechnology* **2010,** 1, (1), 94-100.

143. Brovelli, S.; Schaller, R. D.; Crooker, S.; García-Santamaría, F.; Chen, Y.; Viswanatha, R.; Hollingsworth, J. A.; Htoon, H.; Klimov, V. I. *Nature communications* **2011,** 2, (1), 1-8.

144. Reiss, P.; Protiere, M.; Li, L. *small* **2009,** 5, (2), 154-168.

145. Howes, P. D.; Chandrawati, R.; Stevens, M. M. *Science* **2014,** 346, (6205).

146. Mura, S.; Nicolas, J.; Couvreur, P. *Nature materials* **2013,** 12, (11), 991-1003.

147. Henglein, A.; Gutierrez, M.; Weller, K.; Fojtik, A.; Jirkovský, J. *Berichte der Bunsengesellschaft für physikalische Chemie* **1989,** 93, (5), 593-600.

148. Zhou, H.; Honma, I.; Komiyama, H.; Haus, J. W. *The Journal of Physical Chemistry* **1993,** 97, (4), 895-901.

149. Weller, H.; Koch, U.; Gutierrez, M.; Henglein, A. *Berichte der Bunsengesellschaft für physikalische Chemie* **1984,** 88, (7), 649-656.

150. Spanhel, L.; Weller, H.; Fojtik, A.; Henglein, A. *Berichte der Bunsengesellschaft für physikalische Chemie* **1987,** 91, (2), 88-94.

151. Oron, D.; Kazes, M.; Banin, U. *Physical Review B* **2007,** 75, (3), 035330.

152. Piryatinski, A.; Ivanov, S. A.; Tretiak, S.; Klimov, V. I. *Nano letters* **2007,** 7, (1), 108-115.

153. Danek, M.; Jensen, K. F.; Murray, C. B.; Bawendi, M. G. *Chemistry of Materials* **1996,** 8, (1), 173-180.

154. Peng, X.; Schlamp, M. C.; Kadavanich, A. V.; Alivisatos, A. P. *Journal of the American Chemical Society* **1997,** 119, (30), 7019-7029.

155. Pietryga, J. M.; Werder, D. J.; Williams, D. J.; Casson, J. L.; Schaller, R. D.; Klimov, V. I.; Hollingsworth, J. A. *Journal of the American Chemical Society* **2008,** 130, (14), 4879-4885.

156. De Geyter, B.; Justo, Y.; Moreels, I.; Lambert, K.; Smet, P. F.; Van Thourhout, D.; Houtepen, A. J.; Grodzinska, D.; de Mello Donega, C.; Meijerink, A. *ACS nano* **2011,** 5, (1), 58-66.

157. Wu, K.; Song, N.; Liu, Z.; Zhu, H.; Rodríguez-Córdoba, W.; Lian, T. *The Journal of Physical Chemistry A* **2013,** 117, (32), 7561-7570.

158. de Mello Donega, C. *Chemical Society Reviews* **2011,** 40, (3), 1512-1546.

159. Christodoulou, S.; Vaccaro, G.; Pinchetti, V.; De Donato, F.; Grim, J.; Casu, A.; Genovese, A.; Vicidomini, G.; Diaspro, A.; Brovelli, S. *Journal of Materials Chemistry C* **2014,** 2, (17), 3439-3447.

160. Nasilowski, M.; Spinicelli, P.; Patriarche, G.; Dubertret, B. *Nano letters* **2015,** 15, (6), 3953-3958.

161. Brovelli, S.; Bae, W. K.; Galland, C.; Giovanella, U.; Meinardi, F.; Klimov, V. I. *Nano letters* **2014,** 14, (2), 486-494.

162. Brovelli, S.; Bae, W. K.; Meinardi, F.; Santiago González, B.; Lorenzon, M.; Galland, C.; Klimov, V. I. *Nano letters* **2014,** 14, (7), 3855-3863.

163. Galland, C.; Brovelli, S.; Bae, W. K.; Padilha, L. A.; Meinardi, F.; Klimov, V. I. *Nano letters* **2013,** 13, (1), 321-328.

164. Cassette, E.; Mahler, B.; Guigner, J.-M.; Patriarche, G.; Dubertret, B.; Pons, T. *ACS nano* **2012,** 6, (8), 6741-6750.

165. Rainò, G.; Stöferle, T.; Moreels, I.; Gomes, R.; Kamal, J. S.; Hens, Z.; Mahrt, R. F. *ACS nano* **2011,** 5, (5), 4031-4036.

166. Christodoulou, S.; Rajadell, F.; Casu, A.; Vaccaro, G.; Grim, J. Q.; Genovese, A.; Manna, L.; Climente, J. I.; Meinardi, F.; Raino, G. *Nature communications* **2015,** 6, (1), 1-8.

167. Sitt, A.; Salant, A.; Menagen, G.; Banin, U. *Nano letters* **2011,** 11, (5), 2054-2060.

168. Talapin, D. V.; Nelson, J. H.; Shevchenko, E. V.; Aloni, S.; Sadtler, B.; Alivisatos, A. P. *Nano letters* **2007,** 7, (10), 2951-2959.

169. Kim, M. R.; Miszta, K.; Povia, M.; Brescia, R.; Christodoulou, S.; Prato, M.; Marras, S.; Manna, L. *ACS nano* **2012,** 6, (12), 11088-11096.

170. Mahler, B.; Nadal, B.; Bouet, C.; Patriarche, G.; Dubertret, B. *Journal of the American Chemical Society* **2012,** 134, (45), 18591-18598.

171. Tessier, M.; Mahler, B.; Nadal, B.; Heuclin, H.; Pedetti, S.; Dubertret, B. *Nano letters* **2013,** 13, (7), 3321-3328.

172. Tessier, M. D.; Spinicelli, P.; Dupont, D.; Patriarche, G.; Ithurria, S.; Dubertret, B. *Nano letters* **2014,** 14, (1), 207-213.

173. Javaux, C.; Mahler, B.; Dubertret, B.; Shabaev, A.; Rodina, A.; Efros, A. L.; Yakovlev, D.; Liu, F.; Bayer, M.; Camps, G. *Nature nanotechnology* **2013,** 8, (3), 206-212.

174. Penn, R. L.; Banfield, J. F. *Science* **1998,** 281, (5379), 969-971.

175. Erwin, S. C.; Zu, L.; Haftel, M. I.; Efros, A. L.; Kennedy, T. A.; Norris, D. J. *Nature* **2005,** 436, (7047), 91-94.

176. Norris, D. J.; Efros, A. L.; Erwin, S. C. *Science* **2008,** 319, (5871), 1776-1779.

177. Norris, D. J.; Yao, N.; Charnock, F. T.; Kennedy, T. A. *Nano Letters* **2001,** 1, (1), 3-7.

178. Liu, J.; Zhao, Q.; Liu, J. L.; Wu, Y. S.; Cheng, Y.; Ji, M. W.; Qian, H. M.; Hao, W. C.; Zhang, L. J.; Wei, X. J. *Advanced Materials* **2015,** 27, (17), 2753-2761.

179. Chen, D.; Viswanatha, R.; Ong, G. L.; Xie, R.; Balasubramaninan, M.; Peng, X. *Journal of the American Chemical Society* **2009,** 131, (26), 9333-9339.

180. Bryan, J. D.; Gamelin, D. R. *Prog. Inorg. Chem* **2005,** 54, (47), 47-126.

181. Corrado, C.; Hawker, M.; Livingston, G.; Medling, S.; Bridges, F.; Zhang, J. Z. *Nanoscale* **2010,** 2, (7), 1213-1221.

182. Gul, S.; Cooper, J. K.; Corrado, C.; Vollbrecht, B.; Bridges, F.; Guo, J.; Zhang, J. Z. *The Journal of Physical Chemistry C* **2011,** 115, (43), 20864-20875.

183. Jana, S.; Srivastava, B. B.; Jana, S.; Bose, R.; Pradhan, N. *The journal of physical chemistry letters* **2012,** 3, (18), 2535-2540.

184. Meulenberg, R. W.; van Buuren, T.; Hanif, K. M.; Willey, T. M.; Strouse, G. F.; Terminello, L. J. *Nano Letters* **2004,** 4, (11), 2277-2285.

185. Panda, S. K.; Hickey, S. G.; Demir, H. V.; Eychmüller, A. *Angewandte Chemie International Edition* **2011,** 50, (19), 4432-4436.

186. Pradhan, N.; Battaglia, D. M.; Liu, Y.; Peng, X. *Nano Letters* **2007,** 7, (2), 312-317.

187. Srivastava, B. B.; Jana, S.; Pradhan, N. *Journal of the American Chemical Society* **2011,** 133, (4), 1007-1015.

188. Stouwdam, J. W.; Janssen, R. A. *Advanced Materials* **2009,** 21, (28), 2916-2920.

189. Sahu, A.; Kang, M. S.; Kompch, A.; Notthoff, C.; Wills, A. W.; Deng, D.; Winterer, M.; Frisbie, C. D.; Norris, D. J. *Nano letters* **2012,** 12, (5), 2587-2594.

190. Bussian, D. A.; Crooker, S. A.; Yin, M.; Brynda, M.; Efros, A. L.; Klimov, V. I. *Nature Materials* **2009,** 8, (1), 35-40.

191. Viswanatha, R.; Brovelli, S.; Pandey, A.; Crooker, S. A.; Klimov, V. I. *Nano letters* **2011,** 11, (11), 4753-4758.

192. Pradhan, N.; Goorskey, D.; Thessing, J.; Peng, X. *Journal of the American Chemical Society* **2005,** 127, (50), 17586-17587.

193. Mocatta, D.; Cohen, G.; Schattner, J.; Millo, O.; Rabani, E.; Banin, U. *Science* **2011,** 332, (6025), 77-81.

194. Jana, S.; Srivastava, B. B.; Acharya, S.; Santra, P. K.; Jana, N. R.; Sarma, D.; Pradhan, N. *Chemical Communications* **2010,** 46, (16), 2853-2855.

195. Xie, R.; Peng, X. *Journal of the American Chemical Society* **2009,** 131, (30), 10645-10651.

196. Brovelli, S.; Galland, C.; Viswanatha, R.; Klimov, V. I. *Nano letters* **2012,** 12, (8), 4372-4379.

197. Pinchetti, V.; Di, Q.; Lorenzon, M.; Camellini, A.; Fasoli, M.; Zavelani-Rossi, M.; Meinardi, F.; Zhang, J.; Crooker, S. A.; Brovelli, S. *Nature Nanotechnology* **2018,** 13, (2), 145-151.

198. Capitani, C.; Pinchetti, V.; Gariano, G.; Santiago-González, B.; Santambrogio, C.; Campione, M.; Prato, M.; Brescia, R.; Camellini, A.; Bellato, F. *Nano Letters* **2019,** 19, (2), 1307-1317.

199. Grandhi, G. K.; Tomar, R.; Viswanatha, R. *ACS nano* **2012,** 6, (11), 9751-9763.

200. Broser, I.; Schulz, H. J. *Journal of The Electrochemical Society* **1961,** 108, (6), 545.

201. Peka, P.; Schulz, H.-J. *Physica B: Condensed Matter* **1994,** 193, (1), 57-65.

202. Stringfellow, G. B.; Bube, R. H. *Physical Review* **1968,** 171, (3), 903.

203. Avdonin, A.; Ivanova, G.; Nedeoglo, D.; Nedeoglo, N.; Sirkeli, V. *Physica B: Condensed Matter* **2005,** 365, (1-4), 217-224.

204. Chacham, H.; Alves, J.; De Siqueira, M. *Solid state communications* **1986,** 60, (5), 411-414.

205. Dean, P.; Fitzpatrick, B.; Bhargava, R. *Physical Review B* **1982,** 26, (4), 2016.

206. Poolton, N.; Davies, J.; Nicholls, J.; Fitzpatrick, B. *Journal of Physics C: Solid State Physics* **1987,** 20, (23), 3553.

207. Poolton, N.; Nicholls, J.; Davies, J. *Journal of Crystal Growth* **1988,** 86, (1-4), 609-614.

208. Magnea, N.; Bensahel, D.; Pautrat, J.; Pfister, J. *physica status solidi (b)* **1979,** 94, (2), 627-639.

209. Ochsenbein, S. T.; Gamelin, D. R. *Nature nanotechnology* **2011,** 6, (2), 112-115.

210. Viswanatha, R.; Pietryga, J. M.; Klimov, V. I.; Crooker, S. A. *Physical review letters* **2011,** 107, (6), 067402.

211. Tanabe, Y.; Sugano, S. *Journal of the Physical Society of Japan* **1954,** 9, (5), 766-779.

212. Beaulac, R.; Schneider, L.; Archer, P. I.; Bacher, G.; Gamelin, D. R. *Science* **2009,** 325, (5943), 973-976.

213. Rice, W.; Liu, W.; Pinchetti, V.; Yakovlev, D.; Klimov, V. I.; Crooker, S. *Nano letters* **2017,** 17, (5), 3068-3075.

214. Muckel, F.; Barrows, C. J.; Graf, A.; Schmitz, A.; Erickson, C. S.; Gamelin, D. R.; Bacher, G. *Nano letters* **2017,** 17, (8), 4768-4773.

215. Debnath, T.; Maiti, S.; Ghosh, H. N. *The Journal of Physical Chemistry Letters* **2016,** 7, (7), 1359-1367.

216. Beaulac, R.; Archer, P. I.; Ochsenbein, S. T.; Gamelin, D. R. *Advanced Functional Materials* **2008,** 18, (24), 3873-3891.

217. Begum, R.; Parida, M. R.; Abdelhady, A. L.; Murali, B.; Alyami, N. M.; Ahmed, G. H.; Hedhili, M. N.; Bakr, O. M.; Mohammed, O. F. *Journal of the American Chemical Society* **2017,** 139, (2), 731-737.

218. Guria, A. K.; Dutta, S. K.; Adhikari, S. D.; Pradhan, N. *ACS Energy Letters* **2017,** 2, (5), 1014-1021.

219. Zou, S.; Liu, Y.; Li, J.; Liu, C.; Feng, R.; Jiang, F.; Li, Y.; Song, J.; Zeng, H.; Hong, M. *Journal of the American Chemical Society* **2017,** 139, (33), 11443-11450.

220. Swarnkar, A.; Mir, W. J.; Nag, A. *ACS Energy Letters* **2018,** 3, (2), 286-289.

221. Yao, J.-S.; Ge, J.; Han, B.-N.; Wang, K.-H.; Yao, H.-B.; Yu, H.-L.; Li, J.-H.; Zhu, B.-S.; Song, J.-Z.; Chen, C. *Journal of the American Chemical Society* **2018,** 140, (10), 3626-3634.

222. Liu, W.; Lin, Q.; Li, H.; Wu, K.; Robel, I.; Pietryga, J. M.; Klimov, V. I. *Journal of the American Chemical Society* **2016,** 138, (45), 14954-14961.

223. Akkerman, Q. A.; D'Innocenzo, V.; Accornero, S.; Scarpellini, A.; Petrozza, A.; Prato, M.; Manna, L. *Journal of the American Chemical Society* **2015,** 137, (32), 10276-10281.

224. Makarov, N. S.; Guo, S.; Isaienko, O.; Liu, W.; Robel, I.; Klimov, V. I. *Nano letters* **2016,** 16, (4), 2349-2362.

225. Van der Stam, W.; Geuchies, J. J.; Altantzis, T.; Van Den Bos, K. H.; Meeldijk, J. D.; Van Aert, S.; Bals, S.; Vanmaekelbergh, D.; de Mello Donega, C. *Journal of the American Chemical Society* **2017,** 139, (11), 4087-4097.

226. Mir, W. J.; Jagadeeswararao, M.; Das, S.; Nag, A. *ACS Energy Letters* **2017,** 2, (3), 537-543.

227. Parobek, D.; Roman, B. J.; Dong, Y.; Jin, H.; Lee, E.; Sheldon, M.; Son, D. H. *Nano letters* **2016,** 16, (12), 7376-7380.

228. Li, Z.-J.; Hofman, E.; Davis, A. H.; Khammang, A.; Wright, J. T.; Dzikovski, B.; Meulenberg, R. W.; Zheng, W. *Chemistry of Materials* **2018,** 30, (18), 6400-6409.

229. Volonakis, G.; Filip, M. R.; Haghighirad, A. A.; Sakai, N.; Wenger, B.; Snaith, H. J.; Giustino, F. *The journal of physical chemistry letters* **2016,** 7, (7), 1254-1259.

230. Lin, C. C.; Xu, K. Y.; Wang, D.; Meijerink, A. *Scientific reports* **2017,** 7, 45906.

231. Han, A.; Han, E.; Han Hv, E. **2011**.

232. Hu, X.; Kang, R.; Zhang, Y.; Deng, L.; Zhong, H.; Zou, B.; Shi, L.-J. *Optics express* **2015,** 23, (15), A858-A867.

233. Aldakov, D.; Lefrançois, A.; Reiss, P. *Journal of Materials Chemistry C* **2013,** 1, (24), 3756-3776.

234. Kolny-Olesiak, J.; Weller, H. *ACS applied materials & interfaces* **2013,** 5, (23), 12221-12237.

235. Akkerman, Q. A.; Genovese, A.; George, C.; Prato, M.; Moreels, I.; Casu, A.; Marras, S.; Curcio, A.; Scarpellini, A.; Pellegrino, T. *ACS nano* **2015,** 9, (1), 521-531.

236. McDaniel, H.; Fuke, N.; Pietryga, J. M.; Klimov, V. I. *The journal of physical chemistry letters* **2013,** 4, (3), 355-361.

237. Yarema, O.; Bozyigit, D.; Rousseau, I.; Nowack, L.; Yarema, M.; Heiss, W.; Wood, V. *Chemistry of Materials* **2013,** 25, (18), 3753-3757.

238. McDaniel, H.; Fuke, N.; Makarov, N. S.; Pietryga, J. M.; Klimov, V. I. *Nature communications* **2013,** 4, (1), 1-10.

239. Panthani, M. G.; Akhavan, V.; Goodfellow, B.; Schmidtke, J. P.; Dunn, L.; Dodabalapur, A.; Barbara, P. F.; Korgel, B. A. *Journal of the American Chemical Society* **2008,** 130, (49), 16770-16777.

240. Meinardi, F.; McDaniel, H.; Carulli, F.; Colombo, A. *Nat. Nanotechnol* **2015,** 10, (10), 878-885.

241. Leach, A. D.; Macdonald, J. E. *The journal of physical chemistry letters* **2016,** 7, (3), 572-583.

242. Hu, W.; Ludwig, J.; Pattengale, B.; Yang, S.; Liu, C.; Zuo, X.; Zhang, X.; Huang, J. *The Journal of Physical Chemistry C* **2018,** 122, (1), 974-980.

243. Xia, C.; Wu, W.; Yu, T.; Xie, X.; Van Oversteeg, C.; Gerritsen, H. C.; de Mello Donega, C. *ACS nano* **2018,** 12, (8), 8350-8361.

244. Berends, A. C.; Rabouw, F. T.; Spoor, F. C.; Bladt, E.; Grozema, F. C.; Houtepen, A. J.; Siebbeles, L. D.; de Mello Donegá, C. *The journal of physical chemistry letters* **2016,** 7, (17), 3503-3509.

245. Zang, H.; Li, H.; Makarov, N. S.; Velizhanin, K. A.; Wu, K.; Park, Y.-S.; Klimov, V. I. *Nano letters* **2017,** 17, (3), 1787-1795.

246. Pinchetti, V.; Lorenzon, M.; McDaniel, H.; Lorenzi, R.; Meinardi, F.; Klimov, V. I.; Brovelli, S. *Nano Letters* **2017,** 17, (7), 4508-4517.

247. Fuhr, A. S.; Yun, H. J.; Makarov, N. S.; Li, H.; McDaniel, H.; Klimov, V. I. *ACS photonics* **2017,** 4, (10), 2425-2435.

248. van der Stam, W.; de Graaf, M.; Gudjonsdottir, S.; Geuchies, J. J.; Dijkema, J. J.; Kirkwood, N.; Evers, W. H.; Longo, A.; Houtepen, A. J. *Acs Nano* **2018,** 12, (11), 11244-11253.

249. Yun, H. J.; Lim, J.; Fuhr, A. S.; Makarov, N. S.; Keene, S.; Law, M.; Pietryga, J. M.; Klimov, V. I. *ACS nano* **2018,** 12, (12), 12587-12596.

250. Rice, W. D.; McDaniel, H.; Klimov, V. I.; Crooker, S. A. *The journal of physical chemistry letters* **2014,** 5, (23), 4105-4109.

251. Shabaev, A.; Mehl, M.; Efros, A. L. *Physical Review B* **2015,** 92, (3), 035431.

252. Kobosko, S. M.; Kamat, P. V. *The Journal of Physical Chemistry C* **2018,** 122, (26), 14336-14344.

253. Halpert, J. E.; Morgenstern, F. S.; Ehrler, B.; Vaynzof, Y.; Credgington, D.; Greenham, N. C. *ACS nano* **2015,** 9, (6), 5857-5867.

254. Jara, D. H.; Yoon, S. J.; Stamplecoskie, K. G.; Kamat, P. V. *Chemistry of Materials* **2014,** 26, (24), 7221-7228.

255. Levchuk, I.; Würth, C.; Krause, F.; Osvet, A.; Batentschuk, M.; Resch-Genger, U.; Kolbeck, C.; Herre, P.; Steinrück, H.; Peukert, W. *Energy & Environmental Science* **2016,** 9, (3), 1083-1094.

256. Voggu, V. R.; Sham, J.; Pfeffer, S.; Pate, J.; Fillip, L.; Harvey, T. B.; Brown Jr, R. M.; Korgel, B. A. *ACS Energy Letters* **2017,** 2, (3), 574-581.

257. Tang, J.; Hinds, S.; Kelley, S. O.; Sargent, E. H. *Chemistry of Materials* **2008,** 20, (22), 6906-6910.

258. Bergren, M. R.; Makarov, N. S.; Ramasamy, K.; Jackson, A.; Guglielmetti, R.; McDaniel, H. *ACS Energy Letters* **2018,** 3, (3), 520-525.

259. Li, C.; Chen, W.; Wu, D.; Quan, D.; Zhou, Z.; Hao, J.; Qin, J.; Li, Y.; He, Z.; Wang, K. *Scientific reports* **2015,** 5, 17777.

260. Wu, K.; Li, H.; Klimov, V. I. *Nature Photonics* **2018,** 12, (2), 105-110.

261. Bai, Z.; Ji, W.; Han, D.; Chen, L.; Chen, B.; Shen, H.; Zou, B.; Zhong, H. *Chemistry of Materials* **2016,** 28, (4), 1085-1091.

262. Chen, B.; Zhong, H.; Zhang, W.; Tan, Z. a.; Li, Y.; Yu, C.; Zhai, T.; Bando, Y.; Yang, S.; Zou, B. *Advanced Functional Materials* **2012,** 22, (10), 2081-2088.

263. Tan, Z.; Zhang, Y.; Xie, C.; Su, H.; Liu, J.; Zhang, C.; Dellas, N.; Mohney, S. E.; Wang, Y.; Wang, J. *Advanced materials* **2011,** 23, (31), 3553-3558.

264. Zhang, W.; Lou, Q.; Ji, W.; Zhao, J.; Zhong, X. *Chemistry of Materials* **2014,** 26, (2), 1204-1212.

265. Panthani, M. G.; Khan, T. A.; Reid, D. K.; Hellebusch, D. J.; Rasch, M. R.; Maynard, J. A.; Korgel, B. A. *Nano letters* **2013,** 13, (9), 4294-4298.

266. Sun, Z.; Sitbon, G.; Pons, T.; Bakulin, A. A.; Chen, Z. *Scientific reports* **2015,** 5, 10626.

267. De Trizio, L.; Prato, M.; Genovese, A.; Casu, A.; Povia, M.; Simonutti, R.; Alcocer, M. J.; D'Andrea, C.; Tassone, F.; Manna, L. *Chemistry of Materials* **2012,** 24, (12), 2400-2406.

268. Lox, J. F.; Dang, Z.; Dzhagan, V. M.; Spittel, D.; Martín-García, B.; Moreels, I.; Zahn, D. R.; Lesnyak, V. *Chemistry of Materials* **2018,** 30, (8), 2607-2617.

269. Singh, A.; Coughlan, C.; Milliron, D. J.; Ryan, K. M. *Chemistry of Materials* **2015,** 27, (5), 1517-1523.

270. Zhong, H.; Lo, S. S.; Mirkovic, T.; Li, Y.; Ding, Y.; Li, Y.; Scholes, G. D. *ACS nano* **2010,** 4, (9), 5253-5262.

271. Xia, C.; Meeldijk, J. D.; Gerritsen, H. C.; de Mello Donega, C. *Chemistry of Materials* **2017,** 29, (11), 4940-4951.

272. Zhong, H.; Bai, Z.; Zou, B. *The journal of physical chemistry letters* **2012,** 3, (21), 3167-3175.

273. Wang, Y.; Zhou, Y.; Zhang, Y.; Buhro, W. E. *Inorganic Chemistry* **2015,** 54, (3), 1165-1177.

274. Meinardi, F.; Bruni, F.; Brovelli, S. *Nature Reviews Materials* **2017,** 2, (12), 1-9.

275. Berends, A. C.; Mangnus, M. J.; Xia, C.; Rabouw, F. T.; de Mello Donega, C. *The journal of physical chemistry letters* **2019,** 10, (7), 1600-1616.

276. Hughes, K. E.; Ostheller, S. R.; Nelson, H. D.; Gamelin, D. R. *Nano letters* **2018,** 19, (2), 1318-1325.

277. Knowles, K. E.; Nelson, H. D.; Kilburn, T. B.; Gamelin, D. R. *Journal of the American Chemical Society* **2015,** 137, (40), 13138-13147.

278. Pandey, A.; Brovelli, S.; Viswanatha, R.; Li, L.; Pietryga, J.; Klimov, V. I.; Crooker, S. *Nature nanotechnology* **2012,** 7, (12), 792-797.

279. Liu, W.; Zhang, Y.; Zhai, W.; Wang, Y.; Zhang, T.; Gu, P.; Chu, H.; Zhang, H.; Cui, T.; Wang, Y. *The Journal of Physical Chemistry C* **2013,** 117, (38), 19288-19294.

280. Santiago-González, B.; Monguzzi, A.; Pinchetti, V.; Casu, A.; Prato, M.; Lorenzi, R.; Campione, M.; Chiodini, N.; Santambrogio, C.; Meinardi, F. *ACS nano* **2017,** 11, (6), 6233-6242.

281. Houck, D. W.; Assaf, E. I.; Shin, H.; Greene, R. M.; Pernik, D. R.; Korgel, B. A. *The Journal of Physical Chemistry C* **2019,** 123, (14), 9544-9551.

282. Kraatz, I. T.; Booth, M.; Whitaker, B. J.; Nix, M. G.; Critchley, K. *The Journal of Physical Chemistry C* **2014,** 118, (41), 24102-24109.

283. Leach, A. D.; Shen, X.; Faust, A.; Cleveland, M. C.; La Croix, A. D.; Banin, U.; Pantelides, S. T.; Macdonald, J. E. *The Journal of Physical Chemistry C* **2016,** 120, (9), 5207-5212.

284. Nelson, H. D.; Gamelin, D. R. *The Journal of Physical Chemistry C* **2018,** 122, (31), 18124-18133.

285. Nagamine, G.; Nunciaroni, H. B.; McDaniel, H.; Efros, A. L.; de Brito Cruz, C. H.; Padilha, L. A. *Nano letters* **2018,** 18, (10), 6353-6359.

286. Grandhi, G. K.; Viswanatha, R. *The Journal of Physical Chemistry Letters* **2013,** 4, (3), 409-415.

287. Romestain, R.; Fishman, G. *Physical Review B* **1994,** 49, (3), 1774.

288. Booth, M.; Brown, A. P.; Evans, S. D.; Critchley, K. *Chemistry of Materials* **2012,** 24, (11), 2064-2070.

289. Xie, R.; Rutherford, M.; Peng, X. *Journal of the American Chemical Society* **2009,** 131, (15), 5691-5697.

290. Ridley, B. K., *Quantum processes in semiconductors*. Oxford University Press: 2013.

291. Blokland, J.; Claessen, V.; Wijnen, F.; Groeneveld, E.; de Mello Donegá, C.; Vanmaekelbergh, D.; Meijerink, A.; Maan, J.; Christianen, P. *Physical Review B* **2011,** 83, (3), 035304.

292. Eilers, J.; Van Hest, J.; Meijerink, A.; Donega, C. d. M. *The Journal of Physical Chemistry C* **2014,** 118, (40), 23313-23319.

293. Granados Del Águila, A.; Groeneveld, E.; Maan, J. C.; de Mello Donegá, C.; Christianen, P. C. *ACS nano* **2016,** 10, (4), 4102-4110.

294. Oron, D.; Aharoni, A.; de Mello Donega, C.; Van Rijssel, J.; Meijerink, A.; Banin, U. *Physical review letters* **2009,** 102, (17), 177402.

295. Robert, C.; Amand, T.; Cadiz, F.; Lagarde, D.; Courtade, E.; Manca, M.; Taniguchi, T.; Watanabe, K.; Urbaszek, B.; Marie, X. *Physical review B* **2017,** 96, (15), 155423.

296. Debije, M. G.; Tzikas, C.; Rajkumar, V. A.; de Jong, M. M. *Renewable Energy* **2017,** 113, 1288-1292.

297. Aste, N.; Tagliabue, L. C.; Del Pero, C.; Testa, D.; Fusco, R. *Renewable Energy* **2015,** 76, 330-337.

298. Debije, M. G. *Advanced Functional Materials* **2010,** 20, (9), 1498-1502.

299. Lesyuk, R.; Lesnyak, V.; Herguth, A.; Popovych, D.; Bobitski, Y.; Klinke, C.; Gaponik, N. *Journal of Materials Chemistry C* **2017,** 5, (45), 11790-11797.

300. Uehara, M.; Watanabe, K.; Tajiri, Y.; Nakamura, H.; Maeda, H. *The Journal of Chemical Physics* **2008,** 129, (13), 134709.

301. Meinardi, F.; Ehrenberg, S.; Dhamo, L.; Carulli, F.; Mauri, M.; Bruni, F.; Simonutti, R.; Kortshagen, U.; Brovelli, S. *Nature Photonics* **2017,** 11, (3), 177-185.

302. Boles, M. A.; Engel, M.; Talapin, D. V. *Chemical reviews* **2016,** 116, (18), 11220-11289.

303. Gao, Y.; Tang, Z. *Small* **2011,** 7, (15), 2133-2146.

304. Grzelczak, M.; Vermant, J.; Furst, E. M.; Liz-Marzán, L. M. *ACS nano* **2010,** 4, (7), 3591-3605.

305. Kovalenko, M. V.; Manna, L.; Cabot, A.; Hens, Z.; Talapin, D. V.; Kagan, C. R.; Klimov, V. I.; Rogach, A. L.; Reiss, P.; Milliron, D. J., Prospects of nanoscience with nanocrystals. ACS Publications: 2015.

306. Boles, M. A.; Ling, D.; Hyeon, T.; Talapin, D. V. *Nature materials* **2016,** 15, (2), 141-153.

307. De Trizio, L.; Manna, L. *Chemical reviews* **2016,** 116, (18), 10852-10887.

308. Owen, J.; Brus, L. *Journal of the American Chemical Society* **2017,** 139, (32), 10939-10943.

309. Reiss, P.; Carriere, M.; Lincheneau, C.; Vaure, L.; Tamang, S. *Chemical reviews* **2016,** 116, (18), 10731-10819.

310. Carey, G. H.; Abdelhady, A. L.; Ning, Z.; Thon, S. M.; Bakr, O. M.; Sargent, E. H. *Chemical reviews* **2015,** 115, (23), 12732-12763.

311. Talapin, D. V.; Lee, J.-S.; Kovalenko, M. V.; Shevchenko, E. V. *Chemical reviews* **2010,** 110, (1), 389-458.

312. Bradshaw, L. R.; Knowles, K. E.; McDowall, S.; Gamelin, D. R. *Nano letters* **2015,** 15, (2), 1315-1323.

313. Choi, J.-H.; Oh, S. J.; Lai, Y.; Kim, D. K.; Zhao, T.; Fafarman, A. T.; Diroll, B. T.; Murray, C. B.; Kagan, C. R. *ACS nano* **2013,** 7, (9), 8275-8283.

314. Choi, J.-H.; Wang, H.; Oh, S. J.; Paik, T.; Sung, P.; Sung, J.; Ye, X.; Zhao, T.; Diroll, B. T.; Murray, C. B. *Science* **2016,** 352, (6282), 205-208.

315. Kang, M. S.; Sahu, A.; Frisbie, C. D.; Norris, D. J. *Advanced Materials* **2013,** 25, (5), 725-731.

316. Sahu, A.; Braga, D.; Waser, O.; Kang, M. S.; Deng, D.; Norris, D. J. *Nano letters* **2014,** 14, (1), 115-121.

317. Sharma, M.; Gungor, K.; Yeltik, A.; Olutas, M.; Guzelturk, B.; Kelestemur, Y.; Erdem, T.; Delikanli, S.; McBride, J. R.; Demir, H. V. *Advanced Materials* **2017,** 29, (30), 1700821.

318. Geiregat, P.; Houtepen, A. J.; Sagar, L. K.; Infante, I.; Zapata, F.; Grigel, V.; Allan, G.; Delerue, C.; Van Thourhout, D.; Hens, Z. *Nature Materials* **2018,** 17, (1), 35-42.

319. Wu, K.; Park, Y.-S.; Lim, J.; Klimov, V. I. *Nature Nanotechnology* **2017,** 12, (12), 1140-1147.

320. Voznyy, O.; Zhitomirsky, D.; Stadler, P.; Ning, Z.; Hoogland, S.; Sargent, E. H. *ACS nano* **2012,** 6, (9), 8448-8455.

321. Kirmani, A. R.; Kiani, A.; Said, M. M.; Voznyy, O.; Wehbe, N.; Walters, G.; Barlow, S.; Sargent, E. H.; Marder, S. R.; Amassian, A. *ACS Energy Letters* **2016,** 1, (5), 922-930.

322. Stavrinadis, A.; Rath, A. K.; De Arquer, F. P. G.; Diedenhofen, S. L.; Magén, C.; Martinez, L.; So, D.; Konstantatos, G. *Nature communications* **2013,** 4, (1), 1-7.

323. Luther, J. M.; Jain, P. K.; Ewers, T.; Alivisatos, A. P. *Nature materials* **2011,** 10, (5), 361-366.

324. Kroupa, D. M.; Hughes, B. K.; Miller, E. M.; Moore, D. T.; Anderson, N. C.; Chernomordik, B. D.; Nozik, A. J.; Beard, M. C. *Journal of the American Chemical Society* **2017,** 139, (30), 10382-10394.

325. Kompch, A.; Sahu, A.; Notthoff, C.; Ott, F.; Norris, D. J.; Winterer, M. *The Journal of Physical Chemistry C* **2015,** 119, (32), 18762-18772.

326. Bindra, J. K.; Kurian, G.; Christian, J. H.; Van Tol, J.; Singh, K.; Dalal, N. S.; Mochena, M. D.; Stoian, S. A.; Strouse, G. F. *Chemistry of Materials* **2018,** 30, (23), 8446-8456.

327. Roy, S.; Tuinenga, C.; Fungura, F.; Dagtepe, P.; Chikan, V.; Jasinski, J. *The Journal of Physical Chemistry C* **2009,** 113, (30), 13008-13015.

328. Tuinenga, C.; Jasinski, J.; Iwamoto, T.; Chikan, V. *Acs Nano* **2008,** 2, (7), 1411-1421.

329. Wills, A. W.; Kang, M. S.; Wentz, K. M.; Hayes, S. E.; Sahu, A.; Gladfelter, W. L.; Norris, D. J. *Journal of Materials Chemistry* **2012,** 22, (13), 6335-6342.

330. Mokari, T.; Aharoni, A.; Popov, I.; Banin, U. *Angewandte Chemie* **2006,** 118, (47), 8169-8173.

331. Buonsanti, R.; Milliron, D. J. *Chemistry of Materials* **2013,** 25, (8), 1305-1317.

332. Hassan, A.; Zhang, X.; Liu, X.; Rowland, C. E.; Jawaid, A. M.; Chattopadhyay, S.; Gulec, A.; Shamirian, A.; Zuo, X.; Klie, R. F. *ACS nano* **2017,** 11, (10), 10070-10076.

333. Jawaid, A. M.; Chattopadhyay, S.; Wink, D. J.; Page, L. E.; Snee, P. T. *ACS nano* **2013,** 7, (4), 3190-3197.

334. Ye, X.; Fei, J.; Diroll, B. T.; Paik, T.; Murray, C. B. *Journal of the American Chemical Society* **2014,** 136, (33), 11680-11686.

335. Hassan, A.; Zhang, X.; Liu, C.; Snee, P. T. *The Journal of Physical Chemistry C* **2018,** 122, (20), 11145-11151.

336. Luo, Z.; Yuan, X.; Yu, Y.; Zhang, Q.; Leong, D. T.; Lee, J. Y.; Xie, J. *Journal of the American Chemical Society* **2012,** 134, (40), 16662-16670.

337. De Heer, W. A. *Reviews of Modern Physics* **1993,** 65, (3), 611.

338. Stamplecoskie, K. G.; Kamat, P. V. *Journal of the American Chemical Society* **2014,** 136, (31), 11093-11099.

339. Casaletto, M.; Longo, A.; Martorana, A.; Prestianni, A.; Venezia, A. *Surface and Interface Analysis: An International Journal devoted to the development and application of techniques for the analysis of surfaces, interfaces and thin films* **2006,** 38, (4), 215-218.

340. Thomas, T. D.; Weightman, P. *Physical Review B* **1986,** 33, (8), 5406.

341. Yang, Y. A.; Wu, H.; Williams, K. R.; Cao, Y. C. *Angewandte Chemie* **2005,** 117, (41), 6870-6873.

342. Yu, W. W.; Qu, L.; Guo, W.; Peng, X. *Chemistry of Materials* **2003,** 15, (14), 2854-2860.

343. Knowles, K. E.; Hartstein, K. H.; Kilburn, T. B.; Marchioro, A.; Nelson, H. D.; Whitham, P. J.; Gamelin, D. R. *Chemical reviews* **2016,** 116, (18), 10820-10851.

344. Aven, M.; Segall, B. *Physical Review* **1963,** 130, (1), 81.

345. Georgobiani, A.; Aminov, U.; Dravin, V.; Lepnev, L.; Mullabaev, I.; Ursaki, V.; Iljukhina, Z. *Nuclear Instruments and Methods in Physics Research Section A: Accelerators, Spectrometers, Detectors and Associated Equipment* **1999,** 426, (1), 164-168.

346. Nedeoglo, N.; Avdonin, A.; Ivanova, G.; Nedeoglo, D.; Kolibaba, G.; Sirkeli, V. *Journal of luminescence* **2005,** 112, (1-4), 62-65.

347. Avinor, M.; Meijer, G. *The Journal of Chemical Physics* **1960,** 32, (5), 1456-1458.

348. Poolton, N. *Journal of Physics C: Solid State Physics* **1987,** 20, (34), 5867.

349. Lorenzon, M.; Sortino, L.; Akkerman, Q.; Accornero, S.; Pedrini, J.; Prato, M.; Pinchetti, V.; Meinardi, F.; Manna, L.; Brovelli, S. *Nano letters* **2017,** 17, (6), 3844-3853.

350. Jha, P. P.; Guyot-Sionnest, P. *ACS nano* **2009,** 3, (4), 1011-1015.

351. Galland, C.; Ghosh, Y.; Steinbrück, A.; Sykora, M.; Hollingsworth, J. A.; Klimov, V. I.; Htoon, H. *Nature* **2011,** 479, (7372), 203-207.

352. Makarov, N. S.; McDaniel, H.; Fuke, N.; Robel, I.; Klimov, V. I. *The journal of physical chemistry letters* **2014,** 5, (1), 111-118.

353. Padilha, L. A.; Bae, W. K.; Klimov, V. I.; Pietryga, J. M.; Schaller, R. D. *Nano letters* **2013,** 13, (3), 925-932.

354. Yu, W. W.; Peng, X. *Angewandte Chemie International Edition* **2002,** 41, (13), 2368-2371.

355. Siy, J. T.; Bartl, M. H. *Chemistry of Materials* **2010,** 22, (21), 5973-5982.

356. Yang, C.; Faust, A.; Amit, Y.; Gdor, I.; Banin, U.; Ruhman, S. *The Journal of Physical Chemistry A* **2016,** 120, (19), 3088-3097.

357. Furdyna, J. K. *Journal of Applied Physics* **1988,** 64, (4), R29-R64.

358. Akkerman, Q. A.; Motti, S. G.; Srimath Kandada, A. R.; Mosconi, E.; D'Innocenzo, V.; Bertoni, G.; Marras, S.; Kamino, B. A.; Miranda, L.; De Angelis, F. *Journal of the American Chemical Society* **2016,** 138, (3), 1010-1016.

359. Hoffman, J. B.; Schleper, A. L.; Kamat, P. V. *Journal of the American Chemical Society* **2016,** 138, (27), 8603-8611.

360. Shamsi, J.; Dang, Z.; Bianchini, P.; Canale, C.; Di Stasio, F.; Brescia, R.; Prato, M.; Manna, L. *Journal of the American Chemical Society* **2016,** 138, (23), 7240-7243.

361. Sun, H.; Li, Z.; Kong, L.; Wang, B.; Zhang, C.; Yuan, Q.; Huang, S.; Liu, Y.; Li, L. *Chemical Communications* **2018,** 54, (67), 9345-9348.

362. Kang, J.; Wang, L.-W. *The journal of physical chemistry letters* **2017,** 8, (2), 489-493.

363. Xu, Y.; Chen, Q.; Zhang, C.; Wang, R.; Wu, H.; Zhang, X.; Xing, G.; Yu, W. W.; Wang, X.; Zhang, Y. *Journal of the American Chemical Society* **2016,** 138, (11), 3761-3768.

364. Cauzzi, D.; Pattacini, R.; Delferro, M.; Dini, F.; Di Natale, C.; Paolesse, R.; Bonacchi, S.; Montalti, M.; Zaccheroni, N.; Calvaresi, M. *Angewandte Chemie International Edition* **2012,** 51, (38), 9662-9665.

365. Li, G.; Rivarola, F. W. R.; Davis, N. J.; Bai, S.; Jellicoe, T. C.; de la Peña, F.; Hou, S.; Ducati, C.; Gao, F.; Friend, R. H. *Advanced materials* **2016,** 28, (18), 3528-3534.

366. Yao, E. P.; Yang, Z.; Meng, L.; Sun, P.; Dong, S.; Yang, Y.; Yang, Y. *Advanced Materials* **2017,** 29, (23), 1606859.

367. Zhang, C.; Wang, B.; Zheng, W.; Huang, S.; Kong, L.; Li, Z.; He, G.; Li, L. *Nano Energy* **2018,** 51, 358-365.

368. Akkerman, Q. A.; Gandini, M.; Di Stasio, F.; Rastogi, P.; Palazon, F.; Bertoni, G.; Ball, J. M.; Prato, M.; Petrozza, A.; Manna, L. *Nature Energy* **2016,** 2, (2), 1-7.

369. Christodoulou, S.; Di Stasio, F.; Pradhan, S.; Stavrinadis, A.; Konstantatos, G. *The Journal of Physical Chemistry C* **2018,** 122, (14), 7621-7626.

370. Swarnkar, A.; Marshall, A. R.; Sanehira, E. M.; Chernomordik, B. D.; Moore, D. T.; Christians, J. A.; Chakrabarti, T.; Luther, J. M. *Science* **2016,** 354, (6308), 92-95.

371. Zhang, J.; Wang, Q.; Zhang, X.; Jiang, J.; Gao, Z.; Jin, Z.; Liu, S. F. *RSC advances* **2017,** 7, (58), 36722-36727.

372. Zhang, X.; Wang, Q.; Jin, Z.; Zhang, J.; Liu, S. F. *Nanoscale* **2017,** 9, (19), 6278-6285.

373. Lin, F.; Li, F.; Lai, Z.; Cai, Z.; Wang, Y.; Wolfbeis, O. S.; Chen, X. *ACS applied materials & interfaces* **2018,** 10, (27), 23335-23343.

374. He, T.; Li, J.; Ren, C.; Xiao, S.; Li, Y.; Chen, R.; Lin, X. *Applied Physics Letters* **2017,** 111, (21), 211105.

375. Yuan, X.; Ji, S.; De Siena, M. C.; Fei, L.; Zhao, Z.; Wang, Y.; Li, H.; Zhao, J.; Gamelin, D. R. *Chemistry of Materials* **2017,** 29, (18), 8003-8011.

376. Becker, M. A.; Vaxenburg, R.; Nedelcu, G.; Sercel, P. C.; Shabaev, A.; Mehl, M. J.; Michopoulos, J. G.; Lambrakos, S. G.; Bernstein, N.; Lyons, J. L. *Nature* **2018,** 553, (7687), 189-193.

377. Protesescu, L.; Yakunin, S.; Bodnarchuk, M. I.; Krieg, F.; Caputo, R.; Hendon, C. H.; Yang, R. X.; Walsh, A.; Kovalenko, M. V. *Nano letters* **2015,** 15, (6), 3692-3696.

378. Wang, Q.; Zhang, X.; Jin, Z.; Zhang, J.; Gao, Z.; Li, Y.; Liu, S. F. *ACS Energy Letters* **2017,** 2, (7), 1479-1486.

379. Morozov, Y. V.; Zhang, S.; Brennan, M. C.; Janko, B.; Kuno, M. *ACS Energy Letters* **2017,** 2, (10), 2514-2515.

380. Roman, B. J.; Sheldon, M. *Chemical Communications* **2018,** 54, (50), 6851-6854.

381. Ye, S.; Zhao, M.; Yu, M.; Zhu, M.; Yan, W.; Song, J.; Qu, J. *The Journal of Physical Chemistry C* **2018,** 122, (5), 3152-3156.

382. Bradshaw, L. R.; Hauser, A.; McLaurin, E. J.; Gamelin, D. R. *The Journal of Physical Chemistry C* **2012,** 116, (16), 9300-9310.

383. Diroll, B. T.; Zhou, H.; Schaller, R. D. *Advanced Functional Materials* **2018,** 28, (30), 1800945.

384. Etienne, T.; Mosconi, E.; De Angelis, F. *The Journal of Physical Chemistry Letters* **2016,** 7, (9), 1638-1645.

385. Pfingsten, O.; Klein, J.; Protesescu, L.; Bodnarchuk, M. I.; Kovalenko, M. V.; Bacher, G. *Nano Letters* **2018,** 18, (7), 4440-4446.

386. Cape, J.; White, R.; Feigelson, R. *Journal of Applied Physics* **1969,** 40, (13), 5001-5005.

387. Biswas, S.; Kar, S.; Chaudhuri, S. *The Journal of Physical Chemistry B* **2005,** 109, (37), 17526-17530.

388. Borse, P.; Srinivas, D.; Shinde, R.; Date, S.; Vogel, W.; Kulkarni, S. *Physical review B* **1999,** 60, (12), 8659.

389. Jun, Y.-w.; Jung, Y.-y.; Cheon, J. *Journal of the American chemical society* **2002,** 124, (4), 615-619.

390. Nistor, S. V.; Stefan, M.; Nistor, L. C.; Ghica, D.; Vlaicu, I. D.; Joita, A. C. *The Journal of Physical Chemistry C* **2015,** 119, (41), 23781-23789.

391. Sitbon, G.; Bouccara, S.; Tasso, M.; Francois, A.; Bezdetnaya, L.; Marchal, F.; Beaumont, M.; Pons, T. *Nanoscale* **2014,** 6, (15), 9264-9272.

392. Stowell, C. A.; Wiacek, R. J.; Saunders, A. E.; Korgel, B. A. *Nano Letters* **2003,** 3, (10), 1441-1447.

393. Yang, J.; Gray, H.; Hsu, D.; Qadri, S.; Rubin, G.; Ratna, B.; Warren, W.; Seager, C. *Journal of the Society for Information Display* **1998,** 6, (3), 139-142.

394. Manna, L.; Milliron, D. J.; Meisel, A.; Scher, E. C.; Alivisatos, A. P. *Nature materials* **2003,** 2, (6), 382-385.

395. Yin, Y.; Alivisatos, A. P. *Nature* **2005,** 437, (7059), 664-670.

396. Michalet, X.; Pinaud, F. F.; Bentolila, L. A.; Tsay, J. M.; Doose, S.; Li, J. J.; Sundaresan, G.; Wu, A.; Gambhir, S.; Weiss, S. *science* **2005,** 307, (5709), 538-544.

397. Mahler, B.; Lequeux, N.; Dubertret, B. *Journal of the American Chemical Society* **2010,** 132, (3), 953-959.

398. Xia, Y.; Xiong, Y.; Lim, B.; Skrabalak, S. E. *Angewandte Chemie International Edition* **2009,** 48, (1), 60-103.

399. Ekimov, A.; Efros, A. L. *physica status solidi (b)* **1988,** 150, (2), 627-633.

400. Grabovskis, V. Y.; Dzenis, Y.; Ekimov, A. *Fizika Tverdogo Tela* **1989,** 31, (1), 272-275.

401. Smith, A. M.; Nie, S. *Accounts of chemical research* **2010,** 43, (2), 190-200.

402. Vaxenburg, R.; Rodina, A.; Lifshitz, E.; Efros, A. L. *Nano Letters* **2016,** 16, (4), 2503-2511.

403. Wang, Y.; Ta, V. D.; Gao, Y.; He, T. C.; Chen, R.; Mutlugun, E.; Demir, H. V.; Sun, H. D. *Advanced Materials* **2014,** 26, (18), 2954-2961.

404. Vasudevan, D.; Gaddam, R. R.; Trinchi, A.; Cole, I. *Journal of Alloys and Compounds* **2015,** 636, 395-404.

405. Dai, X.; Deng, Y.; Peng, X.; Jin, Y. *Advanced materials* **2017,** 29, (14), 1607022.

406. Mashford, B. S.; Stevenson, M.; Popovic, Z.; Hamilton, C.; Zhou, Z.; Breen, C.; Steckel, J.; Bulovic, V.; Bawendi, M.; Coe-Sullivan, S. *Nature photonics* **2013,** 7, (5), 407-412.

407. Supran, G. J.; Shirasaki, Y.; Song, K. W.; Caruge, J.-M.; Kazlas, P. T.; Coe-Sullivan, S.; Andrew, T. L.; Bawendi, M. G.; Bulović, V. **2013**.

408. Dang, C.; Lee, J.; Breen, C.; Steckel, J. S.; Coe-Sullivan, S.; Nurmikko, A. *Nature nanotechnology* **2012,** 7, (5), 335-339.

409. Klimov, V.; Mikhailovsky, A.; Xu, S.; Malko, A.; Hollingsworth, J.; Leatherdale, a. C.; Eisler, H.-J.; Bawendi, M. *science* **2000,** 290, (5490), 314-317.

410. Wang, Y.; Li, X.; Song, J.; Xiao, L.; Zeng, H.; Sun, H. *Advanced materials* **2015,** 27, (44), 7101-7108.

411. Bartnik, A.; Efros, A. L.; Koh, W.-K.; Murray, C.; Wise, F. *Physical Review B* **2010,** 82, (19), 195313.

412. Muljarov, E. A.; Zhukov, E.; Dneprovskii, V.; Masumoto, Y. *Physical Review B* **2000,** 62, (11), 7420.

413. Mulyarov, E.; Tikhodeev, S. *Journal of Experimental and Theoretical Physics* **1997,** 84, (1), 151-155.

414. Shabaev, A.; Efros, A. L. *Nano letters* **2004,** 4, (10), 1821-1825.

415. Gippius, N.; Yablonskii, A.; Dzyubenko, A.; Tikhodeev, S.; Kulik, L.; Kulakovskii, V.; Forchel, A. *Journal of applied physics* **1998,** 83, (10), 5410-5417.

416. Keldysh, L. *JETPL* **1979,** 29, 658.

417. Kulik, L.; Kulakovskii, V.; Bayer, M.; Forchel, A.; Gippius, N.; Tikhodeev, S. *Physical Review B* **1996,** 54, (4), R2335.

418. Tikhodeev, S.; Gippius, N.; Yablonskii, A.; Dzyubenko, A.; Kulik, L.; Kulakovskii, V.; Forchel, A. *physica status solidi (a)* **1997,** 164, (1), 179-182.

419. Achtstein, A. W.; Schliwa, A.; Prudnikau, A.; Hardzei, M.; Artemyev, M. V.; Thomsen, C.; Woggon, U. *Nano letters* **2012,** 12, (6), 3151-3157.

420. Benchamekh, R.; Gippius, N. A.; Even, J.; Nestoklon, M.; Jancu, J.-M.; Ithurria, S.; Dubertret, B.; Efros, A. L.; Voisin, P. *Physical Review B* **2014,** 89, (3), 035307.

421. Rashba, E. *Sov. Phys. Solid State* **1962,** 4, 759.

422. Feldmann, J.; Peter, G.; Göbel, E.; Dawson, P.; Moore, K.; Foxon, C.; Elliott, R. *Physical review letters* **1987,** 59, (20), 2337.

423. Kan, C.; Wang, C.; Li, H.; Qi, J.; Zhu, J.; Li, Z.; Shi, D. *Small* **2010,** 6, (16), 1768-1775.

424. Puntes, V. F.; Zanchet, D.; Erdonmez, C. K.; Alivisatos, A. P. *Journal of the American Chemical Society* **2002,** 124, (43), 12874-12880.

425. Huo, Z.; Tsung, C.-K.; Huang, W.; Fardy, M.; Yan, R.; Zhang, X.; Li, Y.; Yang, P. *Nano Letters* **2009,** 9, (3), 1260-1264.

426. Yu, T.; Lim, B.; Xia, Y. *Angewandte Chemie* **2010,** 122, (26), 4586-4589.

427. Ithurria, S.; Dubertret, B. *Journal of the American Chemical Society* **2008,** 130, (49), 16504-16505.

428. Joo, J.; Son, J. S.; Kwon, S. G.; Yu, J. H.; Hyeon, T. *Journal of the American Chemical Society* **2006,** 128, (17), 5632-5633.

429. Kumar, S.; Nann, T. *Small* **2006,** 2, (3), 316-329.

430. Peng, Z. A.; Peng, X. *Journal of the American Chemical Society* **2002,** 124, (13), 3343-3353.

431. Son, J. S.; Wen, X. D.; Joo, J.; Chae, J.; Baek, S. i.; Park, K.; Kim, J. H.; An, K.; Yu, J. H.; Kwon, S. G. *Angewandte Chemie* **2009,** 121, (37), 6993-6996.

432. Liu, Y.-H.; Wang, F.; Wang, Y.; Gibbons, P. C.; Buhro, W. E. *Journal of the American Chemical Society* **2011,** 133, (42), 17005-17013.

433. Liu, Y.-H.; Wayman, V. L.; Gibbons, P. C.; Loomis, R. A.; Buhro, W. E. *Nano letters* **2010,** 10, (1), 352-357.

434. Wang, Y.; Zhang, Y.; Wang, F.; Giblin, D. E.; Hoy, J.; Rohrs, H. W.; Loomis, R. A.; Buhro, W. E. *Chemistry of Materials* **2014,** 26, (7), 2233-2243.

435. Son, J. S.; Park, K.; Kwon, S. G.; Yang, J.; Choi, M. K.; Kim, J.; Yu, J. H.; Joo, J.; Hyeon, T. *Small* **2012,** 8, (15), 2394-2402.

436. Du, Y.; Yin, Z.; Zhu, J.; Huang, X.; Wu, X.-J.; Zeng, Z.; Yan, Q.; Zhang, H. *Nature communications* **2012,** 3, (1), 1-7.

437. Buffard, A.; Nadal, B.; Heuclin, H.; Patriarche, G.; Dubertret, B. *New Journal of Chemistry* **2015,** 39, (1), 90-93.

438. Weidman, M. C.; Goodman, A. J.; Tisdale, W. A. *Chemistry of Materials* **2017,** 29, (12), 5019-5030.

439. Ithurria, S.; Bousquet, G.; Dubertret, B. *Journal of the American Chemical Society* **2011,** 133, (9), 3070-3077.

440. Chen, Y.; Chen, D.; Li, Z.; Peng, X. *Journal of the American Chemical Society* **2017,** 139, (29), 10009-10019.

441. Abécassis, B.; Tessier, M. D.; Davidson, P.; Dubertret, B. *Nano letters* **2014,** 14, (2), 710-715.

442. Jana, S.; Phan, T. N.; Bouet, C.; Tessier, M. D.; Davidson, P.; Dubertret, B.; Abécassis, B. *Langmuir* **2015,** 31, (38), 10532-10539.

443. Tessier, M. D.; Biadala, L.; Bouet, C.; Ithurria, S.; Abecassis, B.; Dubertret, B. *ACS nano* **2013,** 7, (4), 3332-3340.

444. Bouet, C.; Mahler, B.; Nadal, B.; Abecassis, B.; Tessier, M. D.; Ithurria, S.; Xu, X.; Dubertret, B. *Chemistry of Materials* **2013,** 25, (4), 639-645.

445. Hutter, E. M.; Bladt, E.; Goris, B.; Pietra, F.; Van Der Bok, J. C.; Boneschanscher, M. P.; de Mello Donegá, C.; Bals, S.; Vanmaekelbergh, D. l. *Nano letters* **2014,** 14, (11), 6257-6262.

446. Chu, A.; Livache, C.; Ithurria, S.; Lhuillier, E. *Journal of Applied Physics* **2018,** 123, (3), 035701.

447. Christodoulou, S.; Climente, J. I.; Planelles, J.; Brescia, R.; Prato, M.; Martín-García, B.; Khan, A. H.; Moreels, I. *Nano letters* **2018,** 18, (10), 6248-6254.

448. Ithurria, S.; Talapin, D. V. *Journal of the American Chemical Society* **2012,** 134, (45), 18585-18590.

449. Altintas, Y.; Quliyeva, U.; Gungor, K.; Erdem, O.; Kelestemur, Y.; Mutlugun, E.; Kovalenko, M. V.; Demir, H. V. *Small* **2019,** 15, (8), 1804854.

450. Rossinelli, A. A.; Riedinger, A.; Marqués-Gallego, P.; Knüsel, P. N.; Antolinez, F. V.; Norris, D. J. *Chemical Communications* **2017,** 53, (71), 9938-9941.

451. Prudnikau, A.; Chuvilin, A.; Artemyev, M. *Journal of the American Chemical Society* **2013,** 135, (39), 14476-14479.

452. Delikanli, S.; Guzelturk, B.; Hernández-Martínez, P. L.; Erdem, T.; Kelestemur, Y.; Olutas, M.; Akgul, M. Z.; Demir, H. V. *Advanced Functional Materials* **2015,** 25, (27), 4282-4289.

453. Pedetti, S.; Ithurria, S.; Heuclin, H.; Patriarche, G.; Dubertret, B. *Journal of the American Chemical Society* **2014,** 136, (46), 16430-16438.

454. Khan, A. H.; Bertrand, G. H.; Teitelboim, A.; Sekhar M, C.; Polovitsyn, A.; Brescia, R.; Planelles, J.; Climente, J. I.; Oron, D.; Moreels, I. *ACS nano* **2020,** 14, (4), 4206-4215.

455. Maiti, P. S.; Houben, L.; Bar-Sadan, M. *The Journal of Physical Chemistry C* **2015,** 119, (19), 10734-10739.

456. Tenne, R.; Pedetti, S.; Kazes, M.; Ithurria, S.; Houben, L.; Nadal, B.; Oron, D.; Dubertret, B. *Physical Chemistry Chemical Physics* **2016,** 18, (22), 15295-15303.

457. Fan, F.; Kanjanaboos, P.; Saravanapavanantham, M.; Beauregard, E.; Ingram, G.; Yassitepe, E.; Adachi, M. M.; Voznyy, O.; Johnston, A. K.; Walters, G. *Nano letters* **2015,** 15, (7), 4611-4615.

458. Sokolikova, M.; Shlenskaya, N.; Kozlovskii, V.; Vasiliev, R.; Gaskov, A. *Russian Journal of Inorganic Chemistry* **2014,** 59, (10), 1069-1072.

459. Galle, T.; Kazes, M.; Hübner, R.; Lox, J.; Samadi Khoshkhoo, M.; Sonntag, L.; Tietze, R.; Sayevich, V.; Oron, D.; Koitzsch, A. *Chemistry of Materials* **2019,** 31, (14), 5065-5074.

460. Khan, A. H.; Pinchetti, V.; Tanghe, I.; Dang, Z.; Martín-García, B.; Hens, Z.; Van Thourhout, D.; Geiregat, P.; Brovelli, S.; Moreels, I. *Chemistry of Materials* **2019,** 31, (4), 1450-1459.

461. Sharma, M.; Olutas, M.; Yeltik, A.; Kelestemur, Y.; Sharma, A.; Delikanli, S.; Guzelturk, B.; Gungor, K.; McBride, J. R.; Demir, H. V. *Chemistry of Materials* **2018,** 30, (10), 3265-3275.

462. *Landolt-Bornstein Tables, New Series, Group III: Crystals and Solid*

State Physics. Springer-Verlag: Berlin, 1982; Vol. Vol. 17.

463. Gur, I.; Fromer, N. A.; Chen, C.-P.; Kanaras, A. G.; Alivisatos, A. P. *Nano letters* **2007,** 7, (2), 409-414.

464. Xie, X.; Kwok, S.-Y.; Lu, Z.; Liu, Y.; Cao, Y.; Luo, L.; Zapien, J. A.; Bello, I.; Lee, C.-S.; Lee, S.-T. *Nanoscale* **2012,** 4, (9), 2914-2919.

465. Yu, W. W.; Wang, Y. A.; Peng, X. *Chemistry of Materials* **2003,** 15, (22), 4300-4308.

466. Talapin, D. V.; Haubold, S.; Rogach, A. L.; Kornowski, A.; Haase, M.; Weller, H. *The Journal of Physical Chemistry B* **2001,** 105, (12), 2260-2263.

467. Mamedova, N. N.; Kotov, N. A.; Rogach, A. L.; Studer, J. *Nano Letters* **2001,** 1, (6), 281-286.

468. Carbone, L. K., S.; Carlino, E.; Parak, W. J.; Giannini, C.;; Cingolani, R. M., L. J. *Am. Chem. Soc* **2006**, (128 (3),), 748−55.

469. Sun, J.; Buhro, W. E.; Wang, L.-W.; Schrier, J. *Nano letters* **2008,** 8, (9), 2913-2919.

470. Pan, J.; Qian, Y. *Materials Letters* **2012,** 85, 132-134.

471. Tessier, M.; Mahler, B.; Lobo, R. *Nat. Mater* **2011,** 10, 936.

472. Tang, Z. Y. Z., Z. L.; Wang, Y.; Glotzer, S. C.; Kotov, N. A. *Science*

2006, 314 (5797), 274−278.

473. Pedetti, S.; Nadal, B.; Lhuillier, E.; Mahler, B.; Bouet, C. c.; Abécassis, B.; Xu, X.; Dubertret, B. *Chemistry of Materials* **2013,** 25, (12), 2455-2462.

474. Dujardin, C.; Auffray, E.; Bourret-Courchesne, E.; Dorenbos, P.; Lecoq, P.; Nikl, M.; Vasil'Ev, A.; Yoshikawa, A.; Zhu, R.-Y. *IEEE Transactions on Nuclear Science* **2018,** 65, (8), 1977-1997.

475. Li, Z.; Qin, H.; Guzun, D.; Benamara, M.; Salamo, G.; Peng, X. *Nano Research* **2012,** 5, (5), 337-351.